


12-1-2015

Crystalline Phase Change in Steel Alloys due to High Speed Impact

Muna Slewa

University of Nevada, Las Vegas, slewa@unlv.nevada.edu

Follow this and additional works at: <https://digitalscholarship.unlv.edu/thesesdissertations>

 Part of the [Engineering Science and Materials Commons](#), and the [Materials Science and Engineering Commons](#)

Repository Citation

Slewa, Muna, "Crystalline Phase Change in Steel Alloys due to High Speed Impact" (2015). *UNLV Theses, Dissertations, Professional Papers, and Capstones*. 2584.

<https://digitalscholarship.unlv.edu/thesesdissertations/2584>

This Dissertation is brought to you for free and open access by Digital Scholarship@UNLV. It has been accepted for inclusion in UNLV Theses, Dissertations, Professional Papers, and Capstones by an authorized administrator of Digital Scholarship@UNLV. For more information, please contact digitalscholarship@unlv.edu.

CRYSTALLINE PHASE CHANGE IN STEEL ALLOYS DUE TO
HIGH SPEED IMPACT

by

Muna Slewa

Bachelor of Science Mechanical Engineering
Technology University of Baghdad, Baghdad - Iraq

Master of Science in Mechanical Engineering
Technology University of Baghdad, Baghdad - Iraq

Doctorate of Philosophy in Mechanical Engineering
Technology University of Baghdad, Baghdad - Iraq

A dissertation submitted in partial fulfillment
of the requirements for the

Doctor of Philosophy - Mechanical Engineering

Department of Mechanical Engineering
Howard R. Hughes College of Engineering
The Graduate College

University of Nevada, Las Vegas
December 2015

Copyright 2015 Muna Slewa

All Rights Reserved



Dissertation Approval

The Graduate College
The University of Nevada, Las Vegas

May 22, 2015

This dissertation prepared by

Muna Slewa

entitled

Crystalline Phase Change in Steel Alloys Due to High Speed Impact

is approved in partial fulfillment of the requirements for the degree of

Doctor of Philosophy in Engineering – Mechanical Engineering
Department of Mechanical Engineering

Brendan O’Toole, Ph.D.
Examination Committee Chair

Kathryn Hausbeck Korgan, Ph.D.
Graduate College Interim Dean

Mohamed Trabia, Ph.D.
Examination Committee Member

Samaan Ladkany, Ph.D.
Examination Committee Member

Zhiyong Wang, Ph.D.
Examination Committee Member

Moses Karakouzian, Ph.D.
Graduate College Faculty Representative

ABSTRACT

Crystalline Phase Change in Steel Alloys due to High Speed Impact

by

Muna Slewa

Dr. Brendan J. O'Toole, Examination Committee Chair
Professor and Chairman, Department of Mechanical Engineering
University of Nevada, Las Vegas

The effect of hypervelocity projectile impact on the crystalline grain structure near the target impact location of A36 steel has been studied. A36 steel is a mostly single phase body centered cubic material (BCC). Impact velocities ranged from 3.54 to 6.70 km/sec. Target materials were studied before and after impact to determine if these impact conditions result in a phase change of the A36. Scanning electron microscopy, electron back-scatter diffraction, and x-ray diffraction methods were used to investigate deformation, lattice defects, twinning, and phase transformation. A limited number of impacted targets made from 304L and HY100 steels were also examined. These alloys contain the BCC crystalline phase along with face centered cubic (FCC) and hexagonal closed pack (HCP) structures. Grain size near impact is compacted near impact site. Also twinning was present closer to the impact area, and gradually dissipated away further from the impact zone. While increasing impact momentum increased the HCP percentage.

ACKNOWLEDGMENTS

I am greatly thankful for the patience and the genuine support of my advisor Professor B. O'Toole. His continuous support and leadership is an added value with an ocean of knowledge and experience, not merely in the realm of academics and technology achievements, but also in a universe of ethics, spirituality with a great human touch and good humor, as well as, Dr. Mohamed Trabia, effectively co-supervised this large work with much attention and preciseness. I am equally thankful for the practical experience of Dr. Thomas Hartmann and Dr. Dan Kourry, of the physics department at UNLV who have shared generously in support of this study. I would also like to mention and appreciate the generous grants and support of this work by the National Technology Security, LLC, and the University of Nevada Las Vegas (UNLV).

I express my sincere appreciation for members of my panel advisory committee, professors, Dr. Samaan Ladkany, CEEC; Dr. Wang Zhiyong, ME; and Dr. Moses Karakouzian, CEEC; whose massive support, both technical, academic and personal has been beyond outstanding. I admire and value such their great quality, at its best as educators and projects managers. This panel manifested leadership, hard work, authenticity, in their documented achievements and experiences. And yet modesty seems natural and easily detectable in all of them.

I am thankful for my co-workers, friends and family; all have contributed a tremendous care and help shaping the success of this academic work, and my life. Through the endless commitment and authentic care of my friends and family I survived many trials and afflictions. Special thanks to my parents who is without the shield of their love and genuine care and guidance this achievement would never materialize, a special thanks to my mother, Yonya Dawood for her endless love and priceless support and to the memory of my father Rev. Yousif Slewa who sacrificed his life standing for his moral beliefs, and a price for us to be alive and free today.

TABLE OF CONTENTS

ABSTRACT	iii
ACKNOWLEDGMENTS	iv
LIST OF TABLES	ix
LIST OF FIGURES	xii
CHAPTER 1 INTRODUCTION	1
1.1 Background and Problem Definition	1
1.1.1 Summary of Hypervelocity Impact Phenomenon	1
1.1.2 Prior UNLV Research Related to Hypervelocity Impact Phenomenon	2
1.1.3 Material Property Uncertainty in Computational Simulations	4
1.2 Dissertation Objectives	5
1.3 Material Properties and Application Background Information	6
1.3.1 A36 Steel Properties	6
1.3.2 HY100 Steel Properties	6
1.3.3 304L Steel Properties	7
1.4 Material Microstructure Definition	8
1.4.1 Crystalline Phase	8
1.4.2 Close-Packed Definition	9
1.4.3 Body Centered Cubic Structure	9
1.4.4 Face Centered Cubic Structure	10
1.4.5 Hexagonal Closed Packed Structure	10
1.4.6 Lattice Defects	11
1.4.7 Microstructural Basis of Metal Formation Processes	12
1.4.8 Plastic Deformation of Metals and Related Properties	13
1.4.9 Twinning	13
1.4.10 Crystallinity	14
1.4.11 Lattice Parameters	15
1.4.12 Definitions and Variables Important to Unit Cell Geometry and Transformations.....	15
1.5 Dislocation and the Ordination Angle	16
1.6 Relevant Research Literature Review	17
1.7 Research Plan and Dissertation Roadmap	19
CHAPTER 2 EXPERIMENTAL DEVICES AND METHODS	20
2.1 Impact Experiment Geometry and Materials	21
2.2 Target Plate Sectioning and Cross-Section Zones Slicing	22
2.3 Specimen Cutting and Polishing Procedures	25
2.4 Target Damage Zone Descriptions after Impact Experiment	28
2.4.1 A36 Steel (Impact Velocity of 3.54, 4.51, and 5.80 km/s)	30
2.4.2 304L Steel (Impact Velocity of 6.58 km/s)	31
2.4.3 HY100 Steel (Impact Velocity of 6.70 km/s)	31

2.5	Pressure Time Distribution in Target Plates	32
2.5.1	Pressure Time Distribution in Target Plates	33
2.6	Scanning Electron Microscopy (SEM)	35
2.7	Electron Back Scatter Diffraction (EBSD)	42
2.8	X-Ray Diffraction (XRD)	51
2.8.1	Bragg's Law	53
2.9	Summary of All Experimental Measurements	55
CHAPTER 3 A36 STEEL EXPERIMENTAL DATA.....		56
3.1	As Received A36 Steel (No Impact Loading)	56
3.1.1	EBSD Grain Structure Phase Measurements	56
3.1.2	EBSD Misorientation Measurements	58
3.1.3	XRD Lattice Parameter Measurements	60
3.1.3.1	Non-Impact A36 Steel	60
3.1.3.2	A36 Steel Target Impacted at 5.80 km/sec.....	61
3.2	Impact Velocity of 3.54 km/s in A36 Steel	63
3.2.1	Cross-section Location 1-A (75 mm from impact center)	63
3.2.2	Cross-section Location 2-C (35 mm from impact center)	65
3.2.3	Cross-section Location 3-C (7.5 mm from impact center)	65
3.2.4	Cross-section Location 4-A (20 mm from impact center)	68
3.2.5	Cross-section Location 5-D (10 mm from impact center)	69
3.2.6	Cross-section Location 6-A (0 mm from impact center)	70
3.2.7	Cross-section Location 6-B (0 mm from impact center)	71
3.2.8	Cross-section Location 6-C (0 mm from impact center)	72
3.2.9	Cross-section Location 6-D (0 mm from impact center)	73
3.2.10	Cross-section Location 6-E (0 mm from impact center)	74
3.2.11	Cross-section Location 6-F (0 mm from impact center)	74
3.3	Impact Velocity of 4.51 km/s in A36 Steel.....	76
3.3.1	Cross-section Location 1-B (75 mm from impact center)	76
3.3.2	Cross-section Location 2-A (35 mm from impact center)	77
3.3.3	Cross-section Location 3-B (7.5 mm from impact center)	78
3.3.4	Cross-section Location 4-A (20 mm from impact center).....	79
3.3.5	Cross-section Location 5-A (10 mm from impact center).....	80
3.3.6	Cross-section Location 6-A (0 mm from impact center).....	81
3.3.7	Cross-section Location 6-B (0 mm from impact center)	82
3.3.8	Cross-section Location 6-C (0 mm from impact center)	83
3.4	Impact Velocity of 5.8 km/s in A36 Steel	84
3.4.1	Cross-section Location 1-A (75 mm from impact center)	84
3.4.2	Cross-section Location 2-A (35 mm from impact center)	85
3.4.3	Cross-section Location 3-B (7.5 mm from impact center)	86
3.4.4	Cross-section Location 4-D (20 mm from impact center)	87
3.4.5	Cross-section Location 5-D (10 mm from impact center)	88
3.4.6	Cross-section Location 6-A (0 mm from impact center)	89
3.4.7	Cross-section Location 6-B (0 mm from impact center)	90
3.4.8	Cross-section Location 6-C (0 mm from impact center)	91
3.4.9	Cross-section Location 6-D (0 mm from impact center)	92
3.4.10	Cross-section Location 6-E (0 mm from impact center)	93
3.4.11	Cross-section Location 6-F (0 mm from impact center)	93
3.4.12	Cross-section Location 6-G (0 mm from impact center)	94
3.5	EBSD Misorientation Measurements of the impact A36 steel Targets	96

3.5.1	Misorientation Measurement for A36 Steel Target with an Impact Velocity of 3.54 km/sec at Sample Location 6-A	96
3.5.2	Misorientation Measurement for A36 Steel Target with an Impact Velocity of 4.51 km/sec at Sample location 6-A	96
3.5.3	Misorientation Measurement for A36 Steel Target with an Impact Velocity of 4.51 km/sec at Sample Location 6-B	96
3.5.4	Misorientation Impact A36 steel at 5.80 km/sec Sample location 6-G	100
3.5.5	Misorientation Impact A36 steel at 5.80 km/sec Sample location 6-B	102
3.5.6	Misorientation Impact A36 steel at 5.80 km/sec Sample location 6-C	102
3.5.7	Misorientation Impact A36 steel at 5.80 km/sec Sample location 6-D	102
3.5.8	Misorientation Impact A36 steel at 5.80 km/sec Sample location 6-E	106
3.5.9	Misorientation Impact A36 steel at 5.80 km/sec Sample location 6-F	108
3.6	Experimental Grain Size Measurements	109
3.6.1	Impacted and non-impacted A36 steel materia	109
3.6.2	A36 steel impact at 5.80 km/sec	110
CHAPTER 4 304L STEEL EXPERIMENTAL DATA		111
4.1	As Received 304L Steel (No Impact Loading)	112
4.1.1	EBSD Grain Structure Phase Measurements	112
4.1.2	EBSD Misorientation Measurements of Non-Impact 304L Steel	113
4.1.3	Misorientation Impact 304L steel at 6.58 km/sec Sample 6-A and 6-B	114
4.1.4	XRD Lattice Parameter Measurements	116
4.1.4.1	Non-Impact 304L steel	117
4.1.4.2	Impact 304L at 6.58 km/sec	118
4.2	Impact Velocity of 6.58 km/s in 304L Steel	120
4.2.1	Cross-section Location 1-C (75 mm from impact center)	120
4.2.2	Cross-section Location 2-A (35 mm from impact center)	122
4.2.3	Cross-section Location 3-A (7.5 mm from impact center)	123
4.2.4	Cross-section Location 4-D (20 mm from impact center)	124
4.2.5	Cross-section Location 5-D (10 mm from impact center)	125
4.2.6	Cross-section Location 6-A (0 mm from impact center)	127
4.2.7	Cross-section Location 6-B (0 mm from impact center)	128
4.2.8	Cross-section Location 6-C (0 mm from impact center)	129
4.2.9	Cross-section Location 6-E (0 mm from impact center)	130
4.3	Experimental Grain Size Measurements	131
4.3.1	Non-impact 304L steel	131
4.3.2	304L Steel impact at 6.58 km/sec	131
CHAPTER 5 HY100 STEEL EXPERIMENTAL DATA		133
5.1	HY100 Steel (Non-Impact Loading)	133
5.1.1	EBSD Grain Structure Phase Measurements	133
5.1.2	EBSD Misorientation Measurements	135
5.1.2.1	EBSD Non-Impact HY100 Misorientation Measurements	135
5.1.2.2	Misorientation Impact HY100 Steel at 6.70 km/sec for Sample locations 6-B, C, E, F, and G	137
5.1.3	XRD Lattice Parameter Measurements	144
5.1.3.1	Non-Impact HY100 Steel	145
5.1.3.2	Impact HY100 at 6.70 km/sec	145
5.2	Impact Velocity of 6.70 km/s in HY100 Steel	146
5.2.1	Cross-section Location 1-A (75 mm from impact center)	146
5.2.2	Cross-section Location 2-A (35 mm from impact center)	147

5.2.3	Cross-section Location 3-D (7.5 mm from impact center)	148
5.2.4	Cross-section Location 4-C (20 mm from impact center)	149
5.2.5	Cross-section Location 5-B (10 mm from impact center)	151
5.2.6	Cross-section Location 6-A (0 mm from impact center)	153
5.2.7	Cross-section Location 6-B (0 mm from impact center)	155
5.2.8	Cross-section Location 6-C (0 mm from impact center)	156
5.2.9	Cross-section Location 6-D (0 mm from impact center)	156
5.2.10	Cross-section Location 6-E (0 mm from impact center)	157
5.2.11	Cross-section Location 6-F (0 mm from impact center)	157
5.2.12	Cross-section Location 6-G (0 mm from impact center)	158
5.3	Experimental Grain Size Measurements	161
5.3.1	Non-impact HY100 Steel	161
5.3.2	Impact HY100 Steel at 6.70 km/sec	161
CHAPTER 6 DISCUSSION OF RESULTS		163
6.1	A36 Steel	164
6.1.1	First Steel Test Speed for A36 Steel: 3.54 km/s	164
6.1.2	Second Test Speed for A36 Steel: 4.51 km/s	165
6.1.3	Third Test Speed for A36 Steel: 5.81 km/s	165
6.2	304L Steel with Impact Velocity of 6.58 km/sec	167
6.3	HY 100 Steel with Impact Velocity of 6.70 km/s	168
6.4	General Discussion and Overview	168
6.4.1	Five-Stage Tabulated Comparisons: Stage one	169
6.4.2	EBSD Results for All Sections and Speeds for A36 Steel	170
6.4.3	Stage 3: Effect of Impact Speed Demonstrated Impacted A36	172
6.4.4	Stage 4: Comparison of All Three Steel Alloys	175
6.4.5	Stage 5: Overall comparison the three Alloys	177
6.4.6	XRD Diffraction	186
CHAPTER 7 CONCLUSIONS AND RECOMMENDATIONS FOR FUTURE WORK		195
7.1	The Summary of Conclusions	195
7.1.1	Comparison, Comments, and Conclusion	195
7.2	Future Work	199
APPENDICES A		200
APPENDICES B		202
APPENDICES C		204
APPENDICES D		219
APPENDICES E		224
REFERENCES		229
CURRICULUM VITAE		236

LIST OF TABLES

Table 1.1	Chemical compositions (%) of A36, 304L, and HY100 steels [22, 27]	7
Table 1.2	Physical and mechanical properties of A36, HY100, and 304L steels [22, 27].....	7
Table 1.3	Atomic Packing Factors (APF) for Common Atomic Crystal Structures [32]	16
Table 2.1	Location and dimensions of cross-sections for microstructural analysis.....	25
Table 2.2	Peak impact pressure in A36 steel targets predicted from simulations [14].....	31
Table 2.3	Peak impact pressure in 304L and HY100 steel targets predicted from simulations [14].....	31
Table 2.4	Peak impact pressure in A36, 304L and HY100 steel targets predicted from simulation	32
Table 2.5	Sample for collected data from the XRD data as lattice parameter and grain size This sample is for A36 b and some physical properties such as mass, volume and density evaluation...	54
Table 2.6	Summary of Operations for plates and specimens preparation and Experimental Measurements	55
Table 3.1	Non-impact phase ratio	57
Table 3.2	A36-Lattice parameters and quantity for detectable phases	61
Table 3.3	Impact phase ratio of A36 steel at 3.54 km/sec sample location 1-A	65
Table 3.4	Impact phase ratio of A36 steel at 3.54 km/sec sample location 2-C	67
Table 3.5	Impact phase ratio of A36 steel at 3.54 km/sec sample location 3-C	68
Table 3.6	Impact phase ratio of A36 steel at 3.54 km/sec sample location 4-A	69
Table 3.7	Impact phase ratio of A36 steel at 3.54 km/sec sample location 5-D	70
Table 3.8	Impact phase ratio of A36 steel at 3.54 km/sec sample location 6-A	71
Table 3.9	Impact phase ratio of A36 steel at 3.54 km/sec sample location 6-B	71
Table 3.10	Impact phase ratio of A36 steel at 3.54 km/sec sample location 6-C	72
Table 3.11	Impact phase ratio of A36 steel at 3.54 km/sec sample location 6-D	73
Table 3.12	Impact phase ratio of A36 steel at 3.54 km/sec sample location 6-E	74
Table 3.13	Impact phase ratio of A36 steel at 3.54 km/sec sample location 6-F	75
Table 3.14	Impact phase ratio of A36 steel at 4.51 km/sec sample location 1-B	77
Table 3.15	Impact phase ratio of A36 steel at 4.51 km/sec sample location 2-A	78
Table 3.16	Impact phase ratio of A36 steel at 4.51 km/sec sample locaton 3-B	79
Table 3.17	Impact phase ratio of A36 steel at 4.51 km/sec sample location 4-A	80
Table 3.18	Impact phase ratio of A36 steel at 4.51 km/sec sample location 5-A	81
Table 3.19	Impact phase ratio of A36 steel at 4.51 km/sec sample location 6-A	82
Table 3.20	Impact phase ratio of A36 steel at 4.51 km/sec sample location 6-B	82
Table 3.21	Impact phase ratio of A36 steel at 4.51 km/sec sample location 6-C	83
Table 3.22	Impact phase ratio of A36 steel at 5.80 km/sec sample location 1-A	85
Table 3.23	Impact phase ratio of A36 steel at 5.80 km/sec sample location 2-A	86
Table 3.24	Impact phase ratio of A36 steel at 5.80 km/sec sample location 3-B	87
Table 3.25	Impact phase ratio of A36 steel at 5.80 km/sec sample location 4-D	88
Table 3.26	Impact phase ratio of A36 steel at 5.80 km/sec sample location 5-D	89
Table 3.27	Impact phase ratio of A36 steel at 5.80 km/sec sample location 6-A	90
Table 3.28	Impact phase ratio of A36 steel at 5.80 km/sec sample location 6-B	91
Table 3.29	Impact phase ratio of A36 steel at 5.80 km/sec sample location 6-C	92
Table 3.30	Impact phase ratio of A36 steel at 5.80 km/sec sample location 6-D	92
Table 3.31	Impact phase ratio of A36 steel at 5.80 km/sec sample location 6-E	93
Table 3.32	Impact phase ratio of A36 steel at 5.80 km/sec sample location 6-F	94
Table 3.33	Impact phase ratio of A36 steel at 5.80 km/sec sample location 6-G	95
Table 4.1	Non-Impact phase ratio of 304L Steel	112
Table 4.2	304L-Lattice parameters and quantity for detectable phases	119
Table 4.3	Impact phase ratio of 304L steel at 6.58 km/sec sample location 1-C	121
Table 4.4	Impact phase ratio of 304L steel at 6.58 km/sec sample location 2-A	123
Table 4.5	Impact phase ratio of 304L steel at 6.58 km/sec sample location 3-A	124

Table 4.6	Impact phase ratio of 304L steel at 6.58 km/sec sample location 4-D	125
Table 4.7	Impact phase ratio of 304L steel at 6.58 km/sec sample location 5-D	126
Table 4.8	Impact phase ratio of 304L steel at 6.58 km/sec sample location 6-A	128
Table 4.9	Impact phase ratio of 304L steel at 6.58 km/sec sample location 6-B	128
Table 4.10	Impact phase ratio of 304L steel at 6.58 km/sec sample location 6-C	129
Table 4.11	Impact phase ratio of 304L steel at 6.58 km/sec sample location 6-E	130
Table 5.1	Non-Impact phase ratio of HY100 steel	135
Table 5.2	HY100-Lattice parameters and quantity for detectable phases	146
Table 5.3	Impact phase ratio of HY100 steel at 6.70 km/sec sample location 1-A	151
Table 5.4	Impact phase ratio of HY100 steel at 6.70 km/sec sample location 2-A	152
Table 5.5	Impact phase ratio of HY100 steel at 6.70 km/sec sample location 3-B	152
Table 5.6	Impact phase ratio of HY100 steel at 6.70 km/sec sample location 4-C	152
Table 5.7	Impact phase ratio of HY100 steel at 6.70 km/sec sample location 5-B	152
Table 5.8	Impact phase ratio of HY100 steel at 6.70 km/sec sample location 6-A	159
Table 5.9	Impact phase ratio of HY100 steel at 6.70 km/sec sample location 6-B	159
Table 5.10	Impact phase ratio of HY100 steel at 6.70 km/sec sample location 6-C	159
Table 5.11	Impact phase ratio of HY100 steel at 6.70 km/sec sample location 6-D	160
Table 5.12	Impact phase ratio of HY100 steel at 6.70 km/sec sample location 6-E	160
Table 5.13	Impact phase ratio of HY100 steel at 6.70 km/sec sample location 6-F.....	160
Table 5.14	Impact phase ratio of HY100 steel at 6.70 km/sec sample location 6-G	160
Table 6.1	Non-impact phase ratio A36 steel	169
Table 6.2	The ratio of all phases depending on crater location A36 steel at 3.54 km/sec	171
Table 6.3	The ratio of all phases depending on crater location A36 steel at 4.51 km/sec	171
Table 6.4	The ratio of all phases depending on crater location A36 steel at 5.80 km/sec	172
Table 6.5	The error of each crater location (A, B) of A36 steel at 3.54 km/sec	173
Table 6.6	Effect of Impact Velocity Change	174
Table 6.7	The ratio of all phases depends on crater location 304L steel at 6.58 km/sec	176
Table 6.8	The ratio of all phases depending on crater location HY100 steel at 6.70 km/sec	176
Table 6.9	Comparison of phase content in different steels when impacted at similar velocities	177
Table 6.10	Non-impact phase ratio A36 , 304L, and HY100 steel	178
Table 6.11	Less error high reliability at 1000 micron far from the arc of projectile	185
Table 6.12	A36-Lattice parameters and quantity for detectable phases	193
Table 6.13	304L-Lattice parameters and quantity for detectable phases	193
Table 6.14	HY100-Lattice parameters and quantity for detectable phases	194
Table 7.1	Non-impact phase ratio A36 steel	196
Table 7.2	Impact A36 steel phase at 5.80 km/sec	196
Table A1	A36 steel mechanical properties	200
Table C1	Impact phase ratio of A36 steel at 3.54 km/sec sample location 1-D	204
Table C2	Impact phase ratio of A36 steel at 3.54 km/sec sample location 2-D	205
Table C3	Impact phase ratio of A36 steel at 3.54 km/sec sample location 3-D	206
Table C4	Impact phase ratio of A36 steel at 3.54 km/sec sample location 4-C.....	207
Table C5	Impact phase ratio of A36 steel at 3.54 km/sec sample location 5-B.....	208
Table C6	Impact phase ratio of A36 steel at 4.51 km/sec sample location 1-C.....	209
Table C7	Impact phase ratio of A36 steel at 4.51 km/sec sample location 2-B.....	210
Table C8	Impact phase ratio of A36 steel at 4.51 km/sec sample location 3-A	211
Table C9	Impact phase ratio of A36 steel at 4.51 km/sec sample location 4-B.....	212
Table C10	Impact phase ratio of A36 steel at 4.51 km/sec sample location 5-C.....	213

Table C11	Impact phase ratio of A36 steel at 5.80 km/sec sample location 1-D	214
Table C12	Impact phase ratio of A36 steel at 5.80 km/sec sample location 2-D	215
Table C13	Impact phase ratio of A36 steel at 5.80 km/sec sample location 3-A	216
Table C14	Impact phase ratio of A36 steel at 5.80 km/sec sample location 4-A	217
Table C15	Impact phase ratio of A36 steel at 5.80 km/sec sample location 5-A	218
Table D1	Impact phase ratio of 304L steel at 6.58 km/sec location 1-C	219
Table D2	Impact phase ratio of 304L steel at 6.58 km/sec sample location 2-E	220
Table D3	Impact phase ratio of 304L steel at 6.58 km/sec sample location 3-F	221
Table D4	Impact phase ratio of 304L steel at 6.58 km/sec sample location 4-A.....	222
Table D5	Impact phase ratio of 304L steel at 6.58 km/sec sample location 5-A.....	223
Table E1	Impact phase ratio of HY 100 steel at 6.70 km/sec sample location 1-D.....	224
Table E2	Impact phase ratio of HY 100 steel at 6.70 km/sec sample location 2-D.....	225
Table E3	Impact phase ratio of HY 100 steel at 6.70 km/sec sample location 3-C.....	226
Table E4	Impact phase ratio of HY 100 steel at 6.70 km/sec sample location 4-C.....	227
Table E5	Impact phase ratio of HY 100 steel at 6.70 km/sec sample location 5-A.....	228

LIST OF FIGURES

Figure 1.1	UNLV two-stage light gas gun	3
Figure 1.2	The three most common phases in metal crystalline structure: a) Body Centered Cubic (BCC), b) Face Centered Cubic (FCC), and c) Hexagonal Close-Packed Crystalline (HCP)	4
Figure 1.3	Coordination numbers for FCC, HCP, and BCC systems are 12, 12, and 8, respectively ..	5
Figure 1.4	Grain structures	8
Figure 1.5	Body-Centered Cubic (BCC) Structures	9
Figure 1.6	Face Centered Cubic (FCC) Structure	10
Figure 1.7	Hexagonal Closed Packed Structures	11
Figure 1.8	Imperfections in lattice structure	12
Figure 1.9	Slip in an FCC crystal structure.....	13
Figure 1.10	Twinning in an FCC Crystal Structure	14
Figure 1.11	Two inter-penetrating lattices can be realigned by a single rotation about a common axis [uvw] by an angle theta. In the figure the axis is the common [111] direction and the rotation angle 60° [63]	17
Figure 2.1	(a) Target plate mounting configuration and (b) Target mounting plate inside chamber..	21
Figure 2.2	A36 target plate before impact and Lexan projectile (not shown to the same scale)	22
Figure 2.3	Front sides (left) and back side (right) visible damage on an A36 steel target	22
Figure 2.4	(a) Cut lines on a target plate, (b) Target cut in half, (c) Finished T-section ready for further sectioning, and (d) Target plate ready for cutting by the water jet machine	23
Figure 2.5	T-shaped bars with dimensions	24
Figure 2.6	Location of six cross-sectional regions used for microstructural analysis	24
Figure 2.7	Linear Precision Saw (ISOMET 4000) used to slice steel cross-sections	25
Figure 2.8	Linear Precision Saw slicing the A36, 304L and HY100 steel materials.....	26
Figure 2.9	Sliced steel specimens in casting molds	26
Figure 2.10	Epoxy cylinders with steel slices ready for polishing	26
Figure 2.11	Polishing and preparation process of A36, 304L and HY100 steel	27
Figure 2.12	Polishing and Etching A36, 304L and HY100 steel specimens	28
Figure 2.13	Damage zone in A36 steel targets subject to impact velocities of (a) 3.54 km/s, (b) 4.51 km/s, and (c) 5.80 km/sec.....	30
Figure 2.14	Crater zone in 304L (the upper Figure) and HY100 (the lower Figure) targets subject to velocities as indicated.....	31
Figure 2.15	Experimental data and computational simulations of back face velocity versus time during impact of a Lexan projectile (5.3 km/s) into an A36 steel plate [8].	33
Figure 2.16	Relationship between pressure (GPa) and time at a distance of (5.17 mm from the impact crater of A36 steel target and an impact velocity of 5.80 km/sec.....	33
Figure 2.17	Relationship between pressure (GPa) and time at a distance of (0.08 mm from the impact crater of 304L steel target and an impact velocity of 6.58 km/sec)	34
Figure 2.18	Relationship between pressure (GPa) and time at a distance of (0.04 mm from the impact crater of HY100 steel target and an impact velocity of 6.70 km/sec)	34
Figure 2.19	SEM opened sample chamber [48]	38
Figure 2.20	Schematic of an SEM. [48]	39
Figure 2.21	a) EBSD Components Show How an SEM Work Doe [54].....	41
Figure 2.21	b) Schematic for Sample Exposed to an incident Beam, primary backscattered Electrons Show [54]	42
Figure 2.22	a) The angles between the bands are directly related to the angles between planes in the crystal lattice. b) is the symmetry of the crystal lattice is reflected in the pattern [60,66].	44
Figure 2.23	An electron backscatter diffraction pattern	46
Figure 2.24	Electron backscatter diffraction (EBSD)	47

Figure 2.25	A36 Steel, colored area of 75 mm away from crater with mapping photo of grain boundary (X=400)	48
Figure 2.26	A36 Steel, same area as Figure 2.25 with surrounding of grain (boundary condition (BC) and boundary grain (BG) (X=400)	48
Figure 2.27	A36 Steel, same area as Figure 2.25 colored regions indicate crystal phase; green is BCC, blue is FCC, red is HCP, and white shows areas where no phase determination could be made	48
Figure 2.28	Ratio of the phase percentage and the error	49
Figure 2.29	Crystal Orientation Magnification and the original length of the map	49
Figure 2.30	Misorientation angle greater than 45° having twinning	49
Figure 2.31	System configurations and operation [59]	50
Figure 2.32	The basic layout of an X- ray diffractometric [55-57]	52
Figure 2.33	X-ray diffractometric (Bruker) [57]	52
Figure 2.34	Bragg's law and angles related	53
Figure 2.35	Sample of the peak of XRD results show the ratio of BCC of A36 Steel	54
Figure 3.1	EBSD data from non-ImpactA36 steel showing: a) grain, b) 350X magnification and the original length of the map, c) phase map, and D crystal orientation.....	57
Figure 3.2	Misorientation angle measured along four different lines in the non-impacted A36 steel: a) EBSD shows less noise, b) EBSD shows grains, c) EBSD shows boundary grains d) Line 1, e) Line 2, f) Line 3, and g) line 4.....	59
Figure 3.3	Non-impact A36 Steel (Phase 1 "BCC Fe" 100.000 %)	60
Figure 3.4	A36 Steel impacted at 5.80 km/sec, Phase1:"BCC Fe" 65.35 % and Phase 2:"FCC" 34.65 %. (a) the BCC peak fit and (b) the FCC peak fit.	62
Figure 3.5	EBSD specimen locations were taken from 6 locations along two different lines of a T-shaped specimen of the A36 steel target: (a) Along impact crater perpendicular to impact mid-line and (b) Parallel to mid-line cut.	63
Figure 3.6	EBSD data from A36 steel, sample location 1-A, after impact velocity of 3.54 km/sec showing: a) polished sample, b) grain, c) 400X magnification and the original length of the map, d) phase map, and e) crystal orientation.	64
Figure 3.7	EBSD data from A36 steel, sample location 2-C, after impact velocity of 3.54 km/sec showing: a) polished sample, b) grain, c) 370X magnification and the original length of the map, and D) phase map.	66
Figure 3.8	EBSD data from A36 steel, sample location 3-C, after impact velocity of 3.54 km/sec showing: a) polished sample, b) grain, c) 400X magnification and the original length of the map, and d) phase map.	67
Figure 3.9	EBSD data from A36 steel, sample location 4-A, after impact velocity of 3.54 km/sec showing: a) polished sample, b) grain, c) 400X magnification and the original length of the map, and d) phase map.	68
Figure 3.10	EBSD data from A36 steel, sample location 5-D, after impact velocity of 3.54 km/sec showing: a) polished sample, b) grain, c) 400X magnification and the original length of the map, and d) phase map.	69
Figure 3.11	EBSD data from A36 steel, sample location 6-A, after impact velocity of 3.54 km/sec showing: a) polished sample, b) grain, c) 400X magnification and the original length of the map, and d) phase map.	70
Figure 3.12	EBSD data from A36 steel, sample location 6-B, after impact velocity of 3.54 km/sec showing: a) grain, b) 400X magnification and the original length of the map, and c) phase map.	71
Figure 3.13	EBSD data from A36 steel, sample location 6-C, after impact velocity of 3.54 km/sec showing: a) grain, b) 400X magnification and the original length of the map, and C) phase map.	72

Figure 3.14	EBSD data from A36 steel, sample location 6-D, after impact velocity of 3.54 km/sec showing: a) grain, b) 400X magnification and the original length of the map, and c) phase map.	73
Figure 3.15	EBSD data from A36 steel, sample location 6-E, after impact velocity of 3.54 km/sec showing: a) grain, b) 400X magnification and the original length of the map, and c) phase map.	74
Figure 3.16	EBSD data from A36 steel, sample location 6-F, after impact velocity of 3.54 km/sec showing: a) grain, b) 400X magnification and the original length of the map, and c) phase map.	75
Figure 3.17	EBSD data from A36 steel, sample location 1-B, after impact velocity of 4.51 km/sec showing: a) polished sample, b) grain, c) 370X magnification and the original length of the map, d) phase map.	76
Figure 3.18	EBSD data from A36 steel, sample location 2-A, after impact velocity of 4.51 km/sec showing: a) polished sample, b) grain, c) 400X magnification and the original length of the map, and d) phase map.	77
Figure 3.19	EBSD data from A36 steel, sample location 3-B, after impact velocity of 4.51 km/sec showing: a) polished sample, b) grain, c) 400X magnification and the original length of the map, and d) phase map.	78
Figure 3.20	EBSD data from A36 steel, sample location 4-A, after impact velocity of 4.51 km/sec showing: a) polished sample, b) grain, c) 400X magnification and the original length of the map, and d) phase map.	79
Figure 3.21	EBSD data from A36 steel, sample location 5-A, after impact velocity of 4.51 km/sec showing: a) polished sample, b) grain, c) 400X magnification and the original length of the map, and d) phase map.	80
Figure 3.22	EBSD data from A36 steel, sample location 6-A, after impact velocity of 4.51 km/sec showing: a) polished sample, b) grain, c) 400X magnification and the original length of the map, and d) phase map.	81
Figure 3.23	EBSD data from A36 steel, sample location 6-B, after impact velocity of 4.51 km/sec showing: a) grain, b) 400X magnification and the original length of the map, and C) phase map.	82
Figure 3.24	EBSD data from A36 steel, sample location 6-C, after impact velocity of 4.51 km/sec showing: a) grain, b) 400X magnification and the original length of the map, and c) phase map.	83
Figure 3.25	EBSD data from A36 steel, sample location 1-A, after impact velocity of 5.80 km/sec showing: a) polished sample, b) grain, c) 400X magnification and the original length of the map, and d) phase map.	84
Figure 3.26	EBSD data from A36 steel, sample location 2-A, after impact velocity of 5.80 km/sec showing: a) polished sample, b) grain, c) 400X magnification and the original length of the map, and d) phase map.	85
Figure 3.27	EBSD data from A36 steel, sample location 3-B after impact velocity of 5.80 km/sec showing: a) polished sample, b) grain, c) 400X magnification and the original length of the map, and d) phase map.	86
Figure 3.28	EBSD data from A36 steel, sample location 4-D, after impact velocity of 5.80 km/sec showing: a) polished sample, b) grain, c) 400X magnification and the original length of the map, and d) phase map.	87
Figure 3.29	EBSD data from A36 steel, sample location 5-D, after impact velocity of 5.80 km/sec showing: a) polished sample, b) grain, c) 400X magnification and the original length of the map, and d) phase map.	88
Figure 3.30	EBSD data from A36 steel, sample location 6-A, after impact velocity of 5.80 km/sec showing: a) polished sample, b) grain, c) 400X magnification and the original length of the map, and d) phase map.	89

Figure 3.31	EBSD data from A36 steel, sample location 6-B, after impact velocity of 5.80 km/sec showing: a) grain, b) 400X magnification and the original length of the map, and c) phase map.	90
Figure 3.32	EBSD data from A36 steel, sample location 6-C, after impact velocity of 5.80 km/sec showing: a) grain, b) 400X magnification and the original length of the map, and c) phase map.	91
Figure 3.33	EBSD data from A36 steel, sample location 6-D, after impact velocity of 5.80 km/sec showing: a) grain, b) 400X magnification and the original length of the map, and c) phase map.	92
Figure 3.34	EBSD data from A36 steel, sample location 6-E, after impact velocity of 5.80 km/sec showing: a) grain, b) 400X magnification and the original length of the map, and c) phase map.	93
Figure 3.35	EBSD data from A36 steel, sample location 6-F after impact velocity of 5.80 km/sec showing: a) grain, b) 400X magnification and the original length of the map, and c) phase map.	94
Figure 3.36	EBSD data from A36 steel, sample location 6-G, after impact velocity of 5.80 km/sec showing: a) grain, b) 400X magnification and the original length of the map, and c) phase map.	95
Figure 3.37	Misorientation angle measured along four different lines in the Impacted A36 steel, sample location 6-A, after impact velocity of 3.54 km/sec: a) EBSD shows less noise, b) EBSD shows grains; c) Line 1, d) Line 2, e) Line 3, f) Line 4 and G) line 5.	97
Figure 3.48	Misorientation angle measured along four different lines in the Impacted A36 steel, sample location 6-A, after impact velocity of 4.51 km/sec: a) EBSD shows less noise, b) EBSD shows grains; c) Line 1, d) Line 2, e) Line 3, and f) Line 4.	98
Figure 3.39	Misorientation angle measured along four different lines in the Impacted A36 steel, sample location 6-B, after impact velocity of 4.51 km/sec: a) EBSD shows less noise, b) EBSD shows grains; c) Line 1, d) Line 2, e) Line 3, and f) Line 4.	99
Figure 3.40	Misorientation angle measured along four different lines in the Impacted A36 steel, sample location 6-G, after impact velocity of 5.80 km/sec: a) EBSD shows less noise, b) EBSD shows grains; c, d, e, f, g, h, and i) are lines 1, 2, 3, 4, 5, 6, and 7 respectively.	101
Figure 3.41	Misorientation angle measured along four different lines in the Impacted A36 steel, sample location 6-B, after impact velocity of 5.80 km/sec: a) EBSD shows less noise, b) EBSD shows grains; c) Line 1, d) Line 2, e) Line 3, and f) Line 4.	103
Figure 3.42	Misorientation angle measured along four different lines in the Impacted A36 steel, sample location 6-C, after impact velocity of 5.80 km/sec: a) EBSD shows less noise, b) EBSD shows grains; c) Line 1, d) Line 2, e) Line 3, and f) Line 4.	104
Figure 3.43	Misorientation angle measured along four different lines in the Impacted A36 steel, sample location 6-D, after impact velocity of 5.80 km/sec: a) EBSD shows less noise, b) EBSD shows grains; c) Line 1, d) Line 2, e) Line 3, and f) Line 4 and g) line 5.	105
Figure 3.44	Misorientation angle measured along four different lines in the Impacted A36 steel, sample location 6-E after impact velocity of 5.80 km/sec: a) EBSD shows less noise, b) EBSD shows grains; c) Line 1, d) Line 2, e) Line 3, and f) Line 4 and g) line 5.	107
Figure 3.45	Misorientation angle measured along four different lines in the Impacted A36 steel, sample location 6-F after impact velocity of 5.80 km/sec: a) EBSD shows less noise, b) EBSD shows grains; c) Line 1, d) Line 2, and e) Line 3.	108
Figure 3.46	Figure 3.46 EBSD microscopy photos of A36 steel a) non-impact, b) A36 steel impact at 5.80 km/sec Sample.	109
Figure 4.1	Non-impacts and Impact 30L steel and Impact at 6.58 km/sec.	111
Figure 4.2	EBSD data from non-impact 304L steel, sample showing: a) grain, b) 400X magnification and the original length of the map, c) phase map, and d) crystal orientation.	112

Figure 4.3	Misorientation angle measured along four different lines in the non-impacted 304L steel, sample shows: a) EBSD shows less noise, b) EBSD shows grains, c) Line 1, d) Line 2, e) Line 3, and f) Line 4.	113
Figure 4.4	Misorientation angle measured along four different lines in the impacted 304L steel, sample location 6-A after impact velocity of 6.58 km/sec shows: a) EBSD shows less noise, b) EBSD shows grains, c, d, e, and f are the Lines (1, 2, 3, and 4) respectively...	115
Figure 4.5	Misorientation angle measured along four different lines in the impacted 304L steel, sample location 6-B after impact velocity of 6.58 km/sec shows: a) EBSD shows less noise, b) EBSD grains, c) Line 1, d) Line 2, and e) Line 3.	116
Figure 4.6	Non-impact 304L steel phase 1: FCC Iron 93.56 % phase 2: BCC Fe0.8Cr0.2 6.44 % A is the peak fit with BCC, B is the peak fit with FCC.	117
Figure 4.7	Impact 304L steel at 6.58 km/sec Phase 1: "FCC Iron" 72) % Phase 2: "BCC Fe 0.8 Ce 0.2" 28 %A is the peak fit with BCC, B is the peak fit with FCC.....	118
Figure 4.8	EBSD data from 304L steel, sample location 1-C, after impact velocity of 6.58 km/sec showing: a) polished sample, b) grain, c) 400X magnification and the original length of the map, and d) phase map.	121
Figure 4.9	EBSD data from 304L steel, sample location 2-A, after impact velocity of 6.58 km/sec showing: a) polished sample, b) grain, c) 400X magnification and the original length of the map, and d) phase map.	122
Figure 4.10	EBSD data from 304L steel, sample location 3-A, after impact velocity of 6.58 km/sec showing: a) polished sample, b) grain, c) 400X magnification and the original length of the map, and d) phase map.	123
Figure 4.11	EBSD data from 304L steel, sample location 4-D, after impact velocity of 6.58 km/sec showing: a) polished sample, b) grain, c) 400X magnification and the original length of the map, and d) phase map.	125
Figure 4.12	EBSD data from 304L steel, sample location 5-D, after impact velocity of 6.58 km/sec showing: a) polished sample, b) grain, c) 400X magnification and the original length of the map, and d) phase map.	126
Figure 4.13	EBSD data from 304L steel, sample location 6-A, after impact velocity of 6.58 km/sec showing: a) polished sample, b) grain, c) 400X magnification and the original length of the map, and d) phase map.	127
Figure 4.14	EBSD data from 304L steel, sample location 6-B, after impact velocity of 6.58 km/sec showing: a) grain, b) 400X magnification and the original length of the map, and c) phase map.	128
Figure 4.15	EBSD data from 304L steel, sample location 6-C after impact velocity of 6.58 km/sec showing: a) grain, b) 400X magnification and the original length of the map, and c) phase map.	129
Figure 4.16	EBSD data from 304L steel, sample location 6-E, after impact velocity of 6.58 km/sec showing: a) grain, b) 400X magnification and the original length of the map, and c) phase map.	130
Figure 4.17	Experimental Grain Size Measurements 304L steel a) non-Impact, b) impact at 6.58 km/sec.....	132
Figure 5.1	A shows photographs of the HY100 target plates before and after impact at 6.70 km/sec and T-shaped geometry. b) EBSD data from non-impact HY100 steel, sample showing: grain, c) 400X magnification and the original length of the map, d) phase map, and e) crystal orientation.....	135
Figure 5.2	Misorientation angle measured along four different lines in the non-impacted HY100 steel, sample shows: a) EBSD shows less noise, b) EBSD shows grains, c) Line 1, d) Line 2, e) Line 3, and f) Line 4.	137

Figure 5.3	Misorientation angle measured along three different lines in impacted HY100 steel, sample location 6-Bat 6.70 km/sec shows: a) EBSD shows less noise, b) EBSD shows grains, c, d, and e, are the Lines (1, 2, and 3) respectively.	138
Figure 5.4	Misorientation angle measured along three different lines in impacted HY100 steel, sample location 6-C at 6.70 km/sec shows: a) EBSD shows less noise, b) EBSD shows grains, c, d, and e, are the Lines (1, 2, and 3) respectively.	139
Figure 5.5	Misorientation angle measured along three different lines in impacted HY100 steel, sample location 6-F at 6.70 km/sec shows: a) EBSD shows less noise, b) EBSD shows grains, c, d, and e, are the Lines (1, 2, and 3) respectively.	140
Figure 5.6	Misorientation angle measured along three different lines in the impacted HY100 steel, sample location 6-F after impact velocity of 6.70 km/sec shows: a) EBSD shows less noise, b) EBSD shows grains, c, d, and e, are the Lines (1, 2, and 3) respectively.	142
Figure 5.7	Misorientation angle measured along three different lines in the impacted HY100 steel, sample location 6-G after impact velocity of 6.70 km/sec shows: a) EBSD shows less noise, b) EBSD shows grains, c, d, and e, are the Lines (1, 2, and 3) respectively.	143
Figure 5.8	Non-impact HY100 steel Phase 1: "BCC Fe" 100.000 %	145
Figure 5.9	Impact HY100 steel at 6.70 km/sec Phase 1: "BCC Fe" 100.000 %	145
Figure 5.10	EBSD data from HY100 steel, sample location 1-A, after impact velocity of 6.70 km/sec showing: a) polished sample, b) grain, c) 400X magnification and the original length of the map, d) phase map, and e) shows the Crystal Orientation.....	147
Figure 5.11	EBSD data from HY100 steel, sample location 2-A, after impact velocity of 6.70 km/sec showing: a) polished sample, b) grain, c) 400X magnification and the original length of the map, d) phase map.	148
Figure 5.12	EBSD data from HY100 steel, sample location 3-D, after impact velocity of 6.70 km/sec showing: a) polished sample, b) grain, c) 400X magnification and the original length of the map, d) phase map.	149
Figure 5.13	EBSD data from HY100 steel, sample location 4-C, after impact velocity of 6.70 km/sec showing: a) polished sample, b) grain, c) 400X magnification and the original length of the map, d) phase map.	150
Figure 5.14	EBSD data from HY100 steel, sample location 5-B, after impact velocity of 6.70 km/sec showing: a) polished sample, b) grain, c) 400X magnification and the original length of the map, d) phase map.	151
Figure 5.15	EBSD data from HY100 steel, sample location 6-A, after impact velocity of 6.70 km/sec showing: a) polished sample, b) grain, c) 400X magnification and the original length of the map, d) phase map.	154
Figure 5.16	EBSD data from HY100 steel, sample location 6-B, after impact velocity of 6.70 km/sec showing: a) grain, b) 400X magnification and the original length of the map, and c) phase map.	155
Figure 5.17	EBSD data from HY100 steel, sample location 6-C, after impact velocity of 6.70 km/sec showing: a) grain, b) 400X magnification and the original length of the map, and c) phase map.	156
Figure 5.18	EBSD data from HY100 steel, sample location 6-D, after impact velocity of 6.70 km/sec showing: a) grain, b) 400X magnification and the original length of the map, c) phase map.	156
Figure 5.19	EBSD data from HY100 steel, sample location 6-E, after impact velocity of 6.70 km/sec showing: a) grain, b) 400X magnification and the original length of the map, and c) phase map.	157
Figure 5.20	EBSD data from HY100 steel, sample location 6-F, after impact velocity of 6.70 km/sec showing: a) grain, b) 400X magnification and the original length of the map, and c) phase map.	158

Figure 5.21	EBS data from HY100 steel, sample location 6-G after impact velocity of 6.70 km/sec showing: a) grain, b) 400X magnification and the original length of the map, and c) phase map.	159
Figure 5.22	Experimental Grain Size Measurements of a) Non-impact HY100 steel, b) impact at 6.70 km/sec Sample location C.	162
Figure 6.1	Section of A36 steel at 5.80 km/sec speed	165
Figure 6.2	The error of each crater location (A, B) of A36 steel at 3.54 km/sec	173
Figure 6.3	Impact A36 steel 5.80 km/sec sample (6) Misorientation angle (0-60°)	178
Figure 6.4	Misorientation angle measured along four different lines in the Impacted 304L 6.58 km/sec, sample location 6-A, shows: a) EBSD shows less noise, b) EBSD shows grains; c) Line 1, d) Line 2, e) Line 3, and f) Line 4.	180
Figure 6.5	Misorientation angle measured along three different lines in the Impacted HY100 steel at 6.70 km/sec, sample location 6-A, shows: a) EBSD shows grains; b) Line 1, c) Line 2, and d) Line 3.	181
Figure 6.6	Impact A36 Steel location of sample 1 and 5. a) Side View shows sections 1-4. b) Cross section 4 and 5.	184
Figure 6.7	A36, 304L and HY100 EBSD Photos Less Error High Reliability at 1000 Micron far from the Arc of Projectile.	186
Figure 6.8	Non-impact A36 steel (phase 1 "BCC Fe" 100.000 %) (a) BCC fit.	188
Figure 6.9	A36 Steel impact at 5.80 km/sec Phase 1: "BCC Fe" 65.35 % and Phase 2: "FCC" 34.65 %. a) BCC fit and b) FCC fit.	189
Figure 6.10	Non-impact 304L Steel Phase 1: FCC Iron 93.56 % Phase 2: BCC Fe 0.8 Cr 0.2 6.44 a BCC fit, b FCC fit	190
Figure 6.11	Impact 304L Steel at 6.58 km/sec Phase 1: "FCC Iron" 72 % Phase 2: "BCC Fe 0.8 Ce 0.2" 28 %	191
Figure 6.12	Non -impact HY100 Steel Phase 1: "BCC Fe" 100.000 %	192
Figure 6.13	Impact HY100 Steel at 6.70 km/sec Phase 1: "BCC Fe" 100.000 %	192
Figure C1	EBS data from A36 steel, sample location 1-D, after impact velocity of 3.54 km/sec showing: a) grain, b) 400X magnification and the original length of the map, and c) phase map.	204
Figure C2	EBS data from A36 steel, sample location 2-D, after impact velocity of 3.54 km/sec showing: a) grain, b) 400X magnification and the original length of the m and c) phase map.	205
Figure C3:	EBS data from A36 steel, sample location 3-D, after impact velocity of 3.54 km/sec showing: a) grain, b) 400X magnification and the original length of the map and c) phase map.	206
Figure C4:	EBS data from A36 steel, sample location 4-C, after impact velocity of 3.54 km/sec showing: a) grain, b) 400X magnification and the original length of the map, and c) phase map.	207
Figure C5:	EBS data from A36 steel, sample location 5-B, after impact velocity of 3.54 km/sec showing: a) grain, b) 400X magnification and the original length of the map, and c) phase map.	208
Figure C6:	EBS data from A36 steel, sample location 1-C, after impact velocity of 4.51 km/sec showing: a) grain, b) 400X magnification and the original length of the map, and c) phase map.	209

Figure C7:	EBSD data from A36 steel, sample location 2-B after impact velocity of 4.51 km/sec showing: a) grain, b) 400X magnification and the original length of the map, and c) phase map.....	210
Figure C8:	EBSD data from A36 steel, sample location 3-A after impact velocity of 4.51 km/sec showing: a) grain, b) 400X magnification and the original length of the map, and c) phase map.....	211
Figure C9:	EBSD data from A36 steel, sample location 4-B after impact velocity of 4.51 km/sec showing: a) grain, b) 400X magnification and the original length of the map, and c) phase map.....	212
Figure C10:	EBSD data from A36 steel, sample location 5-C after impact velocity of 4.51 km/sec showing: a) grain, b) 400X magnification and the original length of the map, and c) phase map.	213
Figure C11:	EBSD data from A36 steel, sample location 1-D after impact velocity of 5.80 km/sec showing: a) grain, b) 400X magnification and the original length of the map, and c) phase map.	214
Figure C12:	EBSD data from A36 steel, sample location 2-D after impact velocity of 5.80 km/sec showing: a) grain, b) 400X magnification and the original length of the map, and c) phase map.	215
Figure C13:	EBSD data from A36 steel, sample location 3-A after impact velocity of 5.80 km/sec showing: a) grain, b) 400X magnification and the original length of the map, and c) phase map.....	216
Figure C14:	EBSD data from A36 steel, sample location 4-A after impact velocity of 5.80 km/sec showing: a) grain, b) 400X magnification and the original length of the map, and c) phase map.	217
Figure C15 :	EBSD data from A36 steel, sample location 5-A after impact velocity of 5.80 km/sec showing: a) grain, b) 400X magnification and the original length of the map, and c) phase map.	218
Figure D1:	EBSD data from 304L steel, sample location 1-C after impact velocity of 6.58 km/sec showing: a) grain, b) 400X magnification and the original length of the map, and c) phase map.	219
Figure D2:	EBSD data from 304L steel, sample location 2-E after impact velocity of 6.58 km/sec showing: a) grain, b) 400X magnification and the original length of the map, and c) phase map.	220
Figure D3:	EBSD data from 304L steel, sample location 3-F after impact velocity of 6.58 km/sec showing: a) grain, b) 400X magnification and the original length of the map, and c) phase map.	221
Figure D4:	EBSD data from 304L steel, sample location 4-A after impact velocity of 6.58 km/sec showing: a) grain, b) 400X magnification and the original length of the map, and c) phase map.	222
Figure D5:	EBSD data from 304L steel, sample location 5-A after impact velocity of 6.58 km/sec showing: a) grain, b) 400X magnification and the original length of the map, and c) phase map.	223

Figure E1: EBSD data from HY100 steel, sample location 1-D after impact velocity of 6.70 km/sec showing: a) grain, b) 400X magnification and the original length of the map, and c) phase map. 224

Figure E2: EBSD data from HY100 steel, sample location 2-D after impact velocity of 6.70 km/sec showing: a) grain, b) 400X magnification and the original length of the map, and c) phase map. 225

Figure E3: EBSD data from HY100 steel, sample location 3-C after impact velocity of 6.70 km/sec showing: a) grain, b) 400X magnification and the original length of the map, and c) phase map. 226

Figure E4: EBSD data from HY100 steel, sample location 4-C after impact velocity of 6.70 km/sec showing: a) grain, b) 400X magnification and the original length of the map, and c) phase map. 227

Figure E5: EBSD data from HY100 steel, sample location 5-A after impact velocity of 6.70 km/sec showing: a) grain, b) 400X magnification and the original length of the map, and c) phase map. 228

CHAPTER 1

INTRODUCTION

1.1 Background and Problem Definition

When designing many products such as metal structures, heavy machinery, vehicles, many other, it is important to take into consideration the impact properties of the materials. Extensive investigations into the phase transitions of metals and alloys due to high dynamic pressure exposure have been performed by many researchers. Since the discovery about fifty years ago, the discovery of the critical transformation impact loading pressure, the phase transition results were detected by electron microscopy.

Ferrite alloys without heat treatment were found to undergo a shock-induced phase transition at 13 GPa under ambient temperature conditions [1]. Among the large body of research related to the microstructural phase changes in metals and alloys due to impact loading in general, countless papers results have been focused on iron alloys and on steel in particular [1-4].

1.1.1 Summary of Hypervelocity Impact Phenomenon

It was necessary to improve the understanding of material behavior on the microstructure level during very high velocity impact. High impact velocity material properties are dominated by phase changes. The need and desire for a well-controlled and also repeatable hypervelocity launch capability has led to the development of the gas gun. Hypervelocity impact acceleration falls basically into two broad categories; the gun accelerator and the explosive accelerator. Gun accelerators include all accelerators in which the projectile is guided during acceleration.

The first light gas gun was developed due to the need to achieve high projectile velocities. It was determined that high muzzle velocities could be achieved if the column of conventional powder gas driving the projectile was replaced with a light-weight gas such as hydrogen [5]. Since then, single-stage,

two-stage, and three-stage light gas guns have been used for hypervelocity impact studies [6] and the equation of state experiments [7]. When impacted by a high-velocity projectile, strong shock waves are generated in a target specimen. Equation of state data for the target material can then be obtained using a method based on the Rankine-Hugoniot equations [6]. These phenomena have been produced in laboratory equipment where they can be studied closely and measured with high precision. Hypervelocity impacts that produce local stress levels up to nearly 1.0 TPa during planar impact experiments have proven invaluable for studying details of the response of materials to ultra-high-pressure environments [5, 7].

1.1.2 Prior UNLV Research Related to Hypervelocity Impact Phenomenon

Researchers from the University of Nevada Las Vegas (UNLV) and National Security Technologies Incorporated (NSTec) have performed hypervelocity projectile impact experiments on metallic target plates and they have developed computational models to simulate the observed deformation and failure mechanisms. Two-stage light-gas gun was used to fire Lexan projectiles at speeds ranging from 4 – 6.8 km/sec. The projectiles were circular cylinders with a diameter of 5.6 mm and a length of 8.6 mm. All experiments were performed by shooting projectiles into the center of square target plates having dimensions of 152 mm x 152 mm x 12.7 mm. The experiments were designed so that the target would completely stop the projectile. A deep crater was formed on the front side of the target and a large smooth bump was formed on its back side. In-situ deformation measurements were made on the back surface using Photonic Doppler Velocimetry (PDV), Multiplexed Photonic Doppler Velocimetry (MPDV), and high speed video.

The initial impact experiments were performed with A36 steel targets. The computational simulations were performed using LS-Dyna and CTH. A Johnson-Cook material model [8-12] was used for the compression strength and large deformation strain-rate dependent material properties. A Mie-Gruneisen equation of the state was used to model the pressure, temperature, density, and internal energy behavior of

the material as it was subjected to the impact shock wave. These material models do not account for any phase change that might happen in the target material during the impact event. [13]

The computations predicted the overall deformed shape fairly well. Predicting the back face velocity versus time as the bulge grows during impact was more difficult. The experimental data curve shows a distinct plateau region during the initial bulge formation (0.1 – 0.6 μ s). Neither computational model predicts this plateau. This type of plateau was a sign of materials that undergo a phase change during impact loading [19]. The researchers were unsure if A36 steel undergoes a phase change during impact. An extensive literature search found no references on this topic. It was found that HY100 stainless steel undergoes a phase change during impact [14-20]. 304L was found to be a steel material that does not undergo a phase change under impact loading [19].

Figure 1.1 shows the UNLV two-stage light gas gun and some of the key components. A full description of this experimental facility is described in chapter 2.

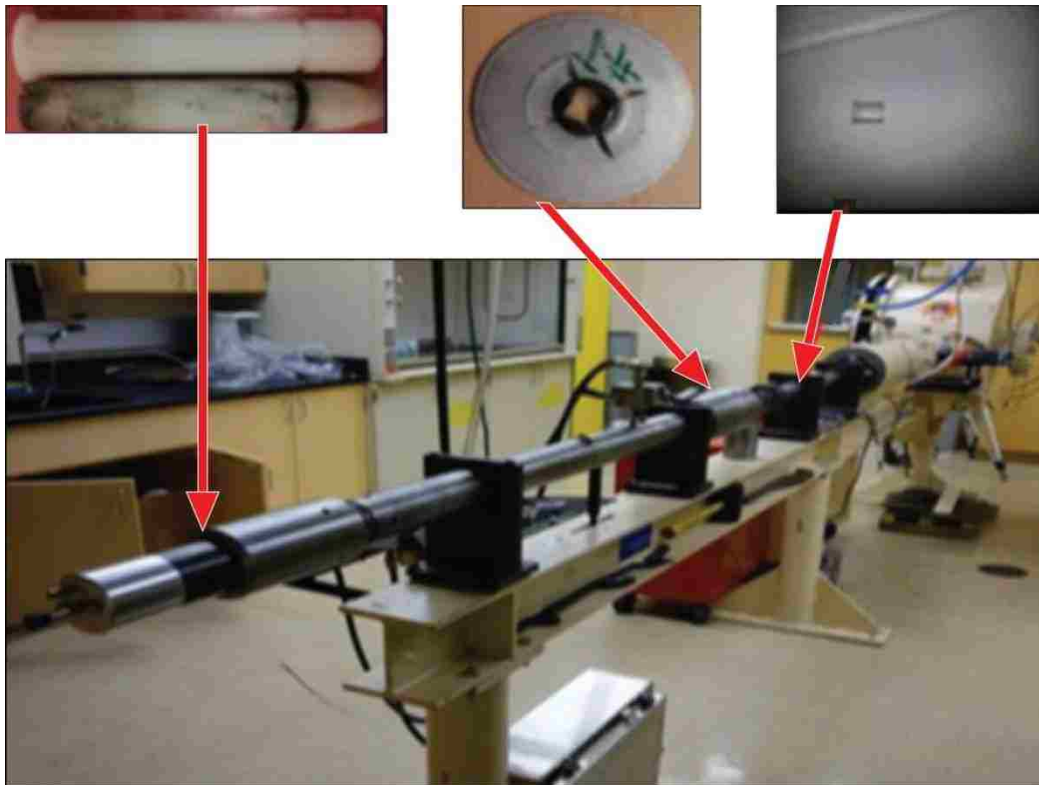


Figure 1.1 UNLV two-stage light gas gun

1.1.3 Material Property Uncertainty in Computational Simulations

Three standard steel alloys that have many global applications are A36, HY100 and 304L steel. The physical characteristics and molecular structure of these steels are well known. However, there is little known about the effect of high velocity impact on the crystalline structure and material phase. Figures 1.2 and 1.3 show a schematic for three commonly known phases that exist in steel alloys. The body centered cubic phase structure is a dominant phase in A36 steel alloy, and it has the shape shown in Figure 1.2a.

FCC, shown in Figure 1.2b, is usually a transitional state into another more complex one. Therefore it is important to be aware of its characteristics and features. The nearest neighbors in the face-centered cubic (FCC) structure are at the corners of a cube surrounding the metal atom in the center. In the hexagonal close-packed (HCP), shown in Figure 1.2c, structures, the atoms pack like stacked cannonballs or billiard balls in layers with a six-coordinate arrangement. Each atom also has six more nearest neighbors from layers above and below. Figures 1.2 and 1.3 indicate the coordination graphic of the three structures. [21]

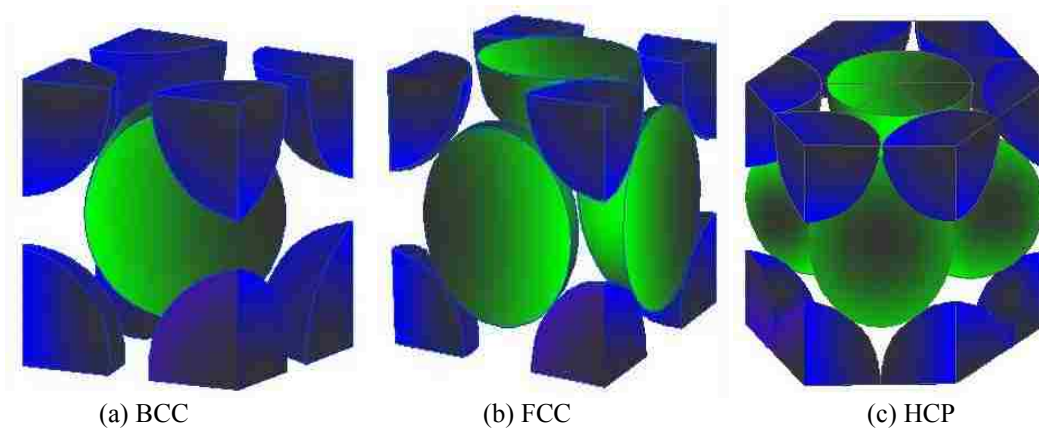


Figure 1.2 The three most common phases in metal crystalline structure: a) Body Centered Cubic (BCC), b) Face Centered Cubic (FCC), and c) Hexagonal Close-Packed Crystalline (HCP).

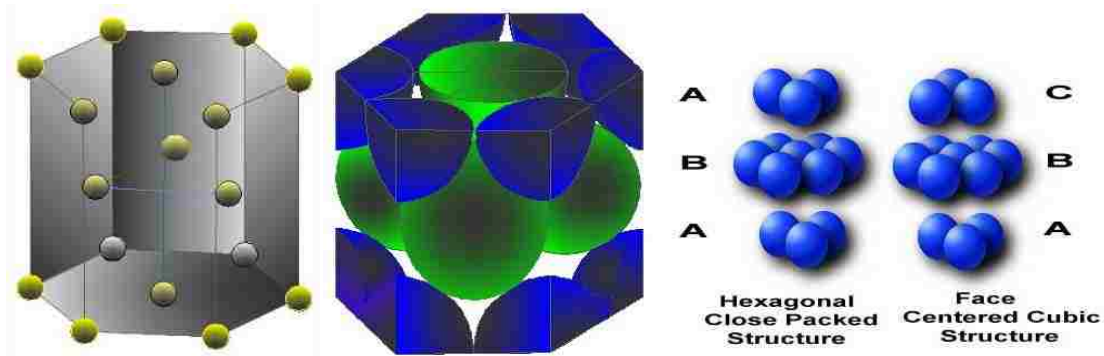


Figure 1.3 Coordination numbers for FCC, HCP, and BCC systems are 12, 12, and 8, respectively.

1.2 Dissertation Objectives

The uncertainty of A36 behavior under impact loading was the motivation for this dissertation research. The overall objective of the dissertation is to determine if evidence of a phase change in A36 can be determined from microstructural analysis of target materials subject to hypervelocity impact. The majority of microstructural analysis was performed on A36 materials. Some microstructural evaluation of 304L and HY100 steel targets was performed as a reference since other impact studies have shown that HY100 does undergo phase change and 304L does not have a phase change caused by impact loading.

No published work could be found describing quantitatively the phase change behavior of A36 steel due to violent impact and sudden heat exposure resulting from high velocity impact loading. This type of loading produces surface and subsurface damage on the subject metal. A36 steel is one kind, among numerous kinds, of steel alloys that has not received enough attention in terms of the effect of such high pressure impact on microstructural phase changes.

A36 steel is a good candidate as a research subject to study its substructure attributes and phase changes due to shock and heat exposure. This research is an enhanced study as a quantitative demonstration of predictive and orderly manner of such phase changes. An added purpose of this experimental work is to determine and quantify the effects of a set of pre-calibrated impacts on A36 steel alloy in terms of microstructure. Additionally and minimally for comparison, two other steel alloys are investigated, 304L and HY100.

This study will focus on determining if a phase change occurs in A36 steel during high velocity impact. Two other steel alloys are also studied for comparison. HY100 has been shown to go through a phase change during impact in previous studies. Also previous studies showed that 304L does not go through a phase change under high velocity impact conditions.

The remainder of this chapter explains the necessity of the work as well as a review of relevant research literature. This chapter will give a background and a road map of the underlying work and the approach to meet the objective: to detect and measure phase changes of three types of steel alloys. [22]

1.3 Material Properties and Application Background Information

1.3.1 A36 Steel Properties

Many favorable features of the low carbon ASTM A36 steel have made it highly attractive for many applications in industry including pre-fabricated buildings, warehouses, industrial and commercial structures, cabinets, enclosures, housings, pipe and tubing. A36 steel is used also in bolted, riveted or welded construction of bridges, buildings and oil rigs. Strength and toughness combined with machinability, ease of fabrication, and other characteristics are just some of the desired properties of A36 Steel [21]. The broad utilization and the vast engineering applications of A36 steel also make it a good candidate as research subject to study its substructure phase changes due to shock and heat exposure. Intuitively, such effect on metal would alter its strength in a predictive and orderly manner. Tables 1.1 and 1.2 list the chemical composition and some of the key physical and mechanical properties of A36 steel [22, 23].

1.3.2 HY100 Steel Properties

HY100 is also a low carbon steel known in industry that has both commercial and mostly military applications in which high strength and toughness is required. It has high tensile strength and ductility, toughness, and atmospheric corrosion resistance. When quenched and tempered this alloy steel is used in construction equipment, pressure vessels, and large structures. HY100 steel carbon content is between 0.12 and 0.2 percent [24, 25].

1.3.3 304L Steel Properties

“304L steel is a heat resisting metal. It is a type T 300 Series Stainless Steel. This steel is an extremely low carbon alloy. Its maximum carbon content is about 0.03 %. This alloy can be used in corrosive conditions as in welding, and food and beverages containers. It is easy to shape by many known industrial and constructional forming and fabrication means [26]”. “Its versatility allows it to be utilized widely [26, 27, and 28].

Table 1.1 Chemical compositions (%) of A36, 304L, and HY100 steels [22, 27]

Element	A36 [22]	HY100 [25]	304L [27]
Iron, Fe	98.0	92.8 – 96.2	66.9 - 74.5
Nickel, Ni	0.00	2.25 – 3.50	8.00 – 10.5
Chromium, Cr	0.00	1.00 – 1.80	17.5 – 19.5
Manganese, Mn	1.03	0.10 – 0.40	0.00 – 2.00
Carbon, C	0.25 - 0.29	0.12 – 0.20	0.00 – 0.03
Copper, Cu	0.20	0.25	0.00
Molybdenum, Mo	0.00	0.20 – 0.60	0.00
Silicon, Si	0.28	0.15 – 0.35	0.00 – 1.00
Phosphorous, P	0.04	0.025	0.00 – 0.05
Vanadium, V	0.00	0.03	0.00
Sulfur, S	0.05	0.025	0.00 – 0.02
Titanium, Ti	0.00	0.02	0.00

Table 1.2 Physical and mechanical properties of A36, HY100, and 304L steels [22, 27]

Property	A36 [22]	HY100 [25]	304L [27]
Density (g/cm³)	7.85	7.87	8.00
Tensile Strength, Ultimate (MPa)	400 - 550		500 - 607
Tensile Strength, Yield (MPa)	250	689	
% Elongation at Break (in 200 mm)	20.0		
% Elongation at Break (in 50 mm)	23.0		
Modulus of Elasticity (GPa)	200	205	193
Bulk Modulus (GPa)	140		
Poisson’s Ratio	0.26	0.28	
Shear Modulus	79.3	80	

1.4 Material Microstructure Definition

The microstructure of solid metallic bodies consists of grains. Grains consist of unit cells in which atoms are arranged in a particular order. The cell structure repeats itself throughout the volume of the grain as shown in Figure 1.4. That is why the grains are also called crystallites. The structure is called lattice in which atoms are placed at lattice points. In metals, generally there is only one atom at a lattice point. There are many types of structures of unit cells for different materials; however, metals generally possess one of the following three cell structures: [29]

1. Body centered cubic structure (BCC).
2. Face centered cubic structure (FCC).
3. Hexagonal closed packed structure (HCP).

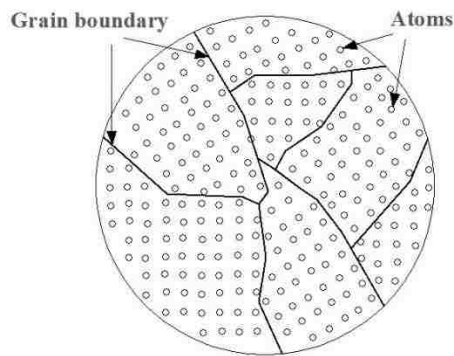


Figure 1.4 Grain structures

1.4.1 Crystalline Phase

In crystallography, crystal structure is an arrangement of atoms in a unit structure pertinent to the type of crystal called a unit cell, which is a set of atoms arranged periodically repeated in three dimensions on a lattice. Crystal lattices have along range of regular order. The distance between a unit cell and one next to it is called Lattice-Distance. The three most common unit cells arrangement will be discussed in the

following sections, namely BCC, FCC, and HCP. These sections are referred to as particular phase structure. [21]

1.4.2 Close-Packed Definition

In both FCC and the HCP structures, but not BCC, the atoms are called close-packed. As the name suggests, some atoms in the cell structure are closer together to each other up to orbit contact, than they are in the BCC structure. The atoms from one layer nest themselves in the vacant spaces among the atoms in-between the next layer. As one may imagine, atoms have their orbits aligned in a matrix of columns and rows [21, 29].

1.4.3 Body Centered Cubic Structure

Typically, as in other unit cells, body centered cubic structures are repeatedly stacked together to generate the entire structure as shown in Figure 1.5. A cubic cell is a cubic shaped element structure that consists of an atom (or molecule) in each corner of the cube and an additional one in the center. Neighbors on all six sides share the 4 atoms side by side. Therefore the corner atom is shared with all the 8 cubical corners of the four cubes that meet at one shared corner point in the structure. Usually, the length of the cell edge is commonly represented by a , as the lattice constant. The distance from any vertex in the cube to the farthest vertex is called body diagonal. The diagonal of the face is the straight line from one corner to the opposite corner (farthest) of the same face. The packing factor is defined by the volume of atoms in a cell per the total volume of a cell. The BCC unit cell has a packing factor of 0.68.[30]

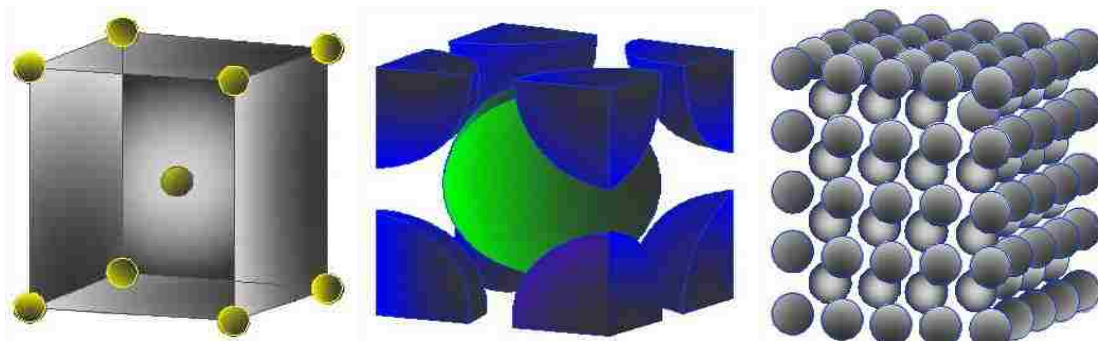


Figure 1.5 Body-Centered Cubic (BCC) Structures

1.4.4 Face Centered Cubic Structure

Coordination number is defined as the number of shared atoms per unit cell. The FCC has a coordination number of 12. The total net number of atoms in a unit cell is 4: one half is shared in each face, times 6 faces, and $1/8^{\text{th}}$ of an atom is in each corner. Figure 1.6 shows a unit cell as a small section of the FCC lattice. As we have defined, the packing factor is the volume of the number of atoms in the cell divided by the total volume of the unit cell. The crystal of FCC packing factor then is 0.74.[21]

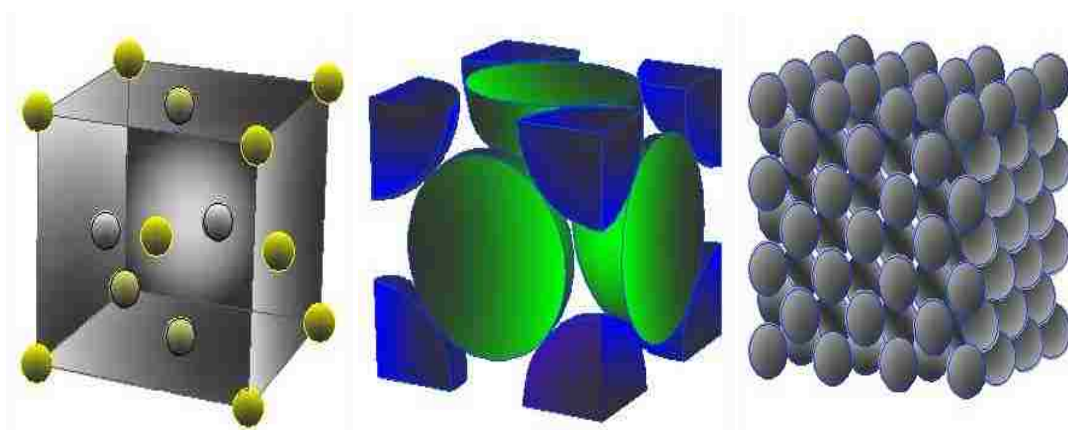


Figure 1.6 Face Centered Cubic (FCC) Structure

1.4.5 Hexagonal Closed Packed Structure

Close-packed crystal structure, HCP, is characterized by a hexagonal prismatic element. There is a regular alternation of two layers; the atoms in each layer lie at the vertices of a series of equilateral triangles, and the atoms in one layer lie directly above the centers of the triangles in the vicinity of nearby layers. As a close-packed structure, some atoms in the cell structure are closer together to each other up to orbit contact, than they are in other surfaces in the hexagonal structure that is where the name, close-packed lattice, came from. In this cell structure there is an atom at each corner of a hexagonal prismatic element; besides, there are three atoms symmetrically placed between the two end faces as shown in Figure 1.7 and one atom each at the center of the flat end faces.

In this cell structure there is an atom at each corner of a hexagonal prismatic element; besides, there are three atoms symmetrically placed between the two end faces as shown in Figure 1.7 and one atom each at the center of the flat end faces. Although the HCP unit cell has a larger lattice than the FCC and BCC, the packing factor is 0.74 which is the same as the FCC unit cell. [21]

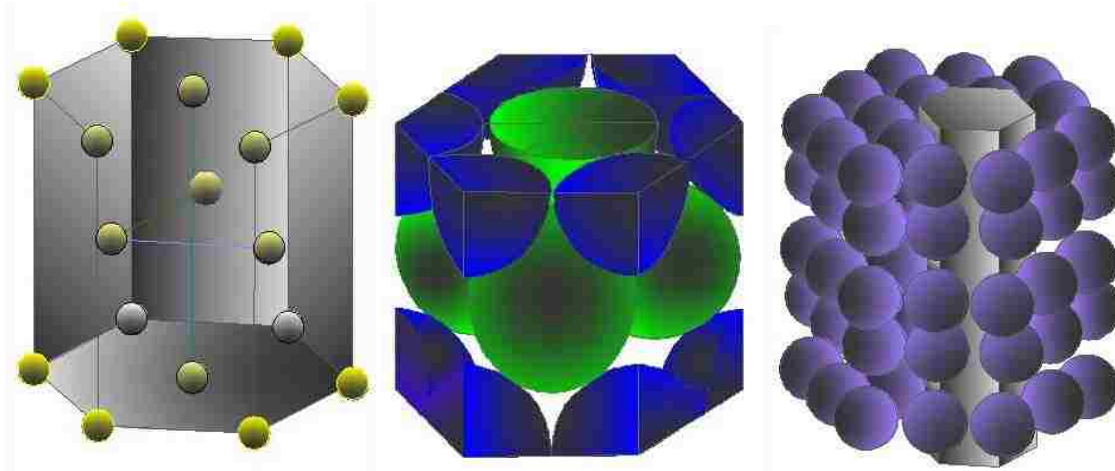


Figure 1.7 Hexagonal Closed Packed Structures

1.4.6 Lattice Defects

Defects may be intentionally induced and controlled by alloying heat treatment, and plastic deformation as a result, occurs in order to obtain a change in the mechanical properties, as does intended alloying. Line defects or dislocations are important causing plastic deformations. The following two types of dislocations are observed: Adding an alloy and forming new boundaries of grains, in addition to inelastic irreversible (plastic) deformation or heat treatment are the main reasons of irregularity and continuity of the repetition of the crystalline structure. The imperfections created are of three major types as indicated in Figure 1.8. Surface deformation is the first type which is on grain boundaries. The second type is line deformation is resulted from dislocation of edges or misorientation. The third type of defect is a point defect. The third one is a fundamental one that itself may cause other kinds of defects and it is resulted from:

- an atom missing from a lattice,

- an atom dislocation out of its usual location in the lattice,
- an atom of the original metal is replaced by a foreign subject or an atom of an alloying material.

Such defects cause either expansion or narrowing of the spaces inside the lattice in between original corners or atom location. They pull and push the natural arrangement of atoms in their vicinity and consequently atoms surrounding the point defect are either stretched apart or are pushed too close. This gives rise to additional pull or push between unit cells and among the atoms that affect the neighborhood in the vicinity of the defective area. If large enough in concentration, such defect will alter the alloy properties [29].

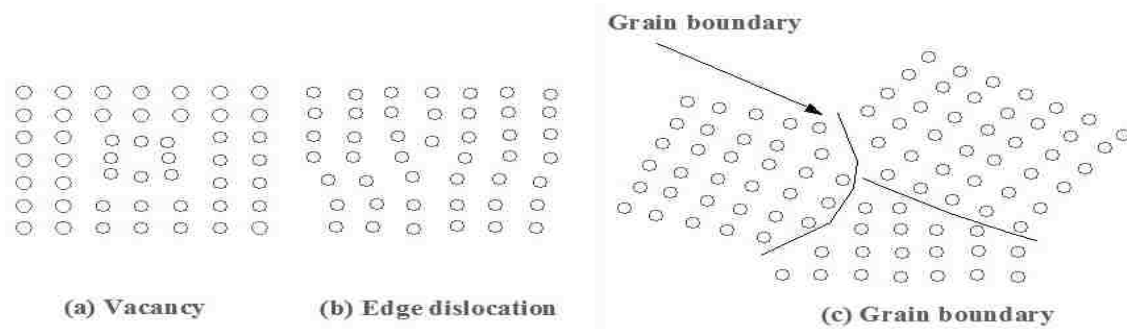


Figure 1.8 Imperfections in lattice structure

1.4.7 Microstructural Basis of Metal Formation Processes

The formation of defects and impurities are summarized in the previous section. But how do these defects travel when subjected to environmental effects such as forces? Figure 1.9 illustrates how these defects travel through the lattice when subjected to shear forces. A dislocation may be restricted by atoms of grain boundaries or by other defects. Two kinds of dislocations exist: edge and screw dislocations. They are determined by the motion and misorientation of the lattice edges [21,29].

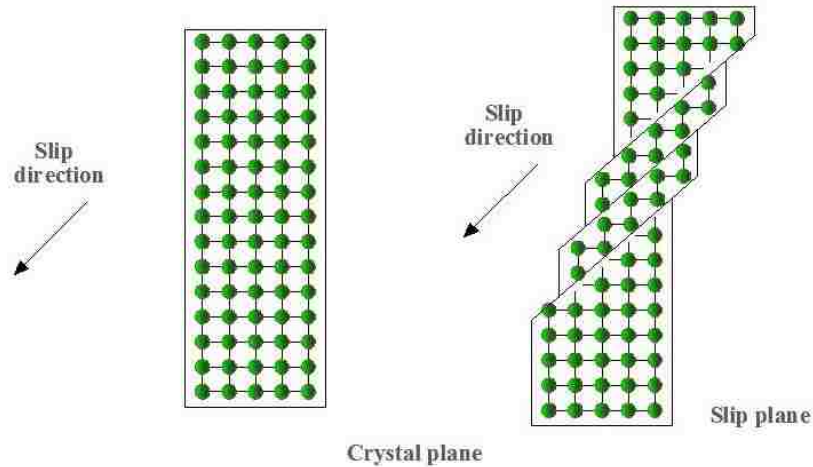


Figure 1.9 Slip in an FCC crystal structure

1.4.8 Plastic Deformation of Metals and Related Properties

Inside a lattice, the atoms are arranged in a particular order and direction. If the neighboring lattice has a deformity that will create a strain of the original lattice and each neighboring one, ultimately it will affect the grain shape and strain and stresses between them. The grain size is a factor in the deformation and movement process. Small grains dislocations can move a short distance before being restrained by other grain boundary. In general that explains why a metal or an alloy become stronger with a smaller grain size, than it is with relatively larger ones, even with the same lattice structure [29, 30].

1.4.9 Twinning

Under certain circumstances, crystals, a specific conditioning and re-formation occurs that we call Twinning. That twinning occurs when two separate crystals share some of the same crystal lattice points in a symmetrical manner. The result is a rebirth of two separate crystals in a variety of particular configurations. A twin boundary or composition surface separates the two crystals. The deformations caused by twinning are described by the twinning surface and direction of twinning. Atoms dislocation may generate twinning shear. About the twinning surface, twinning is a mirror image. The distance that is each atom's position is related to the original system and the twin lattice. Organizations interested in

crystal structure would classify twinned crystals by some twin laws. These twin laws are specific to the particular crystal system. The type of twinning can be a diagnostic tool in natural elements, minerals, or alloys identification [29, 31].

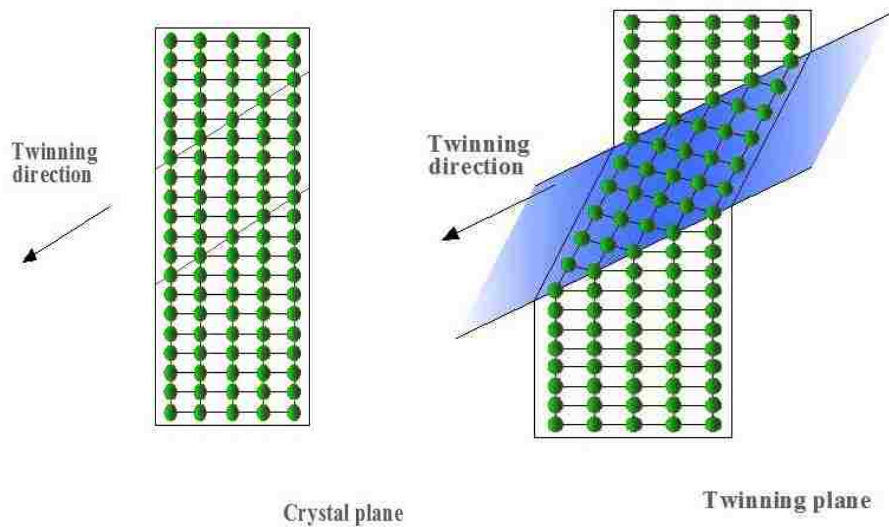


Figure 1.10 Twinning in an FCC crystal structure

1.4.10 Crystallinity

In contrast to a crystalline pattern consisting of a series of sharp peaks, amorphous materials (liquids, glasses, etc.) produce a broad background signal. Many polymers show semi crystalline behavior, i.e. part of the material forms an ordered crystallite by the folding of the molecule. A single polymer molecule may well be folded into two different, adjacent crystallites and thus form a tie between the two. However the tie part is prevented from crystallizing. The result is that the crystallinity will never reach 100 %. Powder XRD can be used to determine the crystallinity by comparing the integrated intensity of the background pattern to that of the sharp peaks. Values obtained from powder XRD are typically comparable, but not quite identical to those obtained from other methods such as DSC [31, 32].

1.4.11 Lattice Parameters

The size and shape of the unit cell of the crystalline phase will determine the position of diffraction peak in the sample electronic viewing. The position of a diffraction peak is independent of the atomic positions within the cell and entirely determined by the size and shape of the unit cell of the crystalline phase. Each peak represents a certain lattice plane and can therefore be characterized by a Miller Index. If the symmetry is high, e.g.: cubic or hexagonal it is usually not too hard to identify the index of each peak, even for an unknown phase.[32]

1.4.12 Definitions and Variables Important to Unit Cell Geometry and Transformations

A unit cell is the smallest divisible volume unit in crystalline matter that contains the crystal phase structural and geometric information; it possesses the symmetry and properties of the mineral. Unit cells in lattices are formed in an array of boxes of parallel sides that are infinitely small and infinitely repeated units periodically in all three dimensional space. Unit cells cannot be viewed using traditional optical lens magnification. Instead, electronic refraction is used in the detection of repeating patterns of unit cells in all three spatial directions. This technique is used in scanning electron microscopy (SEM), back scattered electron diffraction (BSED), and x-ray diffraction (XRD).

The lattice parameters are the length of the edges of the unit cell, the angles between them, and the symmetry property that is particular to the specific crystalline structure. The unit cell consists of a small group of atoms, from eight to as many as hundreds, which have a fixed geometry with respect to one another. The atoms can be placed at the corners, on the edges, on the faces, shared with other cells, or wholly enclosed in the box. Crystals are identical, with a beautiful shape. [29-32]

Variables typically used in unit cell calculations are length, volume, molecular weight, and density. Length at this scale is measured in angstroms, Å (10^{-10} m), or nanometers, nm (10^{-9} m). Cell volume is measured in cubic angstroms (Å³) or cubic nanometers (nm³). Density is measured in grams/cubic centimeter (g/cm³). Molecular weight is measured in grams/mole. The Avogadro constant, 6.022×10^{23} mol⁻¹, is also used in unit cell calculations. And finally, the atomic packing factor (APF), or packing

fraction, is defined as the ratio of volume of atomic particles in a unit cell divided by the total volume of the unit cell. This is a dimensionless quantity that is always less than unity. Theoretical atomic packing factors can be calculated based on the geometry of the unit cell [32].

Typical packing factors for common crystal structures are provided in Table 1.3.

Table 1.3 Atomic Packing Factors (APF) for Common Atomic Crystal Structures [32]

Hexagonal close-packed (HCP)	0.74
Face-centered cubic (FCC)	0.74
Body-centered cubic (BCC)	0.68
Simple cubic (SC)	0.52
Diamond cubic (DC)	0.34

1.5 Dislocation and the Ordination Angle

Definition of misorientation: given two orientations (grains, crystals), the misorientation is the rotation required to transform tensor quantities (vectors, stress, strain) from one set of crystal axis to the other set [passive rotation]. Misorientation is the difference in crystallographic orientation between two crystallites in a polycrystalline material [33, 34].

In crystalline materials, the orientation of a crystallite is defined by a transformation from a sample reference frame (i.e. defined by the direction of a rolling or extrusion process and two basis of the unit cell. In the same way, misorientation is the transformation necessary to move from one local crystal frame to another some other crystal frame. It is the distance in orientation space between two distinct orientations [32-36].

The orientation between two coordinate systems can be defined by the angle-axis pair, $\theta\langle uvw \rangle$. When the coordinate systems define the crystal orientations in different grains of a polycrystalline material, the difference in orientations is called a misorientation. One coordinate system can be superimposed onto the other by rotating by an angle θ around the common axis $\langle uvw \rangle$ as shown in Figure 1.11. Because it is an axis of rotation, the direction $\langle uvw \rangle$ is the same in both coordinate systems. The angle-axis pair notation is normally used to describe the misorientation [36]

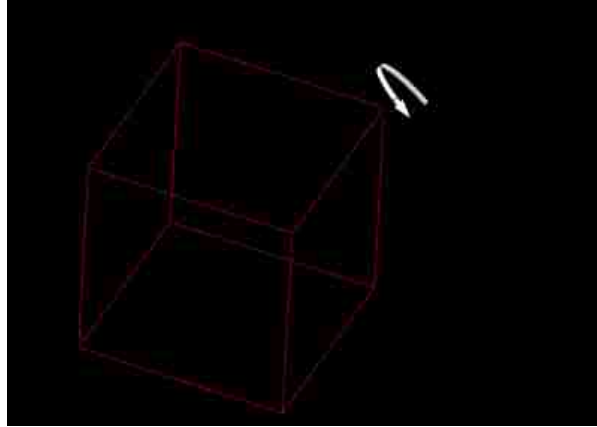


Figure 1.11 Two inter-penetrating lattices can be realigned by a single rotation about a common axis $[uvw]$ by an angle θ . In the figure the axis is the common $[111]$ direction and the rotation angle 60° [36]

1.6 Relevant Research Literature Review

The polymorphic transformation results from shock-loaded iron have been studied in a number of publications. Wang, S. J, et al.[1] have studied phase transition in shock-loaded iron. According to Wang, martensitic transformation α (BCC) in iron under shock-loading, expresses a reversible and transient nature. He observed the transformation $\alpha \rightarrow \epsilon$ (BCC HCP) in iron under shock-loading. In the refined microstructural fingerprints, results were indicative of two sequential martensitic transformations in the reversible α phase transition, even though no HCP is retained in the post-shock samples. Their observations were an ambient temperature and atmospheric conditions; A36 Steel is stable in its BCC (α)-phase body-centered-cubic (BCC) crystal structure. At high impacts or pressures, some phase changes take place, according to this literature and our own experiments; BCC takes on the HCP (ϵ) form, in other word, switching to the hexagonal-closed-packed (HCP) lattice. While the phase diagram of Fe under hydrostatic pressure is well establishes, it is much more challenging to ascertain what happens in Fe when it is subjected to shock-loading. Understanding dynamic phase evolution is critically relevant to many applications of iron and steels under explosion and shock processing conditions, according to Wang[1]

Ibraihim[2] has tested both the quenched & tempered, low alloy steel (used in the pressure vessel industry) and hot rolled carbon steel (used for the manufacture of reinforcement steel bars) in respect to impact properties in relation to the difference in the chemical composition and microstructure for these

two steels. He determined that low alloy steel displays much higher resistance to ductile fracture at high test temperatures, while its resistance to brittle fracture at low test temperatures is a little higher than that of the hot rolled carbon steel. Ibrahim [2] has concluded that Impact properties of steels are primarily dependent on their microstructure. He explains such behavior as that, the microstructure of such steels is of a complex nature and is characterized by a highly dislocated lath structure arranged in packets subdividing the prior austenite grains in addition to the carbides that precipitate during the tempering process. The microstructure of the investigated steels as hot rolled steel shows ferritic-pearlitic structure with a grain size of about 10 nm while the low alloy steel displays bainitic structure with a grain size of about 30 nm[2]

Dougherty,* G.T. Gray et al., [37] found a rare twin linked to high-pressure phase transition in iron. Because certain orientation twins were found near the impact surfaces of only those plates in which the α - ϵ - α transformation occurred, he concluded that, this twin mode is a fingerprint of the α - ϵ - α transformation in iron and iron steels. As such, the presence of these twins in the post-shock microstructures of these metals can serve as a signature to identify regions in which the shock pressure was sufficient to transform BCC-Steel to HCP-steel. [37]

Yang, et al, [38] explains the use of EBSD in finding the markers and fingerprints of the microstructural phase and phase changes in the tested alloys, and they found EBSD results clearly show that the strain path is the crucial factor for deformation twinning in magnesium alloys with strong initial basal texture, and the plastic strain and grain size can affect the amount of deformation twins. They have focused on twinning in AZ31 Magnesium Alloy. EBSD results different twinning processes according to the applied compression strains, clearly show the path is the crucial factor for deformation twinning and the plastic strain and grain size can affect the amount of deformation twins. [38]

Influence of the shock-induced α - ϵ transition in Iron alloy on its post-shock substructure evolution and mechanical behavior, was determined by Gray, Hayes and Hixson [39] In their works a dynamic pressure (impact) above and below the phase transition of 13 GPa applied on high-purity iron alloy, and, on the effect of post-shock compressive stress-strain behavior and substructure evolution besides the

degree of shock hardening was determined in the steel alloy. They found that the effect was higher for shock strength above the transition than below it. The substructure also displayed more deformation twinning for shocks above the phase transition than below so they concluded that the post-shock mechanical response of high-purity iron alloy is significantly increased upon transitioning above the α - ϵ phase transition pressure of 13 GPa. They also concluded the α - ϵ transition front was overtaken and produced a gradient in shock hardening as a function of propagation distance in the tested sample [39]

Angela, et al., in [40] has emphasized the use of EBSD in measuring full crystallographic orientation information. EBSD can produce full crystallographic orientation information. This technique has been used to measure the statistics of misorientations between original 'parent' grains and a recrystallized one [41]. Rollett and Kalu, 2007 defined misorientations and made characterization and microstructural analysis.

In an experimental study by Senkov et al. [42] microstructure of aluminum-iron alloys is studied when subjected to severe plastic deformation. They concluded that severe plastic deformation is an effective method for grain refinement and extension of solid solubility, the dendritic structure of the castings was completely eliminated and the severe plastically deformed structure became a very fine twinned grain structure and partial amorphization occurred in the Al₁₃Fe₄ particles [42].

1.7 Research Plan and Dissertation Roadmap

Chapter 2 will discuss the experimental protocol more elaborately. That includes a description of the gas-gun, cutting and preparation processes, tools, and material used, on the EBSD, and XRD, and viewing protocol and measurement and microstructure phase signature. Detailed test protocols, experimental results, and discussion and conclusion of this dissertation are paced in the following chapters as follows: Chapter 2-Experimental Methods. In chapters 3-5, the experimental results and EBSD phase signature viewing for A36, 304L, and HY100 steel are documented. Results for the latest steels are listed in chapter 6. Chapter 7 includes the conclusion.

CHAPTER 2

EXPERIMENTAL DEVICES AND METHODS

In this chapter we introduce the test specimen description, test sample preparation, test protocol, and tools and equipment used in the test protocol, sample scanning, data acquisition and analysis. After preparing the sample, presenting the test tools, and performing test procedures, the test results are collected and presented in chapters 3-5. Test specimens for A36, 304L, and HY100 alloy steels were randomly selected. The microscopes and data analysis procedures that are used to evaluate specimens before and after impact are described in the following sections.

This dissertation is focused on microstructural characterization of steel alloy plates that were subject to a variety of different high velocity projectile impact conditions. The target and projectile geometries are described in this chapter along with a description of the damage zones produced by the different impact conditions. Each target plate was sectioned to obtain samples from different locations. The sectioning and sample preparation procedures are described in detail. Each specimen was analyzed to determine grain structure phase composition, misorientation, and lattice parameters. The analytical instruments and procedures for each of these measurements are explained in this chapter.

Same protocol in test sample cutting and preparation is applied for the 5 impacted plates of different steel alloys of the same standard dimensions as a target for the gas gun, namely, three square plates of dimensions 15.2 x 15.2 x 1.27 cm of the same alloy A36 steels, 304L and HY100 alloys. Additional samples of each alloy (total of 4 samples) are left for non-impact examination of pertinent microstructure.

Starting with the gas gun impact and followed by the sample cutting and selecting the intended section location for slicing the standard specimen slide for microstructure scanning and followed by introduction to the scanning devices, acquiring the required images which results in the analysis.

2.1 Impact Experiment Geometry and Materials

Target plates are mounted to a support plate that is attached to the internal frame of the target chamber. Figure 2.1(a) shows the target plate in green and the support plate in red. Figure 2.1(b) shows the support plate mounted inside the target chamber.

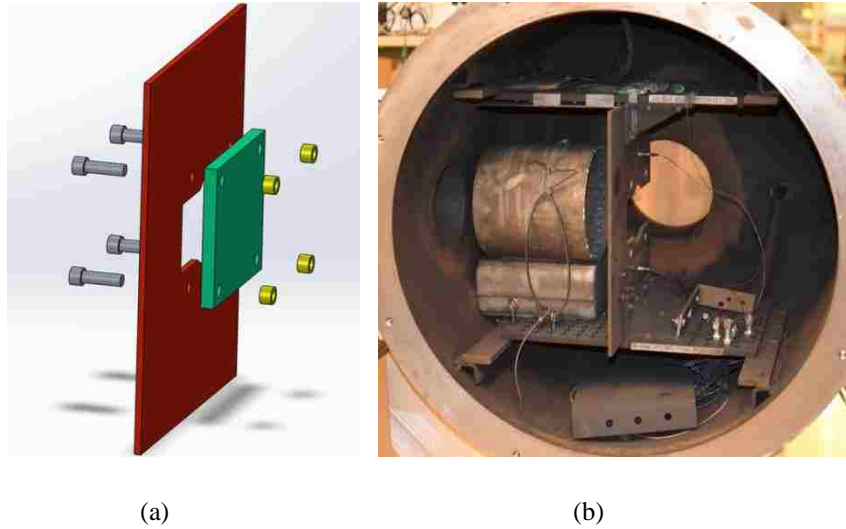


Figure 2.1 (a) Target plate mounting configuration and (b) target mounting plate inside chamber

The target plates are cut into square shapes that fit conveniently inside the target chamber. All target plates have the same dimensions. They are 15.2 cm x 15.2 cm x 1.27 cm. They are impacted with a cylindrical Lexan projectile with a 5.6 mm diameter and 8.6 mm length. An A36 steel target plate and Lexan projectile are shown in Figure 2.2. The target plates are impacted with projectiles at speeds selected to induce significant plastic deformation without completely penetrating the target. The visually observable damage on the front and back side of a typical target plate is shown in Figure 2.3. The crater diameter can be slightly more than three times the projectile diameter (~ 17 mm) for the faster impact velocity. The depth of the crater measured from the flat region on the front surface was up to 6.6 mm and the bulge on the back surface was up to 3.5 mm measured from the flat region of the back surface.



Figure 2.2 A36 target plate before impact and Lexan projectile (not shown to the same scale)



Figure 2.3 front sides (left) and back side (right) visible damage on an A36 steel target

2.2 Target Plate Sectioning and Cross-Section Zones Slicing

Each impacted plate was initially cut in half through the center of the impact crater. The target materials were further cut in to a T-Shape so that six different cross-sections could be exposed and prepared for microstructural analysis. All cutting procedures were controlled to minimize the addition of temperature to the cutting surfaces. A water jet machine was used to make the necessary cuts in the steel targets to obtain the T-shaped bar. The water jet process cools while cutting to help eliminate heat

induced changes to the microstructure. Figure 2.4 shows the results of cutting at various stages including a target plate being prepared for water jet cutting. A top view of the T-shaped bar is shown in Figure 2.5 along with the corresponding dimensions.

Selected Locations of the slides center for EBSD viewing are designated as follows:

Sample (1): Centered 75 mm away from impact crater, thickness is 12.7 mm

Sample (2): Centered 35 mm away from impact crater, thickness is 12.7 mm

Sample (3): Centered 7.5 mm from impact, thickness is 12.7 mm from the other side of the T- Section.

Sample (4): Centered 20 mm and thickness is 12.7 mm

Sample (5): Centered 10 mm and thickness is 12.7 mm

Sample (6): Centered at impact area

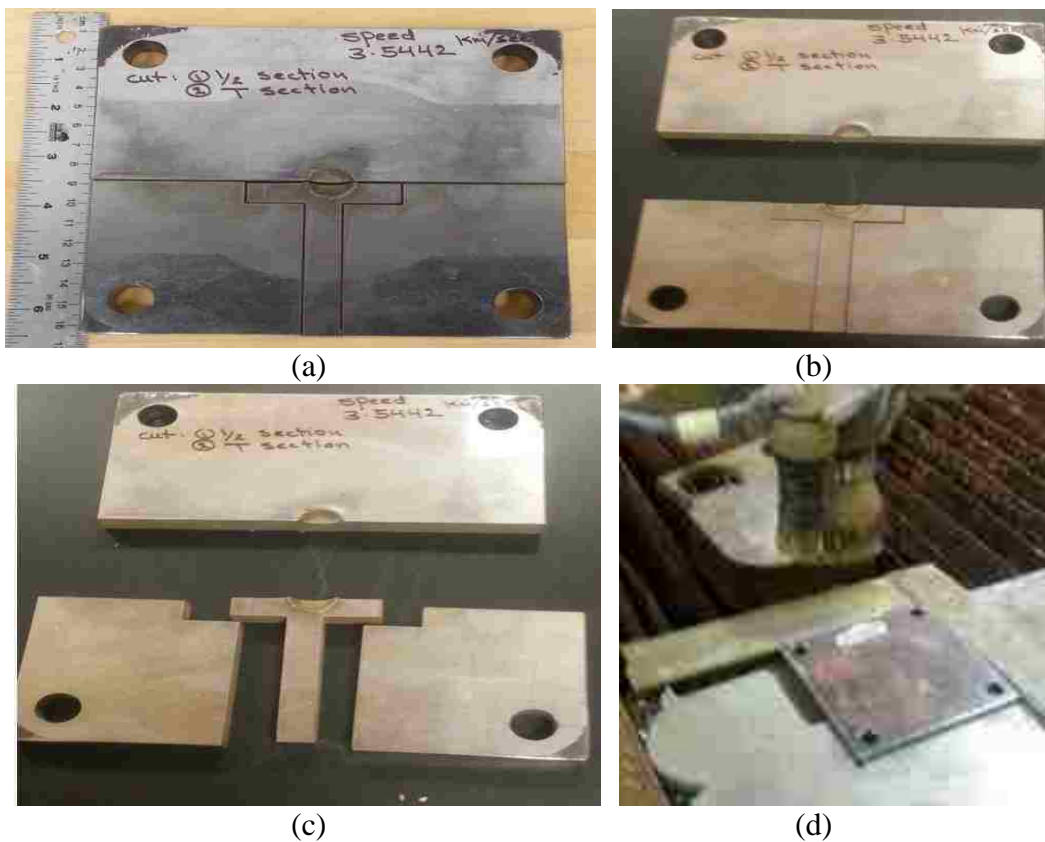


Figure 2.4 (a) Cut lines on a target plate, (b) Target cut in half, (c) Finished T-section ready for further sectioning, and (d) Target plate ready for cutting by the water jet machine.

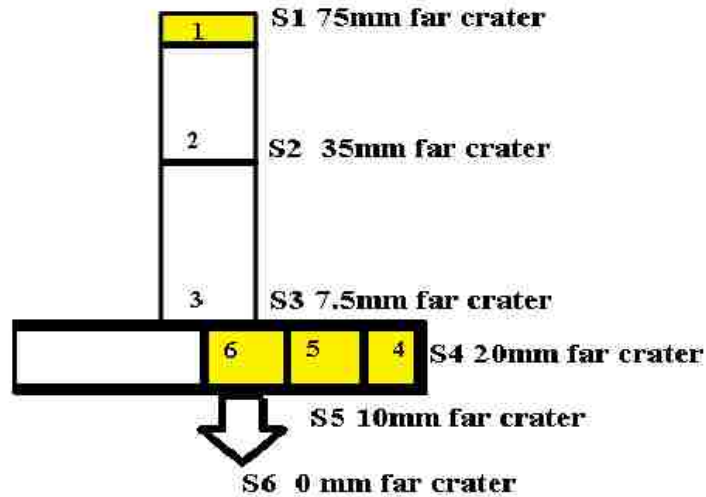


Figure 2.5 T-shaped bars with dimensions

Further cuts were made on each T-bar to expose six different cross-sectional surfaces for microstructural analysis. These secondary cutting procedures and subsequent polishing steps are described in Section 2.3. The locations of the 6 cross-sectional surfaces are shown in Figure 2.6. Sections 1-3 are located along the web of the T-bar and sections 4-6 are located along the flange of the T-bar. Table 2.1 shows the key dimensions for each cross-sectional region. Microstructural analysis is performed at multiple places within each cross-section. Specific places for analysis within a cross-section location are identified in the corresponding data and results sections of this dissertation. Figure 2.6 shows the relative cross section slicing for the pre-selected points for scanning.

Figure 2.6 shows the relative cross section slicing for the pre-selected points for scanning



Figure 2.6 Location of six cross-sectional regions used for microstructural analysis

Table 2-1 expresses the location for the selected scanning position, relative to the impacted surface, and the edges of the plate. Also it indicates the final dimension of the specimens that are prepared for scanning.

Table 2.1 Location and dimensions of cross-sections for microstructural analysis

Cross-Section Zone	Branch of T-Bar	Planar Distance from Impact Center (mm)	Left Edge Distance from Impact Center (mm)	Dimensions of Cross-Section (mm x mm)
1	Web	75	0	12.7x 12.7
2	Web	35	0	12.7 x 12.7
3	Web	7.5	0	12.7 x 12.7
4	Flange	0	20	12.7x 12.7
5	Flange	0	10	12.7 x 12.7
6	Flange	0	0	12.7 x 12.7 (upper left corner missing)

2.3 Specimen Cutting and Polishing Procedures

A precision diamond blade slicing process is used at 6 different locations to cut in a plane orientation that is the same as the projectile direction of impact. Figure 2.7 shows the ISOMET 4000 Linear Precision Saw. The dimensions of the sliced specimens are 1.27 cm x 1.27 cm with a thickness of 2 mm. These are the dimensions required for EBSD microscopy. The specimen slicing direction should produce a surface for EBSD viewing. Those surfaces are cut out of the T-section in a parallel direction to the projectile velocity vector at the selected cross-section locations.



Figure 2.7 Linear Precision Saw (ISOMET 4000) used to slice steel cross-sections

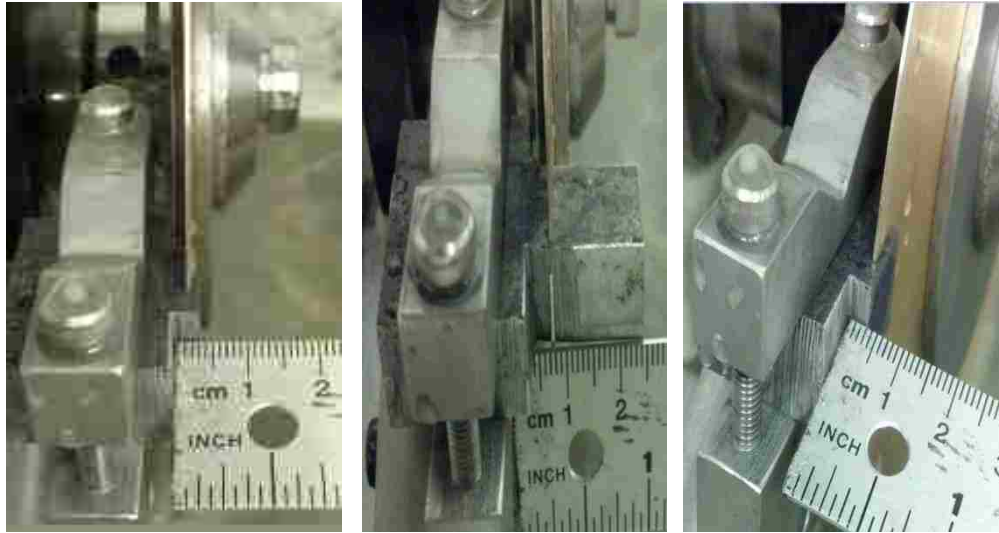


Figure 2.8 Linear Precision Saw slicing the A36, 304L and HY100 steel materials

Each sliced steel section is cast in a circular cylinder of epoxy to facilitate the polishing, etching, and cleaning processes. A set of sliced sections from a target are shown being cast in epoxy in Figure 2.9. The cast epoxy cylinders, ready for polishing, are shown in Figure 2.10.



Figure 2.9 Sliced steel specimens in casting molds



Figure 2.10 Epoxy cylinders with steel slices ready for polishing

In order to prepare the samples for microscope viewing and XRD, they were polished carefully in a BUEHLER Beta Grinder Polisher, as shown in Figure 2.11. Multistage sanding, grinding, and polishing are required. The process includes grinding, using 270, 320, 400, 600 and 800 grit sand papers. A two-stage polishing process follows using a 3 micrometer polishing solution and a 0.05 micrometer polishing solution. Figure 2.12 illustrates the steps in this labor intensive and time consuming process. Etching is the final step to conclude the preparation process that results in a clear surface for microscope viewing. The samples are surface etched using a solution of 96 % HNO₃ acid and 4 % ethanol for 10 seconds.



Figure 2.11 Polishing and preparation process of A36, 304L and HY100 steel

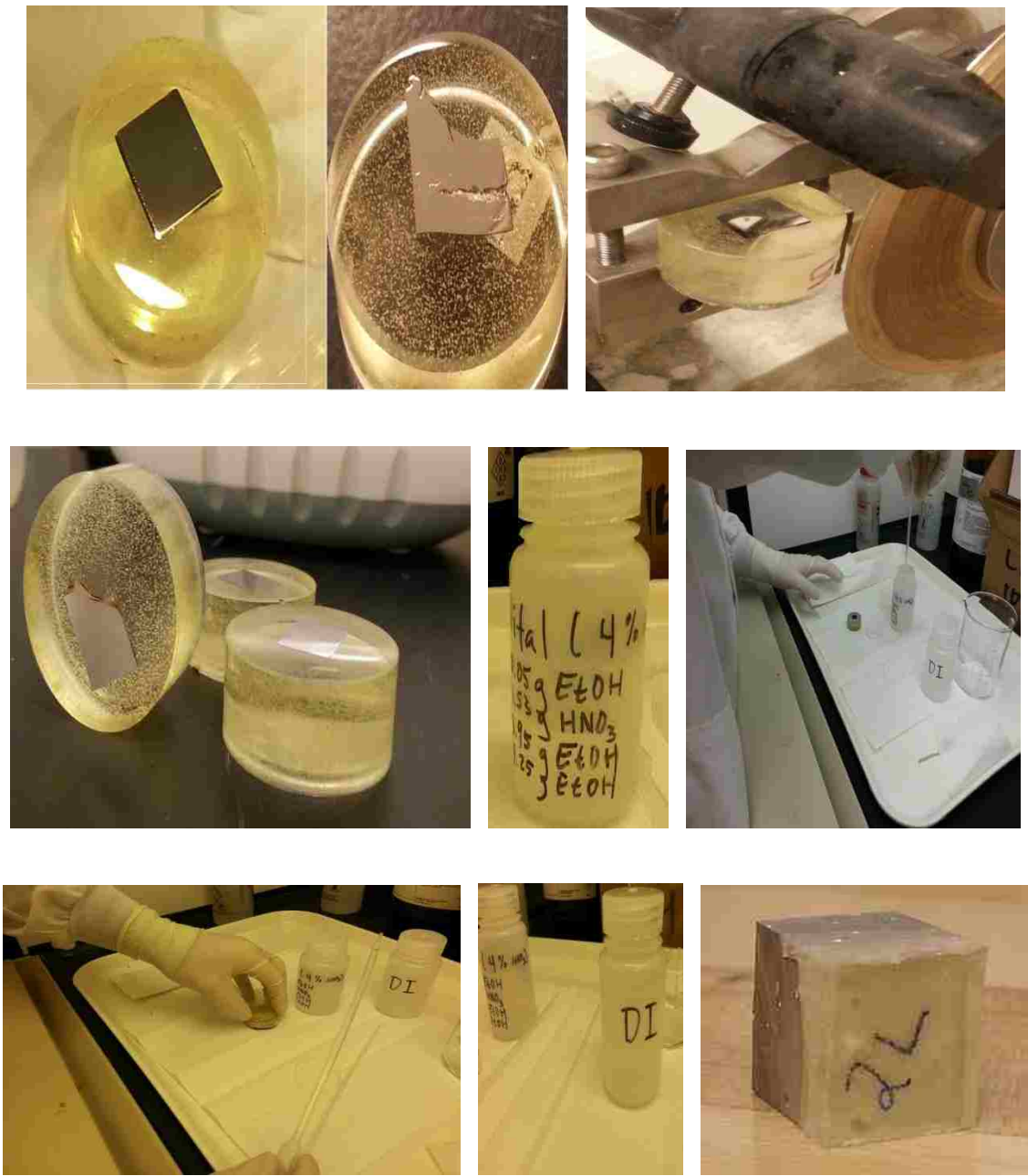


Figure 2.12 Polishing and Etching A36, 304L and HY100 steel specimens

2.4 Target Damage Zone Descriptions after Impact Experiments

The extent of damage is different for each target material and each impact speed. Faster impact speeds induce a higher shock pressure profile within the target materials.

The three different alloys examined have different microstructures for each material and impact velocity, plus one for the non-impact. This section describes the following items for each material and impact velocity:

- Target material
- Impact velocity
- Estimated peak internal pressure values during impact
- Visual inspection and description of damage
- Damage zones of interest and specific locations of these damage zones relative to the impact center [43]

The peak internal pressure values were estimated by another researcher who is conducting computational simulations of these impact experiments. The computational simulations were validated by comparing the size and shape of visible damage caused by the projectile and also, by comparing back face velocity predictions to experimental measurements [include UNLV/NSTec [13-16,44]. It was not possible to validate the internal pressure values, but it is assumed they are reasonable since the deformation and velocity predictions were within 5 – 20 % of experimental measurements. Analysis of the A36 targets was the primary objective of this dissertation. The A36 plates were examined first. Three different impact speed and many damage zone locations were examined. The 304L and HY100 materials were analyzed in part to provide reference data to the A36 measurements.[14, 44]

Only one impact velocity was studied at the higher values because that speed provided more relevant data. A smaller number of damage zones were selected in these materials that focused on the zones that showed the most information.[17, 18, 45, 46]

2.4.1 A36 Steel (Impact Velocity of 3.54, 4.51, and 5.80 km/s)

One A36 target plate from each impact velocity condition was evaluated. The geometry of the damage zone in the A36 target for the three different impact velocities is shown in Figure 2.13. Depth and width of the crater on the front side is measured with calipers.

Enlarged views of the impact section which is given special attention in scanning for more than one point on the surface of that section are shown in Figures 2.13, (a), (b) and (c) for the A36 steel at different impact velocities. Figures 1.14 (a) and (b) are enlarged views for the impacted cross section for 304L and HY100 steels at the designated impact velocities.

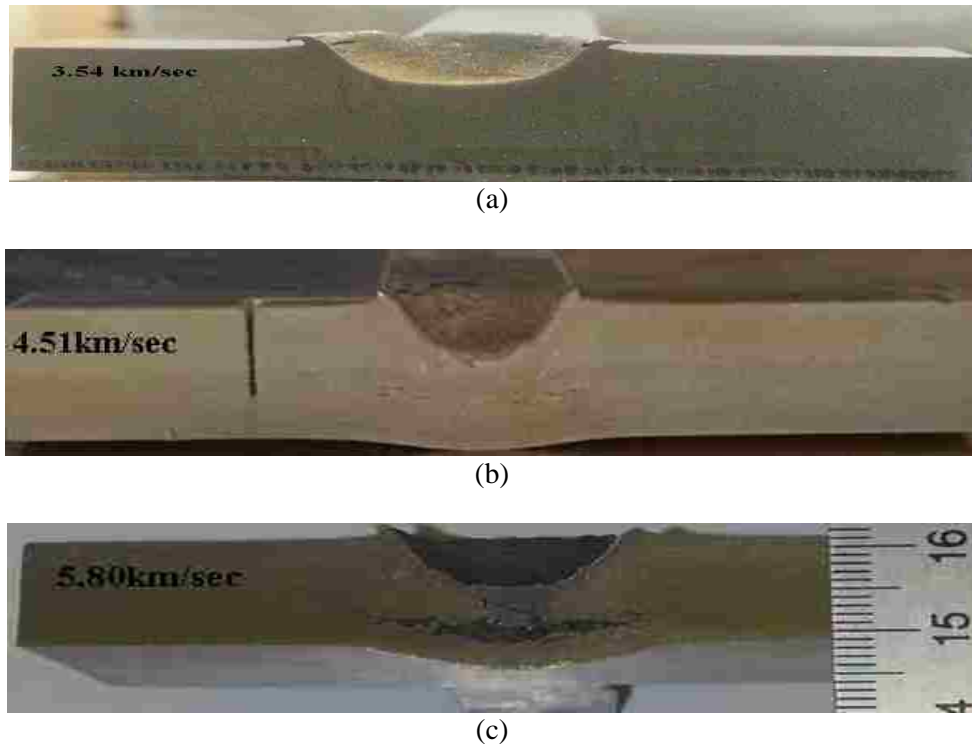


Figure 2.13 Damage zone in A36 steel targets subject to impact velocities of (a) 3.54 km/s, (b) 4.51 km/s, and (c) 5.80 km/sec.

Roy, et al. [15, 16] conducted computational simulations using LS-Dyna and were able to predict pressure profiles versus time at various points in the cross-section.

Table 2.2 shows the peak pressure at various locations in the A36 steel targets for the three different impact velocities.

Table 2.2 Peak impact pressure in A36 steel targets predicted from simulations [14]

Impact Velocity (km/s)	Location (mm)	Peak Pressure GPa
3.54	a (Crater)	60
3.54	b (20mm)	14.2
4.51	a (Crater)	75
4.51	b (20mm)	14.9
5.80	a (Crater)	93
5.80	b (20mm)	14.9

2.4.2 304L Steel (Impact Velocity of 6.58 km/s)

Figure 2.14 shows similarity of both 304L and HY100 steel alloys impact cross section and pressure information for the target plates are listed in Table 2.3

Table 2.3 Peak impact pressure in 304L and HY100 steel targets predicted from simulations. [14]

Impact Velocity (km/sec)	Location (mm)	Peak Pressure (Gpa)
304L @ 6.58 km/s	a (Crater)	60
	b (20mm)	14.2
HY100 @ 6.70 km/s	a (Crater)	75
	b (20mm)	14.9

2.4.3 HY100 Steel (Impact Velocity of 6.70 km/s)

Similar processes were applied to the impacted HY100 steel alloy targets to prepare them for scanning and viewing.

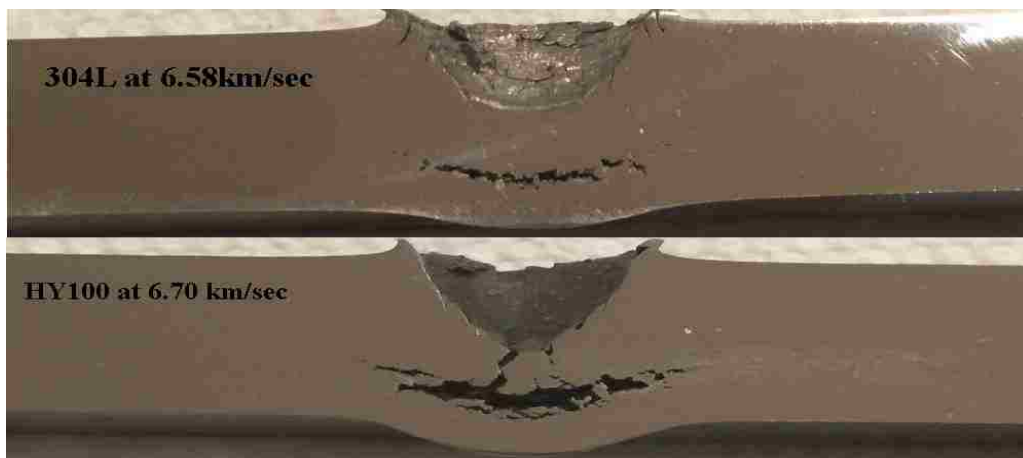


Figure 2.14 Crater zone in 304L (the upper Figure) and HY100 (the lower Figure) targets subject to velocities as indicated

2.5 Pressure Time Distribution in Target Plates

The internal pressure in the target plates during impact varies with time and position relative to impact. It was not possible to measure this pressure during experiments. [16] Performed LS-Dyna computational simulations of the experiments and predicted the pressure versus time at several points within the target for specific impact velocities. The pressure directly under the impacting projectile is much higher than the pressure far away from the impact point. [13-16]

Table 2.4 Peak impact pressure in A36, 304L and HY100 steel targets predicted from simulations

Alloys	Speed (km/sec)	Location, Distance from edge of crater (mm)	Pressure (Gpa)
A36 Steel	5.80	4.08	30
A36 Steel	5.80	5.17	25
A36 Steel	5.80	6.07	20
A36 Steel	5.80	7.27	15
HY100	6.70	0.04	50
HY100	6.70	1.56	30
HY100	6.70	1.08	25
HY100	6.70	4.59	14.9
304L	6.58	0.02	65
304L	6.58	0.08	60
304L	6.58	0.15	35
304L	6.58	2	25

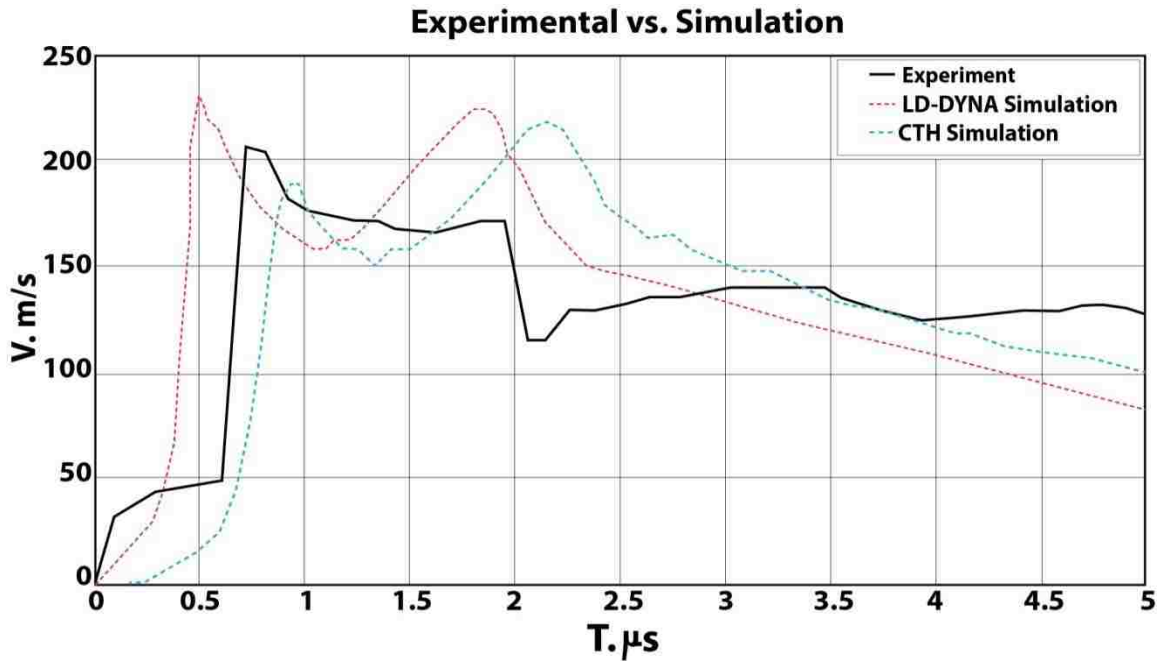


Figure 2.15 Experimental data and computational simulations of back face velocity versus time during impact of a Lexan projectile (5.3 km/s) into an A36 steel plate [8].

2.5.1 Pressure Distribution in Target Plates

Figure 2.16 shows that the pressure is higher than the critical value needed to initiate a phase change from BCC to HCP. The time to reach this peak pressure and drop back below the critical value is less than 4 microseconds.

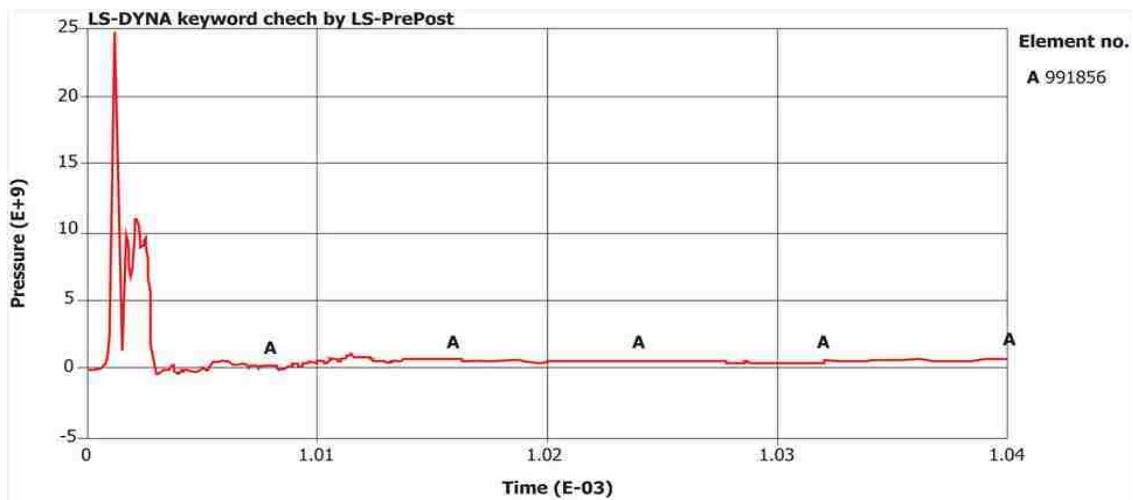


Figure 2.16 Relationship between pressure (GPa) and time at a distance of (5.17 mm from the impact crater of A36 steel target and an impact velocity of 5.80 km/sec

Figure 2.17 shows 304L steel with a pressure higher than the critical value needed to initiate a phase change from BCC to HCP. The time to reach this peak pressure and drop back below the critical value is less than 1 microsecond.

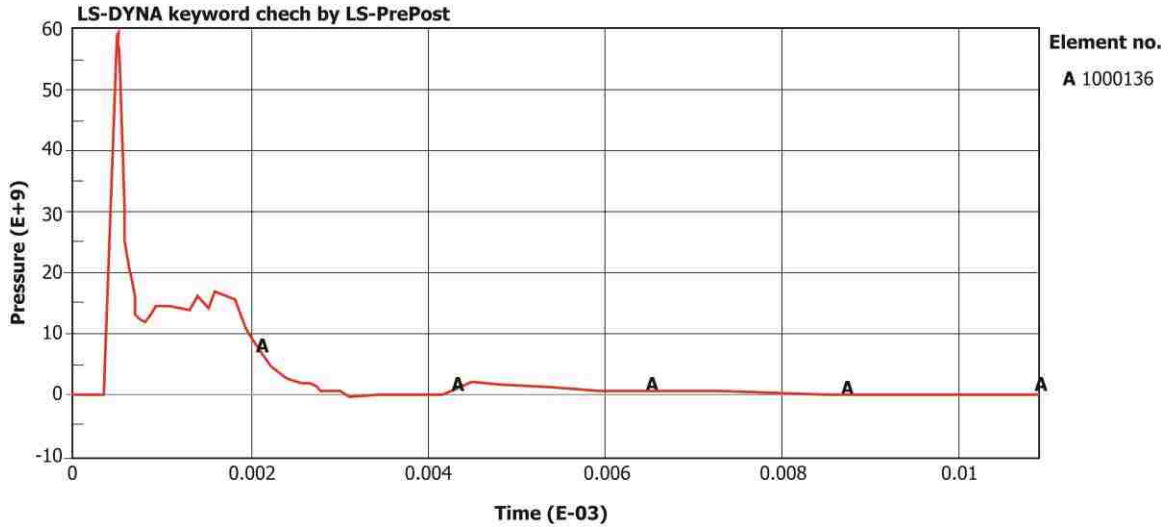


Figure 2.17 Relationship between pressure (GPa) and time at a distance of (0.08 mm) from the impact crater of 304L steel target and an impact velocity of 6.58 km/sec

Figure 2.18 shows that the pressure is so high at this point the phase starts to change from BCC to HCP, through during the short period of time 0.014 milisecond and the distance is 0.04 mm from the impact area.

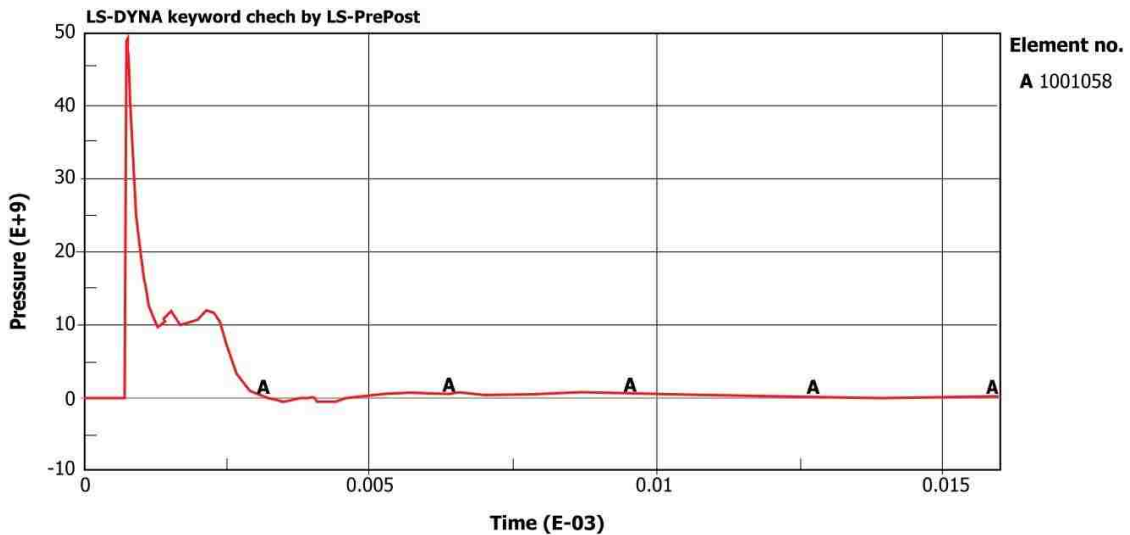


Figure 2.18 Relationship between pressure (GPa) and time at a distance of (0.04 mm) from the impact crater of HY100 steel target and an impact velocity of 6.70 km/sec

This provides images of the pressure change in these areas, where it's starts high in the crater area and then begins to decrease after a short period ranging 5 millisecond and all changes in the iron alloy and change the crystalline phase to be within this time limit.[14]

2.6 Scanning Electron Microscopy (SEM)

SEM is class of electron microscope devices in which a beam of electrons are focused and directed into a scanned object. SEM is a powerful technique in the examination of materials. It is widely applied in metallurgy, chemistry, geology, biology, medicine, and other fields. The main principle of a Scanning Electron Microscopy (SEM) is having a focused beam of electrons, that when directed or pointed to a target sample, the electrons will interact with the atoms in the sample causing a secondary electron beam to be emitted. The secondary beam emitted is then detected as it contains information about the sample's surface such as geometry and composition of the object which can then be analyzed. The beam's position is combined with the detected signal to make a well-defined image. The inclination of the object surface affects the scattered electron beam (secondary beam). Tilted surfaces are partially exposed and more electrons are emitted by scanning the sample and detecting the secondary electrons, which images creates displaying the topography of the surface. Since the detector is not a camera, there is no diffraction limit for resolution as in optical microscopes and telescopes [47]. The high resolution of SEM is significant so that the scanning of the SEM accuracy can be on the order of magnitude of one nanometer. Specimens can be observed in high or low vacuums with elevated temperatures [48]. When the SEM scans the image by producing an electron beam and having it interact with the atoms of the sample, much information is detected about the sample's surface composition. The primary electron beam is scanned in a raster scan pattern and the beam's position is combined with the decanted signal to produce an image with resolution even better than one nanometer. The major source of detection is when the secondary electrons are excited and emitted back into the scanner.

Moreover, reflections from tilted surfaces are less tense than flat exposed surfaces [48, 49]. Although there are electrons that penetrate through the object, most secondary electrons produced by the object are

scattered by the object being collected to form a signature of a three-dimensional image on a CRT-screen. The image mapping made by the transmission electron is a fingerprint that is compared to a database of already identified materials. EBSD and XRD are the only two devices that belong to the SEM class on the microscopes that we have used to scan for the impact effects of the designated steel alloy microstructure. Concepts fundamental to any scanning electron microscope (SEM) are all very similar. The microscope consists of a column, a specimen chamber, and a vacuum system. The scanning process is not entirely simple, yet can be simplified in a few steps which we can conceive from the developed and important underlying scanning concept in SEM devices. To start, an electron beam is accelerated down the column, in which a series of lenses control the diameter of the beam, as well as focus the beam onto the specimen. A series of apertures (micron-scale holes in metal film) which the beam passes through affect properties of that beam, such as controlling the specimen position and orientation (tilt, rotation). Furthermore an area of beam/specimen interaction generates signals that can be detected and processed to produce an image or spectra. The object being imaged is the source diameter (Gaussian intensity distribution) of the electron secondary beam. The produced images are given an accuracy and certainty level by the loaded computing program interface with the microscope. Application of the SEM fundamental concept will be seen in the EBSD application, as well as in the XRD. Only a single point in a single specimen of 1,000 microns is scanned at a time. This is mounted on the specimen holder, which will be discussed in the EBSD and XRD in this chapter. The operation in both cases relies on orienting the specimen or the beam head in order to create an angle of attack appropriate for the correct image response. More than one region is scanned in the specimen, one at a time, and selection of the subject points depends on the purpose of scanning. [50-53]

The development of electron optics in the 1920 was essentially the beginning of a revolution in electronic scanning. In a short summary, the very first true SEM was developed in 1942 by Zworykin, while attempting to manipulate secondary electrons. However, the two discoveries in electron optics, in the early twentieth century (1926), the idea of an electron microscope had sparked and the project was

initiated. To start things off, Busch, when he tracked the trajectories of charged particles through the field, had shown that axially symmetric electric and magnetic fields could act as particle lenses.

Ruska and Knoll tried to implement Busch's lens formula experimentally. They produced in the construction of the first transmission electron microscope (TEM) in 1931. In 1937, Von Ardenne built a true microscope with high magnification by scanning a very small raster with a highly focused electron beam [32, 34]. This led to the construction of the very first high magnification SEM which included various methods of detection, possibilities, followed by the Cambridge group and Cambridge Scientific Instrument Company groups in the 1950s and early 1960s and marketed as the "Stereo-scan" in 1965 [48-51].

The environment of the acquired data and its format depends on the device as we can see in EBSD and XRD. Data is processed, quantized, plotted or tabulated in accordance with the mounted computer software. Limitations of the processed data size can be caused by the attached computer hardware and software. Most of the data is analyzed by the software and the researcher as indicated by the EBSD and XRD sections. There is a large mass of figures, tables, and plots that can always be obtained. However, only two cross section location specimens for each speed and material have been analyzed for the space, but most of the acquired data is included in the supplemented appendices, so that the same analysis may be applied to or can be used for extended researches.

Analyzed charts, graphs data information and discussion are presented in the results chapters 6 and 7 and defined in the EBSD and XRD sections. Statistical analysis of the data is needed to show the confidence in the data and mapping the scanned scanning data with the built in data base.[52,53]

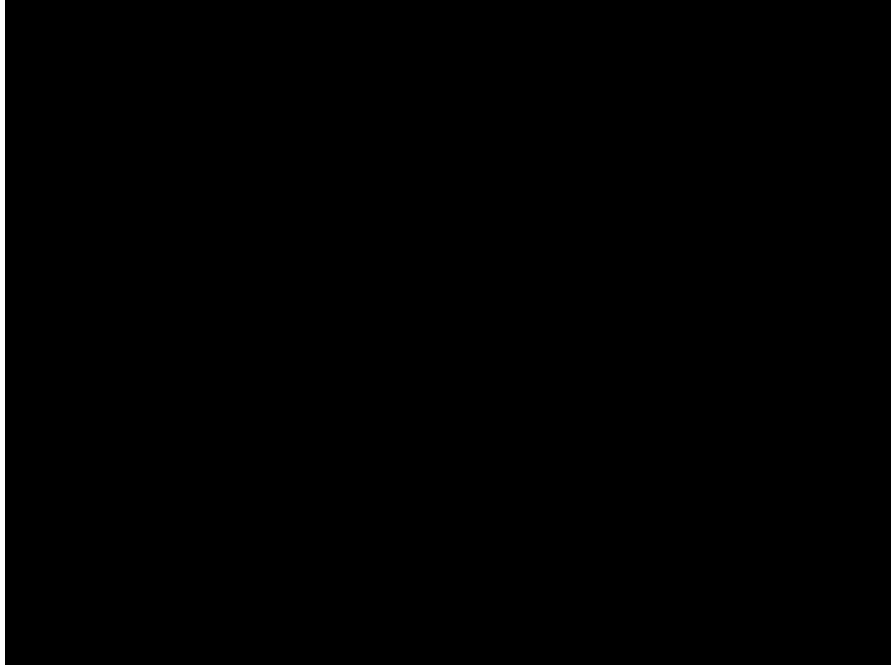


Figure 2.19 SEM opened sample chamber [48]

An electron beam in the SEM device is emitted from an electron gun fitted with a tungsten filament cathode, allowing it to be heated for electron emission. The energy exchange between the electron beam and the sample results in the reflection of high-energy electrons by elastic scattering, emission of secondary electrons by inelastic scattering, and the emission of electromagnetic radiation, each of which can be detected by specialized detectors.

The beam current absorbed by the specimen can also be detected and used to create images of the distribution of the specimen current. Electronic amplifiers of various types are used to amplify the signals, which are displayed as variations in brightness on a computer monitor (or, for vintage models, on a cathode ray tube) [48-53].

When the primary electron beam interacts with the sample, the electrons start to lose energy as repeated random scattering occurs, as well as absorption within a teardrop-shaped volume of the specimen known as the interaction volume, which extends from less than 100 nm to approximately 5 μm into the surface. The size of the interaction volume depends on the electron's landing energy, which is also the atomic number of the specimen and the specimen's density [29].

Each pixel found in the computer video memory is synchronized precisely with the position of the beam on the specimen in the microscope, and the resulting image is a distribution map of the intensity of the signal being emitted from the scanned area of the specimen creating a very clear image. Modern machines save the image to the computer's data storage. The magnification in a SEM can be controlled from a range of up to 6 orders of magnitude from roughly 10 to 500,000 times [48,50,51]. In divergence with optical and transmission electron microscopes, image magnification in the SEM is not a function of the power of the objective lens.

In contrast with the optical microscope, the electron scanning microscope does not need focusing or condensing. Knowing that the electron beam already has a fine and focused beam during reflection, the scanning beam has different intensity that depends on the object's orientation, location, size, and point. Collectively the simple sustenance of point forms a picture which includes the data from the reflecting surface. The data on the image is interpreted by the microscope. For example the unit cell lattice constant and other crystal information are calculated by the SEM system. The electron beam, typically, has an energy ranging from (0.2 - 40) keV, and is focused by one or two condenser lenses to a spot about 0.4 nm to 5 nm in diameter. The beam passes through pairs of scanning coils or pairs of deflector plates in the electron column, typically in the final lens, which deflect the beam in the x and y axis' so that it scans in a raster fashion over a rectangular area of the sample surface [48,51].

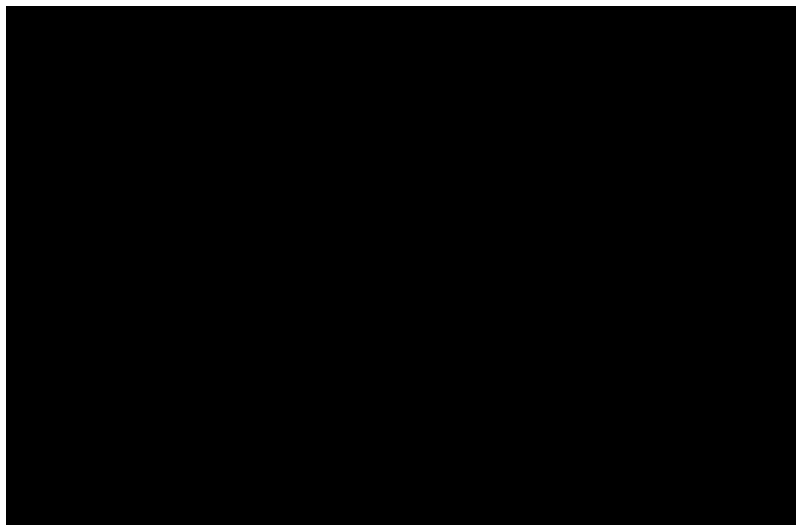


Figure 2.20 Schematic of an SEM. [48]

The SEM is routinely used to generate high-resolution images of shapes of objects (SEI) and to show spatial variations in chemical compositions:

- 1) Acquiring elemental maps or spot chemical analyses
- 2) Discrimination of phases based on a mean atomic number (commonly related to relative density).
- 3) The SEM is also widely used to identify phases based on qualitative chemical analysis and/or crystalline structure.

Precise measurement of very small features and objects down to 50 nm in size is also accomplished using the SEM. Backscattered electron images (BSE) can be used for rapid discrimination of phases in multiphase samples and SEMs equipped with diffracted backscattered electron detectors (EBSD).

Furthermore, the polished sample is placed in the SEM and inclined approximately 70° relative to the normal incidence of the electron beam. The detector is actually a camera equipped with a phosphor screen integrated with a digital frame grabber. In contrast with a traditional microscope which usually depends on lenses to do the magnification function, it is quite different for the SEM microscope as the SEM microscope depends on an electron beam following a vertical path through the microscope which is later focused into the sample.

The reflected beam from the object sample can be detected by the screen similar to a television screen which then produces the final image. Some of the many advantages of the electron microscope versus the typical microscope are the huge magnifications that can detect object details which are most likely beyond the range of any powerful physical lenses; this is the main reason that made the SEM microscope more useful than traditional microscopes [58-60]. The pattern of Kikuchi lines on the phosphor screen is electronically digitized and processed to recognize the individual lines. These pieces of data are used to identify the phase, to index the pattern, and to determine the orientation of the crystal from which the pattern was originally generated. Individual mineral grains can also be selected for identification and determination of crystal orientation, or data may be acquired on a grid over a selected area of the surface of the sample to determine the identity, orientations, and spatial relations between large numbers of

grains. These pieces of data can be used to make statistical studies of the crystalline fabric of the sample, to reveal systematic textural relations between individual grains or phases, and even to determine relative abundances of phases in a multi-phase sample [48-55].

Figure 2.19b shows a schematic for the sequence process of sample viewing by an incident beam, in Backscattered Electrons [50].

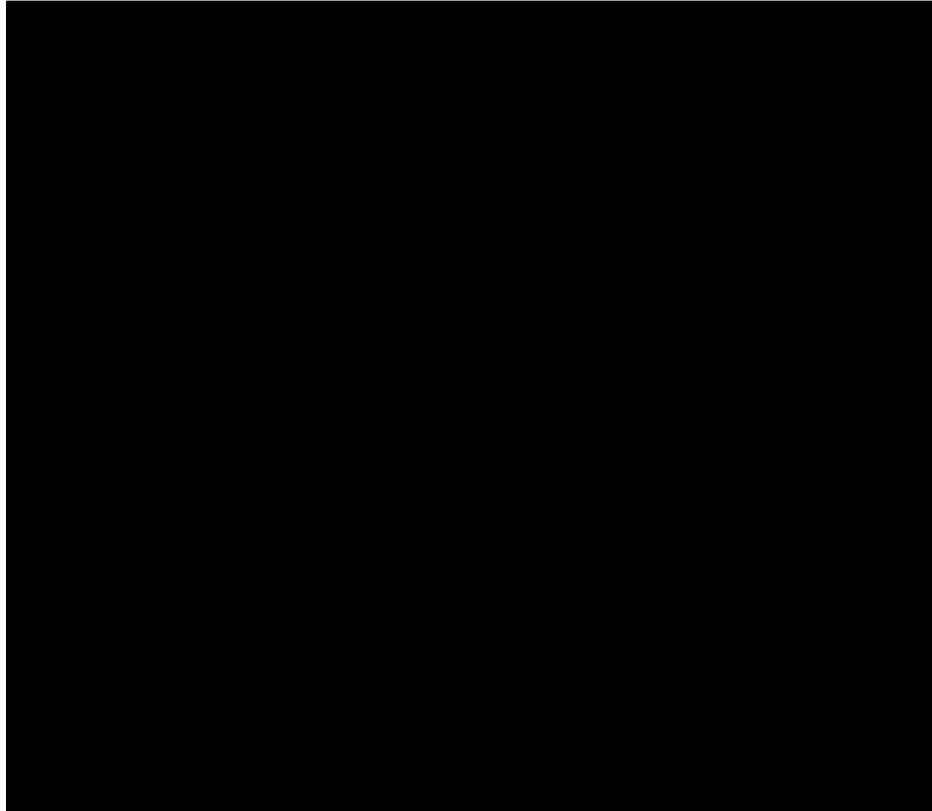


Figure 2.21 a EBSD Components Show How an SEM Work Doe [54]

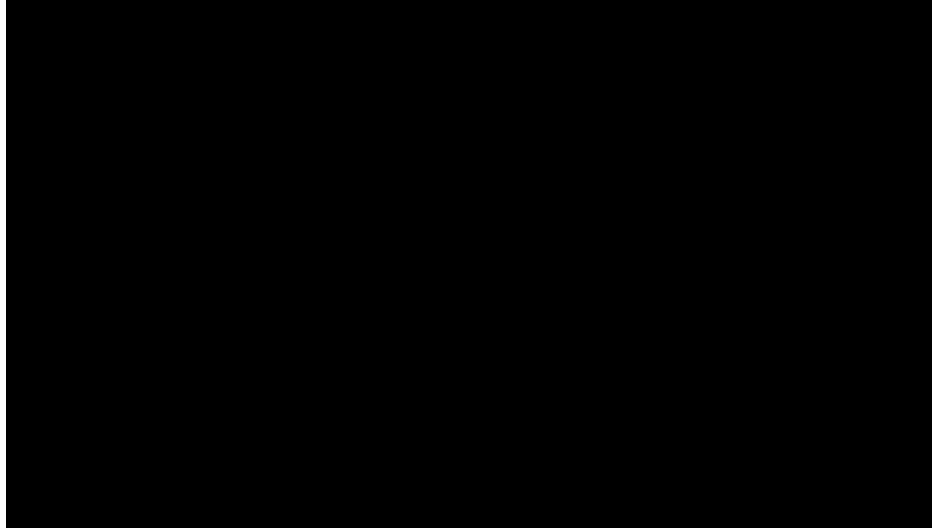


Figure 2.21 b Schematic for Sample Exposed to an incident Beam, primary backscattered Electrons Show [54]

2.7 Electron Back Scatter Diffraction (EBSD)

The classification of materials by directly linking microstructure and crystallographic texture to provide very rich and quantitative datasets make it a very useful tool for our specific application use which includes helping to define and analyses the underlying microstructure.

EBSD has now been used for many aspects of materials characterization including characterization of grain boundary types, establishing relationships between layers on substrates in metal, semiconductor and superconductor systems, characterizing texture and its changes during deformation and annealing in metal alloys and geological samples, establishing links between grain size and texture components during deformation as in the case of our application of high dynamic pressure on the plates of A36, 304L and HY100 steels. EBSD is also the fastest most reliable way to attain data for crystalline structure and orientation in a solid crystalline phase. Moreover, it is possible to acquire data for phases of all symmetries and opaque phases. This data gives a very true and rich 3-dimensional orientation for individual crystals. The spatial resolution can be on the order of few microns, which is far more superior to the resolution which is attainable using other techniques. EBSD data is usually acquired using either a scanned electron beam, or an automated stage.

A stationary electron beam can include analyses of thousands of individual grains in a run accomplished in hours; acquisition of data for thousands of individual spots in a single one-day run is routine in most laboratories. Sample preparation is considerably more involved and the scanned area is relatively small then in other techniques such as, TEM and XRD, compared with areas accessible using EBSD.[54-57].

Additionally, accelerated electrons in the primary beam of a scanning electron microscope (SEM) can be diffracted by atoms in the crystalline layers in crystalline materials. These secondary electrons can be detected by the screen which then generates visible lines called electron backscatter patterns. These patterns are merely projections of the geometry of the framework planes in the crystal, and they give direct information about the crystalline structure and crystallographic orientation of the grain from which they originate. When used in unification with a data base that includes crystallographic structure information for phases of interest and with software for processing the EPSP's and indexing the lines, the data can be used to identify phases based on crystal structure.

A scanning electron microscope was presented by McMullan and Knoll who originally produced it [48, 58]. Charles Oatley with the Cambridge group, in 1950 have started the first commercial applications for a scanning electron Microscope, based on Ardenne 1973 scanning with magnification power with a small aberration [48] theory of electron scanning microscope together with construction of the first high magnification of an electron scanning microscope [58- 59].

This method has been historically, and still is, used for the identification and classification of minerals, and what is amazing is that it can be used for any materials, even amorphous ones, so long as a suitable reference pattern is either known or can be constructed [45].

In this research, Electron Backscattering Diffraction (EBSD) is used to examine and detect crystalline structure of the A36, 304L and HY100 steel pre-impact and post impacts. The impact shots were fired at different speeds and the examination points were considered at specifically selected locations relative to the crater surface created by the resulted impact. However the pre-impact atomic structure is already well

known; nevertheless the imperfect chemical contents, since there is no guarantee of the exact alloy contents the ASTM standard prescribes the guidelines[53].

When the beam of a Scanning Electron Microscope (SEM) gets into contact with a crystalline material mounted at an incline of around 70degrees, the electrons disperse beneath the surface, subsequently diffracting among the crystallographic planes. The diffracted beam produces a pattern consisting of intersecting bands, termed electron backscatter patterns, or EBSPs. These patterns can be imaged by placing suitable films or phosphor screens in close proximity to the sample in the SEM sample chamber.

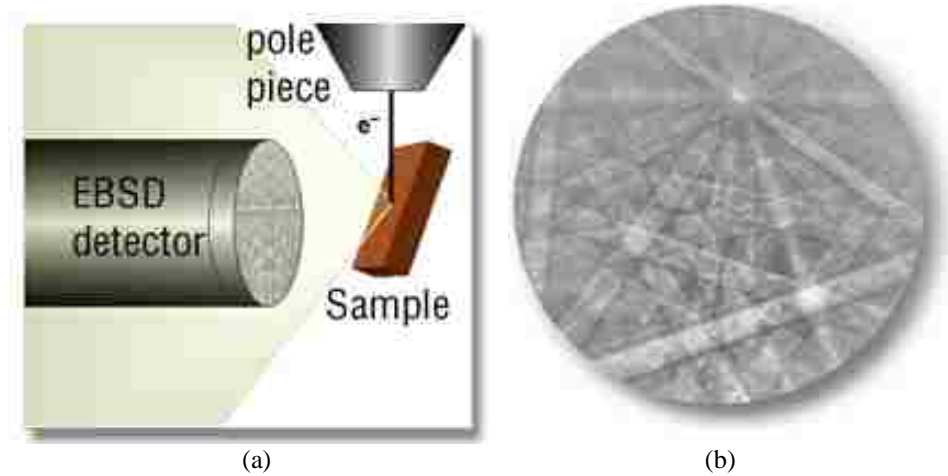


Figure 2.22 a) The angles between the bands are directly related to the angles between planes in the crystal lattice. b) is the symmetry of the crystal lattice is reflected in the pattern [60,66].

The bands in the pattern are referred to as Kikuchi bands and are directly related to the crystal lattice structure in the sampled region. As such, analyzing the pattern and bands can provide key information about the crystal structure for the measured phase.

Alignment of the crystal lattice with respect to some laboratory reference frame in a material known as crystal structure. The core to almost everything that goes on in EBSD is "indexing" the pattern. If the sample produces good diffraction patterns, getting the proper indexing is a process of:

1. Locating the bands

2. Determining the angles between the bands
3. Comparing the angles to theoretical values
4. Determining the phase

This technique allows microstructural phase and crystal orientation information to be determined at very specific points in a sample. The spatial resolution varies with the accelerating voltage, beam current, and spot size of the SEM along with the atomic number of the sample material. Also, index-able patterns can be acquired from about 50 nanometers with a field emission source [59-63].

For an EBSD measurement, a flat/polished crystalline specimen is positioned in the SEM cavity at a highly tilted angle ($\sim 70^\circ$ from horizontal) towards the diffraction camera, which then increases the contrast in the resultant electron backscatter diffraction pattern. The phosphor screen is located inside of the specimen chamber of the SEM at an angle of approximately 90° to the pole piece and is united to a compact lens which focuses the image from the phosphor screen onto the CCD camera. Throughout this configuration, some electrons which originally enter the sample backscatter can actually escape. As these electrons exit the sample, they may exit at the Bragg condition related to the spacing of the periodic atomic lattice planes of the crystalline structure and diffract. These diffracted electrons can escape the material while others will collide and become excited that the phosphor will start causing it to fluoresce [64-66].

In addition to the previous topic, an electron backscatter diffraction pattern (EBSP) is also created when many diverse planes diffract dissimilar electrons to form Kikuchi bands which correspond to each of the lattice diffracting planes. If the system geometry is well termed, it is also possible to relate the bands present in the EBSP to the fundamental crystal phase and orientation of the material within the electron interaction volume. Likewise, each band can be indexed individually by the Miller indices of the diffracting plane which formed it. In most materials, only three bands and/or planes that intercept are required to describe an exclusive solution to the crystal orientation (based upon their inter-planar angles) and most commercial systems use look-up tables with international crystal data bases to perform indexing [60-63].

Factually, the hardest part in the process of indexing is the core step of identifying the Kikuchi bands. The bands' locations were usually a result from a tedious operation and drawing the lines on an image. Distinctions in image intensity, background, pattern quality, etc., complicated and caused frustration in most attempts to automate band identification with image-analysis techniques until the famous Hough transform was applied to the process. Essentially, the Hough transform converts bands in an image to points in Hough space, which are afterwards easier to identify and localize in an image using computer software. In the images that follow, the color-coded Kikuchi bands in the right image have been identified from the same colored peaks in the Hough space image shown to the left in Figure 2.23. Once the bands have been identified, the next step is to determine the angles between the bands. The subsequent process, which determines the actual indexing, involves comparing the information derived from the Kikuchi bands to the theoretical values for reflectors in known phase reference tables [60, 63].

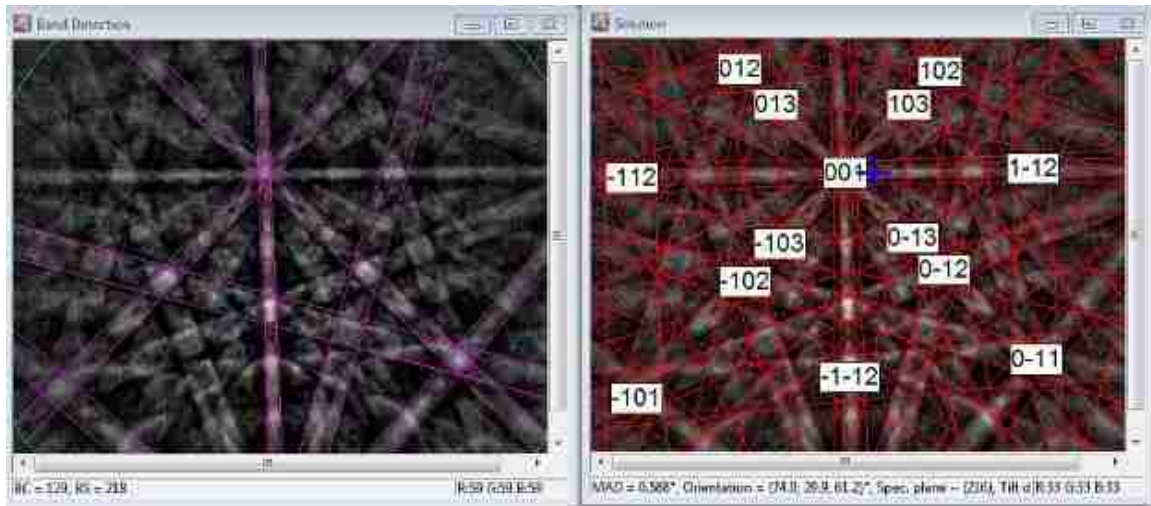


Figure 2.23 An electron backscatter diffraction pattern.

EBSD can be used to find the crystal orientation of the material located within the incident electron beam's interaction volume. Typically when in a square or hexagonal grid, modifying for the correct image causes foreshortening due to the sample tilt, which then results in many maps. These maps can spatially describe the crystal orientation of the material being interrogated and can be used to examine

microstructure and sample morphology. Some of these maps describe grain orientation, grain boundary, and diffraction pattern (image) quality. There are numerous statistical tools that can be used to find the quantity of the average misorientation, grain size, and crystallographic texture.

From this data-set; numerous maps, charts and plots can be produced. From the orientation data, a wealth of information can be invented that aids in the understanding of the sample's microstructure and processing history. In more recent years, there have developments. These developments include understanding the prior texture of parent phases at elevated temperature; the storage and residual deformation after mechanical testing and the population of various microstructural features, including precipitates and grain boundary character [60-65].

Figures 2.24 show the EBSD, Figure 2.25, 2.26, 2.27, 2.28, 2.29, and 2.30 show the scanning results of actual steel alloys of this current research.

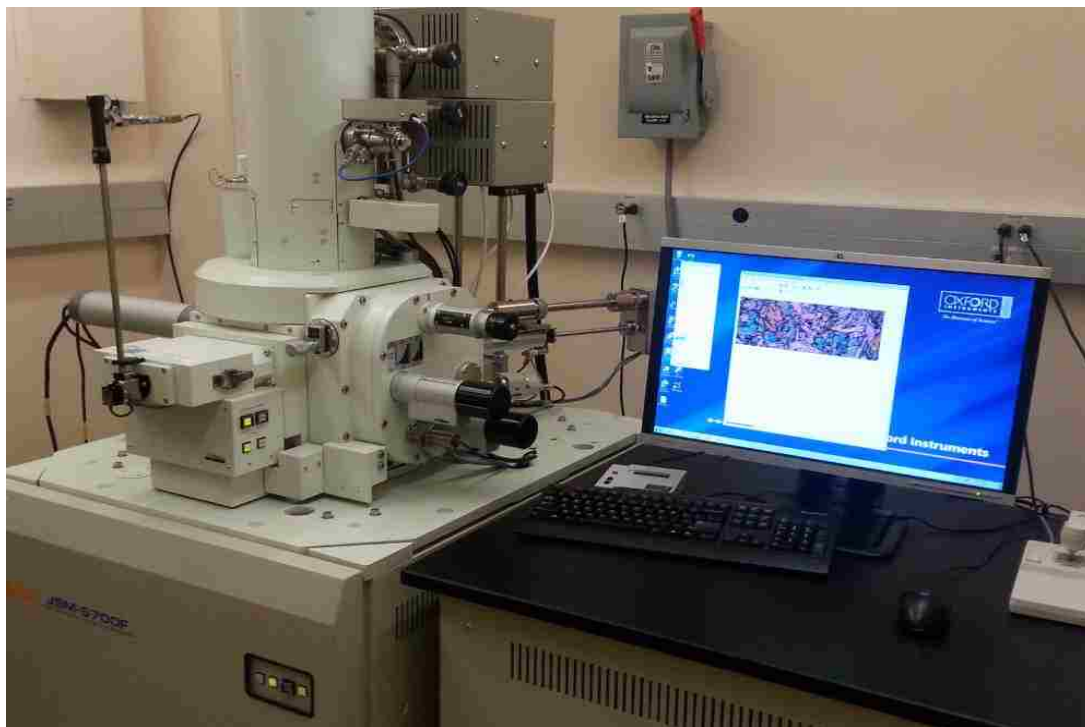


Figure 2.24 Electron backscatter diffraction (EBSD)

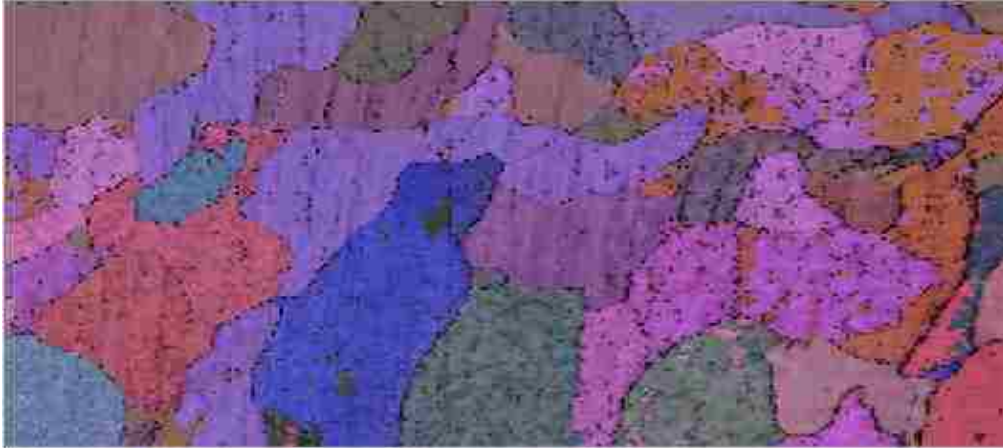


Figure 2.25 A36 Steel, colored area of 75 mm away from crater with mapping photo of grain boundary (X=400)

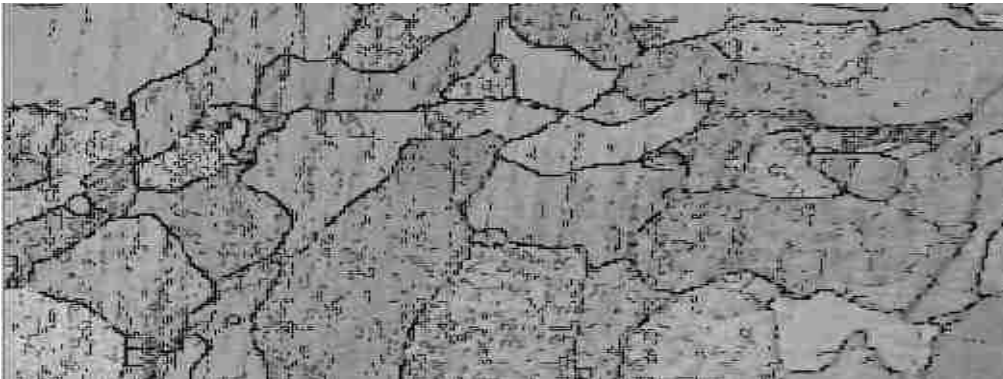
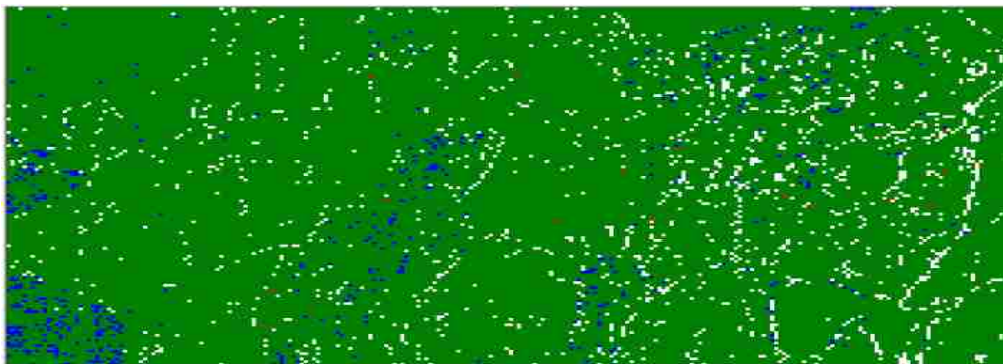


Figure 2.26 A36 Steel, same area as Figure 2.25 with surrounding of grain (boundary condition (BC) and boundary grain (BG) (X=400)



BCC
 FCC
 HCP

Figure 2.27 A36 Steel, same area as Figure 2.25 colored regions indicate crystal phase; green is BCC, blue is FCC, red is HCP, and white shows areas where no phase determination could be made.

Phase photo of each phase different colordeepeningon input data

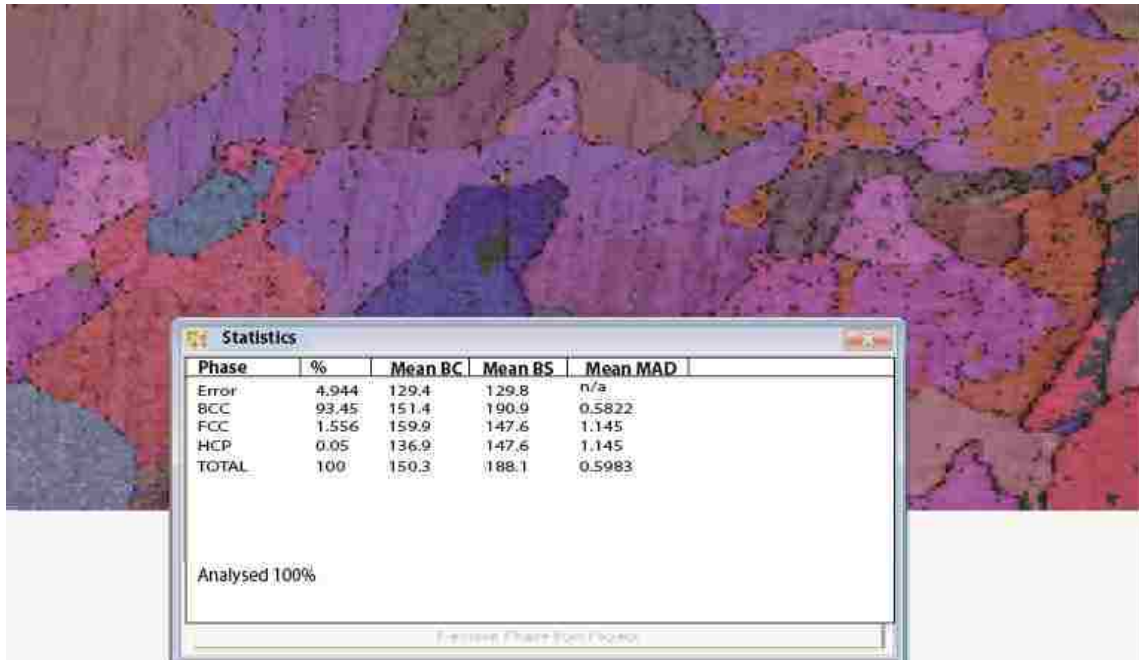


Figure 2.28 Ratio of the phase percentage and the error

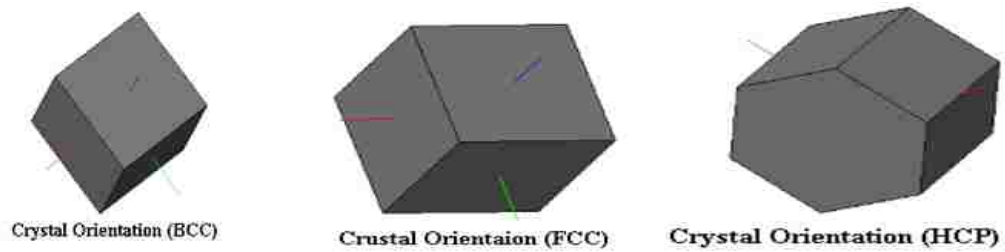


Figure 2.29 Crystal Orientation Magnification and the original length of the map

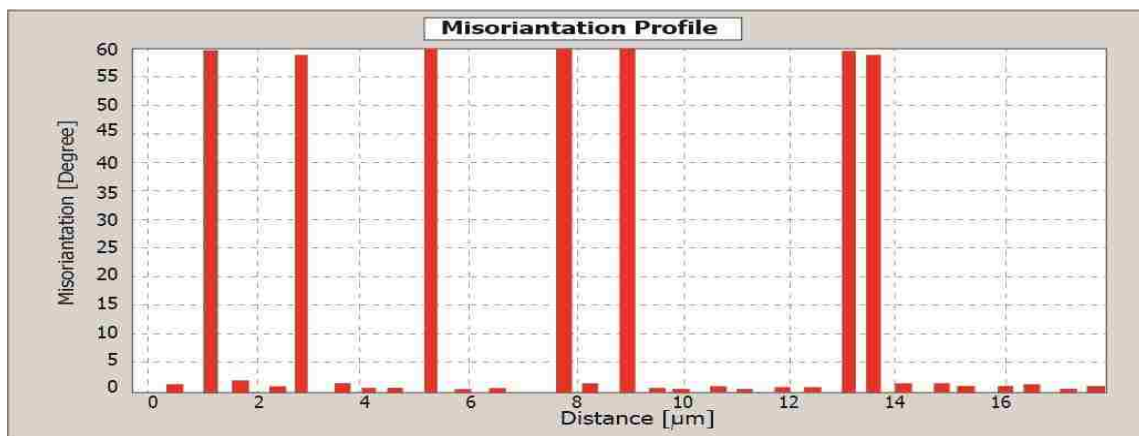


Figure 2.30 Misorientation angle greater than 45° having twinning

In close proximity of the sample, a specially coated phosphor screen is placed inside the specimen chamber in a majority of commercial systems which are used for automated EBSD mapping and phase identification applications. YAG crystals have also been used instead of the phosphor, but due to their costs, it prevents more general usage.

A camera is mounted on the SEM and images on the phosphor screen. Then, the electron beam is fixated on a particular point of interest in the sample. The contact of the beam and the microstructure results in an EBSD image being created on the phosphor screen, which is then captured by the mounted camera and then further processed and enhanced. Using dedicated signal processors or special PC software, the image is usually adjusted for background effects. Essentially, a digital image of the Kikuchi bands is made existent in the computer for indexing Figure 2.31 shows the system configurations and operation [59].

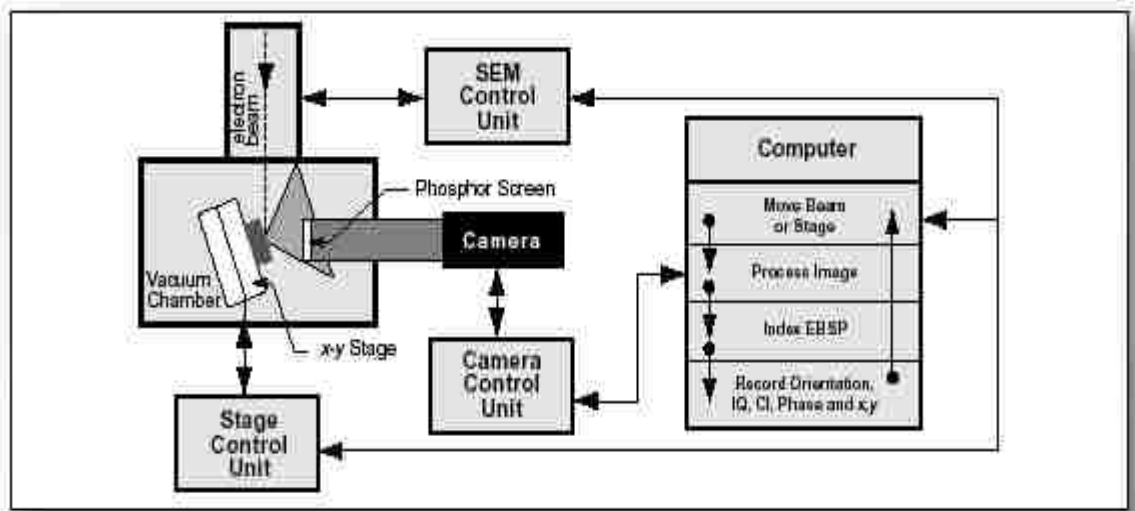


Figure 2.31 System Configurations and Operation [59]

Great amounts of crystallographic data from a specimen can also be collected by fixating the electron beam on the specimen under manual or automatic control and then repeating the indexing procedure at each beam position. While the system is put under automatic control, the beam can easily be fixated sequentially on the different points of the grid to scan an area of particular interest on the specimen. This allows for the data to be collected and examined without having any operator intervention after the initial setup [59].

2.8 X-Ray Diffraction (XRD)

In 1913, Bragg, a British physicist, developed an association to explain why the cleavage faces of crystals appear to reflect X-ray beams at certain angles of incidences (θ , q). The variable d is the distance between atomic layers in a crystal, the λ is wavelength of the incident X-ray beam and n is an integer. This specific observation is an example of X-ray wave interference, commonly known as X-ray diffraction (XRD), and is used as direct evidence for the periodic atomic structure of crystals postulated for several centuries. Diffraction is a physical phenomenon that consists in electromagnetic waves avoiding obstacles if the size of the obstacles is comparable to the wavelength. This equation can be applied to the analysis of materials as the atom plans are placed at comparable distances to X-ray lengths. X-rays are electromagnetic waves similar to light, but whose wavelength, are much shorter ($= 0, 2 - 200 \text{ \AA}$).

XRD is produced as a reflection at well-defined angles. Equally, every crystalline phase has its own diffraction image. The diffraction image contains a small number of maximum points that not all the families of crystallographic planes. Crystallographic planes give maximum diffraction points; all the crystalline phases with the same type of elementary cell will experience the same succession of Miller indices for the crystalline planes families giving diffraction maximum points.

For the XRD analysis we use diffraction devices (diffractometers), mainly according to the Bragg–Brentano system (Figure 2.32a) (the sample rotates at a diffraction angle “ Θ ”, while the detector rotates at the angle “ 2Θ ”).

In Figure 2.32b, the X ray diffractometric (Bruker) is shown. The diffractogram is made up of a sequence of diffraction maximum points, showing the concentration of the diffracted X radiation on the ordinate measured in pulses/second, and the angle “ 2θ ” on the abscissa, where “ θ ” is the Bragg angle, measured in degrees. The diffraction image depends upon the material structure. The diffraction methods allow for the presentation of the following studies: the determination of the crystalline structures, the phase quantitative and qualitative analysis, the study of phase transformations, the study of the crystallographic texture, the size of the crystallites, the internal stresses in the sample, etc.[54, 64].

The identification of the crystalline phases can be carried out with the X ray diffraction method if the respective phase represents more than 3 – 4 % mass. The identification can be made by calculation with Bragg’s relationship or computer-based, software [57-66].

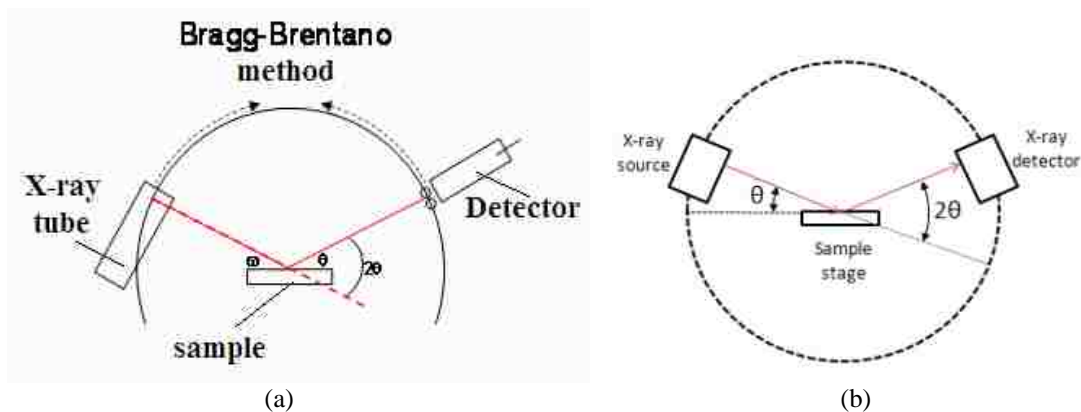


Figure 2.32 The basic layout of an X-ray diffractometric [55-57]



Figure 2.33 X-ray diffractometric (Bruker) [57]

2.8.1 Bragg's law

In terms of X-rays, are usually partially scattered by atoms when they strike the surface of a crystal. The part of the X-ray that is not scattered, passes through to the next layer of atoms, where again part of the X-ray is scattered and part passes through to the next layer.

This causes an overall diffraction pattern, comparable to how a grating diffracts a beam of light. In order for an X-ray to diffract, the sample must be crystalline and the spacing between atom layers must be close to the radiation wavelength.

If beams diffracted by two different layers are in phase, constructive interference occurs and the diffraction pattern shows a peak, however if they are out of phase, destructive interference occurs and there is no peak [57] as shown in Figure 2.34.

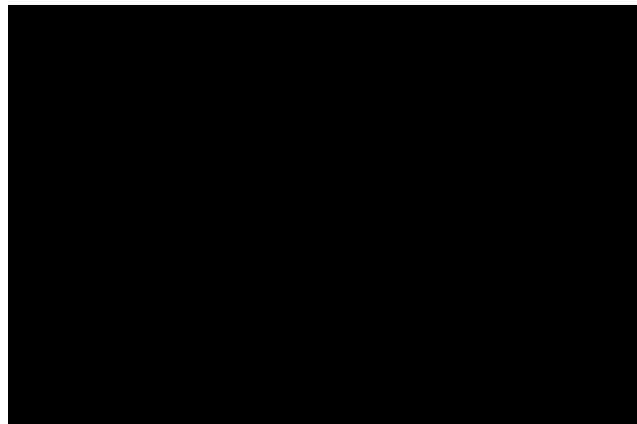


Figure 2.34 Bragg's law and angles related

The angle of incidence is defined as:

$$\sin\theta = \frac{n\lambda}{2d} \quad (2.1)$$

Where:

θ the angle of incidence of the X-ray,

n is an integer,

λ the wavelength, and

d the spacing between atom layers.

Since a highly regular structure is needed for diffraction to occur, only crystalline solids will diffract; amorphous materials will not show up in a diffraction pattern.

Table 2.5 Sample for collected data from the XRD data as lattice parameter and grain size. This sample is for A36 b and some physical properties such as mass, volume and density evaluation

	BCC		FCC	
	Lattice Parameter.	Weight %	Lattice Parameter.	Weight %
Non-impact	2.869×10^{-10} m	100 %	0 %	0 %
Impact	2.875×10^{-10} m	65 %	3.526×10^{-10} m	35 %

BCC	Cell Mass (g)	Cell Volume (Å ³)	Crystal Density (g/cm ³)	Crystallite Size (nm)	FCC	Cell Mass (g)	Cell Vol (Å ³)	Crystal Size (nm)
Non-impact A36	111.69	23.606	7.857	10000 (44000)	Non-impact A36	0	0	0
Impact A36	110.15	23.744	7.704	10000 (160000)	Impact A36	223.387	46.435	66 (25)

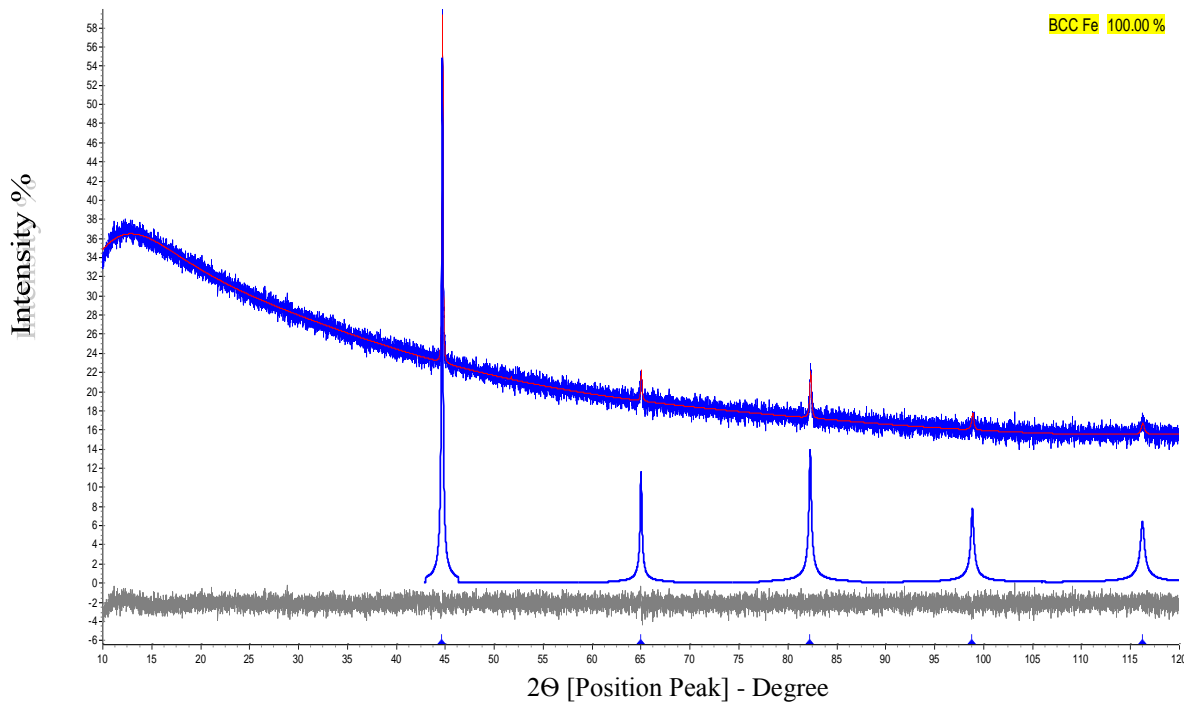


Figure 2.35 Sample of the peak of XRD results show the ratio of BCC of A36 Steel

2.9 Summary of All Experimental Measurements

A summary of all specimen preparation operations and experiments conducted is presented in Table 2.6.

Table 2.6 Summary of Operations for plates and specimens preparation and Experimental Measurements

PROCESS	A36	304L	HY100
Cutting to half and T-section to impact plate (water jet machine) Cut section (non-impact)	Three plate different speed 3.54 km/sec ,4.51 km/sec and 5.80 km/sec one plate non-impact	one plate at 6.58 km/sec one plate non-impact	one plate at 6.70 km/sec one plate non-impact
Slicing(Linear Saw Precision ISOMET4000)	6 cross-section samples in each speed	6 cross-section samples	6 cross-section samples
Epoxy toexamination by EBSD	All samples (non-impact and all cross-section impact samples)	All samples (non-impact and all cross-section impact samples)	All samples (non-impact and all cross-section impact samples)
Sanding Polish(Beta Grinder Polisher BUEHLER)	All samples (non-impact and all cross-section impact samples)	All samples (non-impact and all cross-section impact samples)	All samples (non-impact and all cross-section impact samples)
Etching with HNO3 96 % and Ethanol 4 % at 15 seconds	Three samples in each speed (cratersample S6)	One sample (cratersample S6)	One sample (crater sample S6)
Examination by EBSD microscopy	All samples (non-impact and all cross-section impact samples)	All samples (non-impact and all cross-section impact samples)	All samples (non-impact and all cross-section impact samples)

CHAPTER 3

A36 STEEL EXPERIMENTAL DATA

In this chapter, the results of microscopic examination for test samples are viewed. Examination of the prepared samples in the study depended on two kind of microscopy, EBSD and XRD. The first one, EBSD, is used to find the unit cell of the crystal system and determine the phase percentage with a microstructure map of the grain and phase. The XRD is capable of measuring the distance between the lattice parallel surfaces and is known as the lattice constant (d). Some samples examined by the (EBSD) have been scanned by XRD also. This is in order to obtain more confidence in the results, especially, for the highest impact speeds at the crater section. Existence of a new phase transformation or twinning can be detected by acquiring the Lattice constant.

3.1 As Received A36 Steel (No Impact Loading)

3.1.1 EBSD Grain Structure Phase Measurements

The images shown in Figure 3.1, obtained from EBSD microscopy, show the grain structure of A36 steel that has not been impacted. Figure 3.1 indicates 4 views that explain grain, the magnification 350X and the original length of the map, the phase, and the crystal unit cells orientation. Also, Table 3.1 lists non-impact material phase ratios.

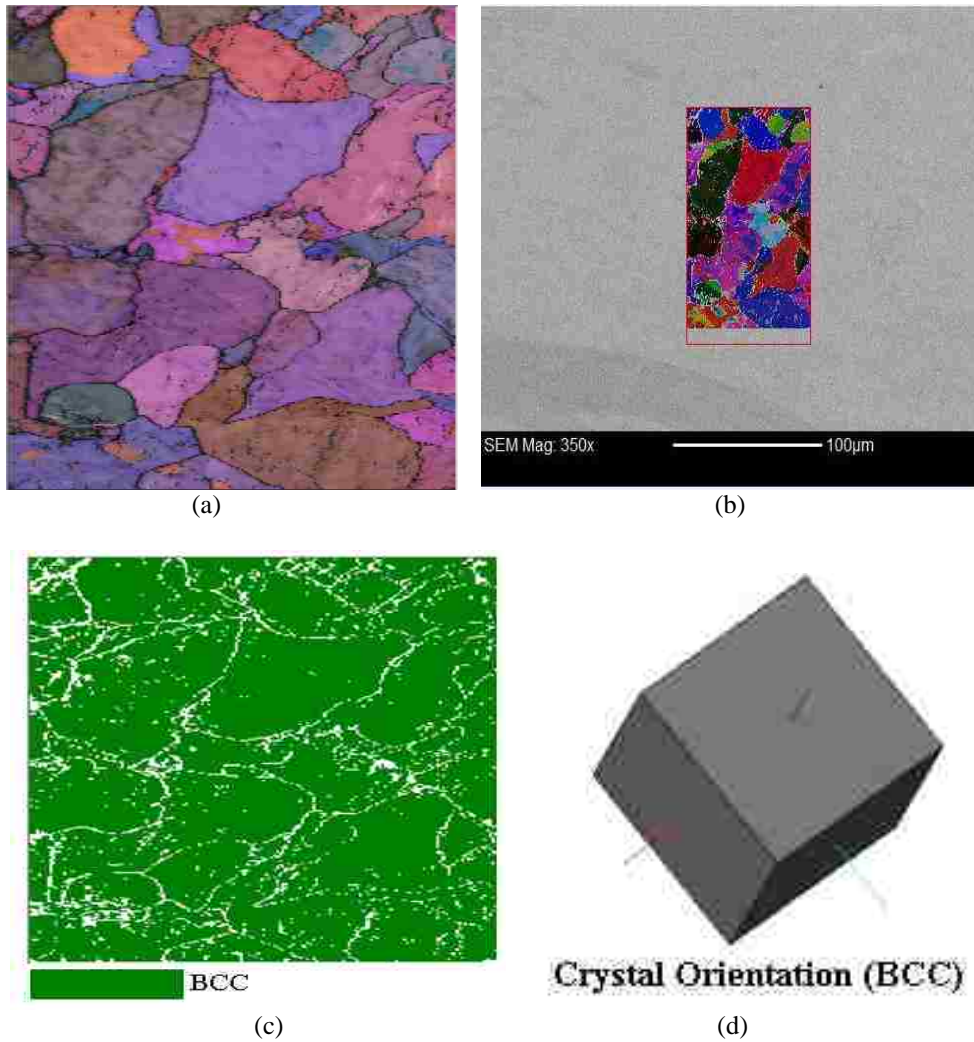


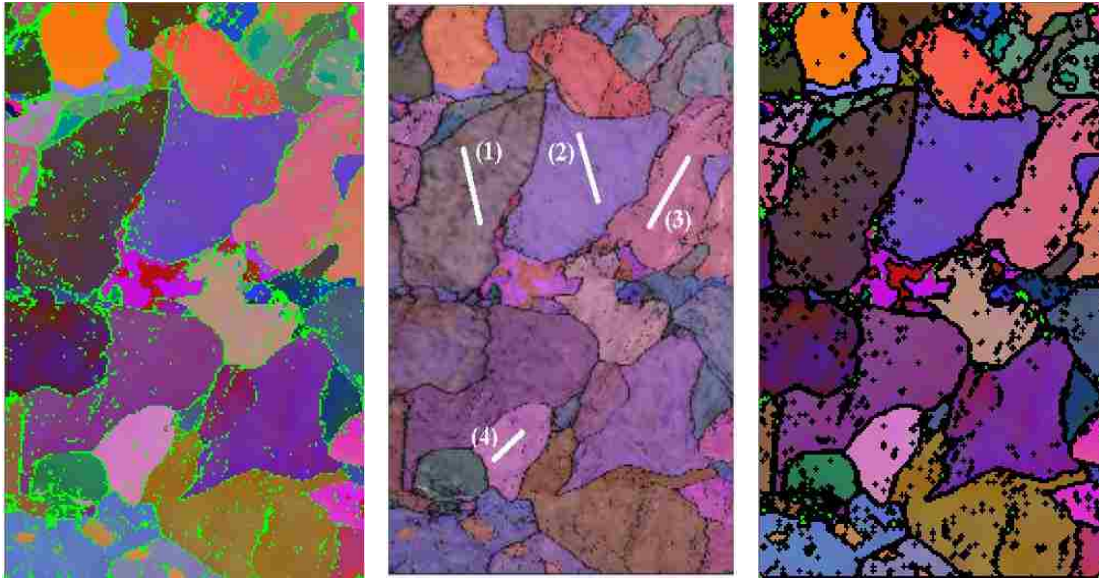
Figure 3.1 EBSD data from non-impact A36 steel showing: a) grain, b) 350X magnification and the original length of the map, c) phase map, and D crystal orientation.

Table 3.1 Non-impact phase ratio

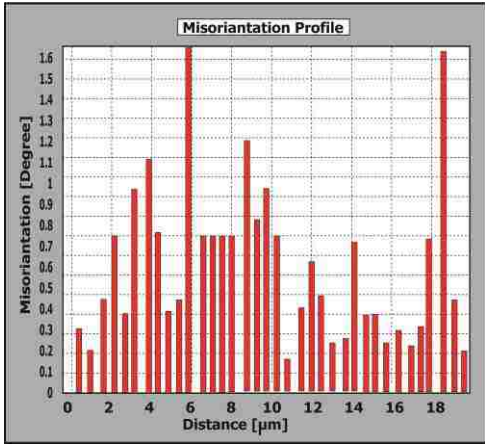
Crystal Unit Cell Structures	Non-Impact A36 Steel Phase
BCC	99.98 %
FCC	0.002 %
HCP	0 %

3.1.2 EBSD Misorientation Measurements

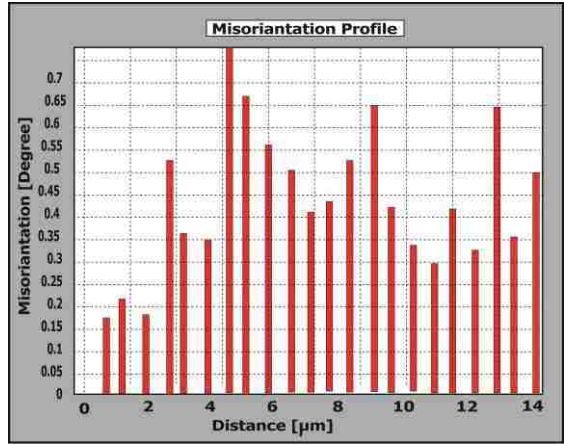
Misorientation is calculated from the product (or composition) of one orientation and the inverse of the other. This photo shows the angle phase crystalline transition in the grain boundaries of non-impact A36 steel where the raw material is stable and clear and the big grain of the misorientation angle is in small crystals ranging from 0-1.60°



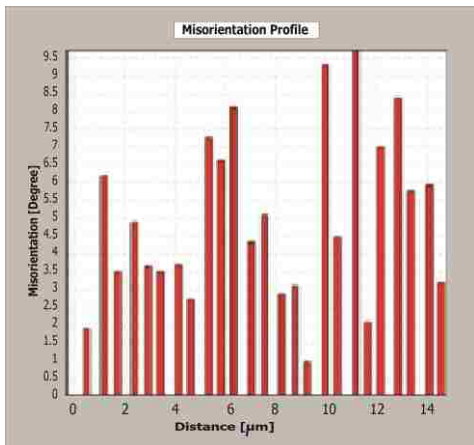
(a) (b) (c)



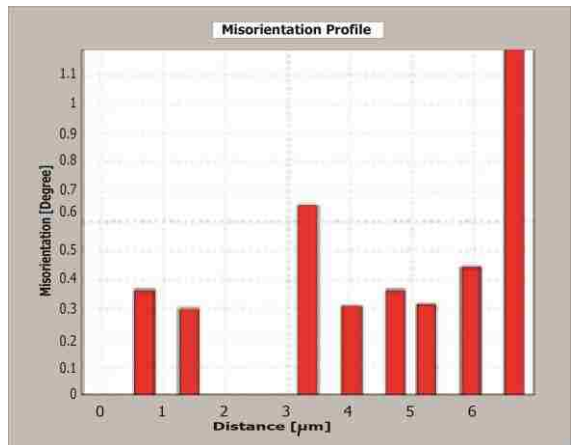
(d)



(e)



(f)



(g)

Figure 3.2 Misorientation angle measured along four different lines in the non-impacted A36 steel: a) EBSD shows less noise, b) EBSD shows grains, c) EBSD shows boundary grains d) Line 1, e) Line 2, f) Line 3, and g) line 4.

3.1.3 XRD Lattice Parameter Measurements

The XRD can be used to measure patterns of solid surfaces, such as metals. However, the S/N ratio will be much lower than that of a crystalline powder. This section shows the result of the test of XRD diffraction on A36 steel without impact and after impact.

3.1.3.1 Non-Impact A36 Steel

Figure 3.3 shows a significant peak in the shape of the XRD curve for non-impacted A36 steel. The percentage of each phase of this steel is determined and only the BCC phase appears, as one would expect. The Table 3.2 shows Lattice parameters and quantity for detectable phases with some microorganisms and physical properties of A36 steel before and after the impact.

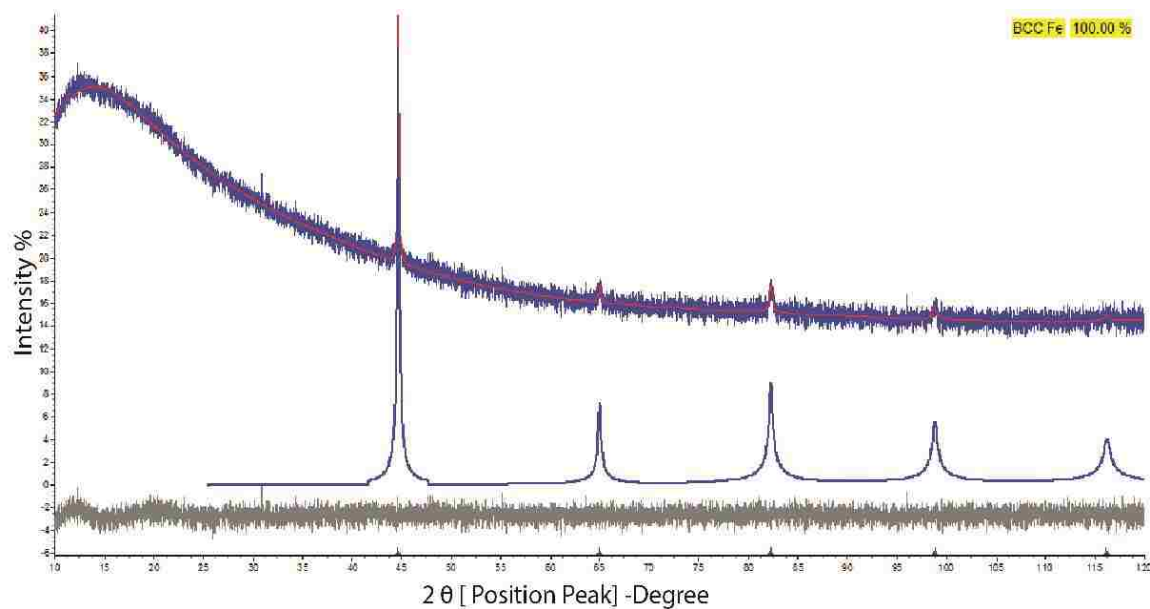


Figure 3.3 Non-impact A36 Steel (Phase 1 "BCC Fe" 100.000 %)

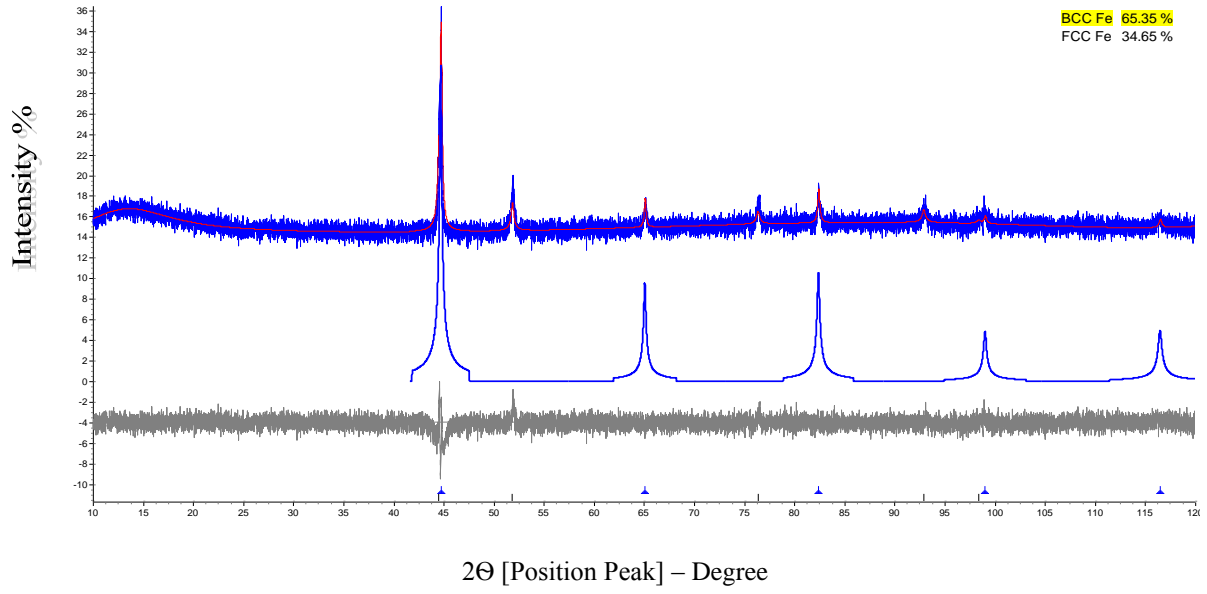
Table 3.2 A36-Lattice parameters and quantity for detectable phases

	BCC		FCC	
	Lattice Parameter.	Weight %	Lattice Parameter.	Weight %
Non-impact	2.869×10^{-10} m	100 %	0 %	0 %
Impact	2.875×10^{-10} m	65 %	3.526×10^{-10} m	35 %

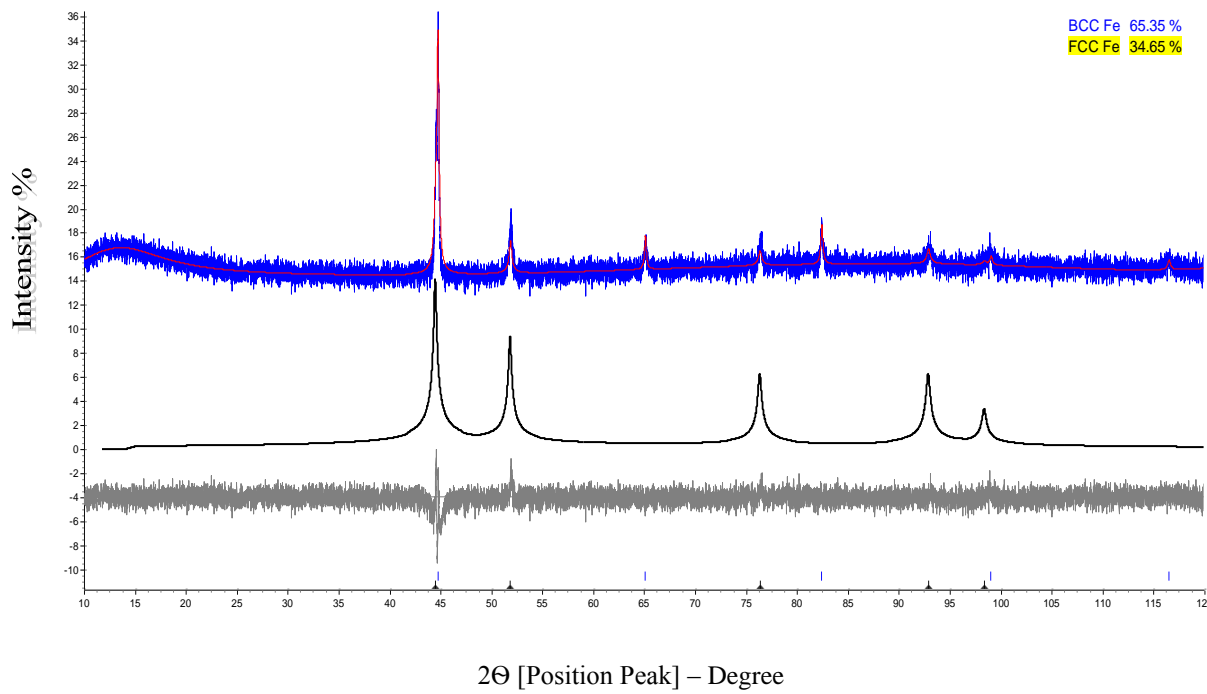
BCC	Cell Mass (g)	Cell Volume (\AA^3)	Crystal Density (g/cm^3)	Crystallite Size (nm)	FCC	Cell Mass (g)	Cell Vol (\AA^3)	Crystal Size (nm)
Non-impact A36	111.69	23.606	7.857	10000 (44000)	Non-impact A36	0	0	0
Impact A36	110.15	23.744	7.704	10000 (160000)	Impact A36	223.387	46.435	66 (25)

3.1.3.2 A36 Steel Target Impacted at 5.80 km/sec

Figure 3.4 shows the clarified crystalline phase, from XRD analysis that appeared in the A36 steel post-traumatic stress. The impacted A36 steel shows both FCC and BCC phases indicating a phase change due to the impact conditions.



(a) BCC Fit



(b) FCC Fit

Figure 3.4 A36 Steel impacted at 5.80 km/sec, Phase1:"BCC Fe" 65.35 % and Phase 2:"FCC" 34.65 %. (a) the BCC peak fit and (b) the FCC peak fit.

3.2 Impact Velocity of 3.54 km/s in A36 Steel

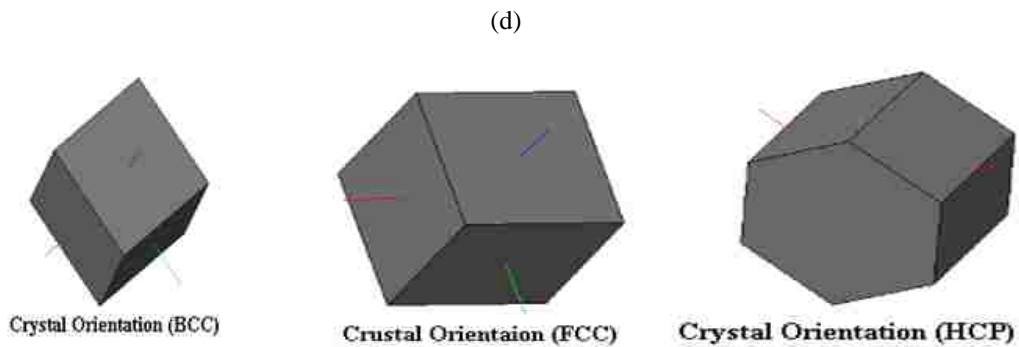
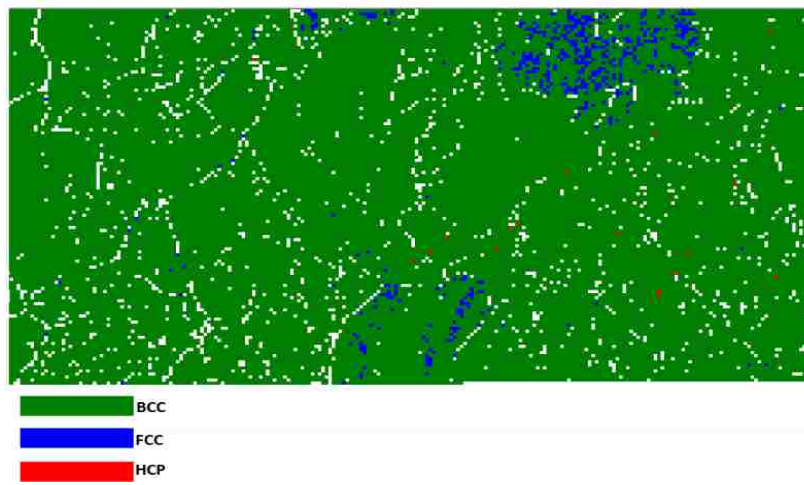
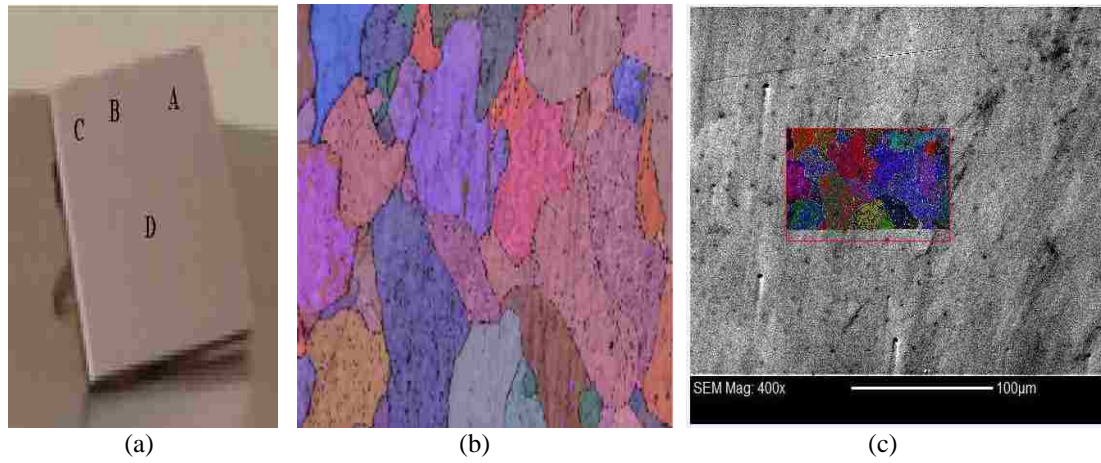
While examining A36 steel post impact, not only were the effects visible by the naked eye, but the micro-structure was also significantly changed. The post impact samples were observed under the EBSD microscope to examine the microscopic changes of each speed the six locations of sample scanning depends on the crater and each location sample has five maps. In this study we present two points in each sample. Figure 3.5 shows the location in the target where EBSD measurements were taken. The following subsections show EBSD results from each of these cross-section locations.



Figure 3.5 EBSD specimen locations were taken from 6 locations along two different lines of a T-shaped specimen of the A36 steel target: (a) Along impact crater perpendicular to impact mid-line and (b) Parallel to mid-line cut.

3.2.1 Cross-section Location 1-A (75 mm from impact center)

In this section we discuss the EBSD results from the A36 steel target that was impacted by a 3.54 km/sec projectile. Figure 3.6 shows the polished sample, grain, the magnification 400x and the original length of the map, the phase, and the crystal orientation. Table 3.3 lists the impact phase ratios of A36 steel at 3.54 km/sec sample location 1-A.



(e)

Figure 3.6 EBSD data from A36 steel, sample location 1-A, after impact velocity of 3.54 km/sec showing: a) polished sample, b) grain, c) 400X magnification and the original length of the map, d) phase map, and e) crystal orientation.

Table 3.3 Impact phase ratio of A36 steel at 3.54 km/sec sample location 1-A

Crystal Unit Cell Structures	Impact A36 Steel Phase at 3.54 km/sec
BCC	98.074 %
FCC	1.8366 %
HCP	0.063 %

3.2.2 Cross-section Location 2-C (35 mm from impact center)

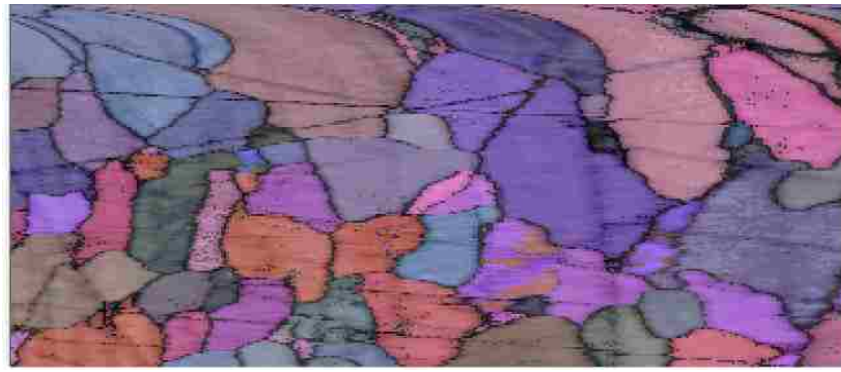
Figure 3.7 shows the EBSD microscopy data for location 2-C in the A36 steel target after an impact velocity of 3.54 km/sec. The figure shows the polished sample, grain, 370X magnification and the original length of the map, and the phase distribution.

3.2.3 Cross-section Location 3-C (7.5 mm from impact center)

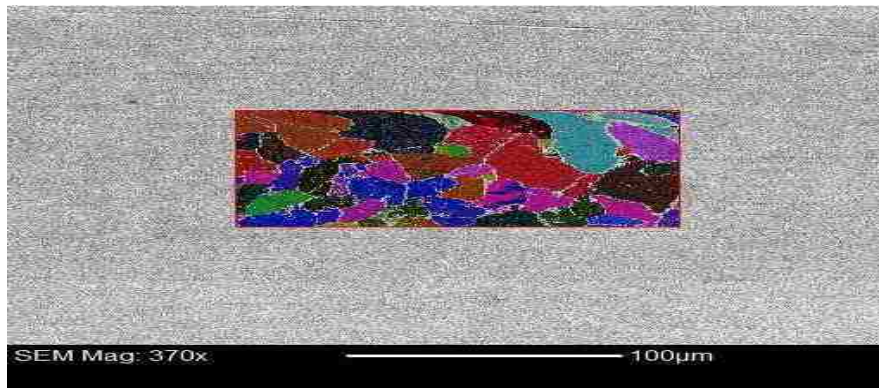
Figure 3.8 observes the A36 steel post-impact 3.54 km/sec impact sample 3 according to EBSD microscopy viewing which shows the sample, grain, the magnification 400X and the original length of the map and, Show the Phase. Table 3.5 lists the impact phase ratios of A36 steel at 3.54 km/sec sample location 3-C.



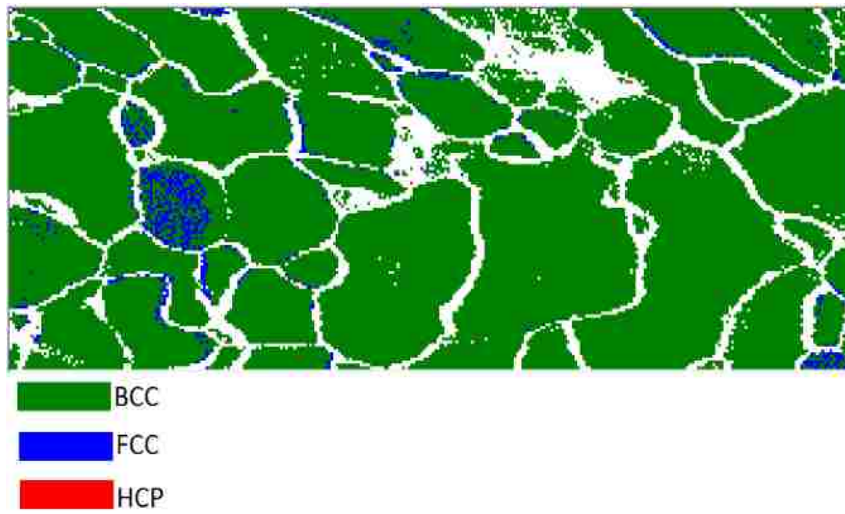
(a)



(b)



(c)



(d)

Figure 3.7 EBSD data from A36 steel, sample location 2-C, after impact velocity of 3.54 km/sec showing: a) polished sample, b) grain, c) 370X magnification and the original length of the map, and D) phase map.

Table 3.4 Impact phase ratio of A36 steel at 3.54 km/sec sample location 2-C

Crystal Unit Cell Structures	Impact A36 Steel Phase at 3.54 km/sec
BCC	98.382 %
FCC	1.546 %
HCP	0.072 %

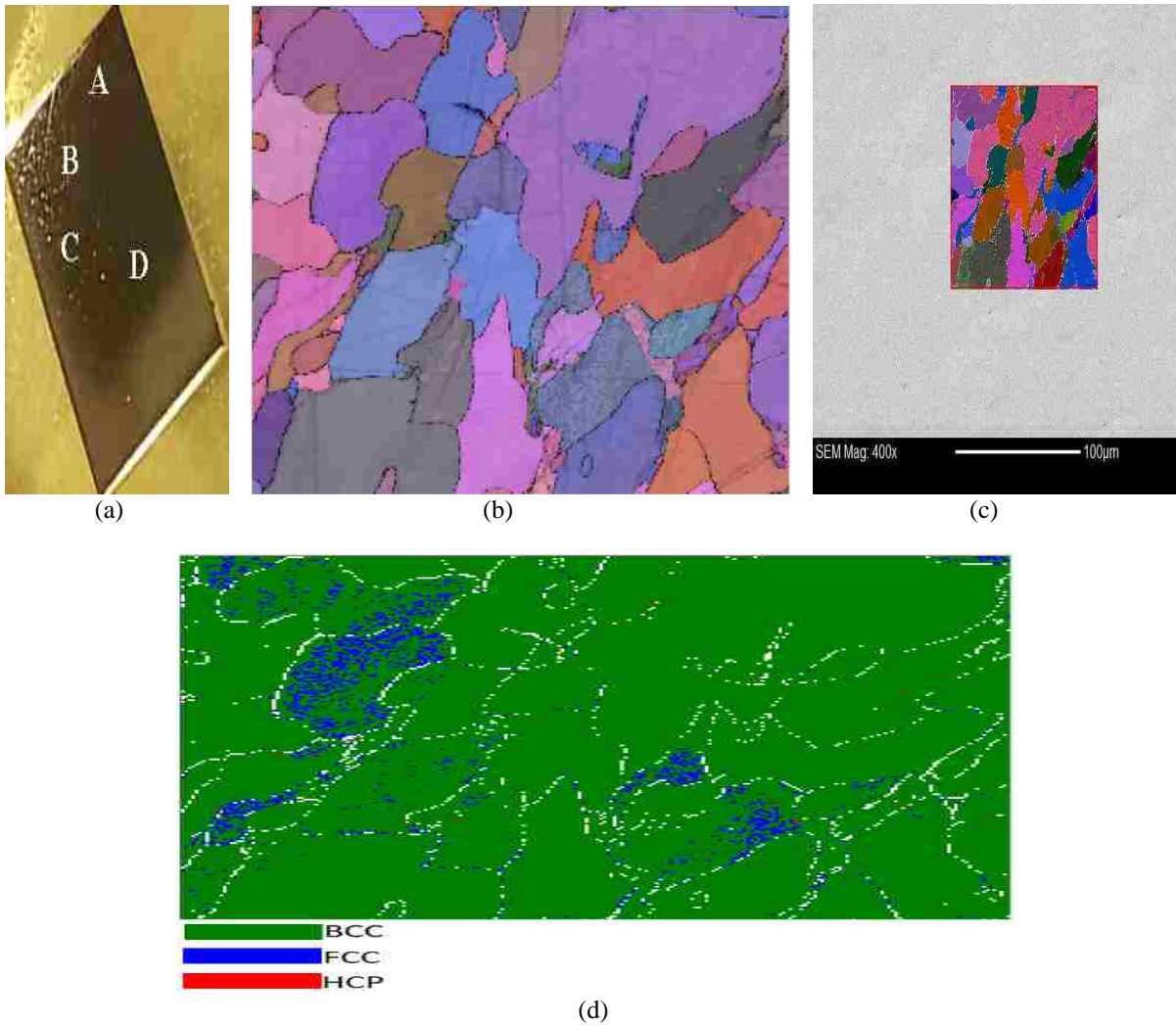


Figure 3.8 EBSD data from A36 steel, sample location 3-C, after impact velocity of 3.54 km/sec showing: a) polished sample, b) grain, c) 400X magnification and the original length of the map, and d) phase map.

Table 3.5 Impact phase ratio of A36 steel at 3.54 km/sec sample location 3-C

Crystal Unit Cell Structures	Impact A36 Steel Phase at 3.54 km/sec
BCC	96.35 %
FCC	3.629 %
HCP	0.079 %

3.2.4 Cross-section Location 4-A (20 mm from impact center)

In this section we discuss the A36 steel post-impact 3.54 km/sec impact. Figure 3.9 shows the sample, grain, the magnification 400X and the original length of the map, and shows the phase. Table 3.6 lists the impact phase ratios of A36 steel at 3.54 km/sec sample location 4-A.

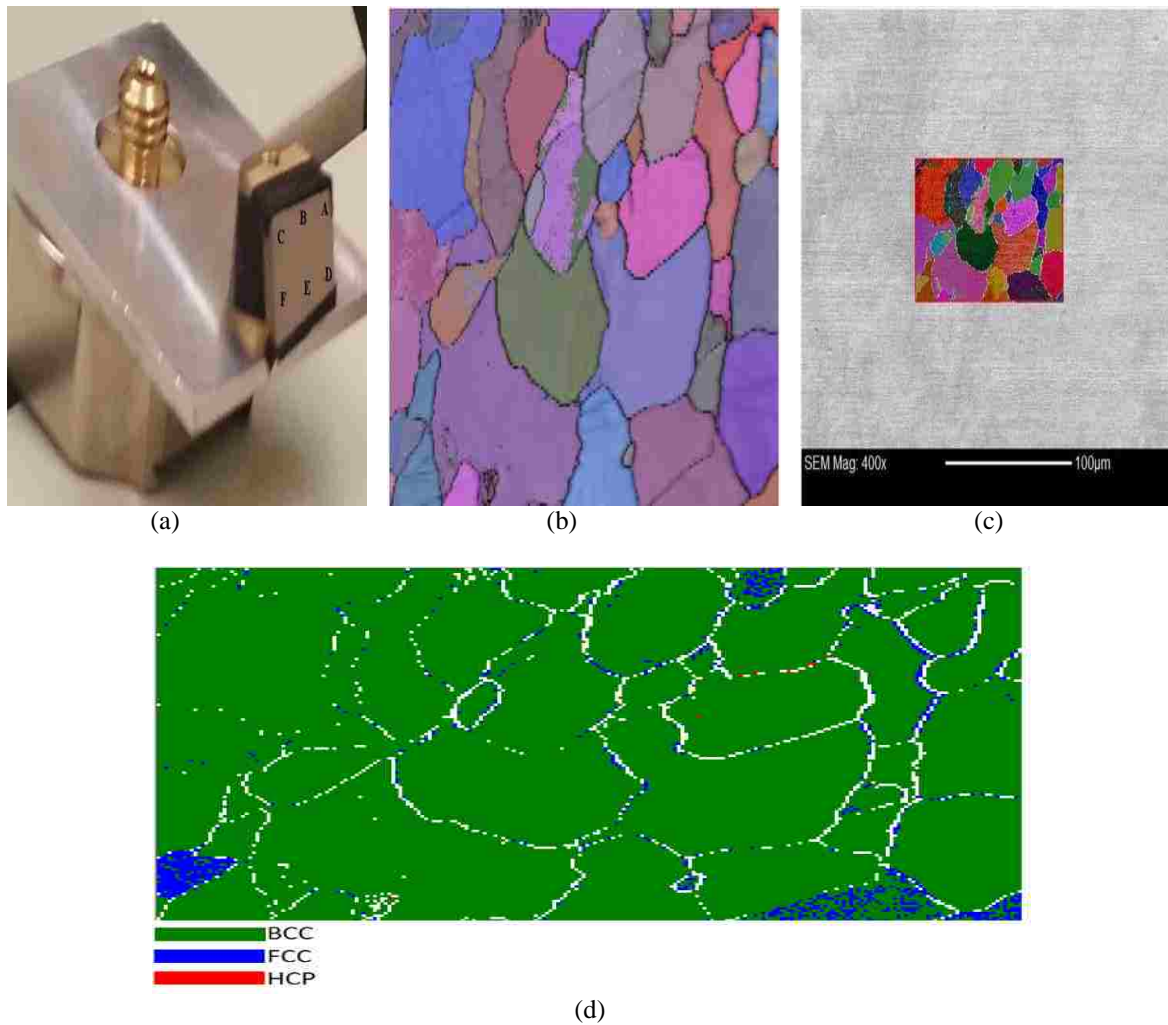


Figure 3.9 EBSD data from A36 steel, sample location 4-A, after impact velocity of 3.54 km/sec showing: a) polished sample, b) grain, c) 400X magnification and the original length of the map, and d) phase map.

Table 3.6 Impact phase ratio of A36 steel at 3.54 km/sec sample location 4-A

Crystal Unit Cell Structures	Impact A36 Steel Phase at 3.54 km/sec
BCC	97.076 %
FCC	2.9514 %
HCP	0.081 %

3.2.5 Cross-section Location 5-D (10 mm from impact center)

Figure 3.10 shows A36 steel post-impact 3.54 km/sec the sample, grain, the magnification 400X and the original length of the map, and the phase. Table 3.7 lists the impact phase ratios of A36 steel at 3.54 km/sec sample location 5-D.

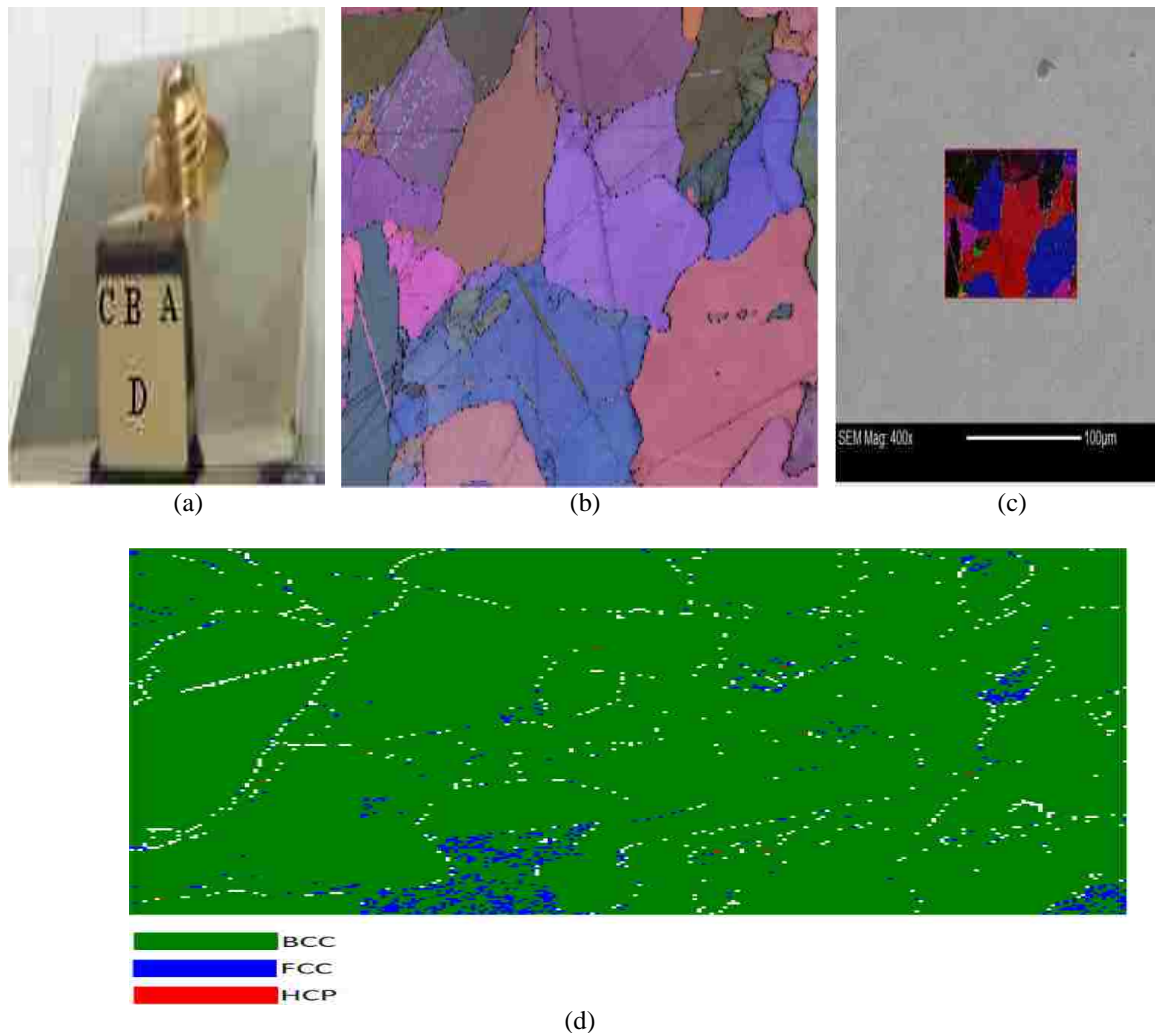


Figure 3.10 EBSD data from A36 steel, sample location 5-D, after impact velocity of 3.54 km/sec showing: a) polished sample, b) grain, c) 400X magnification and the original length of the map, and d) phase map.

Table 3.7 Impact phase ratio of A36 steel at 3.54 km/sec sample location 5-D

Crystal Unit Cell Structures	Impact A36 Steel Phase at 3.54 km/sec
BCC	94.028 %
FCC	5.826 %
HCP	0.1457 %

3.2.6 Cross-section Location 6-A (0 mm from impact center)

The locations of many points' have been selected as being involved the crater center. Figure 3.11 shows the sample, grain, the magnification 400X and the original length of the map, and shows the phase.

Table 3.8 lists the impact phase ratio of A36 Steel at 3.54 km/sec sample location 6-A.

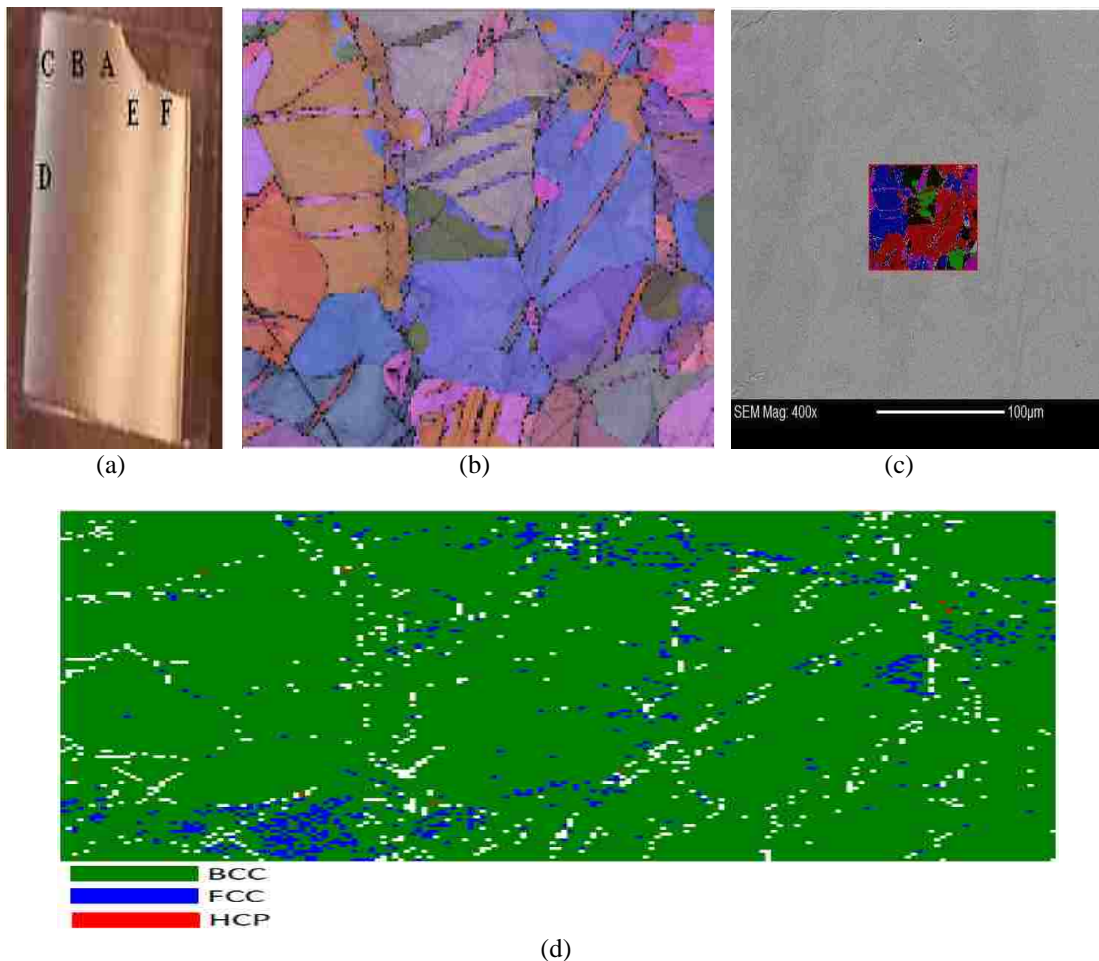


Figure 3.11 EBSD data from A36 steel, sample location 6-A, after impact velocity of 3.54 km/sec showing: a) polished sample, b) grain, c) 400X magnification and the original length of the map, and d) phase map.

Table 3.8 Impact phase ratio of A36 steel at 3.54 km/sec sample location 6-A

Crystal Unit Cell Structures	Impact A36 Steel Phase at 3.54 km/sec
BCC	96.545 %
FCC	3.4155 %
HCP	0.03984 %

3.2.7 Cross-section Location 6-B (0 mm from impact center)

We relied on comparison for the impact section on point B which is located at section number 6, as the most affected region during impact. On the other hand, at that section, the EBSD reading certainty is high enough to be considered for our purpose. It is shown in Figure 3.12 which shows grain, the magnification 400X and the original length of the map, and the phase. Table 3.9 lists the impact phase ratio of A36 steel at 3.54 km/sec sample location 6-B.

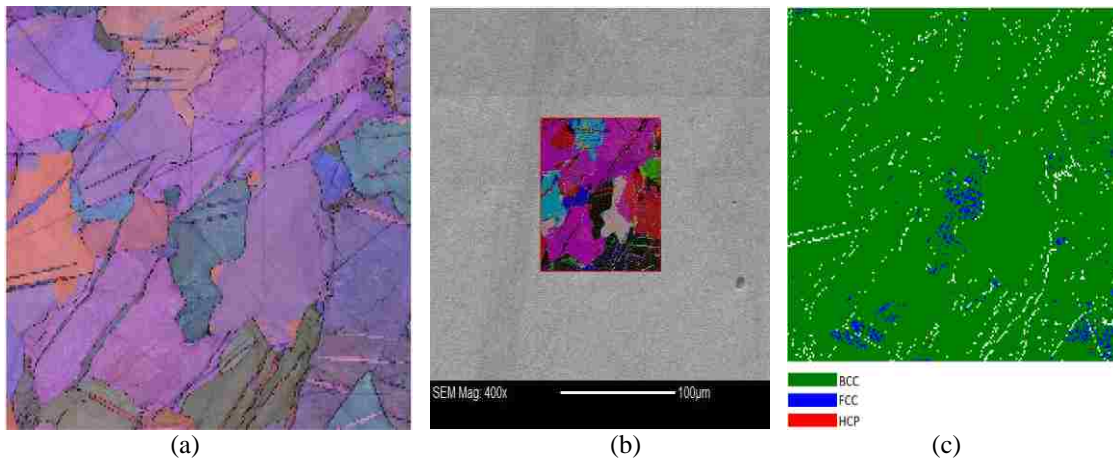


Figure 3.12 EBSD data from A36 steel, sample location 6-B, after impact velocity of 3.54 km/sec showing: a) grain, b) 400X magnification and the original length of the map, and c) phase map.

Table 3.9 Impact phase ratio of A36 steel at 3.54 km/sec sample location 6-B

Crystal Unit Cell Structures	Impact A36 Steel Phase at 3.54 km/sec
BCC	98.280 %
FCC	1.6644 %
HCP	0.05530 %

3.2.8 Cross-section Location 6-C (0 mm from impact center)

Figure 3.13 shows A36 steel post-impact 3.54 km/sec the sample, grain, the magnification 400X and the original length of the map, and the phase. Table 3.10 lists the impact phase ratios of A36 steel at 3.54 km/sec sample location 6-C.

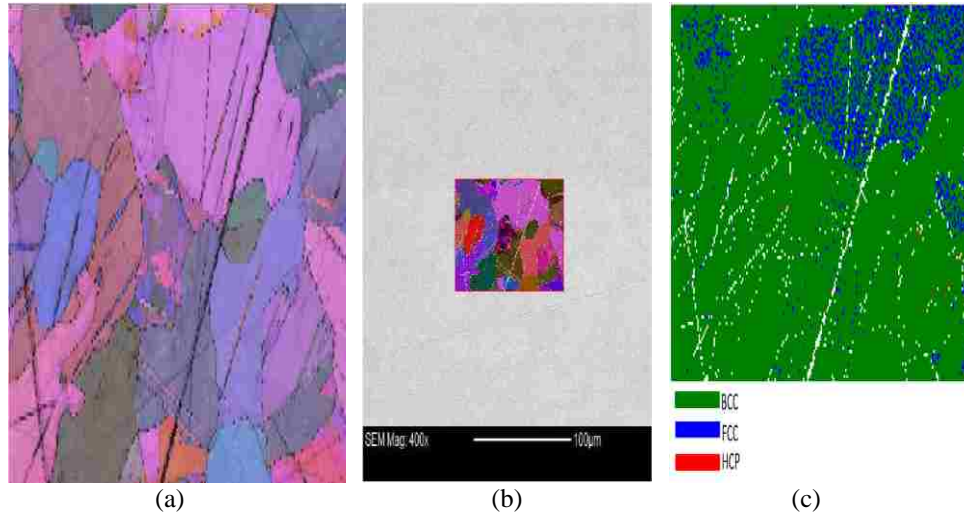


Figure 3.13 EBSD data from A36 steel, sample location 6-C, after impact velocity of 3.54 km/sec showing: a) grain, b) 400X magnification and the original length of the map, and C) phase map.

Table 3.10 Impact phase ratio of A36 steel at 3.54 km/sec sample location 6-C

Crystal Unit cell	Impact A36 Steel phase at 3.54 km/sec
BCC	90.30 %
FCC	9.5583 %
HCP	0.1460 %

3.2.9 Cross-section Location 6-D (0 mm from impact center)

Figure 3.14 shows A36 steel post-impact 3.54 km/sec the sample, grain, the magnification 400X and the original length of the map, and the phase. Table 3.11 lists the impact phase ratios of A36 steel at 3.54 km/sec sample location 6-D.

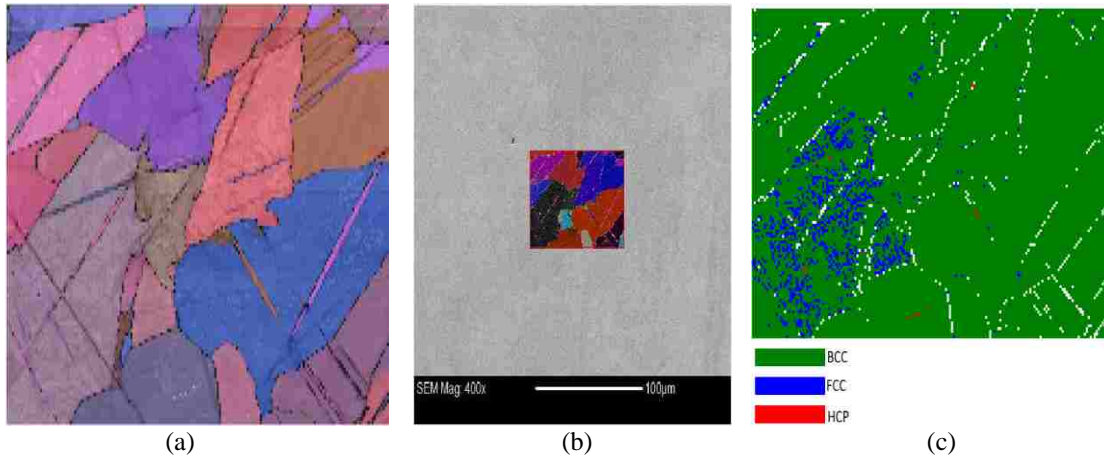


Figure 3.14 EBSD data from A36 steel, sample location 6-D, after impact velocity of 3.54 km/sec showing: a) grain, b) 400X magnification and the original length of the map, and c) phase map.

Table 3.11 Impact phase ratio of A36 steel at 3.54 km/sec sample location 6-D

Crystal Unit cell	Impact A36 Steel phase at 3.54 km/sec
BCC	97.845 %
FCC	1.1026 %
HCP	1.04824 %

3.2.10 Cross-section Location 6-E (0 mm from impact center)

Figure 3.15 shows A36 steel post-impact 3.54 km/sec the sample, grain, the magnification 400X and the original length of the map, and the phase. Table 3.12 lists the impact phase ratios of A36 steel at 3.54 km/sec sample location 6-E.

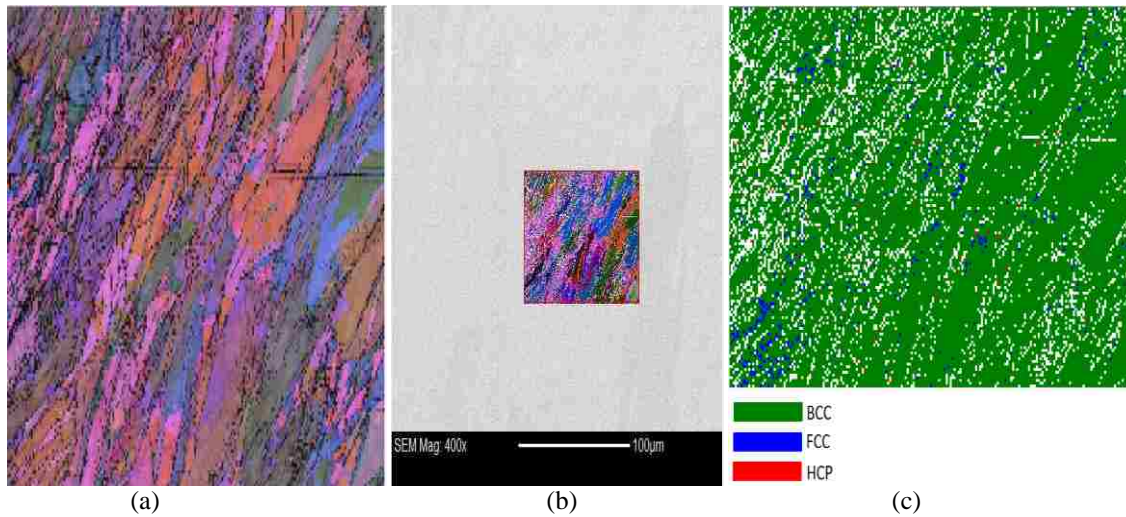


Figure 3.15 EBSD data from A36 steel, sample location 6-E, after impact velocity of 3.54 km/sec showing: a) grain, b) 400X magnification and the original length of the map, and c) phase map.

Table 3.12 Impact phase ratio of A36 steel at 3.54 km/sec sample location 6-E

Crystal Unit cell	Impact A36 Steel phase at 3.54 km/sec
BCC	97.663 %
FCC	2.122 %
HCP	0.2155 %

3.2.11 Cross-section Location 6-F (0 mm from impact center)

Figure 3.16 shows A36 steel post-impact 3.54 km/sec the sample, grain, the magnification 400X and the original length of the map, and the phase. Table 3.13 lists the impact phase ratios of A36 steel at 3.54 km/sec sample location 6-F.

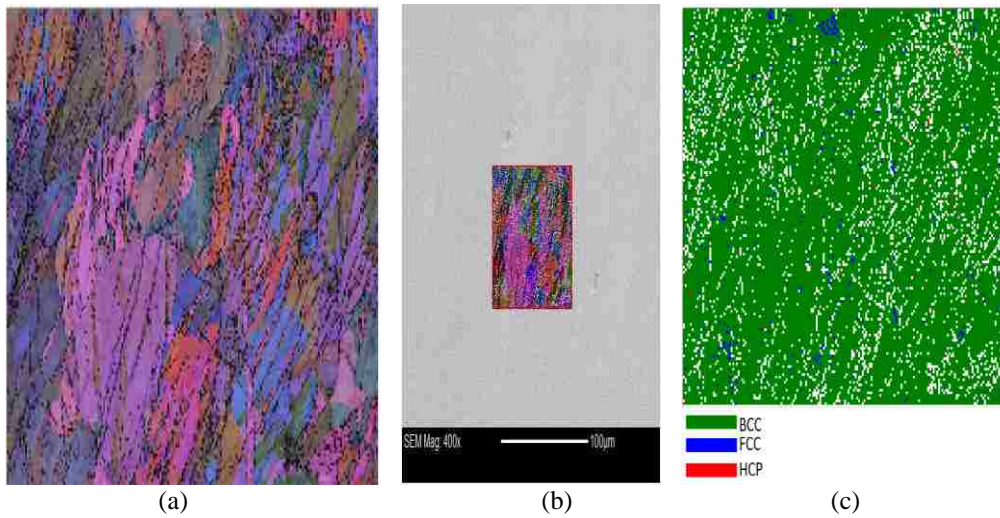


Figure 3.16 EBSD data from A36 steel, sample location 6-F, after impact velocity of 3.54 km/sec showing: a) grain, b) 400X magnification and the original length of the map, and c) phase map.

Table 3.13 Impact phase ratio of A36 steel at 3.54 km/sec sample location 6-F

Crystal Unit Cell Structures	Impact A36 Steel Phase at 3.54 km/sec
BCC	98.702 %
FCC	1.18744 %
HCP	0.112 %

Figures 3.6 – 3.16 show EBSD data from six different cross-section locations in the A36 steel target that was impacted at 3.54 km/sec. Locations 6-E and 6-F, which are the closest to the impact crater show obvious signs of twinning. A smaller amount of twinning is observed in locations further from the impact center including 6-A, 6-B, 6-C, and locations 3-5. Almost no twinning was observed at locations 1 and 2 which were furthest from the impact crater. The Percentage of crystal modes for these locations is summarized in Tables 3.3 – 3.13. The selection of sites and the locations C, D and E that the rate of errors is small and the rate of confidence in results is high is discussed in Chapter 6.

3.3 Impact Velocity of 4.51 km/s in A36 Steel

3.3.1 Cross-section Location 1-B (75 mm from impact center)

Figure 3.17 shows the EBSD microscopy data for location 1-B in the A36 steel target after an impact velocity of 4.51 km/sec. The figure shows the polished sample, grain, 400X magnification and the original length of the map, and the phase distribution.

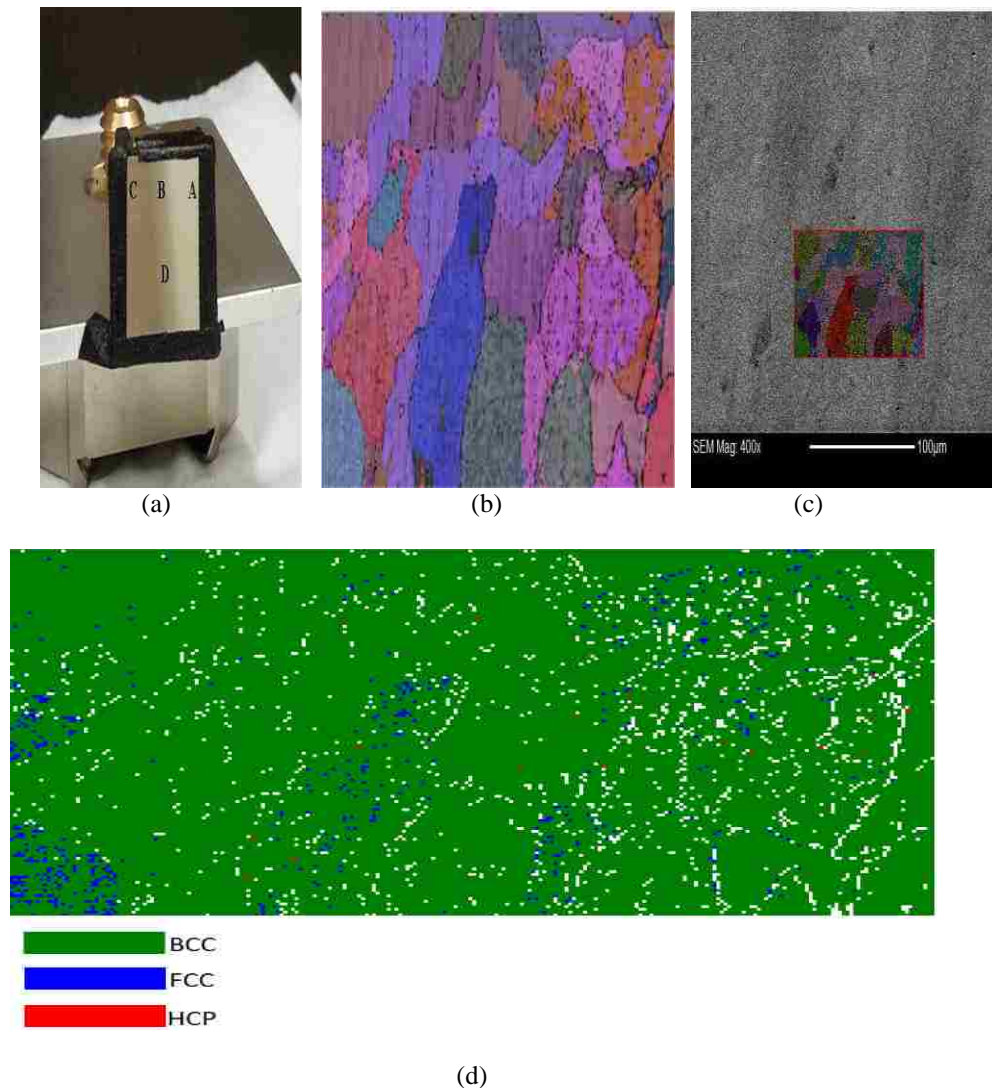


Figure 3.17 EBSD data from A36 steel, sample location 1-B, after impact velocity of 4.51 km/sec showing: a) polished sample, b) grain, c) 370X magnification and the original length of the map, d) phase map.

Table 3.14 Impact phase ratio of A36 steel at 4.51 km/sec sample location 1-B

Crystal Unit Cell Structures	Impact A36 Steel Phase at 4.51 km/sec
BCC	98.3105 %
FCC	1.6865 %
HCP	0.075 %

3.3.2 Cross-section Location 2-A (35 mm from impact center)

Figure 3.18 shows the EBSD microscopy data for location 2-A in the A36 steel target after an impact velocity of 4.51 km/sec. The figure shows the polished sample, grain, 400X magnification and the original length of the map, and the phase distribution.

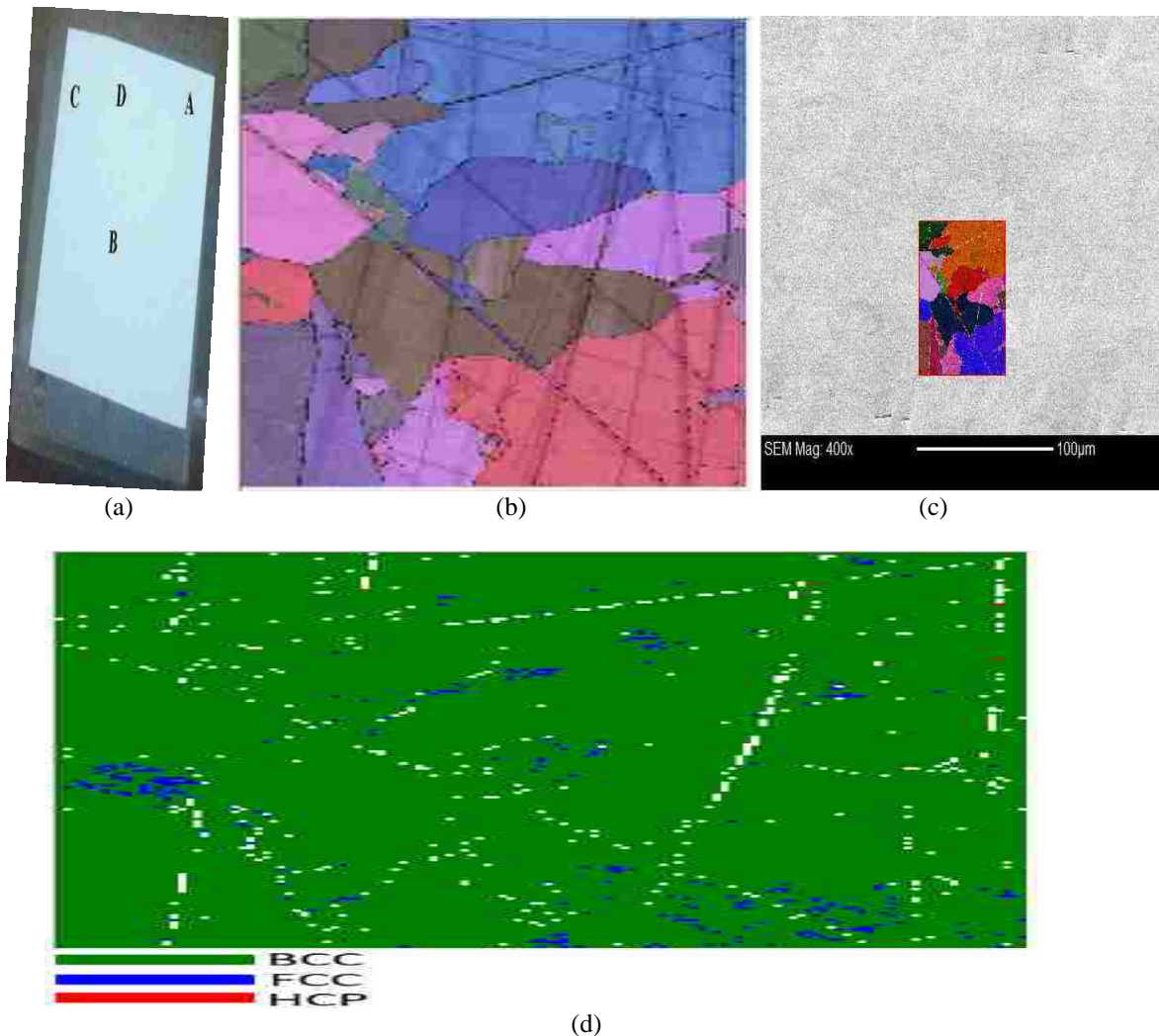


Figure 3.18 EBSD data from A36 steel, sample location 2-A, after impact velocity of 4.51 km/sec showing: a) polished sample, b) grain, c) 400X magnification and the original length of the map, and d) phase map.

Table 3.15 Impact phase ratio of A36 steel at 4.51 km/sec sample location 2-A

Crystal Unit Cell Structures	Impact A36 Steel Phase at 4.51 km/sec
BCC	98.507 %
FCC	1.485 %
HCP	0.078 %

3.3.3 Cross-section Location 3-B (7.5 mm from impact center)

Figure 3.19 shows the EBSD microscopy data for location 3-B in the A36 steel target after an impact velocity of 4.51 km/sec. The figure shows the polished sample, grain, 400X magnification and the original length of the map, and the phase distribution.

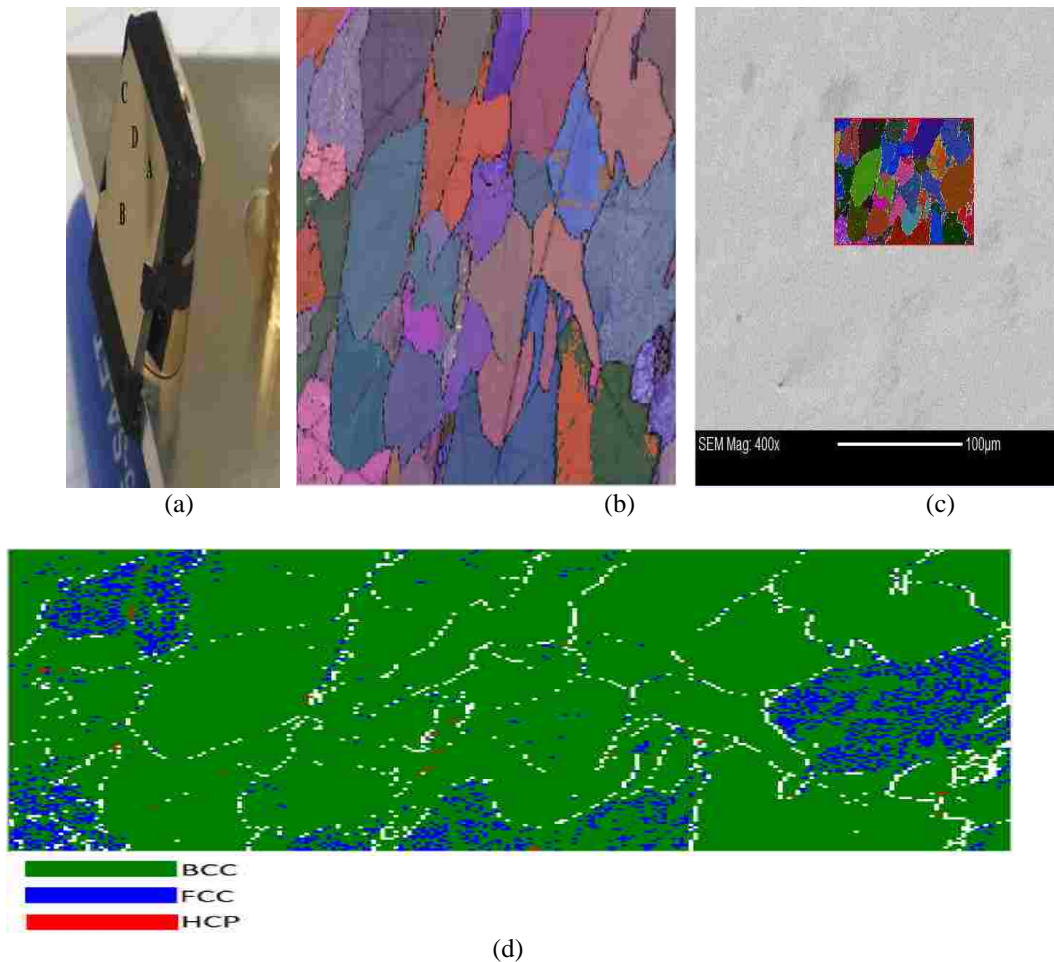


Figure 3.19 EBSD data from A36 steel, sample location 3-B, after impact velocity of 4.51 km/sec showing: a) polished sample, b) grain, c) 400X magnification and the original length of the map, and d) phase map.

Table 3.16 Impact phase ratio of A36 steel at 4.51 km/sec sample 3-B

Crystal Unit Cell Structures	Impact A36 Steel Phase at 4.51 km/sec
BCC	92.77 %
FCC	7.114 %
HCP	0.117 %

3.3.4 Cross-section Location 4-A (20 mm from impact center)

Figure 3.20 shows the EBSD microscopy data for location 4-A in the A36 steel target after an impact velocity of 4.51 km/sec. The figure shows the polished sample, grain, 400X magnification and the original length of the map, and the phase distribution.

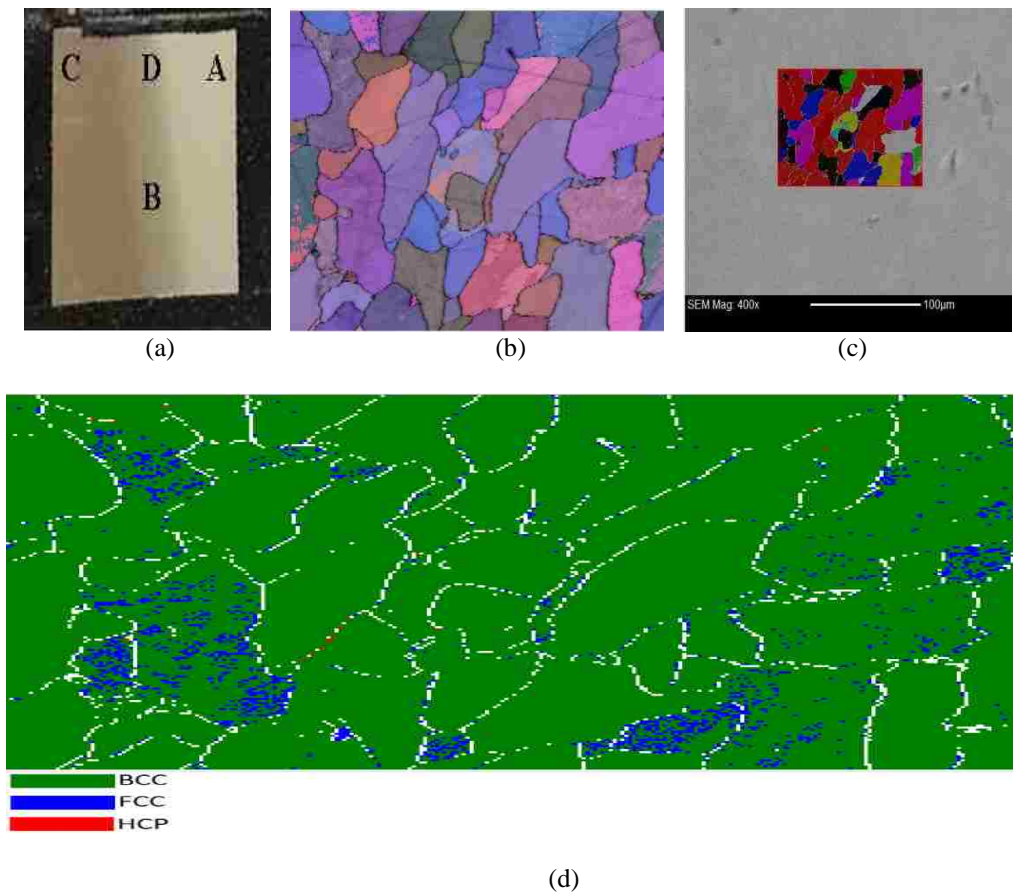


Figure 3.20 EBSD data from A36 steel, sample location 4-A, after impact velocity of 4.51 km/sec showing: a) polished sample, b) grain, c) 400X magnification and the original length of the map, and d) phase map.

Table 3.17 Impact phase ratio of A36 steel at 4.51 km/sec sample location 4-A

Crystal Unit Cell Structures	Impact A36 Steel Phase at 4.51 km/sec
BCC	96.096 %
FCC	3.953 %
HCP	0.1190 %

3.3.5 Cross-section Location 5-A (10 mm from impact center)

Figure 3.21 shows the EBSD microscopy data for location 5-A in the A36 steel target after an impact velocity of 4.51 km/sec. The figure shows the polished sample, grain, 400X magnification and the original length of the map, and the phase distribution.

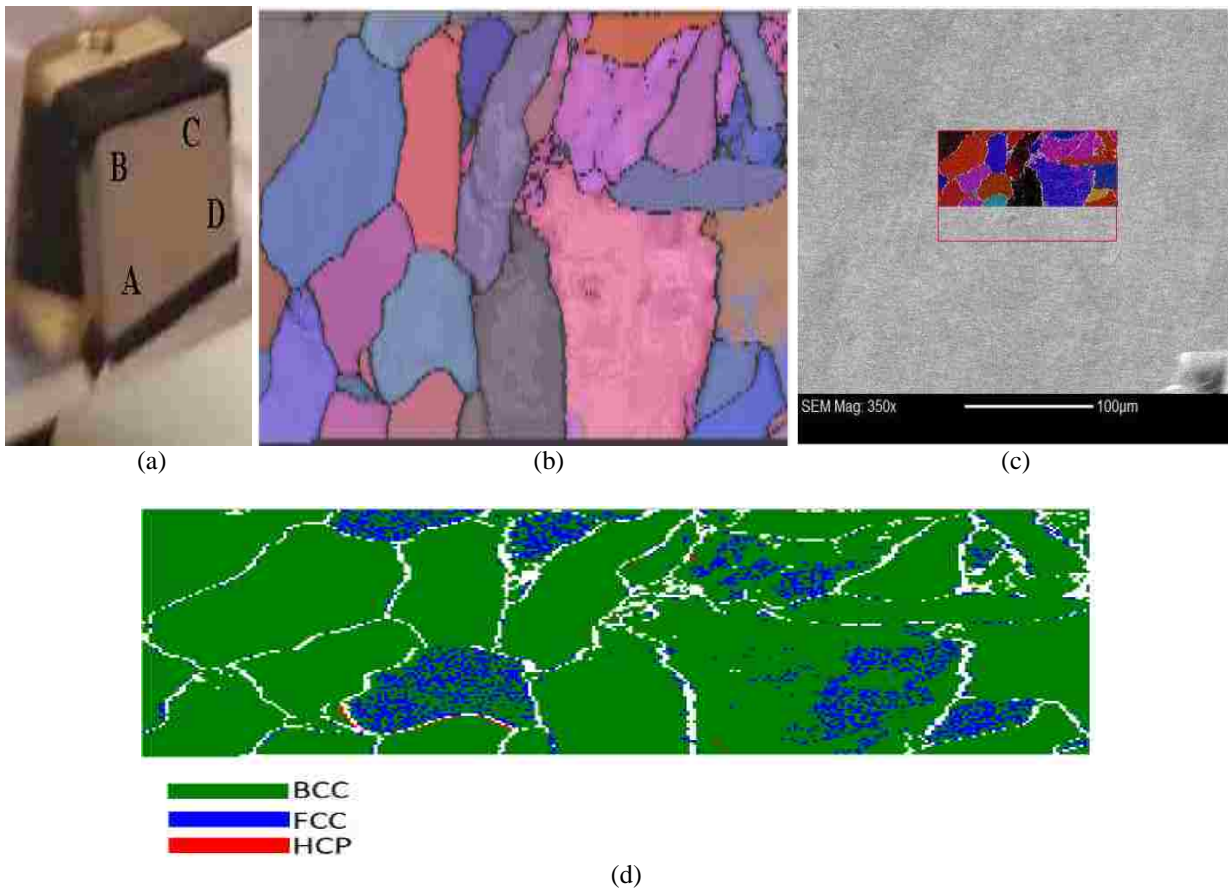


Figure 3.21 EBSD data from A36 steel, sample location 5-A, after impact velocity of 4.51 km/sec showing: a) polished sample, b) grain, c) 400X magnification and the original length of the map, and d) phase map.

Table 3.18 Impact phase ratio of A36 steel at 4.51 km/sec sample location 5-A

Crystal Unit Cell Structures	Impact A36 Steel Phase at 4.51 km/sec
BCC	91.65 %
FCC	8.31 %
HCP	0.220 %

3.3.6 Cross-section Location 6-A (0 mm from impact center)

Figure 3.22 shows the EBSD microscopy data for location 6-A in the A36 steel target after an impact velocity of 4.51 km/sec. The figure shows the polished sample, grain, 400X magnification and the original length of the map, and the phase distribution.

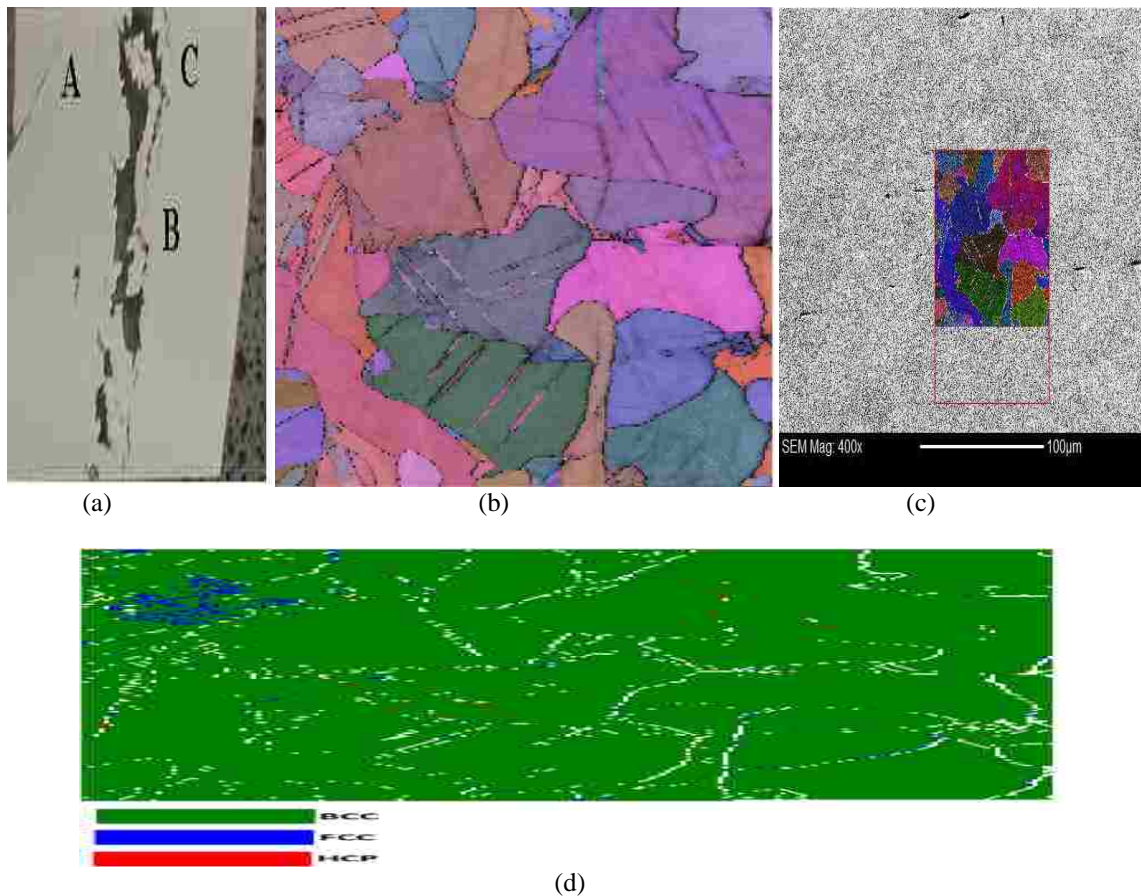


Figure 3.22 EBSD data from A36 steel, sample location 6-A, after impact velocity of 4.51 km/sec showing: a) polished sample, b) grain, c) 400X magnification and the original length of the map, and d) phase map.

Table 3.19 Impact phase ratio of A36 steel at 4.51 km/sec sample location 6-A

Crystal Unit Cell Structures	Impact A36 Steel Phase at 4.51 km/sec
BCC	96.68 %
FCC	2.87 %
HCP	0.44 %

3.3.7 Cross-section Location 6-B (0 mm from impact center)

Figure 3.23 shows the EBSD microscopy data for location 6-B in the A36 steel target after an impact velocity of 4.51 km/sec. The figure shows grain, 400X magnification and the original length of the map, and the phase distribution.

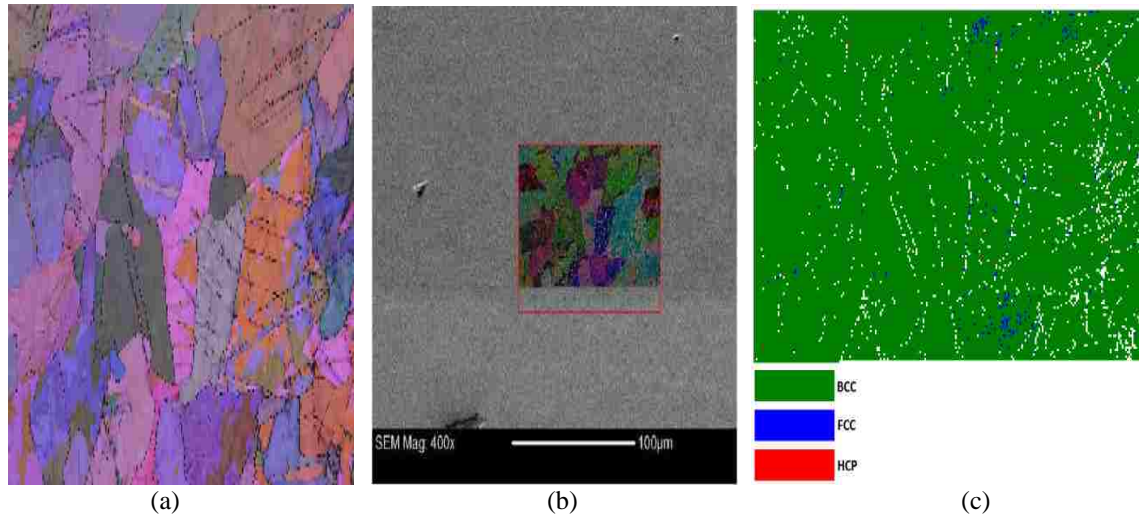


Figure 3.23 EBSD data from A36 steel, sample location 6-B, after impact velocity of 4.51 km/sec showing: a) grain, b) 400X magnification and the original length of the map, and C) phase map.

Table 3.20 Impact phase ratio of A36 steel at 4.51 km/sec sample location 6-B

Crystal Unit Cell Structures	Impact A36 Steel Phase at 4.51 km/sec
BCC	98.22 %
FCC	0.71 %
HCP	1.17 %

3.3.8 Cross-section Location 6-C (0 mm from impact center)

Figure 3.24 shows the EBSD microscopy data for location 6-C in the A36 steel target after an impact velocity of 4.51 km/sec. The figure shows grain, 400X magnification and the original length of the map, and the phase distribution.

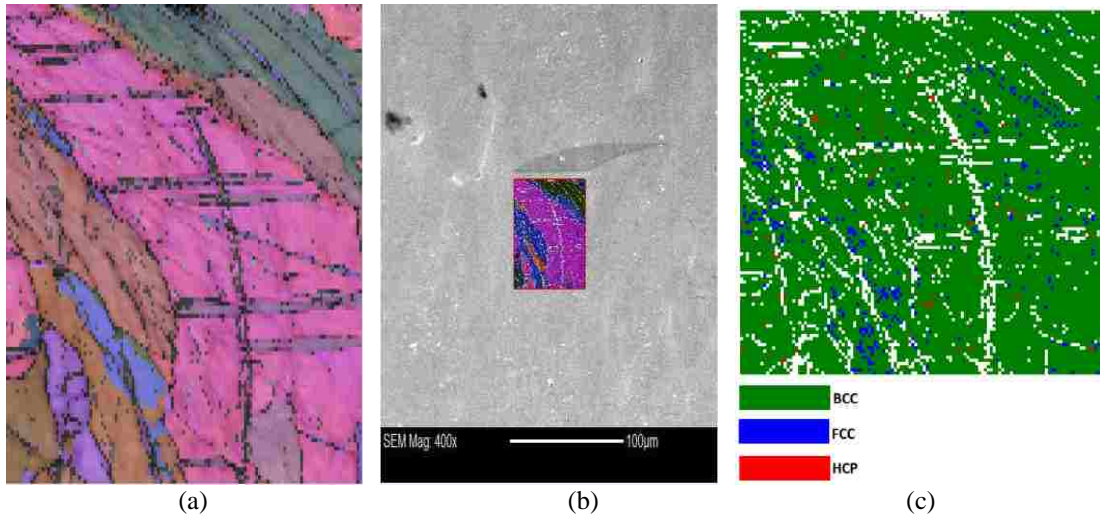


Figure 3.24 EBSD data from A36 steel, sample location 6-C, after impact velocity of 4.51 km/sec showing: a) grain, b) 400X magnification and the original length of the map, and c) phase map.

Table 3.21 Impact phase ratio of A36 steel at 4.51 km/sec sample location 6-C

Crystal Unit Cell Structures	Impact A36 Steel Phase at 4.51 km/sec
BCC	97.89 %
FCC	0.95 %
HCP	1.153 %

All figures of 4.51 km/sec speed show the trend of twinning change starting with sample number 4. The most dense twinning region is around the shock center. Quantitatively, all tales of each sample indicates the ratios of the phase mix relationship and shows the estimation of BCC, being the dominant phase pre-impact, remains so after impact at all slides. However, HCP started to appear near impact and existed in the far locations but with insignificant proportions. FCC existed with insignificant

pre-impact and became significant after impact location at the impact and the neighborhood near the impact, however with a lower percentage and became insignificant again away from the impact

3.4 Impact Velocity of 5.8 km/s in A36 Steel

3.4.1 Cross-section Location 1-A (75 mm from impact center)

Figure 3.25 shows the EBSD microscopy data for location 1-A in the A36 steel target after an impact velocity of 5.80 km/sec. The figure shows the polished sample, grain, 400X magnification and the original length of the map, and the phase distribution.

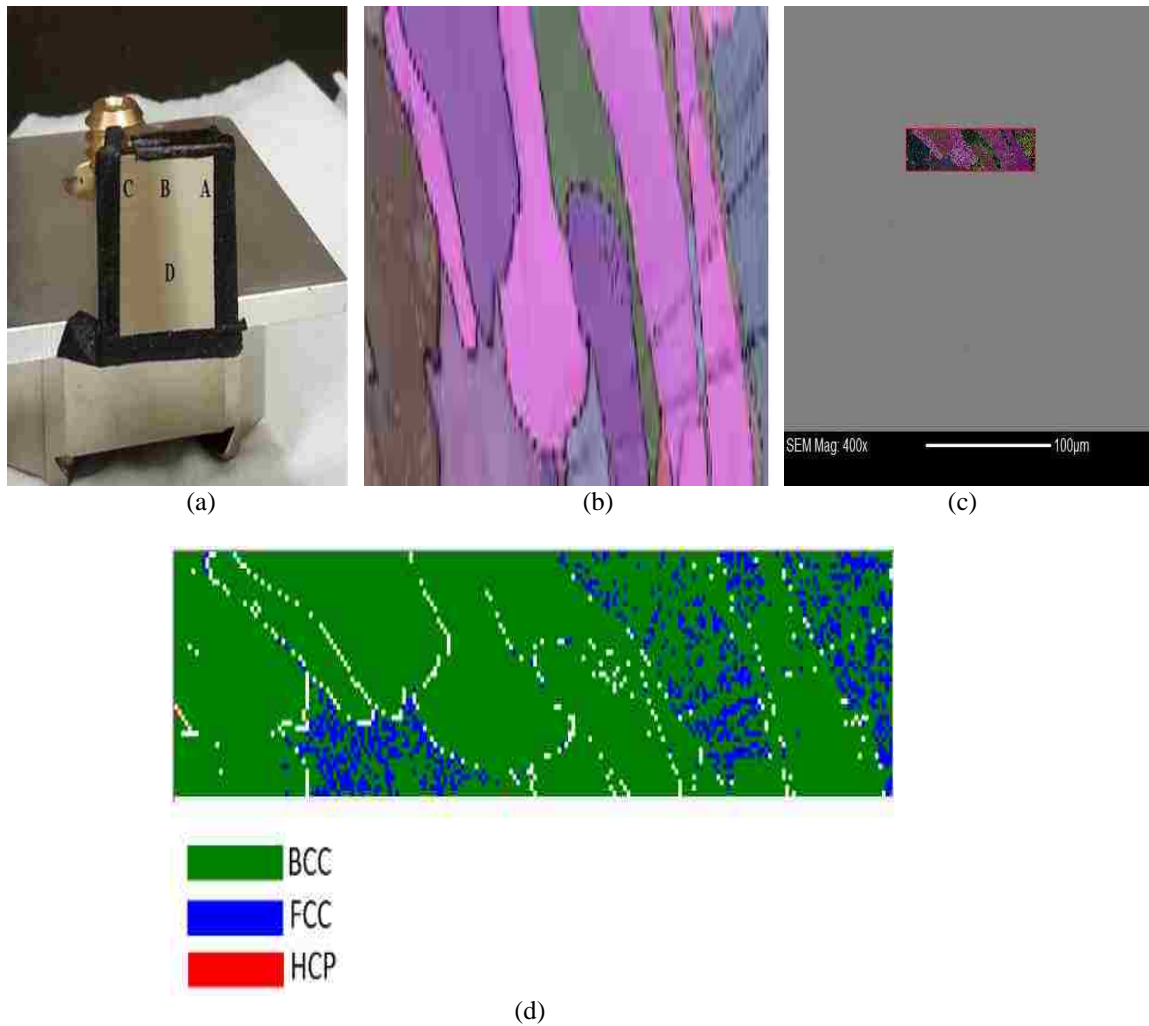


Figure 3.25 EBSD data from A36 steel, sample location 1-A, after impact velocity of 5.80 km/sec showing: a) polished sample, b) grain, c) 400X magnification and the original length of the map, and d) phase map.

Table 3.22 Impact phase ratio of A36 steel at 5.80 km/sec sample location 1-A

Crystal Unit Cell Structures	Impact A36 Steel Phase at 5.80 km/sec
BCC	89.876 %
FCC	10.079 %
HCP	0.442 %

3.4.2 Cross-section Location 2-A (35 mm from impact center)

Figure 3.26 shows the EBSD microscopy data for location 2-A in the A36 steel target after an impact velocity of 5.80 km/sec. The figure shows the polished sample, grain, 400X magnification and the original length of the map, and the phase distribution.

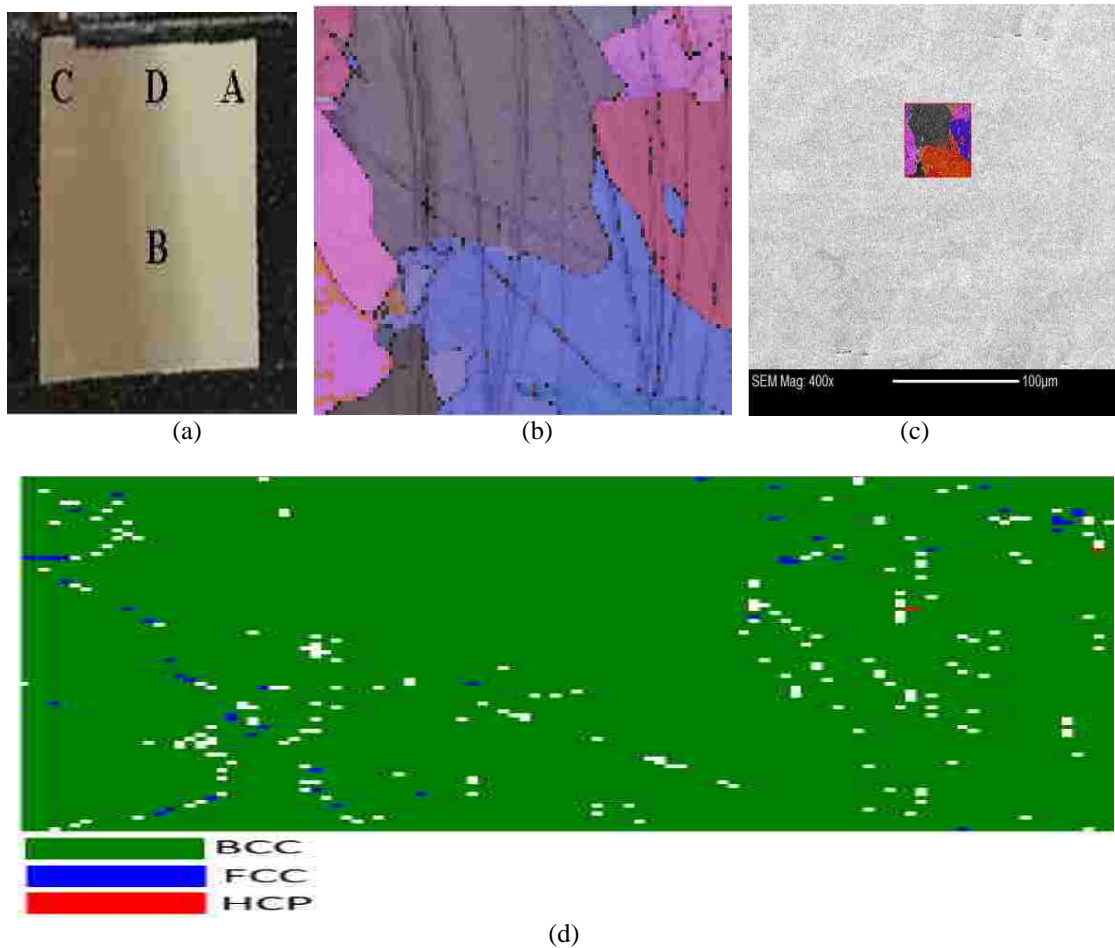


Figure 3.26 EBSD data from A36 steel, sample location 2-A, after impact velocity of 5.80 km/sec showing: a) polished sample, b) grain, c) 400X magnification and the original length of the map, and d) phase map.

Table 3.23 Impact phase ratio of A36 steel at 5.80 km/sec sample location 2-A

Crystal Unit Cell Structures	Impact A36 Steel Phase at 5.80 km/sec
BCC	99.4806 %
FCC	0.928 %
HCP	0.452 %

3.4.3 Cross-section Location 3-B (7.5 mm from impact center)

Figure 3.27 shows the EBSD microscopy data for location 3-B in the A36 steel target after an impact velocity of 5.80 km/sec. The figure shows the polished sample, grain, 400X magnification and the original length of the map, and the phase distribution.

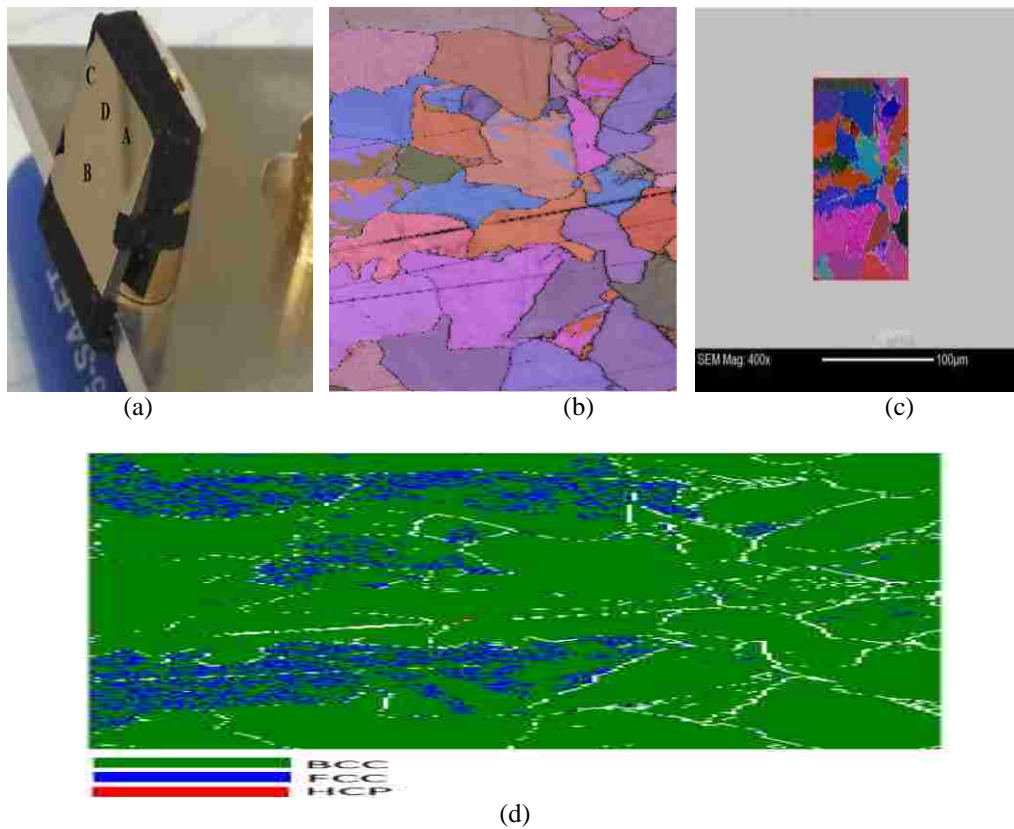


Figure 3.27 EBSD data from A36 steel, sample location 3-B after impact velocity of 5.80 km/sec showing: a) polished sample, b) grain, c) 400X magnification and the original length of the map, and d) phase map.

Table 3.24 Impact phase ratio of A36 steel at 5.80 km/sec sample location 3-B

Crystal Unit Cell Structures	Impact A36 Steel Phase at 5.80 km/sec
BCC	91.1078 %
FCC	9.3748 %
HCP	0.523 %

3.4.4 Cross-section Location 4-D (20 mm from impact center)

Figure 3.28 shows the EBSD microscopy data for location 4-D in the A36 steel target after an impact velocity of 5.80 km/sec. The figure shows the polished sample, grain, 400X magnification and the original length of the map, and the phase distribution.

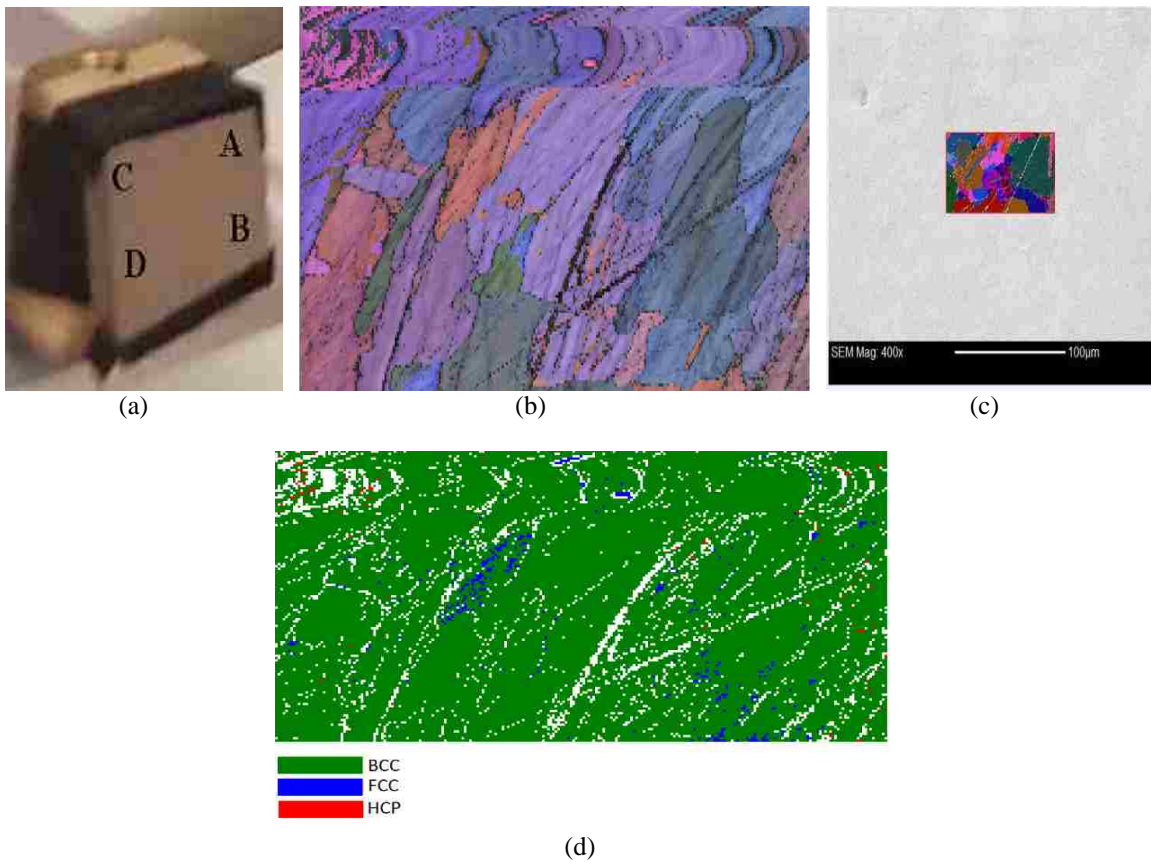


Figure 3.28 EBSD data from A36 steel, sample location 4-D, after impact velocity of 5.80 km/sec showing: a) polished sample, b) grain, c) 400X magnification and the original length of the map, and d) phase map.

Table 3.25 Impact phase ratio of A36 steel at 5.80 km/sec sample location 4-D

Crystal Unit Cell Structures	Impact A36 Steel Phase at 5.80 km/sec
BCC	98.4246 %
FCC	1.6866 %
HCP	0.556 %

3.4.5 Cross-section Location 5-D (10 mm from impact center)

Figure 3.29 shows the EBSD microscopy data for location 5-D in the A36 steel target after an impact velocity of 5.80 km/sec. The figure shows the polished sample, grain, 400X magnification and the original length of the map, and the phase distribution.

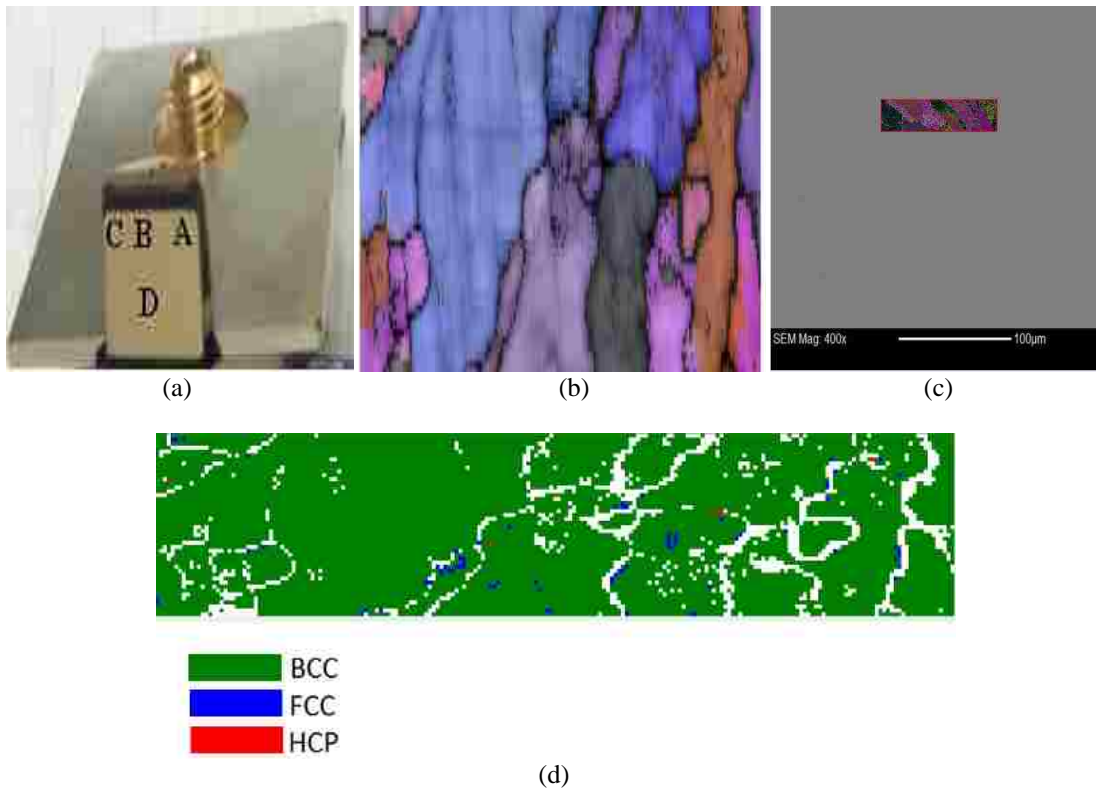


Figure 3.29 EBSD data from A36 steel, sample location 5-D, after impact velocity of 5.80 km/sec showing: a) polished sample, b) grain, c) 400X magnification and the original length of the map, and d) phase map.

Table 3.26 Impact phase ratio of A36 steel at 5.80 km/sec sample location 5-D

Crystal Unit Cell Structures	Impact A36 Steel Phase at 5.80 km/sec
BCC	99.03 %
FCC	0.88 %
HCP	0.88 %

3.4.6 Cross-section Location 6-A (0 mm from impact center)

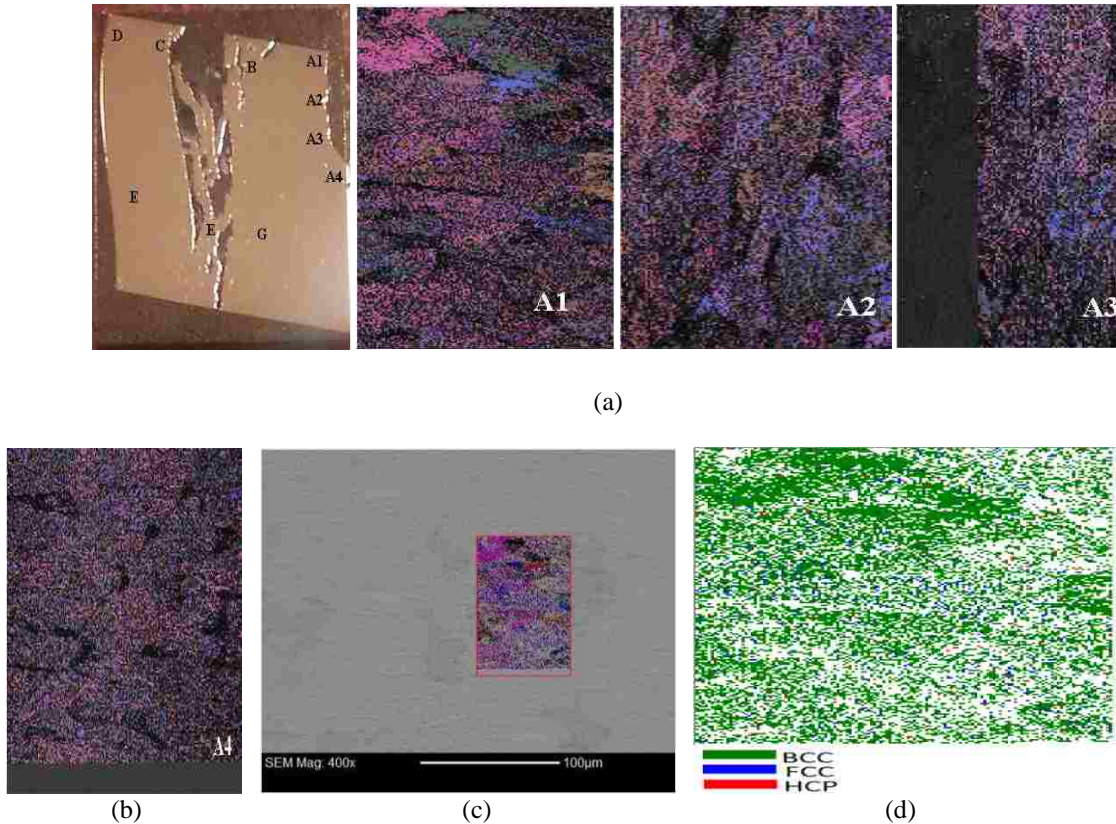


Figure 3.30 EBSD data from A36 steel, sample location 6-A, after impact velocity of 5.80 km/sec showing: a) polished sample, b) grain, c) 400X magnification and the original length of the map, and d) phase map.

The observation of the samples from the EBSD imaging (post-impact) was that the grain size significantly decreased closer to the impact area (Arc of the projectile) plane that EBSD cannot scan and the error of this area was so high and confidence so little as shown at location A, so the result is the average of this area.

Table 3.27 Impact phase ratio of A36 steel at 5.80 km/sec sample location 6-A

Crystal Unit Cell Structures	Impact A36 Steel Phase at 5.80 km/sec
BCC	95.273 %
FCC	3.849 %
HCP	0.88 %

3.4.7 Cross-section Location 6-B (0 mm from impact center)

Figure 3.31 shows the EBSD microscopy data for location 6-B in the A36 steel target after an impact velocity of 5.80 km/sec. The figure shows the grain, 400X magnification and the original length of the map, and the phase distribution. The percentage of twinning visible in this community site because the grain left the site exposed to a shock angle and the plastic deformation twinning here ranged from 55 to 60 degrees.

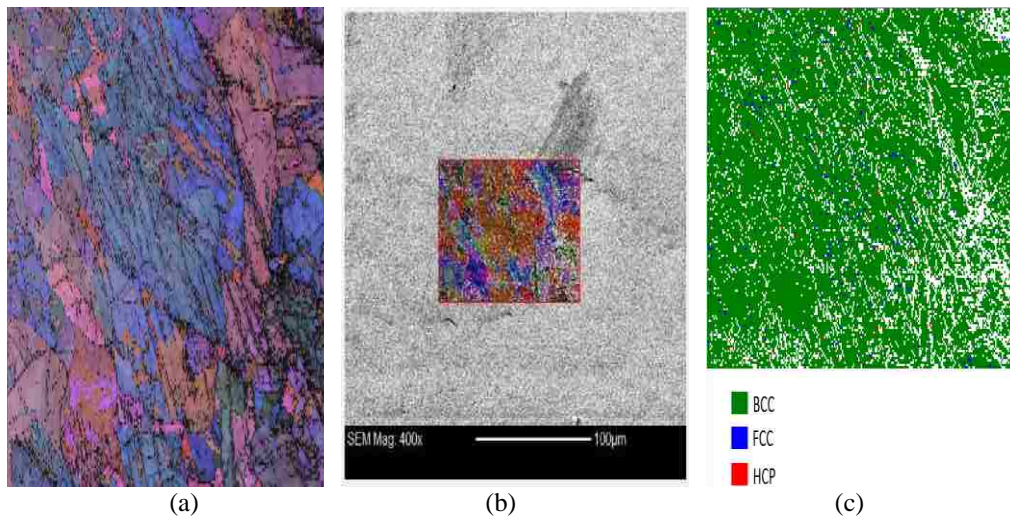


Figure 3.31 EBSD data from A36 steel, sample location 6-B, after impact velocity of 5.80 km/sec showing: a) grain, b) 400X magnification and the original length of the map, and c) phase map.

Table 3.28 Impact phase ratio of A36 steel at 5.80 km/sec sample location 6-B

Crystal Unit Cell Structures	Impact A36 Steel Phase at 5.80 km /sec
BCC	98.20 %
FCC	0.613 %
HCP	1.2 %

3.4.8 Cross-section Location 6-C (0 mm from impact center)

Figure 3.32 shows the EBSD microscopy data for location 6-c in the A36 steel target after an impact velocity of 5.80 km/sec. The figure shows the grain, 400X magnification and the original length of the map, and the phase distribution.

Sample 6 is most important for our analysis. One reason is that it's located intuitively nearest to the impact section. And an EBSD reading shows many changes accrued, as expected at this section, across the board.

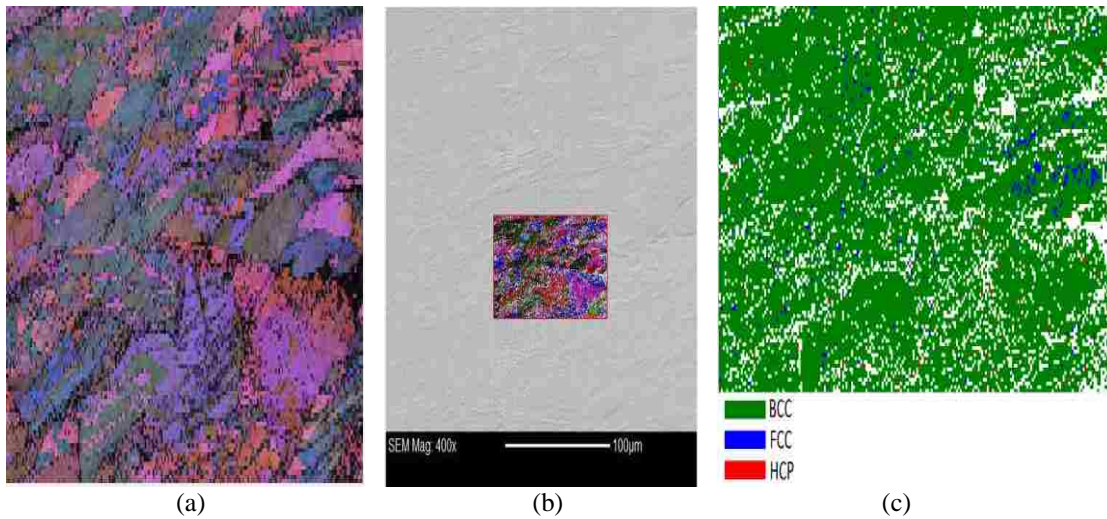


Figure 3.32 EBSD data from A36 steel, sample location 6-C, after impact velocity of 5.80 km/sec showing: a) grain, b) 400X magnification and the original length of the map, and c) phase map.

Table 3.29 Impact phase ratio of A36 steel at 5.80 km/sec sample location 6-C

Crystal Unit Cell Structures	Impact A36 Steel Phase at 5.80 km/sec
BCC	97.42 %
FCC	1.0123 %
HCP	1.488 %

3.4.9 Cross-section Location 6-D (0 mm from impact center)

Figure 3.33 shows the EBSD microscopy data for location 6-D in the A36 steel target after an impact velocity of 5.80 km/sec. The figure shows the grain, 400X magnification and the original length of the map, and the phase distribution.

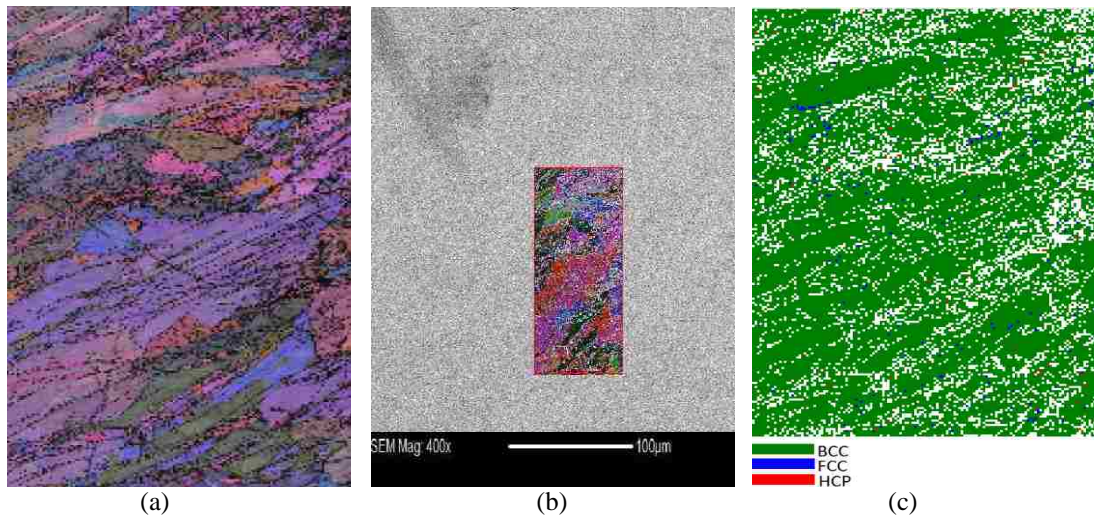


Figure 3.33 EBSD data from A36 steel, sample location 6-D, after impact velocity of 5.80 km/sec showing: a) grain, b) 400X magnification and the original length of the map, and c) phase map.

Table 3.30 Impact phase ratio of A36 steel at 5.80 km/sec sample location 6-D

Crystal Unit Cell Structures	Impact A36 Steel Phase at 5.80 km/sec
BCC	97.101 %
FCC	2.043 %
HCP	1.222 %

3.4.10 Cross-section Location 6-E (0 mm from impact center)

Figure 3.34 shows the EBSD microscopy data for location 6-E in the A36 steel target after an impact velocity of 5.80 km/sec. The figure shows the grain, 400X magnification and the original length of the map, and the phase distribution. In this picture, the lineage pairing is clear and large because the area of the crater and influence seems evident on the face change in the crystal table ratios (3.31).

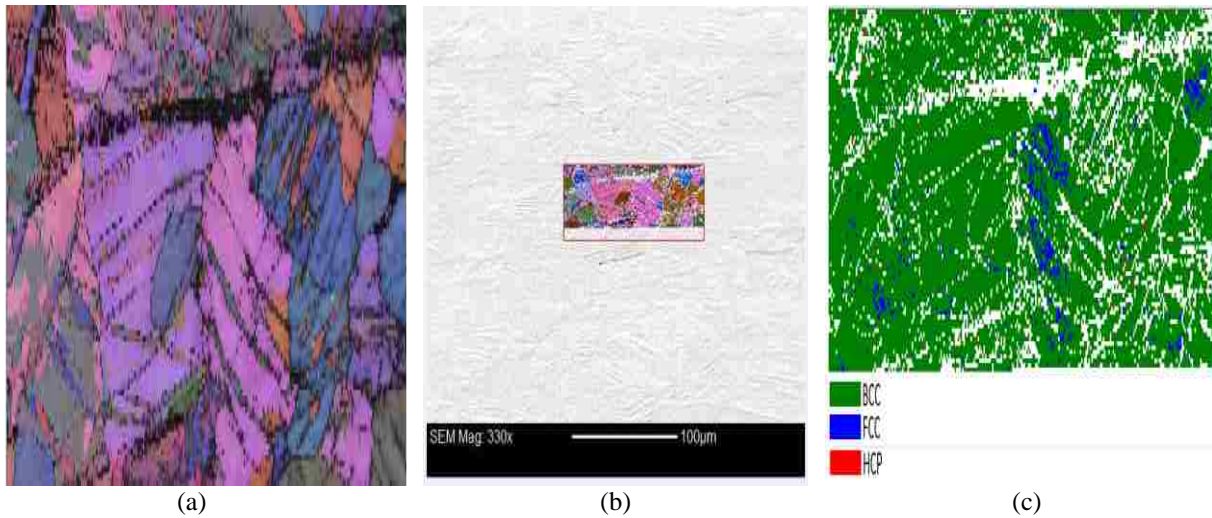


Figure 3.34 EBSD data from A36 steel, sample location 6-E, after impact velocity of 5.80 km/sec showing: a) grain, b) 400X magnification and the original length of the map, and c) phase map

Table 3.31 Impact phase ratio of A36 steel at 5.80 km/sec sample location 6-E

Crystal Unit Cell Structures	Impact A36 Steel Phase at 5.80 km/sec
BCC	96.6808 %
FCC	1.1043 %
HCP	2.215 %

3.4.11 Cross-section Location 6-F (0 mm from impact center)

Figure 3.35 shows the EBSD microscopy data for location 6-B in the A36 steel target after an impact velocity of 5.80 km/sec. The figure shows the grain, 400X magnification and the original length of the map, and the phase distribution. This location is about 2.5mm from the diameter of the arc of the crater and the grains seem to shift into a plastically clear shape and shows that twinning is growing and

the HCP percentage is 2.204 %. The observation of the image at this location proves that the plastic deformation is deformed as a twinning and ranges from 55 to 60 degrees.

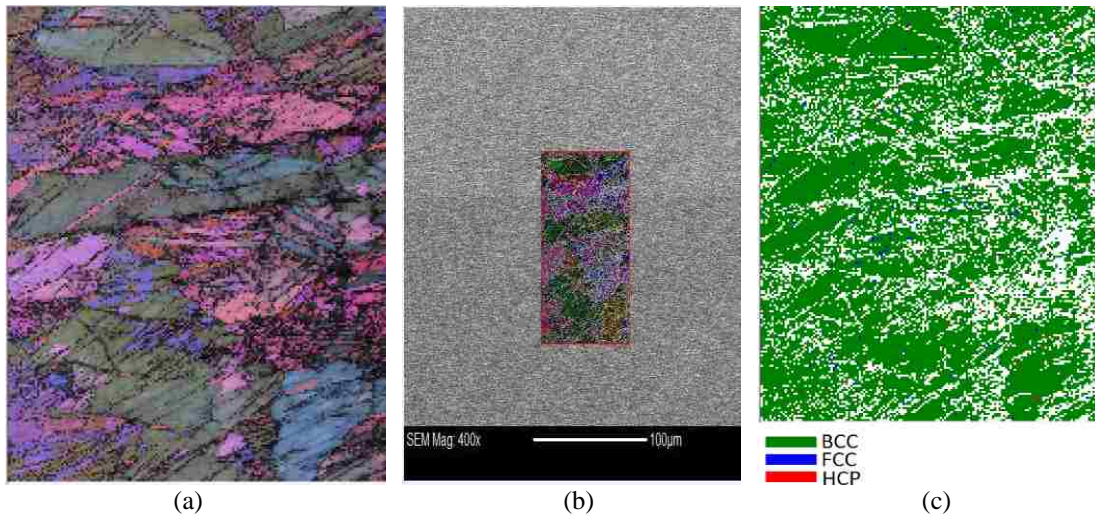


Figure 3.35 EBSD data from A36 steel, sample location 6-F after impact velocity of 5.80 km/sec showing: a) grain, b) 400X magnification and the original length of the map, and c) phase map.

Table 3.32 Impact phase ratio of A36 steel at 5.80 km/sec sample location 6-F

Crystal Unit Cell Structures	Impact A36 Steel Phase at 5.80 km/sec
BCC	97.180 %
FCC	0.6157 %
HCP	2.204 %

3.4.12 Cross-section Location 6-G (0 mm from impact center)

Figure 3.36 shows the EBSD microscopy data for location 6-G in the A36 steel target after an impact velocity of 5.80 km/sec. The figure shows the grain, 400X magnification and the original length of the map, and the phase distribution. This site is about 2 mm diameter of the arc of the projectile shock and seems to shift into shape plastically clear and twinning is growing and the obvious HCP percentage is 3.204 % The cross section sample (6) was etched with (HNO₃ 96 % and Ethanol 4 %) for 15 seconds.

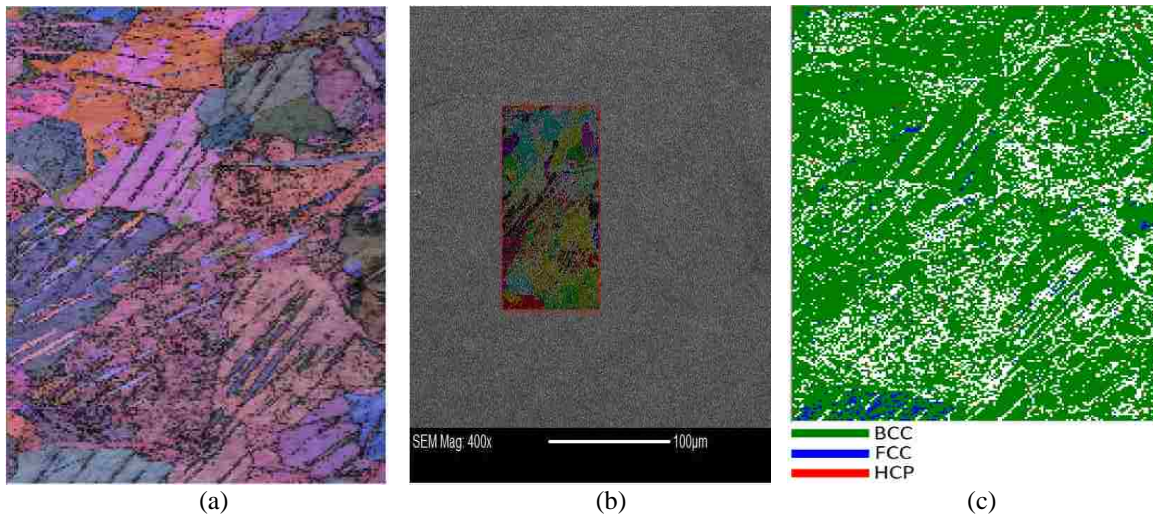


Figure 3.36 EBSD data from A36 steel, sample location 6-G, after impact velocity of 5.80 km/sec showing: a) grain, b) 400X magnification and the original length of the map, and c) phase map

Table 3.33 Impact phase ratio of A36 steel at 5.80 km/sec sample location 6-G

Crystal Unit Cell Structures	Impact A36 Steel Phase at 5.80 km/sec
BCC	96.180 %
FCC	0.6157 %
HCP	3.204 %

The dense twinning region is around the shock center. Quantitatively, all tables of sample 6 start from location B and indicate the ratio of the phase mix relationship and show the estimation of BCC, being the dominant phase, pre-impact and remain so after impact on all slides. However, HCP started to appear near impact and existed in the far locations but with insignificant proportion. FCC existed with insignificant pre-impact and became significant after impact at the impact and the neighborhood near impacts; however, with a lower percentage and became insignificant again away from impact. Location point G is chosen for discussion that will be addressed in the conclusion, Chapter 7. That is because of the low percentage of error and higher confidence.

3.5 EBSD Misorientation Measurements of the Impact A36 steel Targets

3.5.1 Misorientation Measurement for A36 Steel Target with an Impact Velocity of 3.54 km/sec at

Sample Location 6-A

These photos (Figure 3.37) show the Misorientation angle around these lines. Each line shows that the angle is between $55-60^\circ$ and the percentage of HCP is increased at the crater location at the impact speed 3.54 km/sec.

3.5.2 Misorientation Measurement for A36 Steel Target with an Impact Velocity of 4.51 km/sec at

Sample location 6-A.

Figure 3.38 shows the plastic deformation on A36 steel at 4.51 km/sec and all lines that test show that the angle of this transformation is between ($55-60^\circ$) and the HCP phase was increase in this location and the twinning increased too.

3.5.3 Misorientation Measurement for A36 Steel Target with an Impact Velocity of 4.51 km/sec at

Sample Location 6-B.

This photo explain the misorientation angle in another location of A36 steel at 4.51 km/sec and all lines that choice in this area shows that the angle is greater than 45° that is mean the plastic deformation was formed on this location and the twinning percentage decrease. Figure 3.39

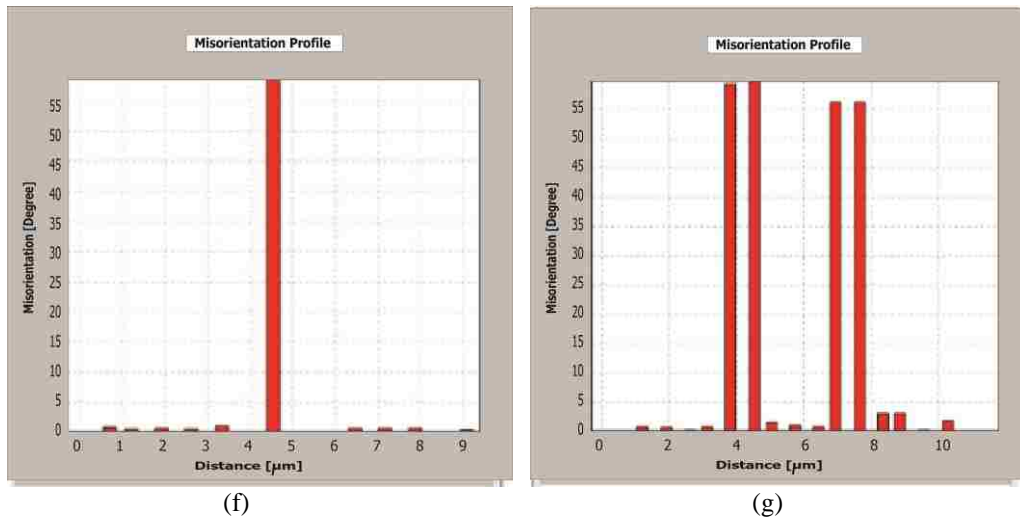
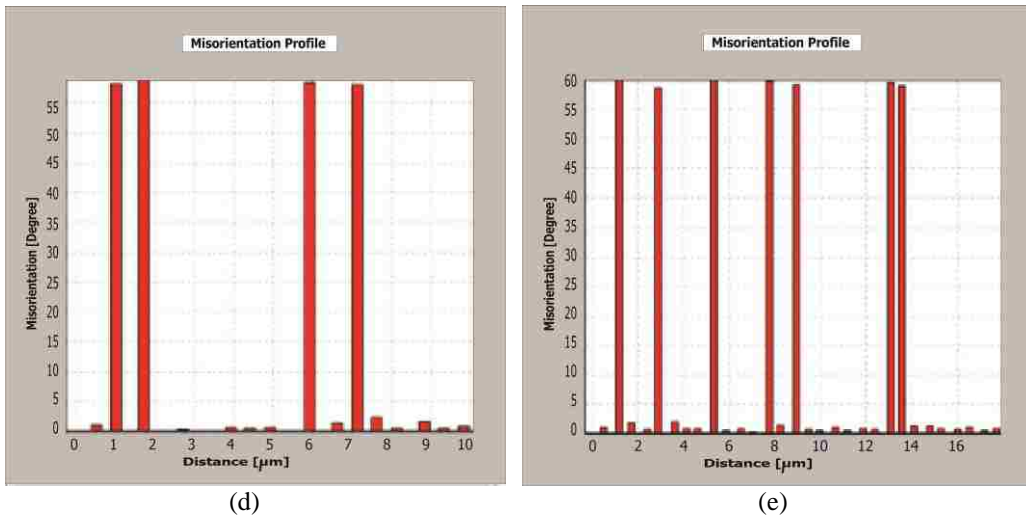
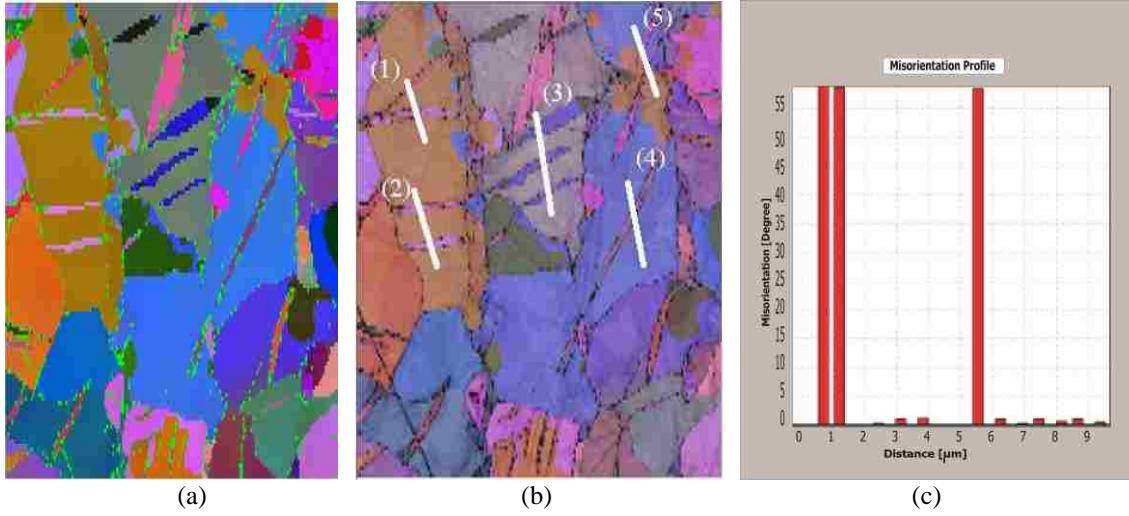


Figure 3.37 Misorientation angle measured along four different lines in the Impacted A36 steel, sample location 6-A, after impact velocity of 3.54 km/sec: a) EBSD shows less noise, b) EBSD shows grains; c) Line 1, d) Line 2, e) Line 3, f) Line 4 and G) line 5.

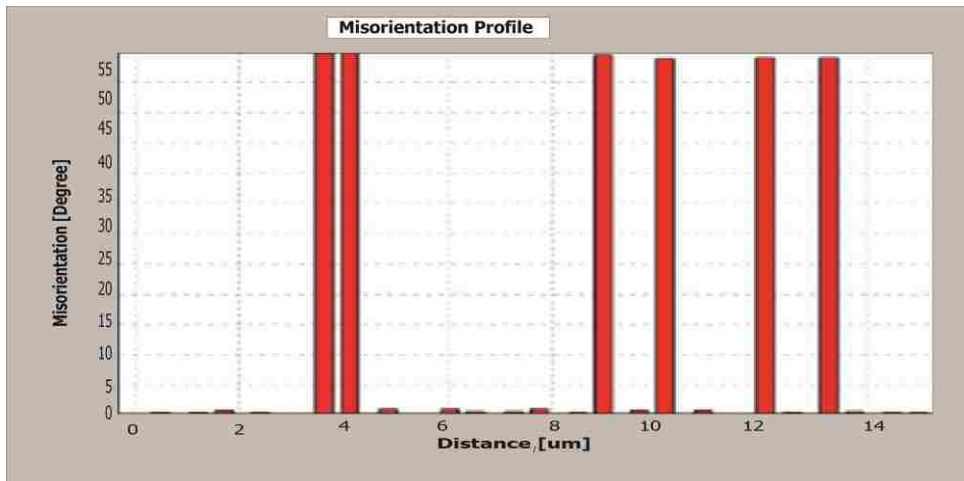
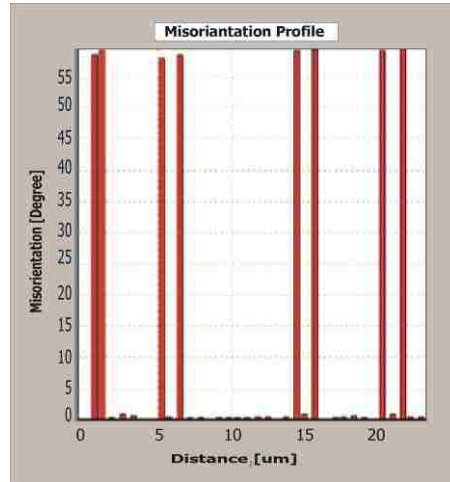
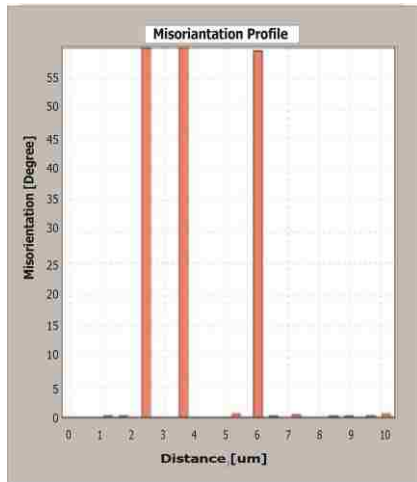
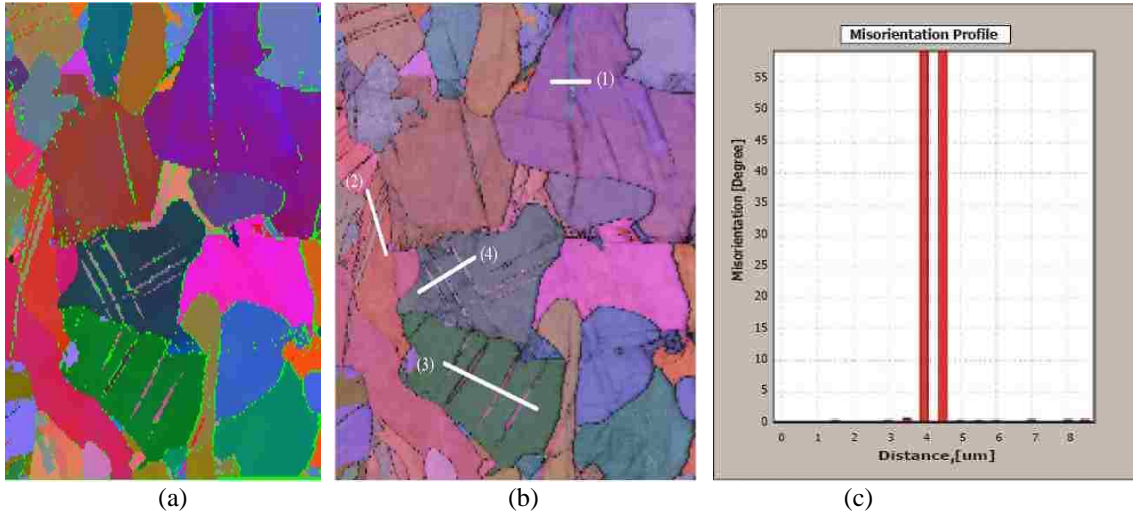


Figure 3.38 Misorientation angle measured along four different lines in the Impacted A36 steel, sample location 6-A, after impact velocity of 4.51 km/sec: a) EBSD shows less noise, b) EBSD shows grains; c) Line 1, d) Line 2, e) Line 3, and f) Line 4.

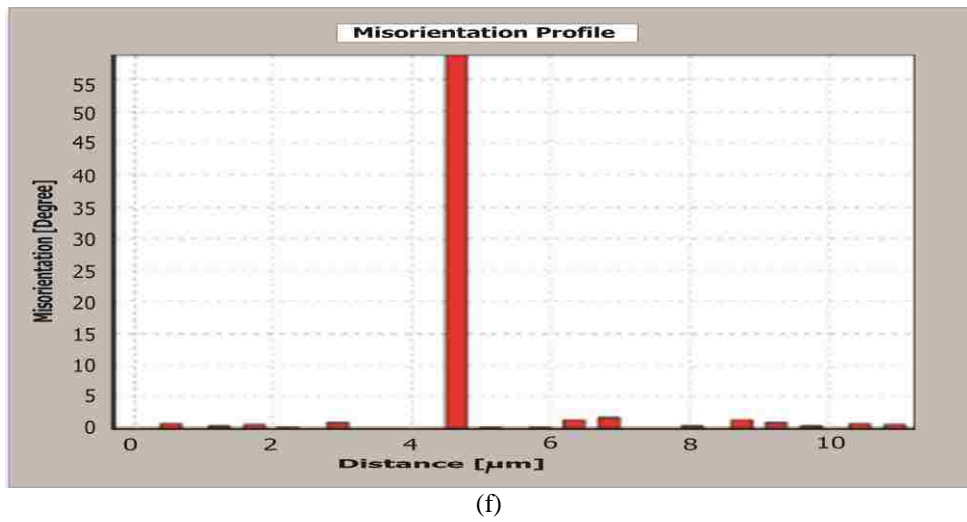
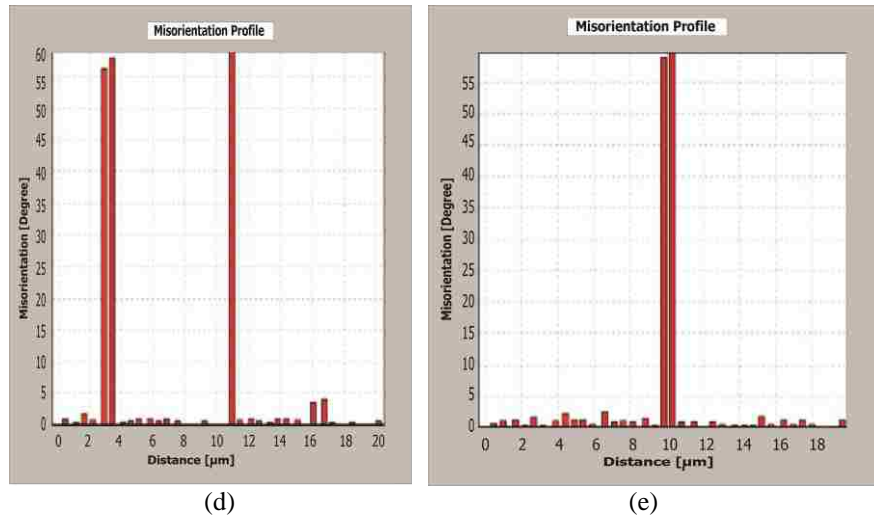
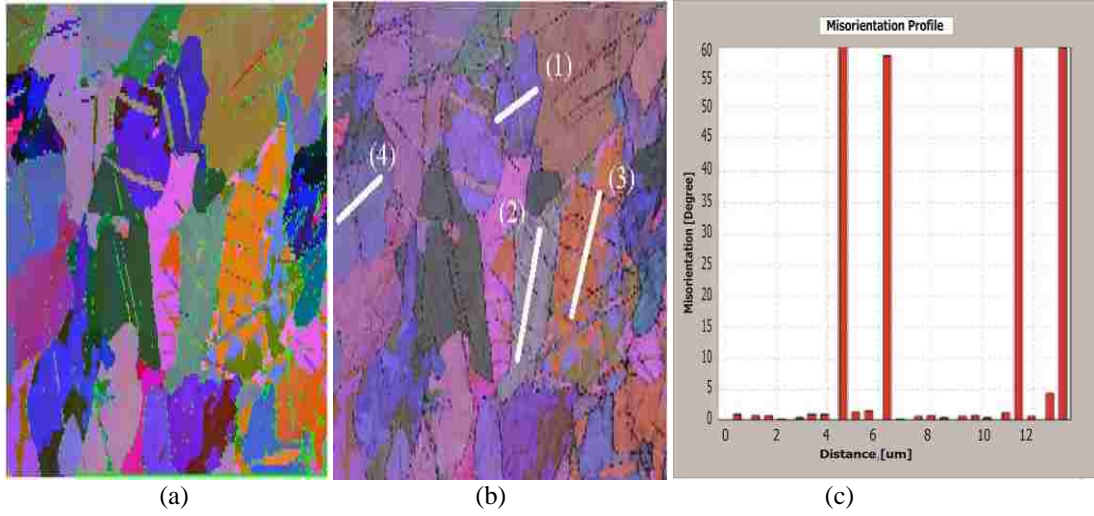
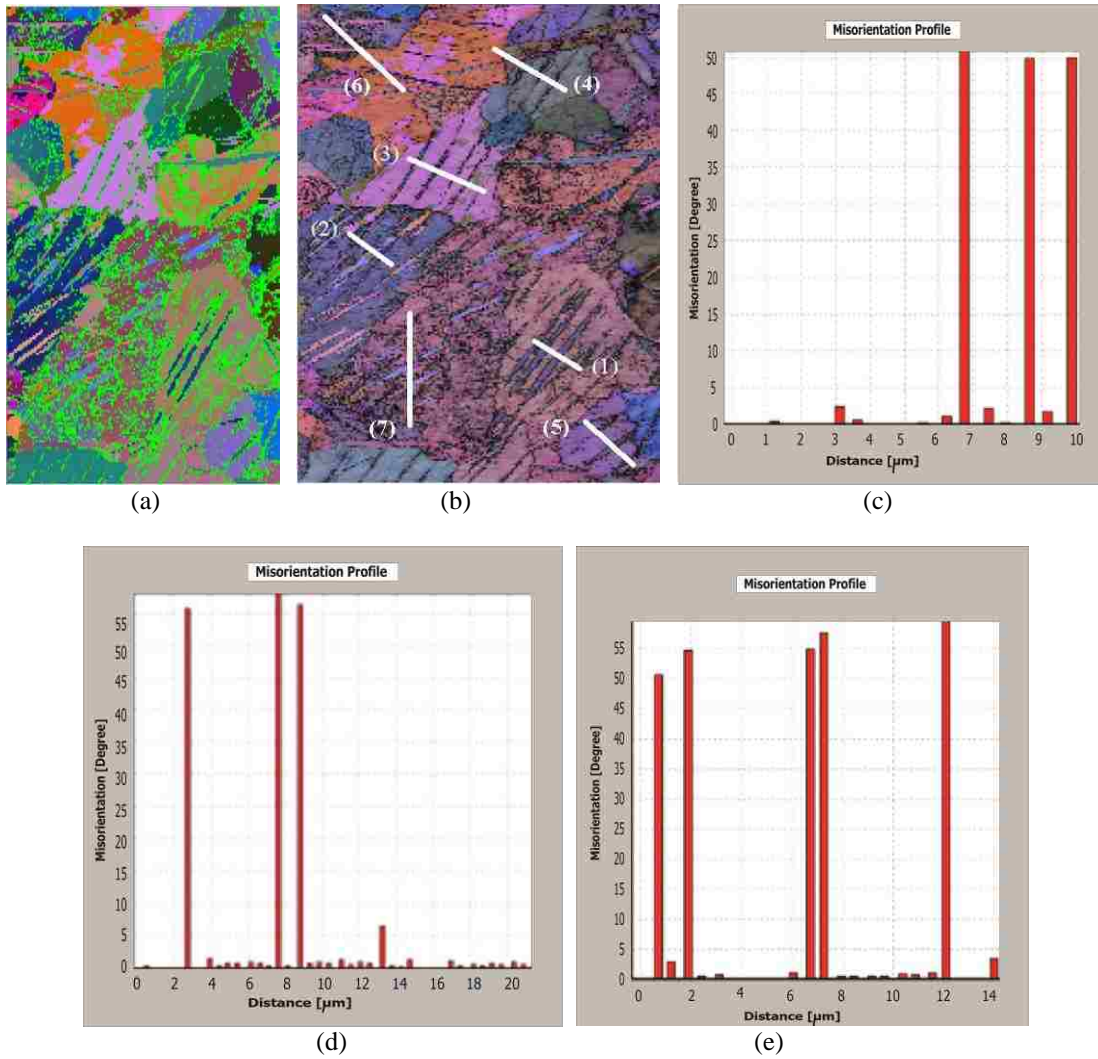
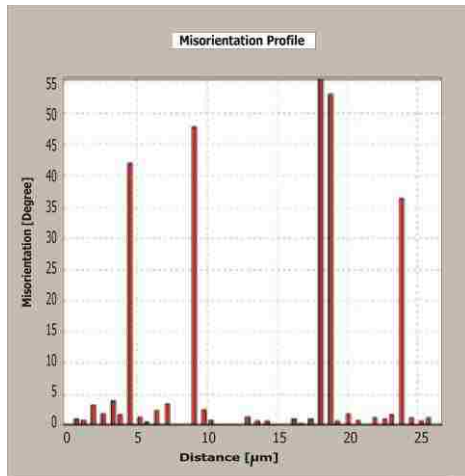


Figure 3.39 Misorientation angle measured along four different lines in the Impacted A36 steel, sample location 6-B, after impact velocity of 4.51 km/sec: a) EBSD shows less noise, b) EBSD shows grains; c) Line 1, d) Line 2, e) Line 3, and f) Line 4.

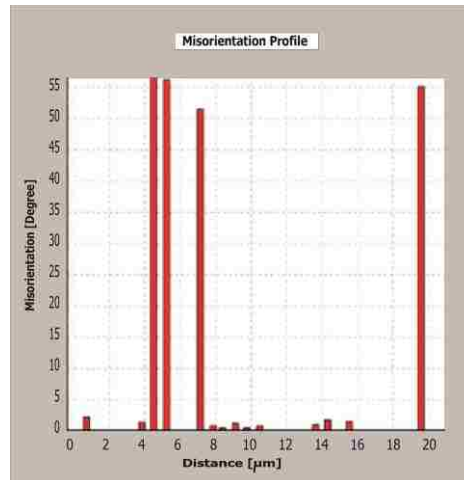
3.5.4 Misorientation Impact A36 steel at 5.80 km/sec Sample location 6-G.

Figure 3.40 the EBSD microscopy photos show the Misorientation angles at 3mm far from the impact arc of the projectile. The HCP phase in this location increased and the twinning increase also. All lines show that the new deformation starts here and it changes the phase from BCC to FCC and HCP.

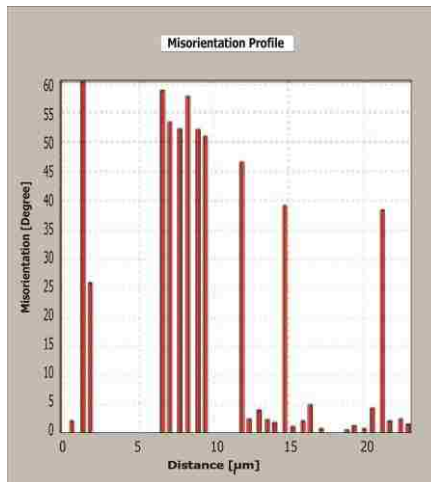




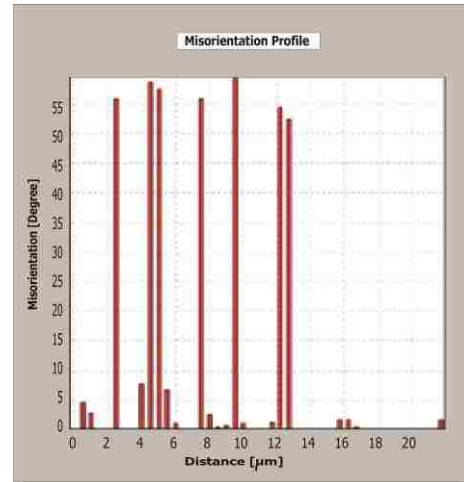
(f)



(g)



(h)



(i)

Figure 3.40 Misorientation angle measured along four different lines in the Impacted A36 steel, sample location 6-G, after impact velocity of 5.80 km/sec: a) EBSD shows less noise, b) EBSD shows grains; c, d, e, f, g, h, and i) are lines 1, 2, 3, 4, 5, 6, and 7 respectively.

3.5.5 Misorientation Impact A36 steel at 5.80 km/sec Sample location 6-B

Figure 3.41 these photos show the Misorientation angles of a few areas on location B and the all lines that have some percentage of twinning and the angles are between (55-60°).

3.5.6 Misorientation Impact A36 at steel 5.80 km/sec Sample location 6-C

Figure 3.42 EBSD microscopy photos show the Misorientation angles of a few areas on location C and that all lines have some percentage of twinning and the angles are between (55-60) degrees.

3.5.7 Misorientation Impact A36 steel at 5.80 km/sec Sample location 6-D

Figure 3.43 These photos show the Misorientation angles of a few areas on location D and that all lines have some percentage of twinning and the angle are between (55-60) degrees.

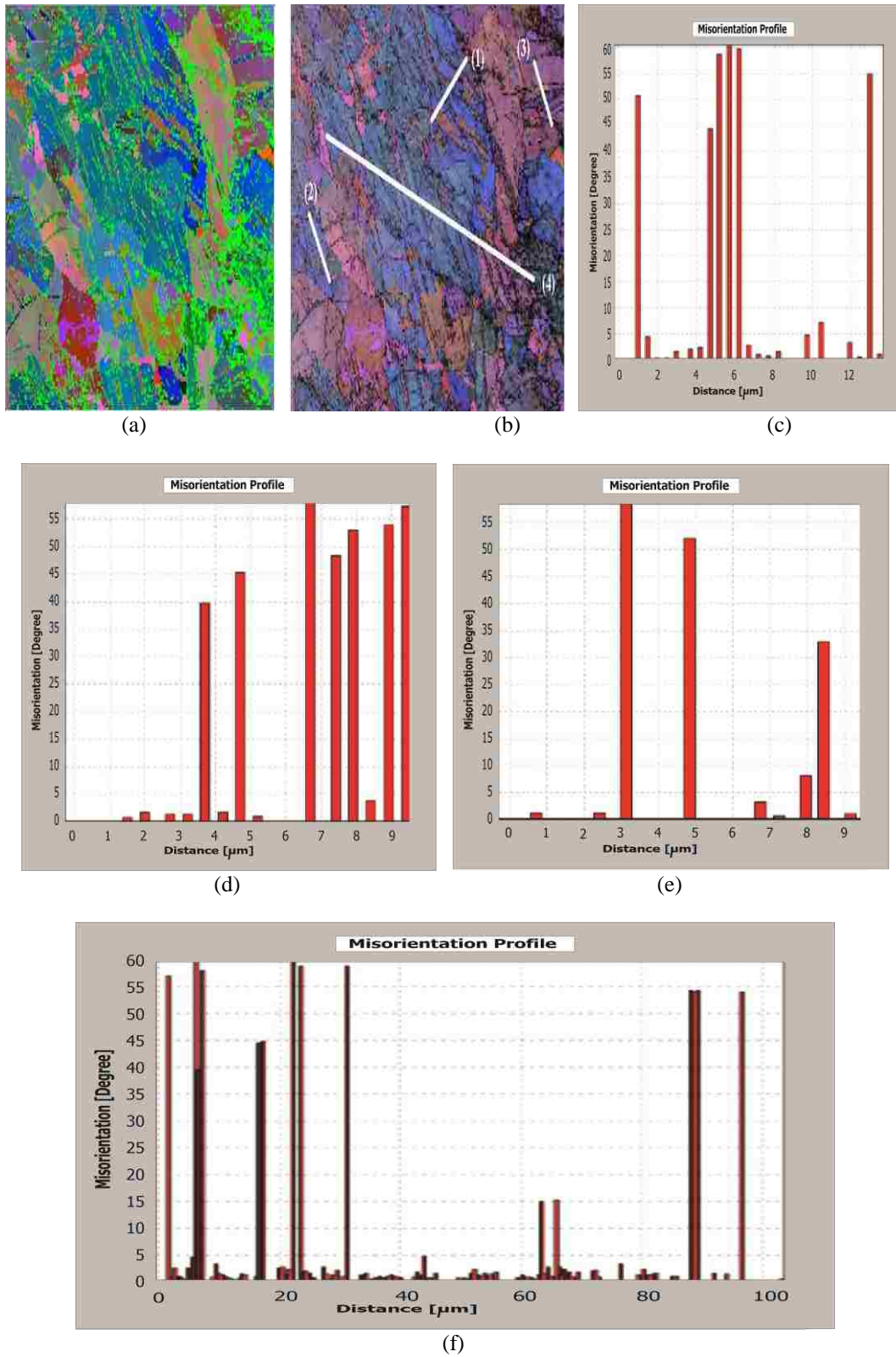
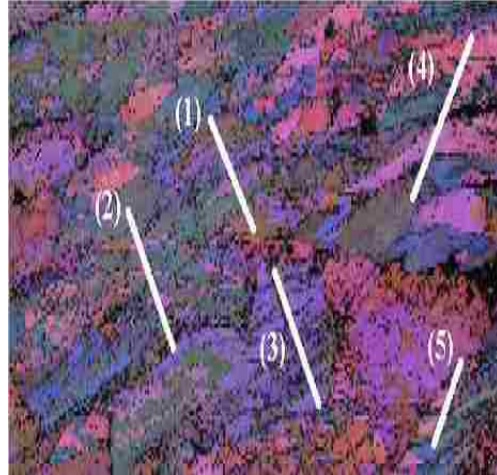


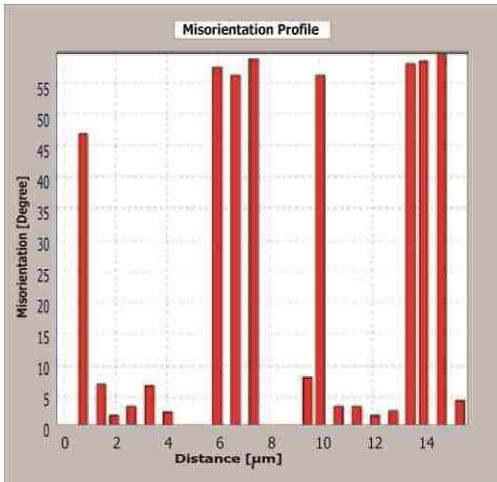
Figure 3.41 Misorientation angle measured along four different lines in the Impacted A36 steel, sample location 6-B, after impact velocity of 5.80 km/sec: a) EBSD shows less noise, b) EBSD shows grains; c) Line 1, d) Line 2, e) Line 3, and f) Line 4



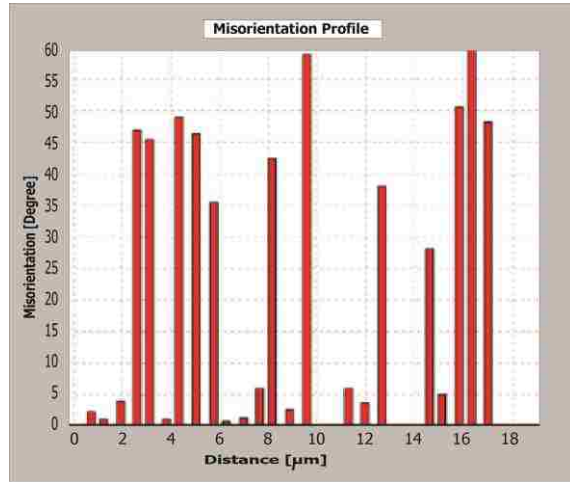
(a)



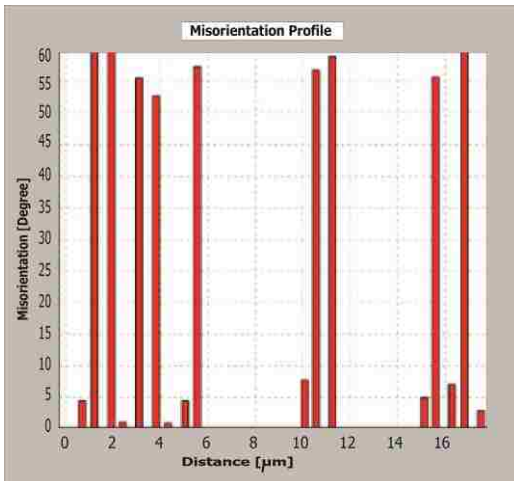
(b)



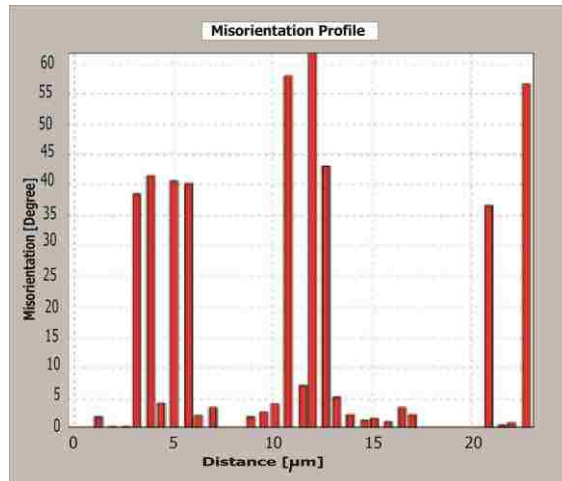
(c)



(d)



(e)



(f)

Figure 3.42 Misorientation angle measured along four different lines in the Impacted A36 steel, sample location 6-C, after impact velocity of 5.80 km/sec: a) EBSD shows less noise, b) EBSD shows grains; c) Line 1, d) Line 2, e) Line 3, and f) Line 4

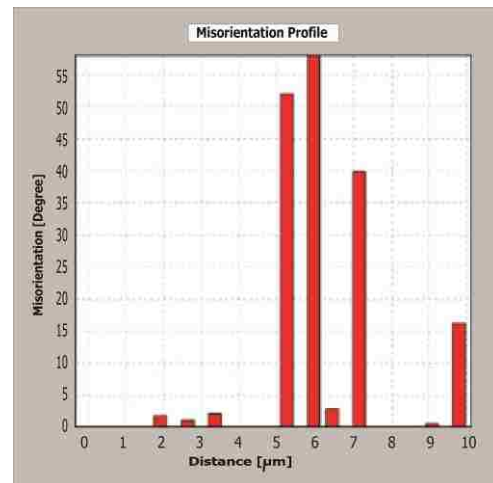
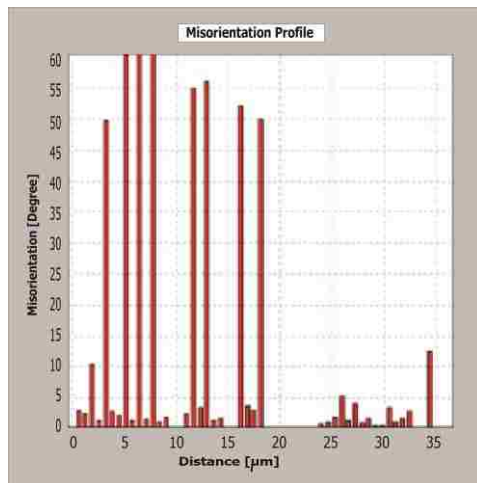
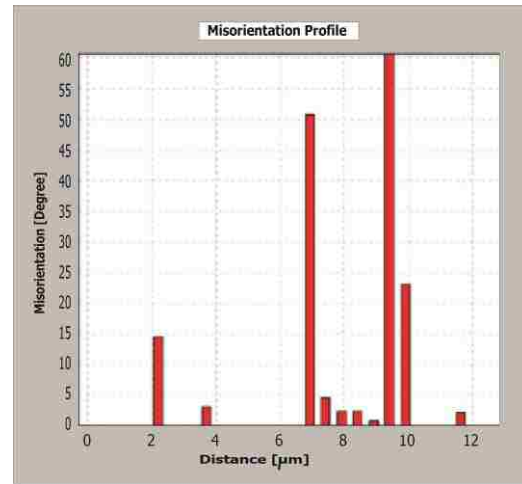
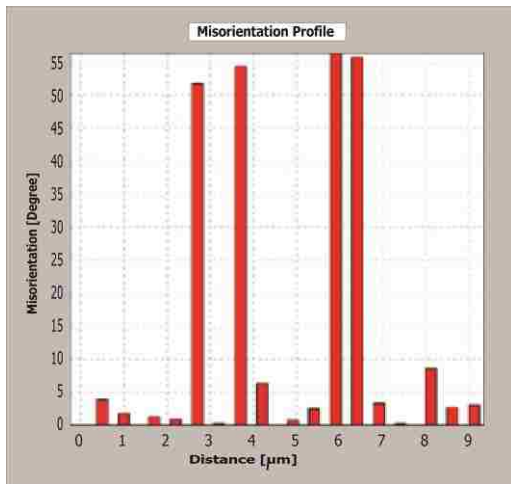
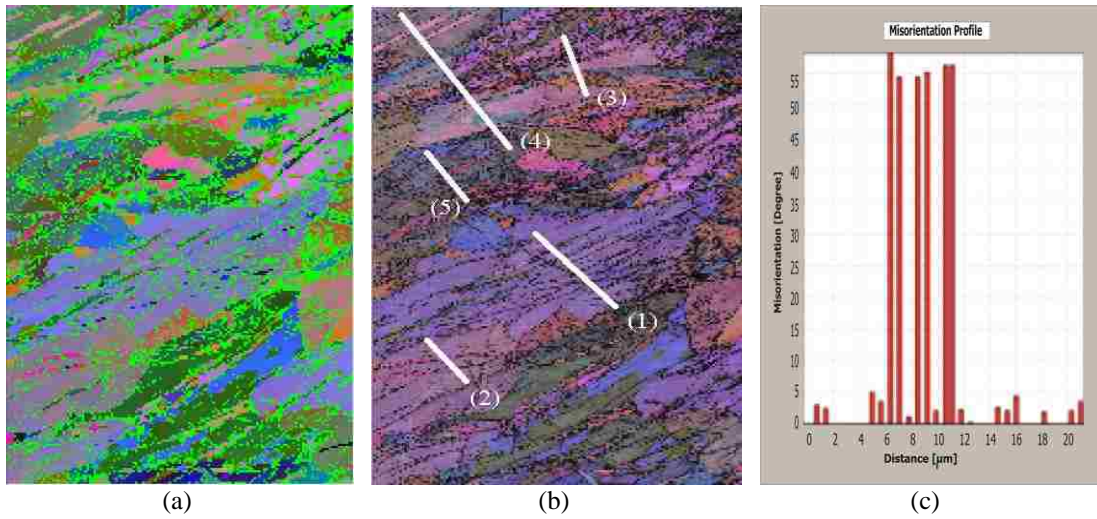
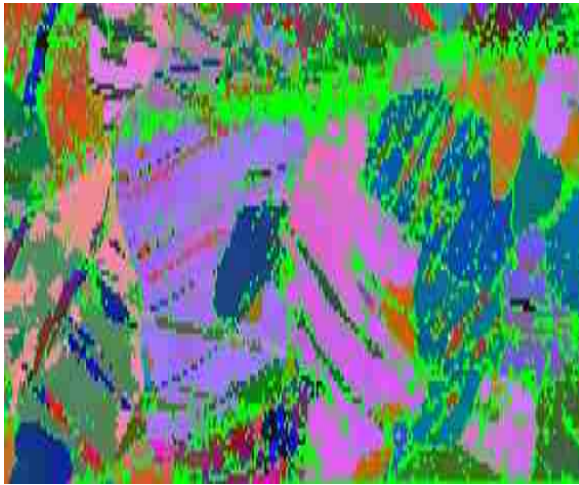


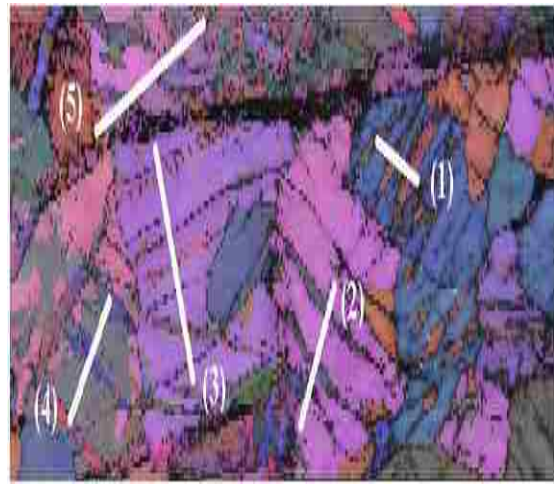
Figure 3.43 Misorientation angle measured along four different lines in the Impacted A36 steel, sample location 6-D, after impact velocity of 5.80 km/sec: a) EBSD shows less noise, b) EBSD shows grains; c) Line 1, d) Line 2, e) Line 3, and f) Line 4 and g) line 5.

3.5.8 Misorientation Impact A36 steel at 5.80 km/sec Sample location 6-E.

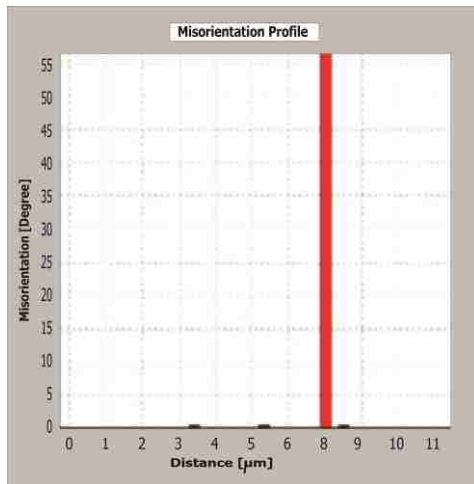
These photos explain the Misorientation angles in another location of A36 steel at 5.80 km/sec. All lines are chosen in this area show that the angle is greater than 45° , that means the plastic deformation was formed at this location and the twinning percentage decreased.



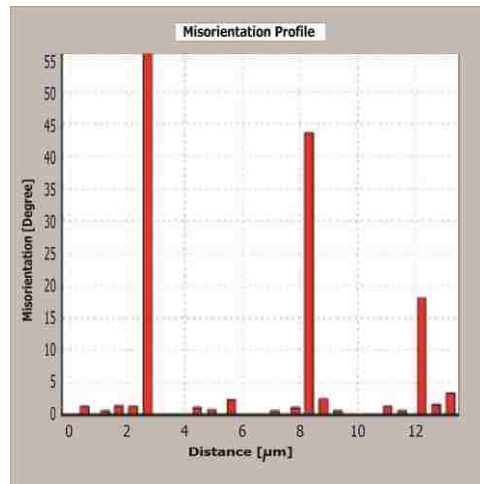
(a)



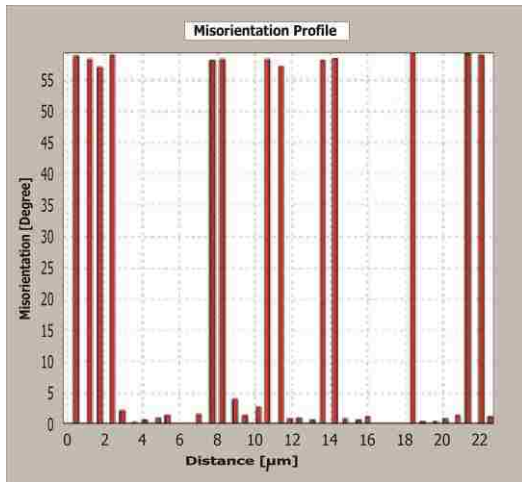
(b)



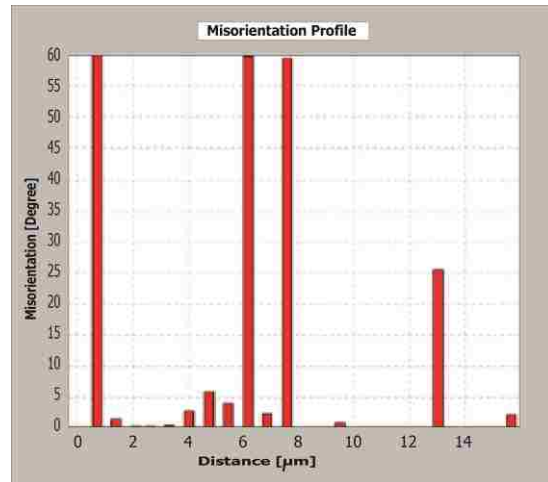
(c)



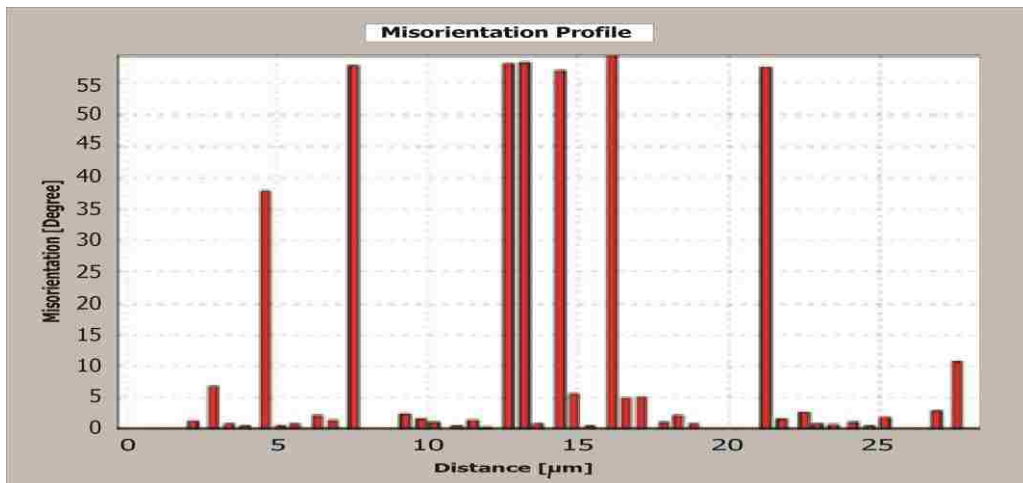
(d)



(e)



(f)



(g)

Figure 3.44 Misorientation angle measured along four different lines in the Impacted A36 steel, sample location 6-E after impact velocity of 5.80 km/sec: a) EBSD shows less noise, b) EBSD shows grains; c) Line 1, d) Line 2, e) Line 3, and f) Line 4 and g) line 5.

3.5.9 Misorientation Impact A36 steel at 5.80 km/sec Sample location 6-F

These photos show the Misorientation angles of a few areas on location D and all lines have some percentage of twinning and the angles between (55-60) degrees.

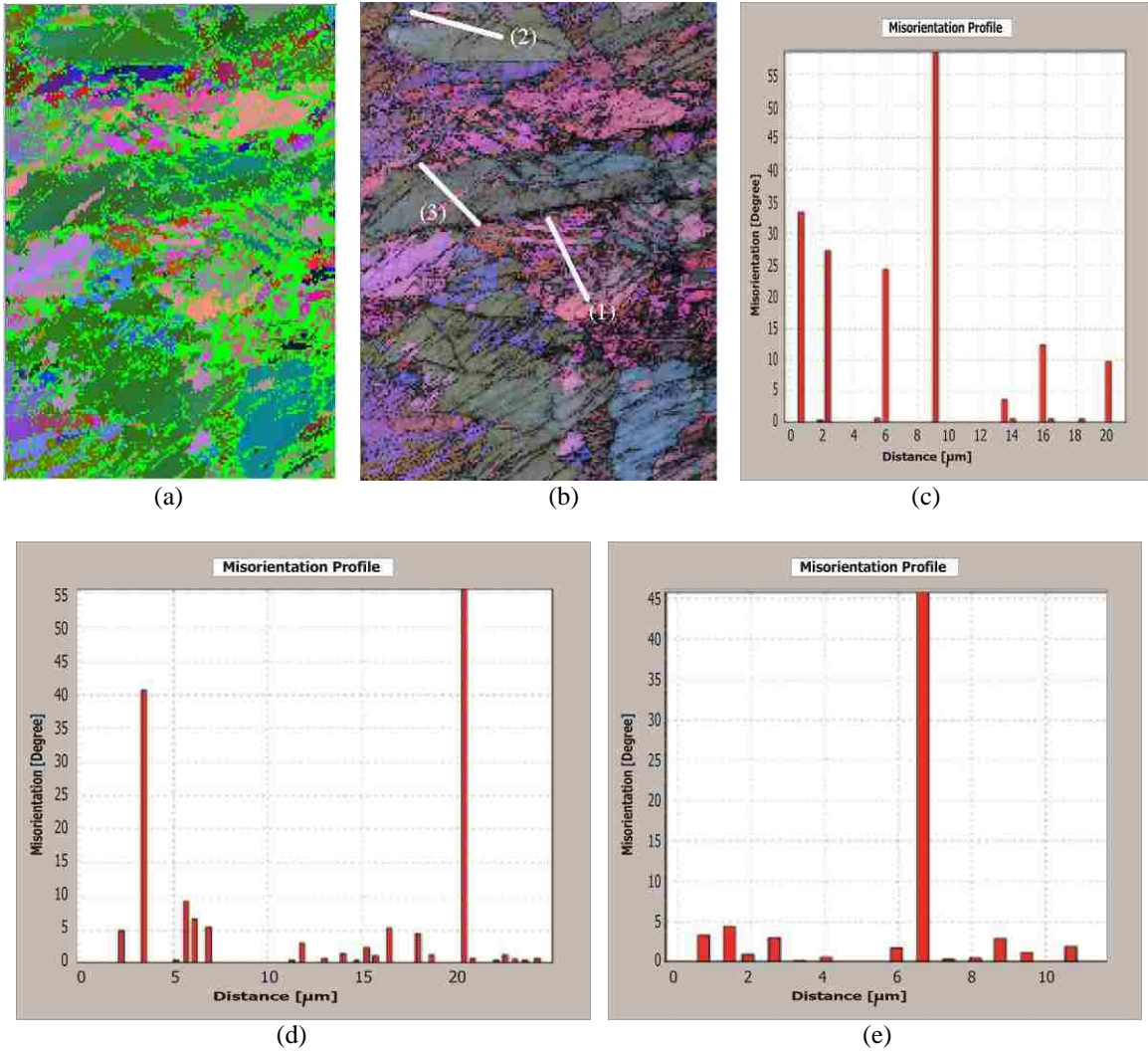


Figure 3.45 Misorientation angle measured along four different lines in the Impacted A36 steel, sample location 6-F after impact velocity of 5.80 km/sec: a) EBSD shows less noise, b) EBSD shows grains; c) Line 1, d) Line 2, and e) Line 3.

3.6 Experimental Grain Size Measurements

3.6.1 Impacted and non-impacted A36 steel material

Figure 3.46 shows the method used to calculate size of the grains in the A36 material. The diameters of different circuits were painted, the grain boundaries under each radius were calculated, and then the arithmetic average of the range of these radiuses was determined.



Figure 3.46 EBSD microscopy photos of A36 steel a) non-impact, b) A36 steel impact at 5.80 km/sec Sample locations 6-G.

$$\text{Grain size} = \frac{2\pi r}{n-1} \quad \dots\dots\dots 3.1$$

n: grains boundaries r: radius of circuit

At r = 40.5 μm n = 13

$$G.S = \frac{2 * \pi * 40.05 \mu m}{13 - 1}$$

$$G.S = 21.195 \mu m$$

To calculate the grains size of A36 steel has not been subjected to shock draw, circles samdiameters diffrend location at the same sample obtained from EBSD.Counting theboundaries grains in that area resulted in the arithmetic average grains size.In case the shock process is the toughest in the calculation of grain boundaries, because the shock effect makes smaller grains and crystals areformed plastically by the reaction of pregnancy and the so-called twinning.

3.6.2 A36 steel impact 5.80 km/sec

In case the shock process is the toughest in the calculation of grain boundaries, because the shock effect makes smaller grains and crystals areformed plastically by the reaction of creation and this so-called twinning.

At $r = 37.5\mu m$ $n = 63$

$$\text{Grain size} = \frac{2\pi r}{n-1}$$

$$G.S = \frac{2 * 3.14 * 37.5\mu m}{28 - 1}$$

$$G.S = 3.798\mu m$$

$$G.S = 3.80\mu m$$

CHAPTER 4

304L STEEL EXPERIMENTAL DATA

In this chapter, the results of microscopic examination of test samples are viewed. Examination of the prepared samples in the study depended on two kind of microscopy EBSD and XRD. The first one is used to find the unit cell of the crystal system and determine the phase percentage with microstructure maps of the grain and phase. The second one is used to measure the lattice parameters and the orientation. Figure 4.1 shows photographs of the 304L target plates before and after impact, along with the sample preparation cutting T-shaped geometry which is similar to the geometry used for the A36 targets.

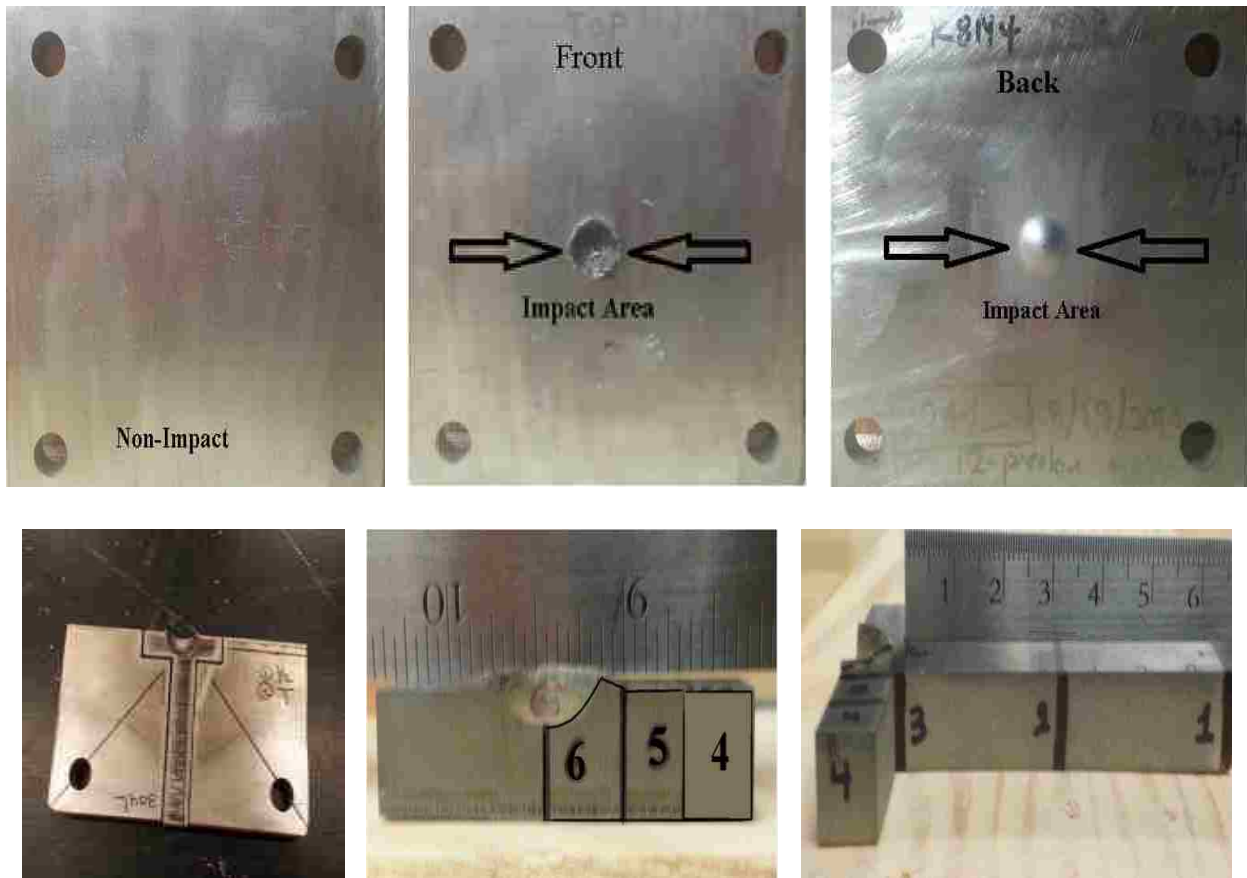


Figure 4.1 Non-impacts and Impact 30L steel and Impact at 6.58 km/sec

4.1 As Received 304L Steel (non-impact)

With 304L steel, the results show it has three phases BCC, FCC some small percentage of HCP as shown in figure 4.2 and table 4.1. The real phase of this kind of steel is BCC and FCC.

4.1.1 EBSD Grain Structure Phase Measurements

Figure 4.2 shows the grains boundary and the magnification of the microscopy 400X and the crystal orientation, with phase percentage ratio shown in Table 4.1.

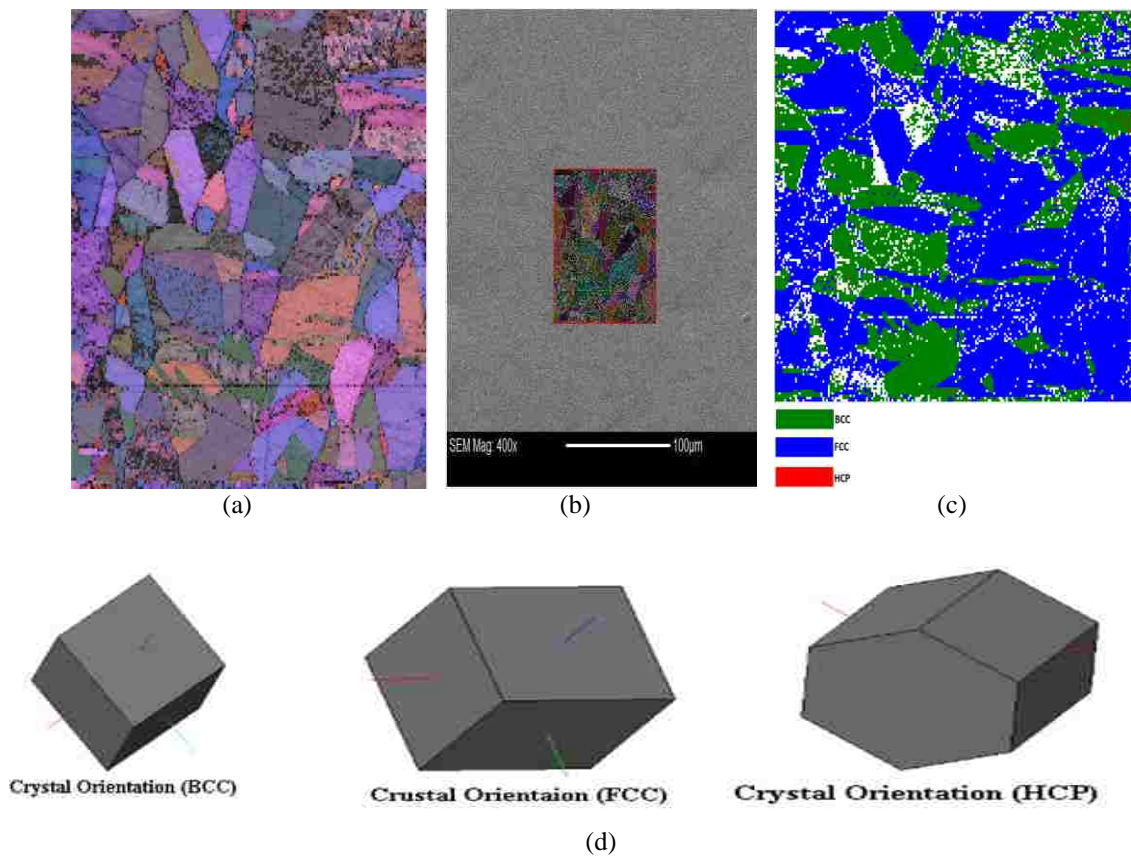


Figure 4.2 EBSD data from non-impact 304L steel, sample showing: a) grain, b) 400X magnification and the original length of the map, c) phase map, and d) crystal orientation.

Table 4.1 Non-Impact phase ratio of 304L steel

Crystal Unit Cell Structures	Non-Impact 304L Steel Phase
BCC	33.1092 %
FCC	66.718 %
HCP	0.1724 %

4.1.2 EBSD Misorientation Measurements Misorientation of Non-Impacted 304L Steel

304L steel is a heat resisting metal, the photos that show the state system and the Misorientation angles are between $(0-1.30^\circ)$ this means no orientation or dislocation in plan of the crystals

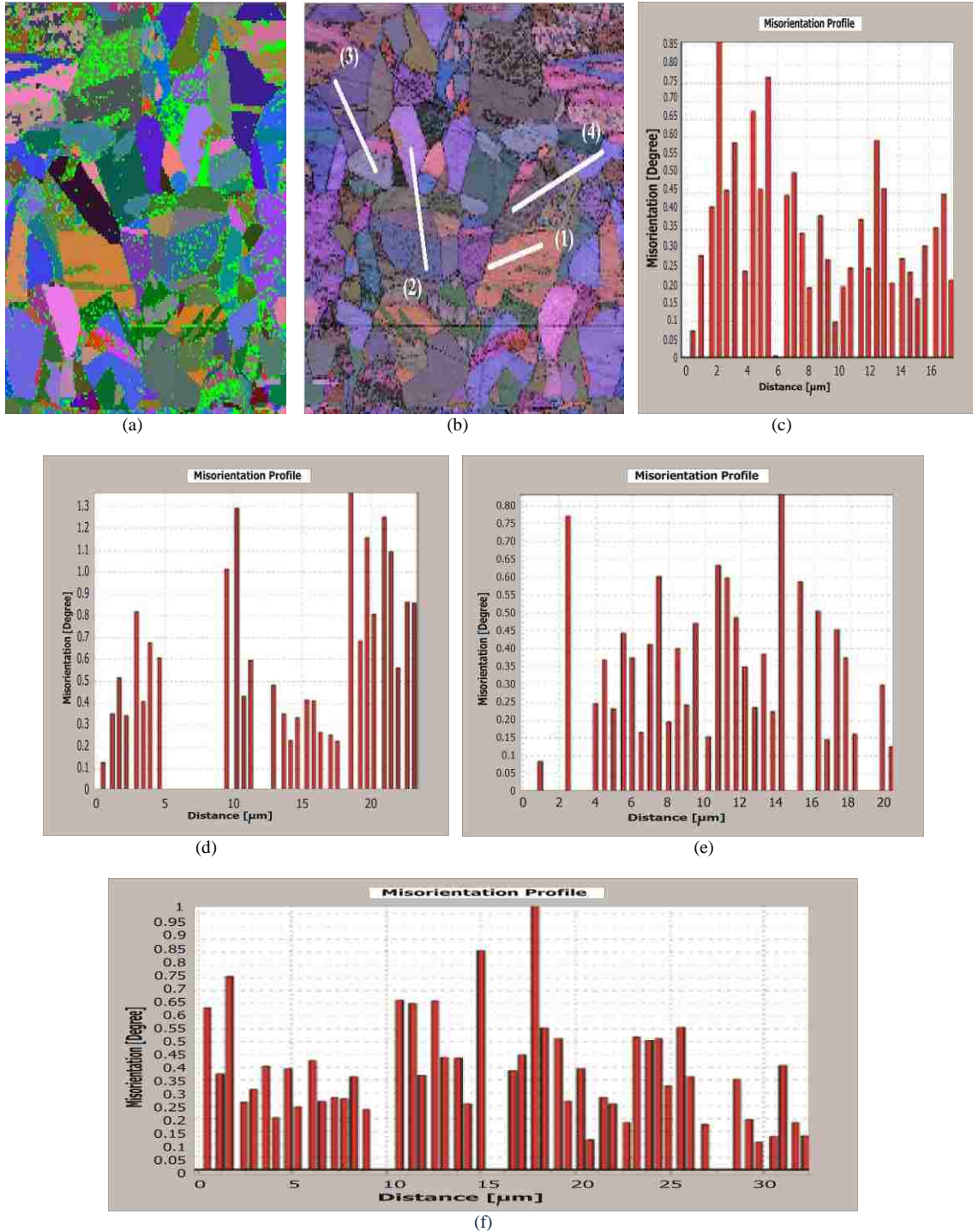


Figure 4.3 Misorientation angle measured along four different lines in the non-impacted 304L steel, sample shows: a) EBSD shows less noise, b) EBSD shows grains, c) Line 1, d) Line 2, e) Line 3, and f) Line 4.

4.1.3 Misorientation Impact 304L steel at 6.58 km/sec Sample location 6-A and 6-B

This kind of Iron alloys (304L) steel does not change its crystalline phase during impact shock under a high temperature and pressure. Through the pictures below note that 304L steel does not change in the phase of crystalline and the grained stable on the crystalline level, did not exceed the plastic limits or twinning deformation crystalline. This shows that this kind of Iron alloys is unimpaired when shocked under high pressure and temperature and has been the crater area test near crack Figures 4.4 and 4.5.

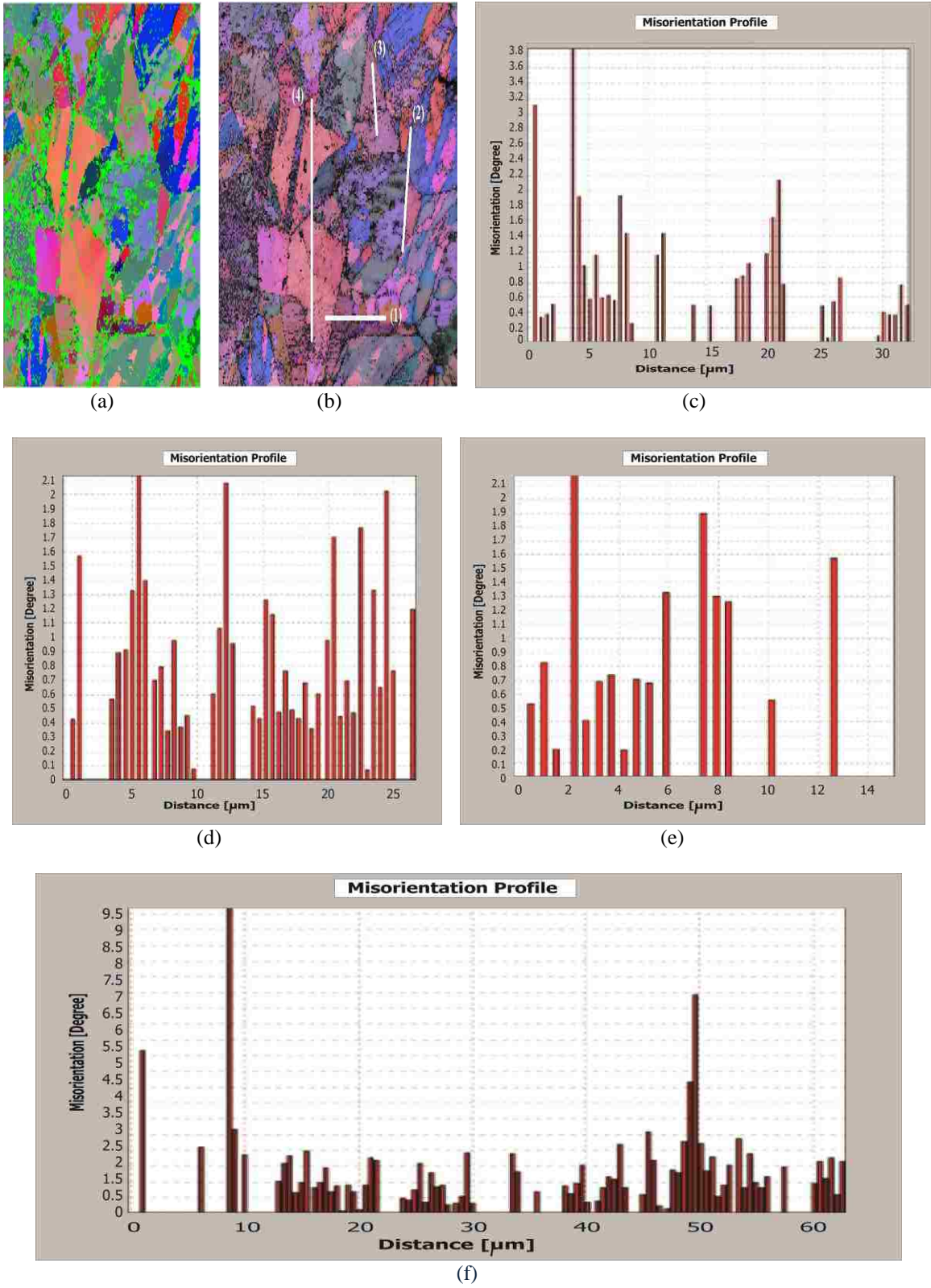


Figure 4.4 Misorientation angle measured along four different lines in the impacted 304L steel, sample location 6-A after impact velocity of 6.58 km/sec shows: a) EBSD shows less noise, b) EBSD shows grains, c, d, e, and f are the Lines (1, 2, 3, and 4) respectively.

Sample (6) location B

Figure 4.5 shows no change in phase in this location, the grain boundaries Misorientation angles still state (0-2.8) degrees and no new deformation starts in the crater sample, this means this kind of steel does not show any change under impact with phase crystal and deformation.

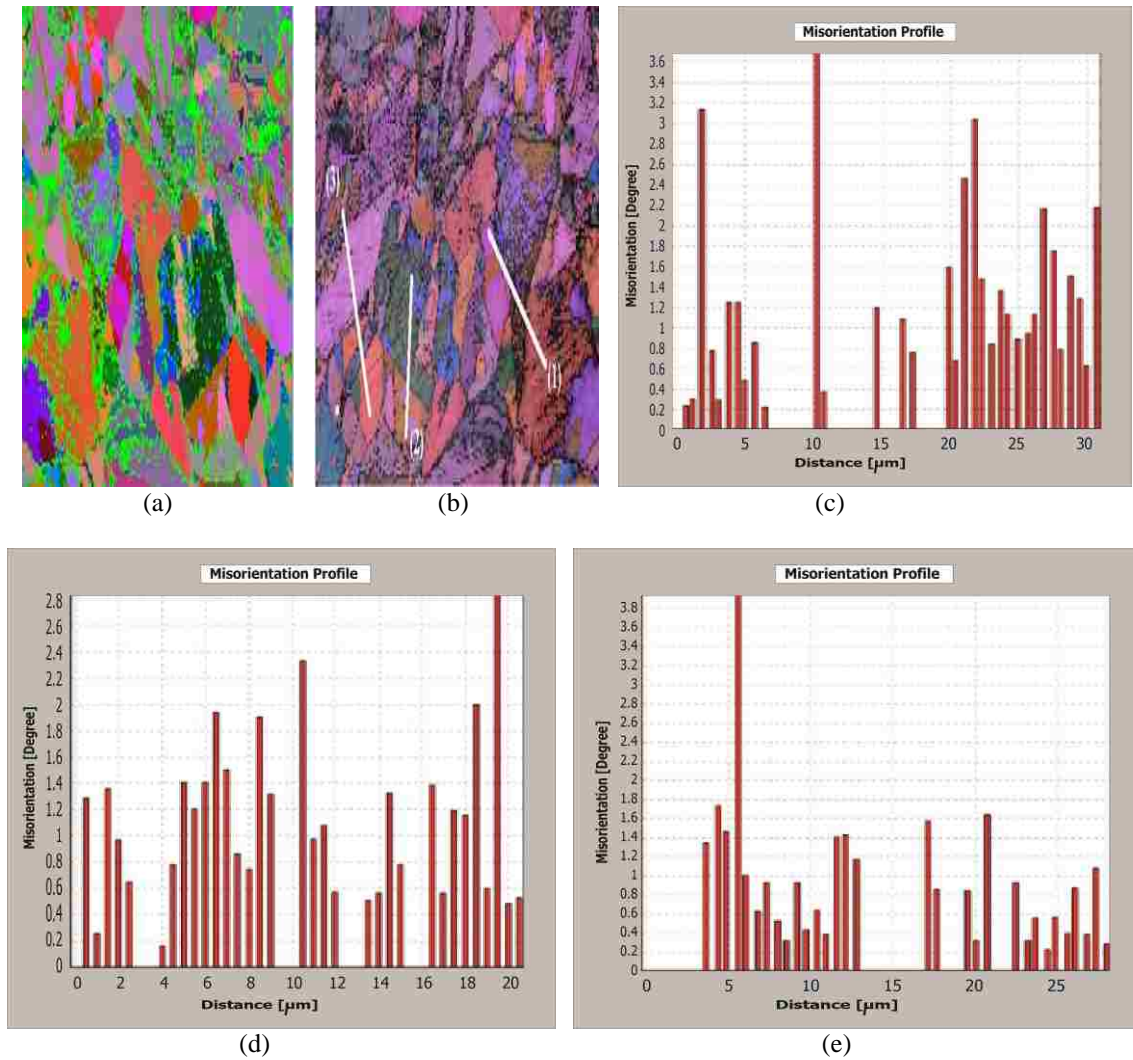
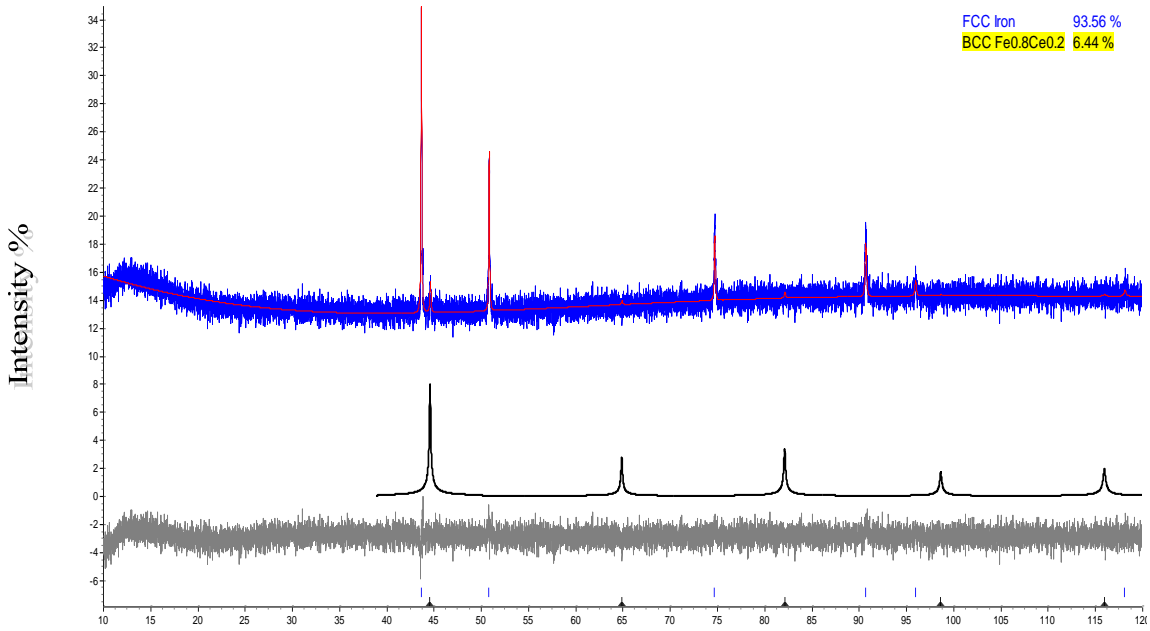


Figure 4.5 Misorientation angle measured along four different lines in the impacted 304L steel, sample location 6-B after impact velocity of 6.58 km/sec shows: a) EBSD shows less noise, b) EBSD grains, c) Line 1, d) Line 2, and e) Line 3.

4.1.4 XRD Lattice Parameter Measurements

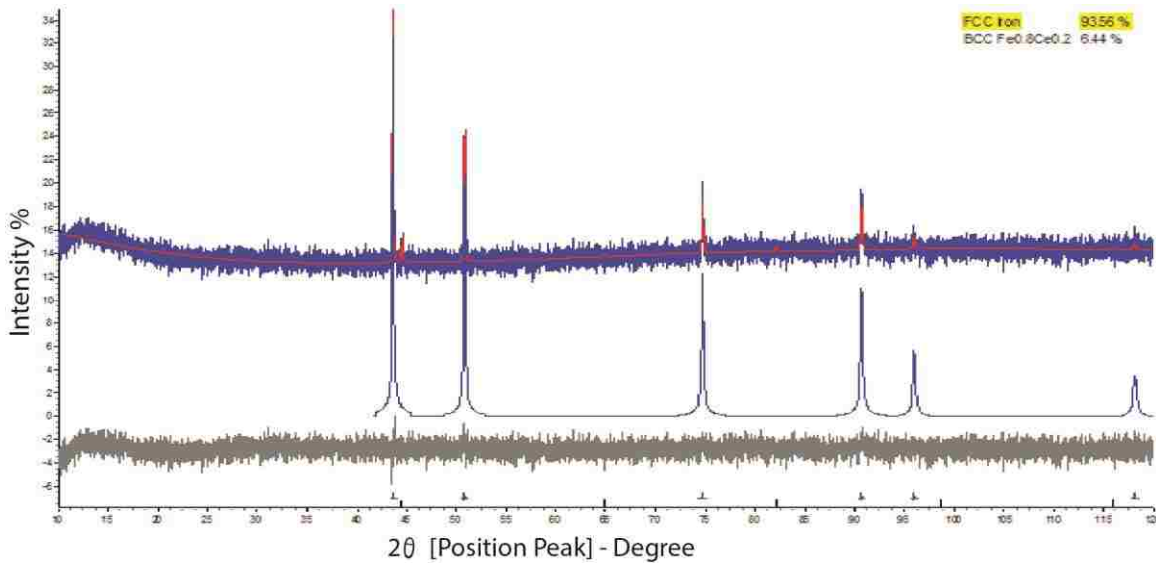
In the case of 304L steel, the predominant FCC phase of the non-impact sample is reduced and the BCC phase is increased on the impact sample.

4.1.4.1 Non-Impact 304L Steel



The peak show the BCC ratio is 6.44 %

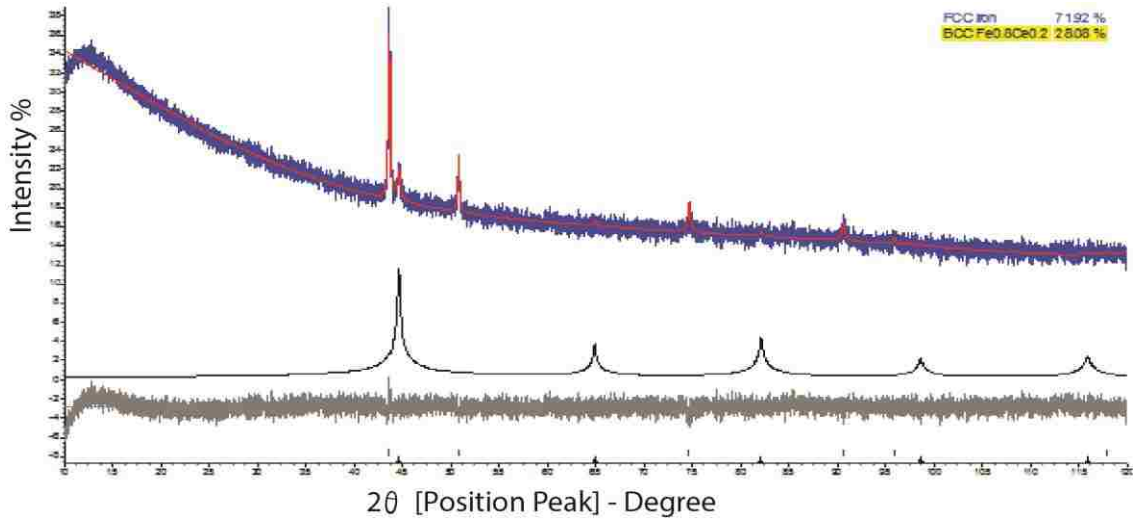
(a) BCC Fit



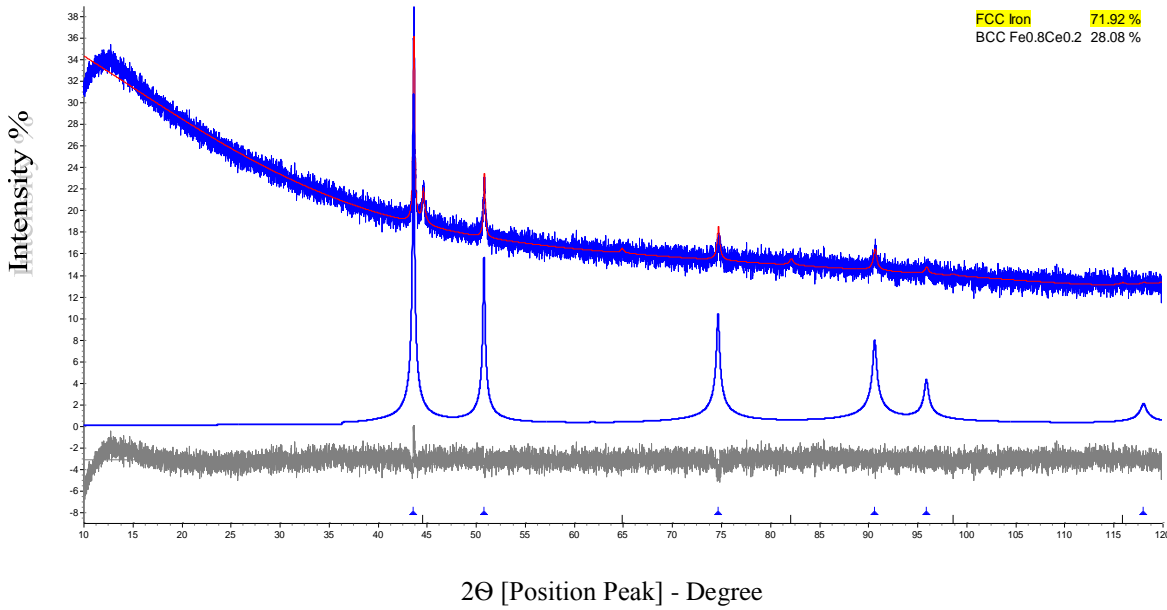
(b) FCC Fit

Figure 4.6 Non-impact 304L steel phase 1: FCC Iron 93.56 % phase 2: BCC Fe 0.8 Cr 0.2 6.44 % A is the peak fit with BCC, B is the peak fit with FCC.

4.1.4.2 Impact 304L at 6.58 km/sec



(a) BCC Fit



(b) FCC Fit

Figure 4.7 Impact 304L steel at 6.58 km/sec Phase 1: "FCC Iron" 72) % Phase 2: "BCC Fe 0.8 Ce 0.2" 28 %A is the peak fit with BCC, B is the peak fit with FCC

Table 4.2 304L-Lattice parameters and quantity for detectable phases

	BCC		FCC	
	Lattice Parameter.	Weight %	Lattice Parameter.	Weight %
Non-impact	2.873×10^{-10} m	6 %	3.593×10^{-10} m	94 %
Impact	2.874×10^{-10} m	28 %	3.594×10^{-10} m	72 %

BCC	Cell Mass (g)	Cell Volume (Å³)	Crystal Density g/cm³	Crystal Size (nm)	FCC	Cell Mass (g)	Cell Vol (Å³)	Crystal Size (nm)
Non-impact 304L	110.153	23.7162	7.7126	100(19)	Non-impact 304L	234.761	46.3714	8.4067
Impact 304L	110.153	23.744	7.7036	66(25)	Impact 304L	223.387	46.435	7.9884

4.2 Impact Velocity of 6.58 km/sec in 304L Steel

4.2.1 Cross-section Location 1-C (75 mm from impact center)

In this site sample 75 mm away from the crater, note in this picture that the 304L steel in this site was not affected, phase crystalline stayed the same, and did not shows any sign of the formation of the plastic or twinning. Figure 4.8 shows the EBSD microscopy data for location 1-C in the 304L steel target after an impact velocity of 6.58 km/sec. The figure shows the polished sample, grain, 400X magnification and the original length of the map, and the phase distribution.

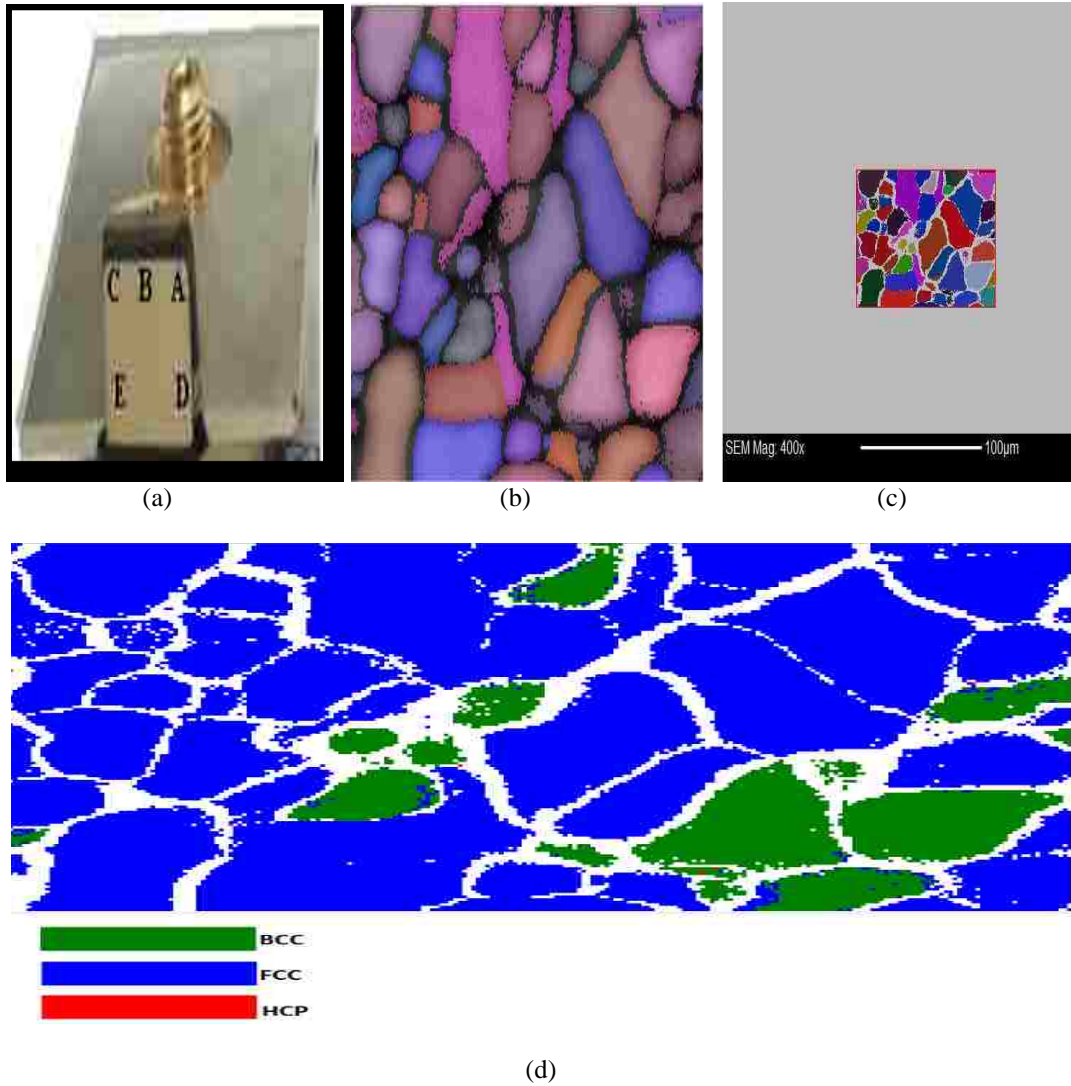


Figure 4.8 EBSD data from 304L steel, sample location 1-C, after impact velocity of 6.58 km/sec showing: a) polished sample, b) grain, c) 400X magnification and the original length of the map, and d) phase map.

Table 4.3 Impact phase ratio of 304L steel at 6.58 km/sec sample location 1-C

Crystal Unit Cell Structures	Impact 304L Steel Phase at 6.58 km/sec
BCC	16.340 %
FCC	83.64 %
HCP	0.0188 %

4.2.2 Cross-section Location 2-A (35 mm from impact center)

Figure 4.9 shows the EBSD microscopy data for location 2-A in 304L steel target after an impact velocity of 6.58 km/sec. The figure shows the polished sample, grain, 400X magnification and the original length of the map, and the phase distribution. Table 4.4 lists the Impact phase ratio of 304L steel at 6.58 km/sec sample location 2-A.

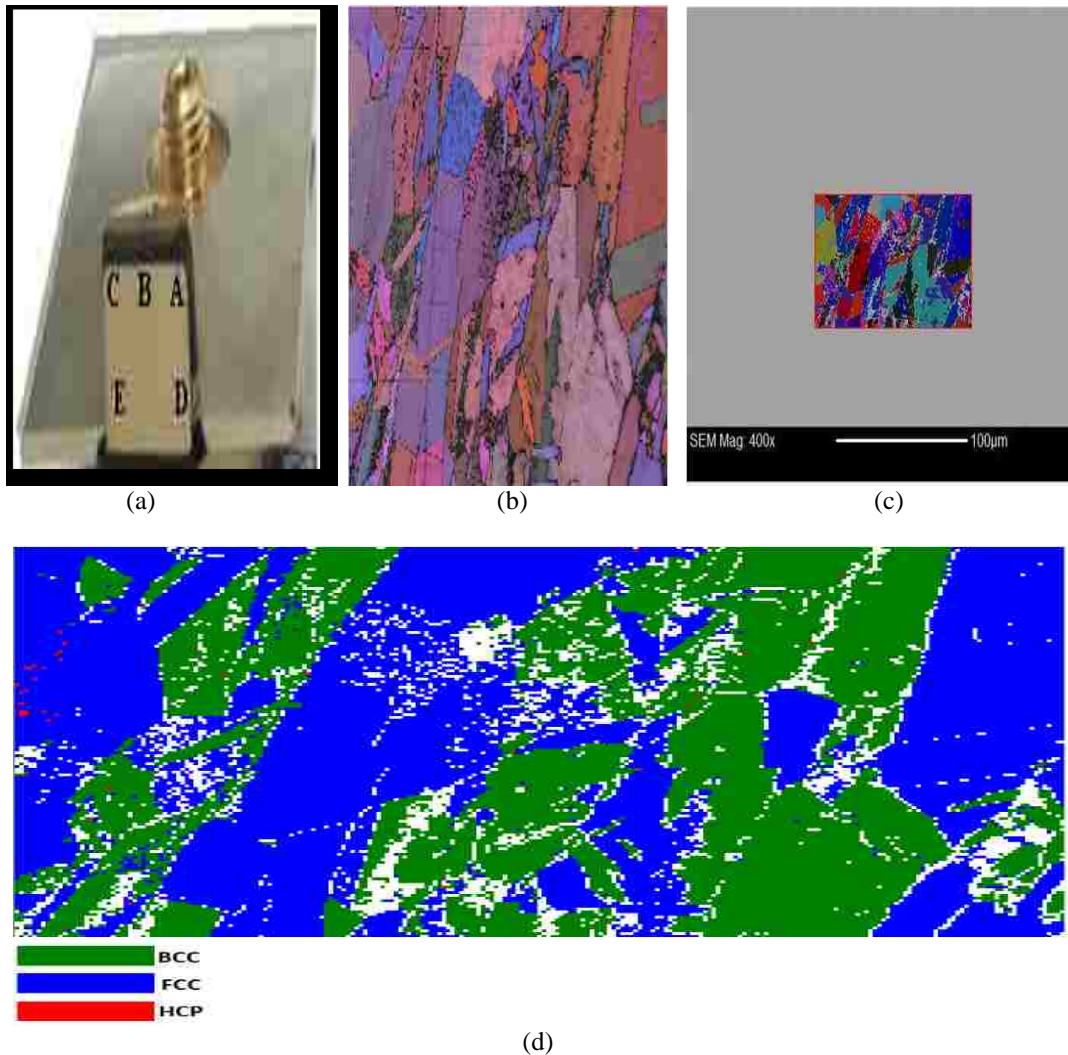


Figure 4.9 EBSD data from 304L steel, sample location 2-A, after impact velocity of 6.58 km/sec showing: a) polished sample, b) grain, c) 400X magnification and the original length of the map, and d) phase map.

Table 4.4 Impact phase ratio of 304L steel at 6.58 km/sec sample location 2-A

Crystal Unit Cell Structures	Impact 304L Steel Phase at 6.58 km/sec
BCC	44.045 %
FCC	55.84 %
HCP	0.1223 %

4.2.3 Cross-section Location 3-A (7.5 mm from impact center)

Figure 4.10 shows the EBSD microscopy data for location 3-A in 304L steel target after an impact velocity of 6.58 km/sec. The figure shows the polished sample, grain, 400X magnification and the original length of the map, and the phase distribution. Table 4.5 lists Impact phase ratios of 304L steel at 6.58 km/sec sample location 3-A.

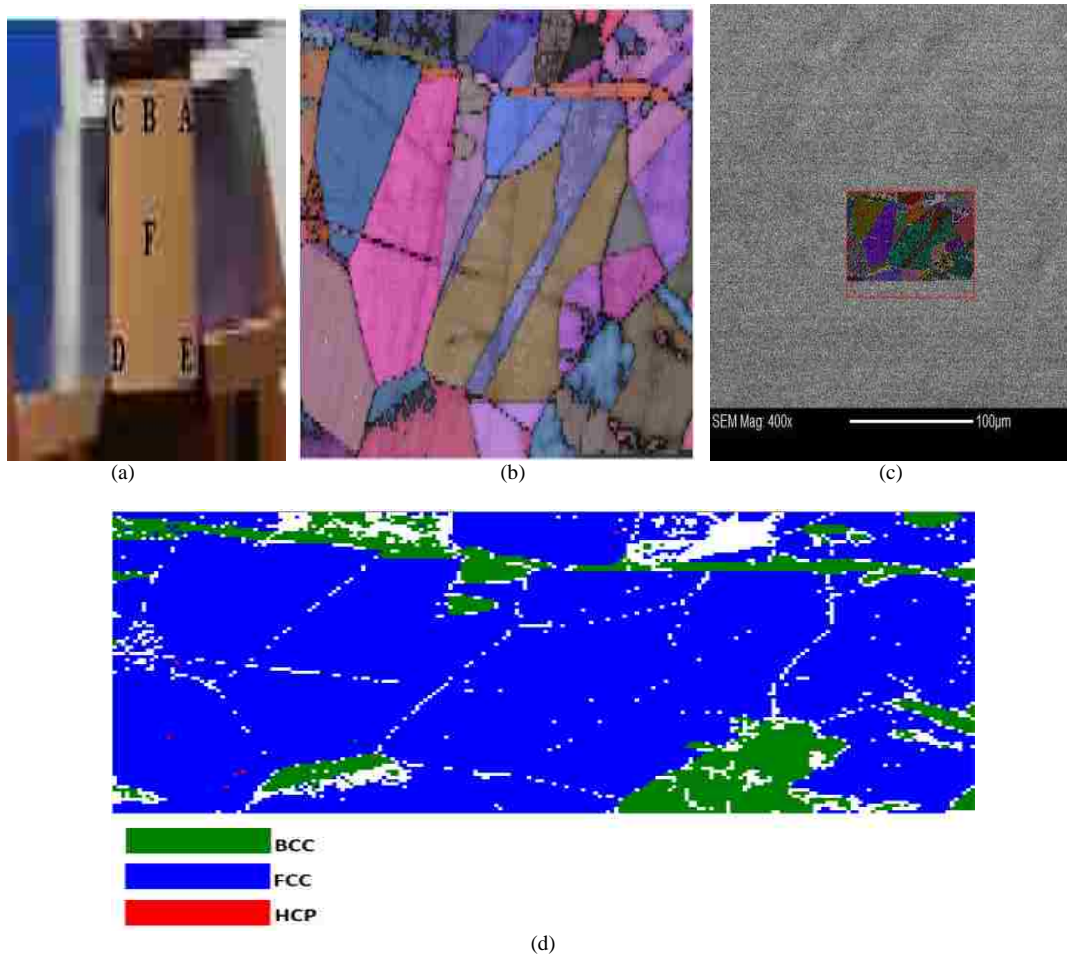


Figure 4.10 EBSD data from 304L steel, sample location 3-A, after impact velocity of 6.58 km/sec showing: a) polished sample, b) grain, c) 400X magnification and the original length of the map, and d) phase map.

Table 4.5 Impact phase ratio of 304L steel at 6.58 km/sec sample location 3-A

Crystal Unit Cell Structures	Impact 304L Steel Phase at 6.58 km/sec
BCC	12.54 %
FCC	87.599 %
HCP	0.221 %

4.2.4 Cross-section Location 4-D (20 mm from impact center)

Figure 4.11 shows the EBSD microscopy data for location 4-D in 304L steel sample after an impact velocity of 6.58 km/sec, it shows the polished sample, grain, 400X magnification and the original length of the map, and the phase distribution. This site, which is near for the crater, is still a large-grained Photomicrograph showing no change in the crystal face or any semblance of plastic deformation. Table 4.6 shows the percentage of each phase of the crystal.

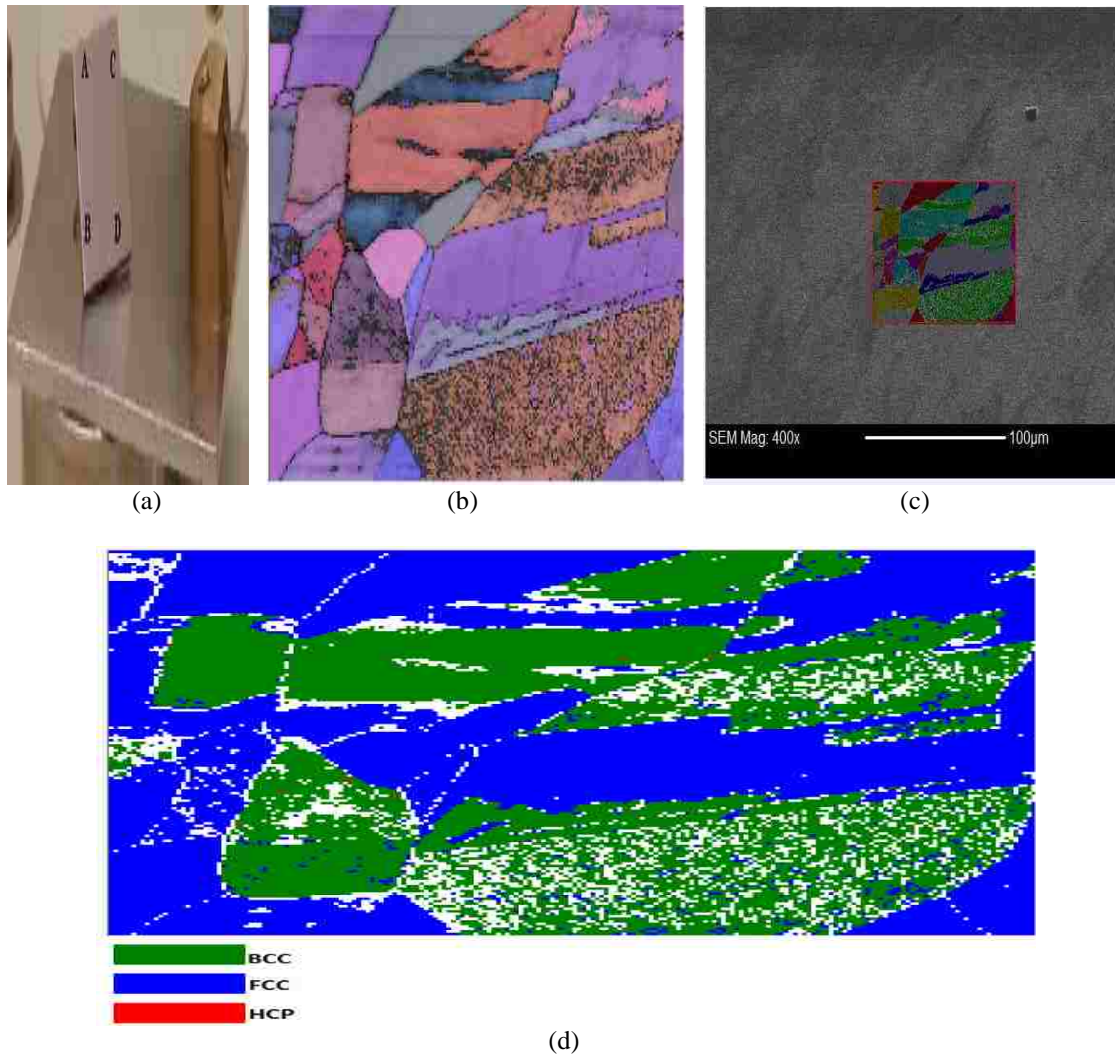


Figure 4.11 EBSD data from 304L steel, sample location 4-D, after impact velocity of 6.58 km/sec showing: a) polished sample, b) grain, c) 400X magnification and the original length of the map, and d) phase map.

Table 4.6 Impact phase ratio of 304L steel at 6.58 km/sec sample location 4-D

Crystal Unit Cell Structures	Impact 304L Steel Phase at 6.58 km/sec
BCC	46.2524 %
FCC	53.9614 %
HCP	0.281 %

4.2.5 Cross-section Location 5-D (10 mm from impact center)

Figure 4.12 shows the EBSD microscopy data for location 3-A in the 304L steel target after an impact velocity of 6.58 km/sec. The figure shows the polished sample, grain, 400X magnification and the

original length of the map, and the phase distribution.. Table 4.7 lists the Impact phase ratio of 304L steel at 6.58 km/sec sample location 5-D. This photo shows that a one grain boundary is 100 % HCP.

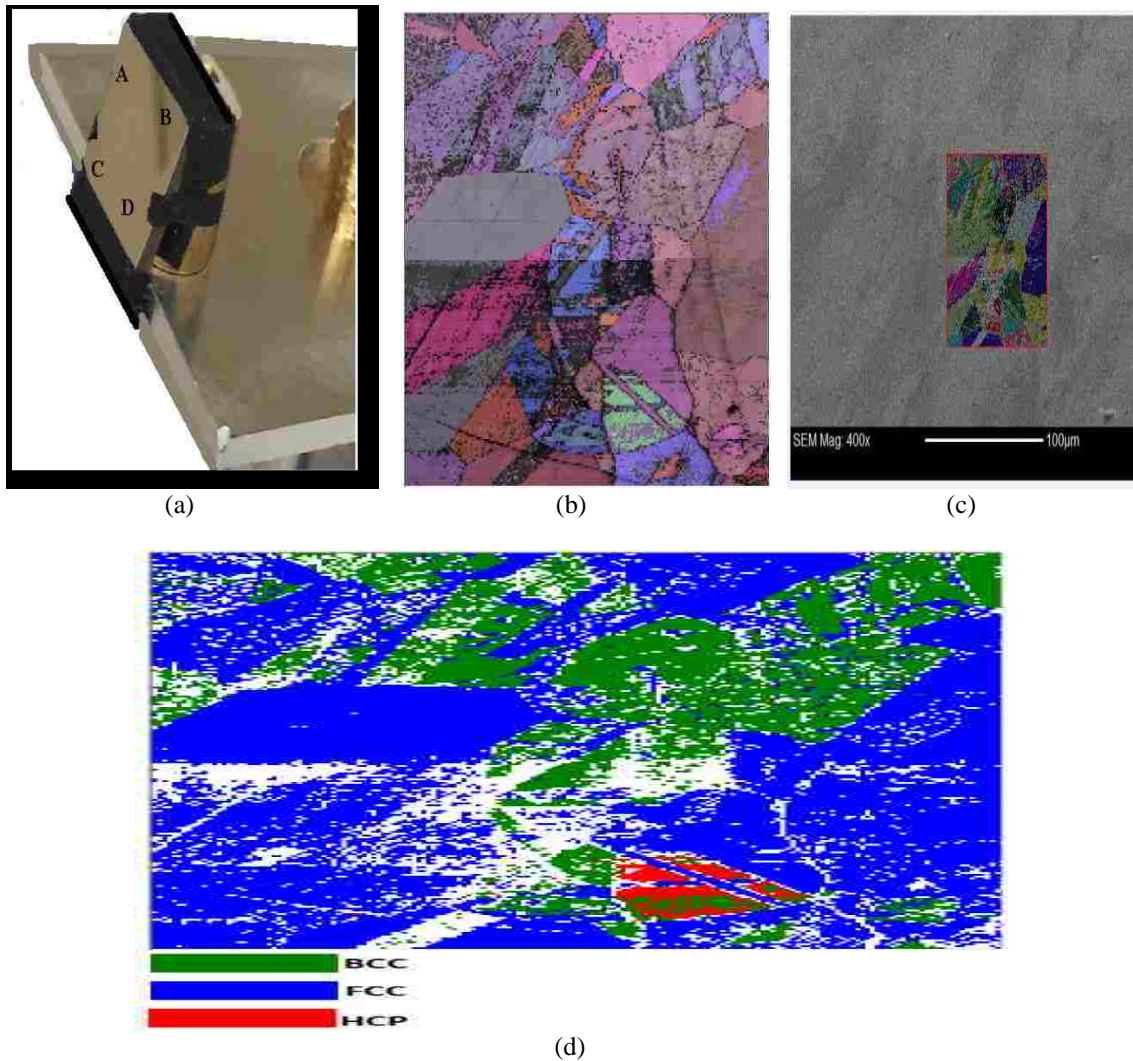


Figure 4.12 EBSD data from 304L steel, sample location 5-D, after impact velocity of 6.58 km/sec showing: a) polished sample, b) grain, c) 400X magnification and the original length of the map, and d) phase map.

Table 4.7 Impact phase ratio of 304L steel at 6.58 km/sec sample location 5-D

Crystal Unit Cell Structures	Impact 304L Steel Phase at 6.58 km/sec
BCC	27.308 %
FCC	71.047 %
HCP	1.644 %

4.2.6 Cross-section Location 6-A (0 mm from impact center)

Figure 4.13 shows the EBSD microscopy data for location 6-A in 304L steel target after an impact velocity of 6.58 km/sec. The figure shows the polished sample, grain, 400X magnification and the original length of the map, and the phase distribution. Although the location is close to the vicinity of arc shot but the image of EBSD microscope became apparent and did not show any change in the particle size or the presence of any form of plasticity. This means that the alloy was not affected by the shock under a high-temperature and a high-pressure.

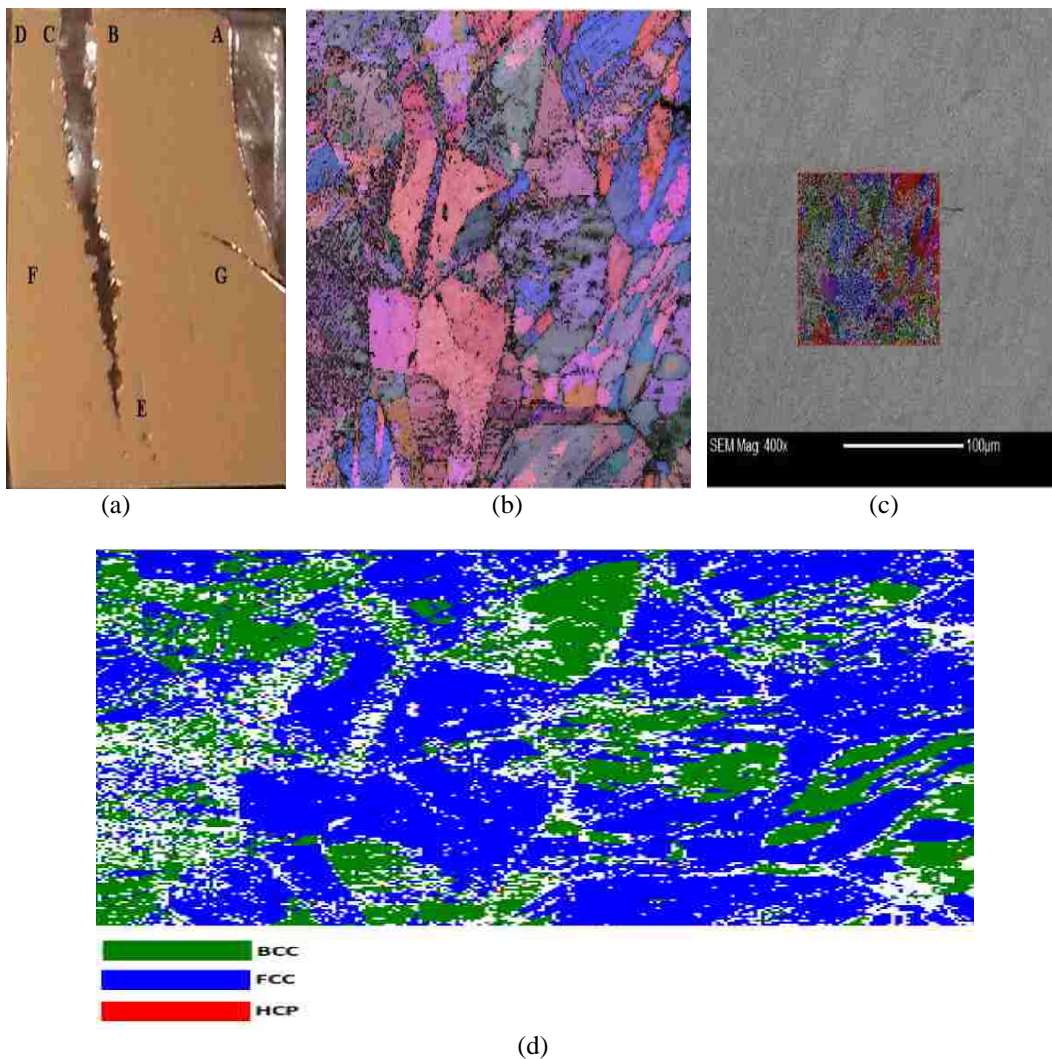


Figure 4.13 EBSD data from 304L steel, sample location 6-A, after impact velocity of 6.58 km/sec showing: a) polished sample, b) grain, c) 400X magnification and the original length of the map, and d) phase map.

Table 4.8 Impact phase ratio of 304L steel at 6.58 km/sec sample location 6- A

Crystal Unit Cell Structures	Impact 304L Steel Phase at 6.58 km/sec
BCC	32.7754 %
FCC	68.67 %
HCP	1.699 %

4.2.7 Cross-section Location 6-B (0 mm from impact center)

Figure 4.14 shows the EBSD microscopy data for location 3-A in 304L steel target after an impact velocity of 6.58 km/sec. The figure shows the polished sample, grain, 400X magnification and the original length of the map, and the phase distribution. Table 4.9 lists the Impact phase ratios of 304L steel at 6.58 km/sec sample location 6-B.

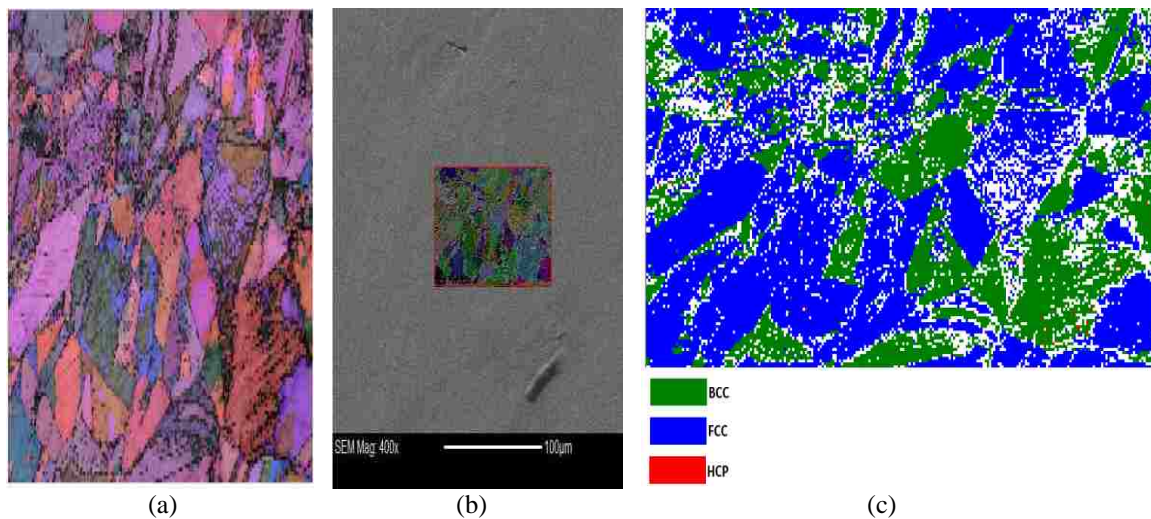


Figure 4.14 EBSD data from 304L steel, sample location 6-B, after impact velocity of 6.58 km/sec showing: a) grain, b) 400X magnification and the original length of the map, and c) phase map.

Table 4.9 Impact phase ratio of 304L steel at 6.58 km/sec sample location 6-B

Crystal Unit Cell Structures	Impact 304L Steel Phase at 6.58 km/sec
BCC	34.0440 %
FCC	65.765 %
HCP	0.1907 %

4.2.8 Cross-section Location 6-C (0 mm from impact center)

Figure 4.15 shows the EBSD microscopy data for location 6-C in 304L steel target after an impact velocity of 6.58 km/sec. The figure shows the polished sample, grain, 400X magnification and the original length of the map, and the phase distribution. No significant or dramatic changes occurred post-impact of 304L steel under this high speed of impact. The low percentage of error and higher confidence at this location will be discussed in chapter 6 and 7.

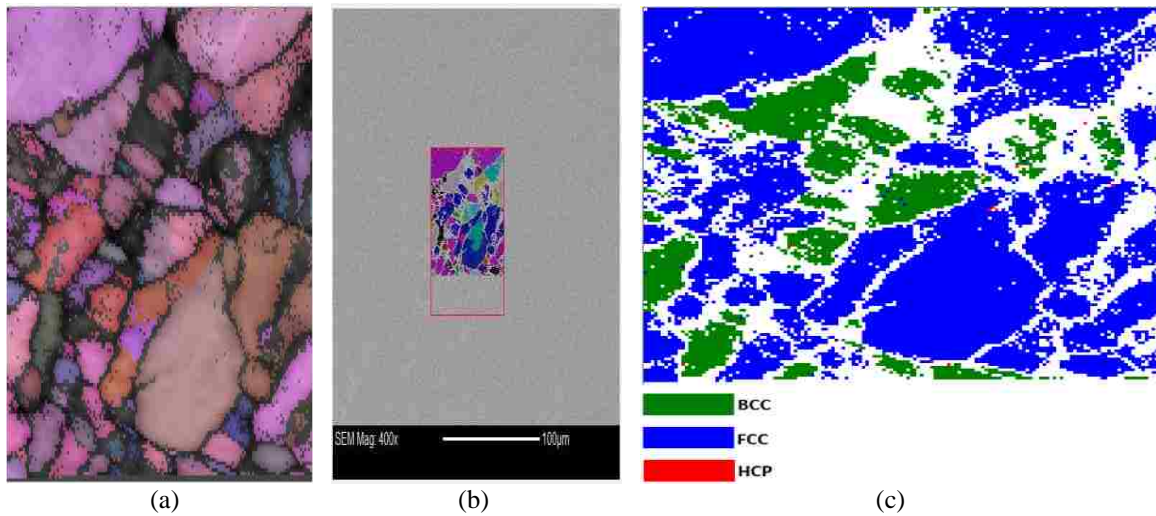


Figure 4.15 EBSD data from 304L steel, sample location 6-C after impact velocity of 6.58 km/sec showing: a) grain, b) 400X magnification and the original length of the map, and c) phase map.

Table 4.10 Impact phase ratio of 304L steel at 6.58 km/sec sample location 6-C

Crystal Unit Cell Structures	Impact 304L Steel Phase at 6.58 km/sec
BCC	22.579 %
FCC	77.328 %
HCP	0.092 %

4.2.9 Cross-section Location 6-E (0 mm from impact center)

Figure 4.16 shows the EBSD microscopy data for location 6-E in 304L steel target after an impact velocity of 6.58 km/sec. The figure shows the polished sample, grain, 400X magnification and the original length of the map, and the phase distribution. No significant or dramatic changes occurred post-impact 304L steel under this high speed of impact. Although the lowest impact had an effect of A36 steel, let alone an even more effect on the HY100 steel, the existence of FCC having significantly a high percentage, have affected the results. Before impact (BCC and FCC), since FCC is a transitional phase before transfer and reaches the hexagonal HCP phase. This is the reason the percentage of FCC is high through all locations of samples of 304L. The reason for the selection sample 6 locations C because the low percentage of error and higher confidence as illustrated and discuss in chapter 6 and 7.

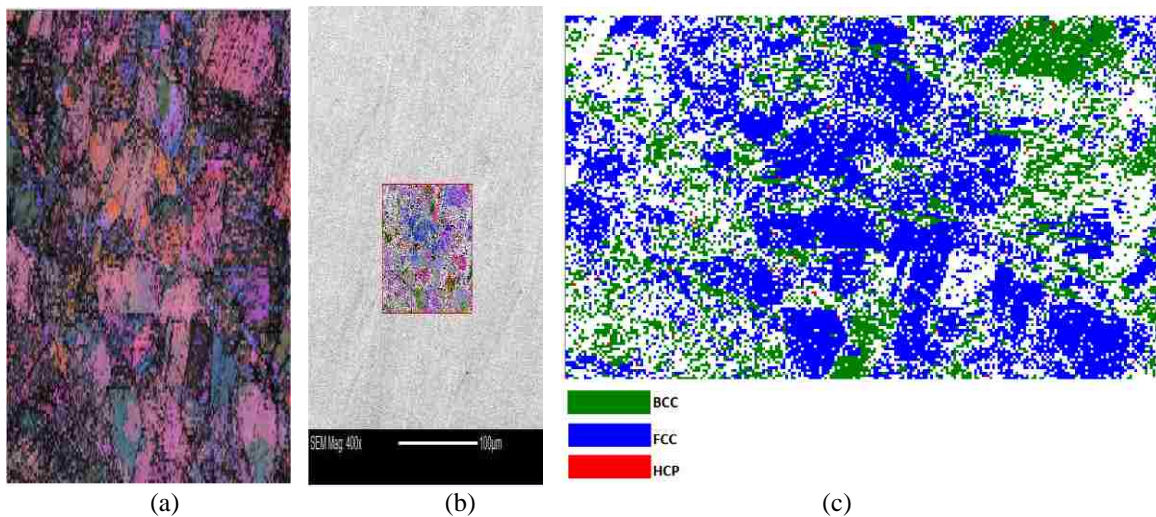


Figure 4.16 EBSD data from 304L steel, sample location 6-E, after impact velocity of 6.58 km/sec showing: a) grain, b) 400X magnification and the original length of the map, and c) phase map.

Table 4.11 Impact phase ratio of 304L steel at 6.58 km/sec sample location 6-E

Crystal Unit Cell Structures	Impact 304L Steel Phase at 6.58 km/sec
BCC	34.853 %
FCC	65.233 %
HCP	0.231 %

4.3 Experimental Grain Size Measurements

4.3.1 Non-impact 304L steel

This type of iron alloy was not affected by shock, although the speed was 6.58 km/sec, the observation of 304L steel shows that the grain size after the shock has still steady and significant regions that have been holding these accounts. It was calculated under XRD X-ray diffraction as shown in this chapter.

All results show that 304L does not change during impact.

At $r = 35.5\mu\text{m}$ $n = 17$

$$\text{Grain size} = \frac{2\pi r}{n-1}$$

$$G.S = \frac{2 * 3.14 * 35.5\mu\text{m}}{17 - 1}$$

$$G.S = 13.934\mu\text{m}$$

$$G.S \text{ average} = 13.40\mu\text{m}$$

4.3.2 304L steel impact at 6.58 km/sec

Account did not notice a significant change in grains size in 304L steel since before impact was 4.60mm and after impact it was 5.27mm.

At $r = 35.5\mu\text{m}$ $n = 44$

$$\text{Grain size} = \frac{2\pi r}{n-1}$$

$$G.S = \frac{2 * 3.14 * 35.5\mu\text{m}}{44 - 1}$$

$$G.S = 5.18465 \mu\text{m}$$

$$G.S \text{ average} = 5.12 \mu\text{m}$$

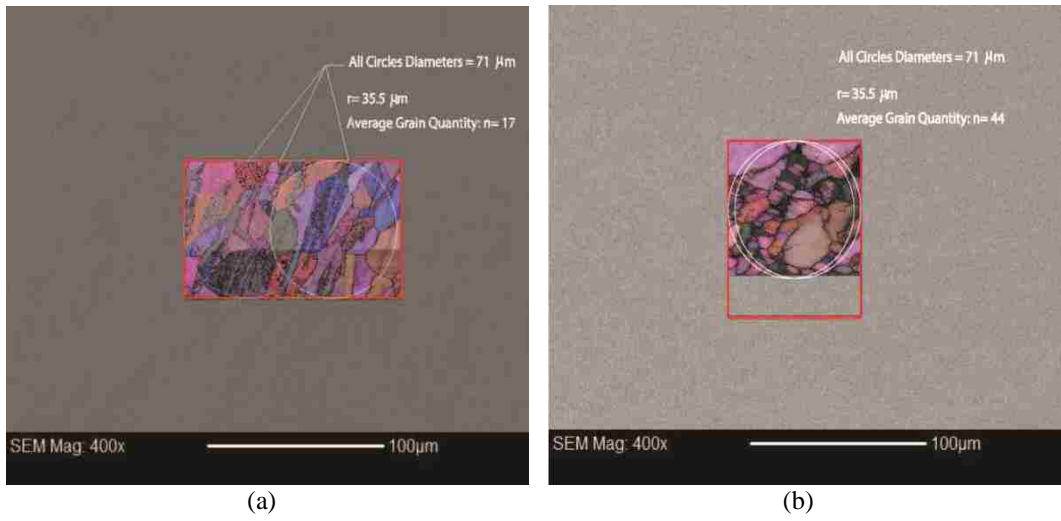


Figure 4.17 Experimental Grain Size Measurements 304L steel a) non-Impact, b) impact at 6.58 km/sec.

CHAPTER 5

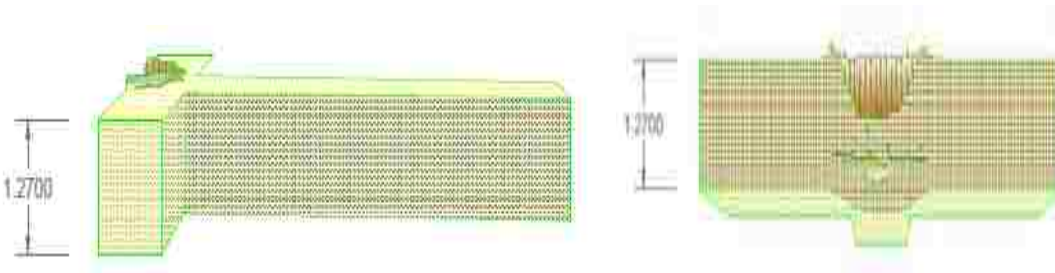
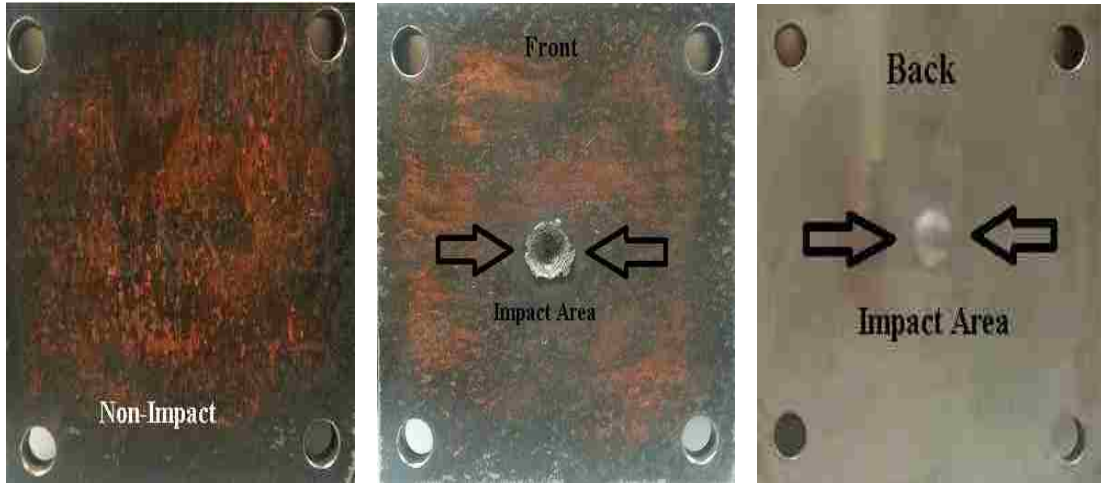
HY100 STEEL EXPERIMENTAL DATA

5.1 HY100 Steel (Non-Impact Loading)

In the fifth chapter will examine and consider some samples of the alloy HY100 and take samples near and far from the crater and examine under two types of electron microscopes EBSD and XRD and observe if this type of alloy is affected by shock under high pressure and temperatures.

5.1.1 EBSD Grain Structure Phase Measurements

Figure 5.1 shows photographs of the HY100 target plates before and after impact at 6.70 km/sec, along with the sample preparation cutting T-shaped geometry which is similar to the geometry used for the A36 targets. Figure 5.1-B, C, D, D, and E shows the polished sample, grain, 400X magnification and the original length of the map, the phase distribution, and crystal orientation of non-Impact HY100 steel. Table 5.1 shows the phase percentage ratios.



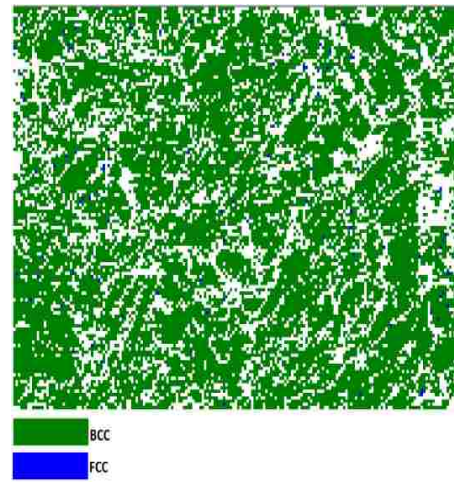
(a)



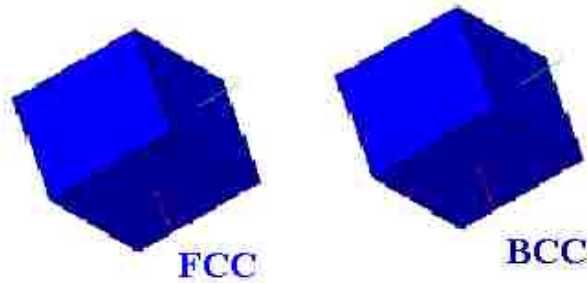
(b)



(c)



(d)



(e)

Figure 5.1 A shows photographs of the HY100 target plates before and after impact at 6.70 km/sec and T-shaped geometry. b) EBSD data from non-impact HY100 steel, sample showing: grain, c) 400X magnification and the original length of the map, d) phase map, and e) crystal orientation.

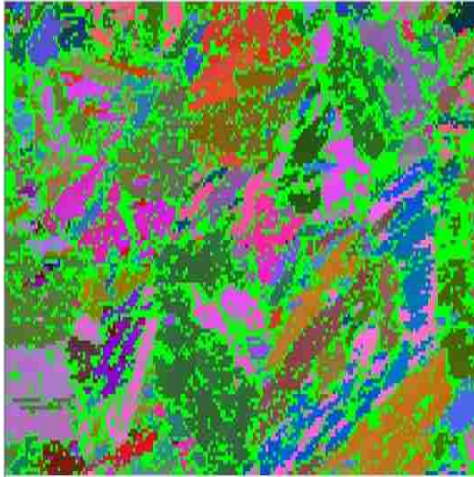
Table 5.1 Non- Impact phase ratio of HY100 steel

Crystal Unit Cell Structures	Non-Impact HY100 Steel
BCC	99.78 %
FCC	0.22 %
HCP	0 %

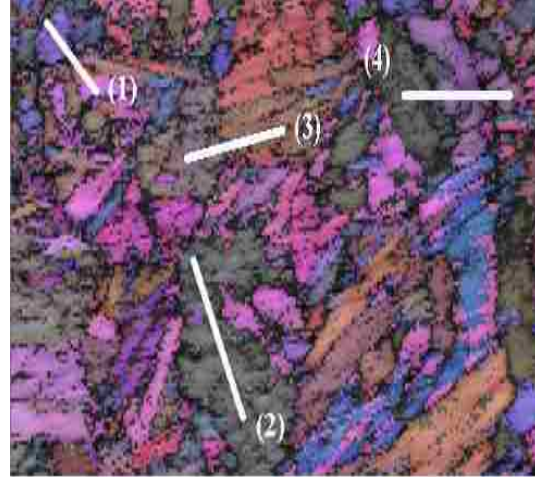
5.1.2 EBSD Misorientation Measurements

5.1.2.1 EBSD Non-Impact HY100 Misorientation Measurements

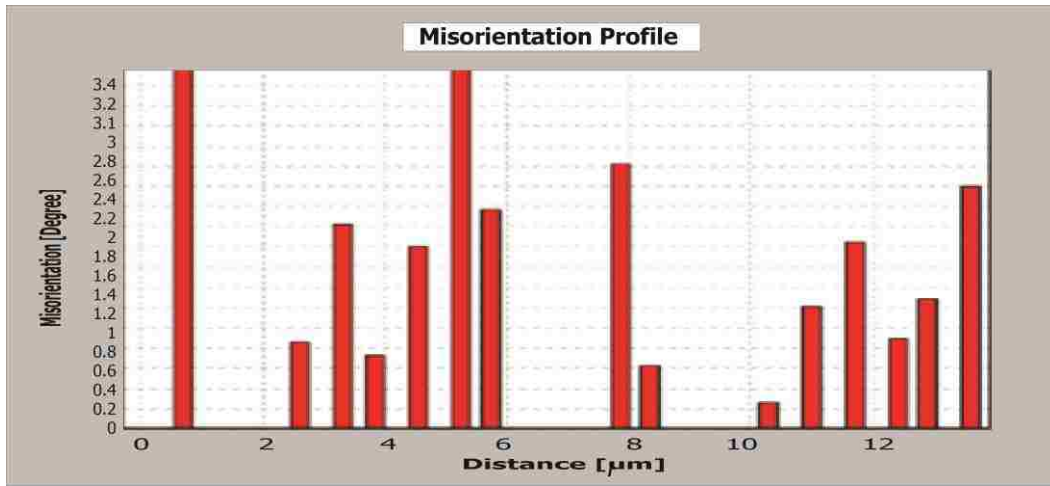
Figure 5.2 explain the Misorientation angle measured along four different lines in the non-impacted HY100 steel, when transition and change locations of the grains inside the crystal of non-Impact HY100 steel were examined before the shock, the angle ranging is (0-4.5) degrees. This is because the crystal system and stable raw material were not exposed to any load.



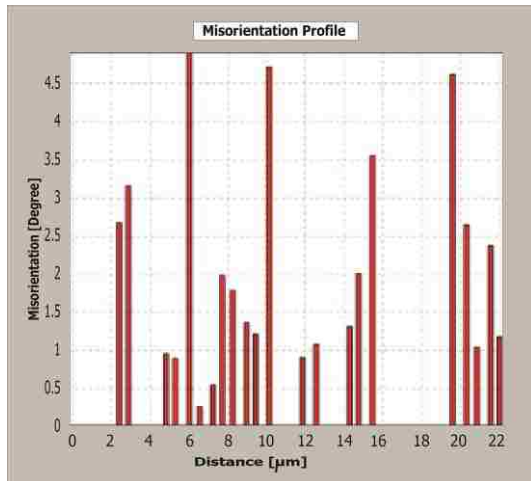
(a)



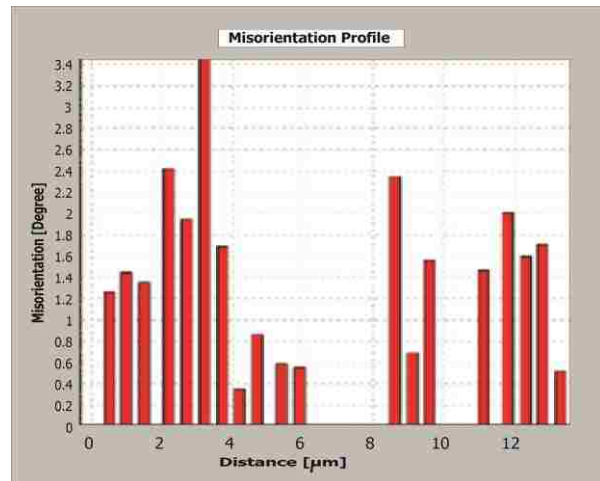
(b)



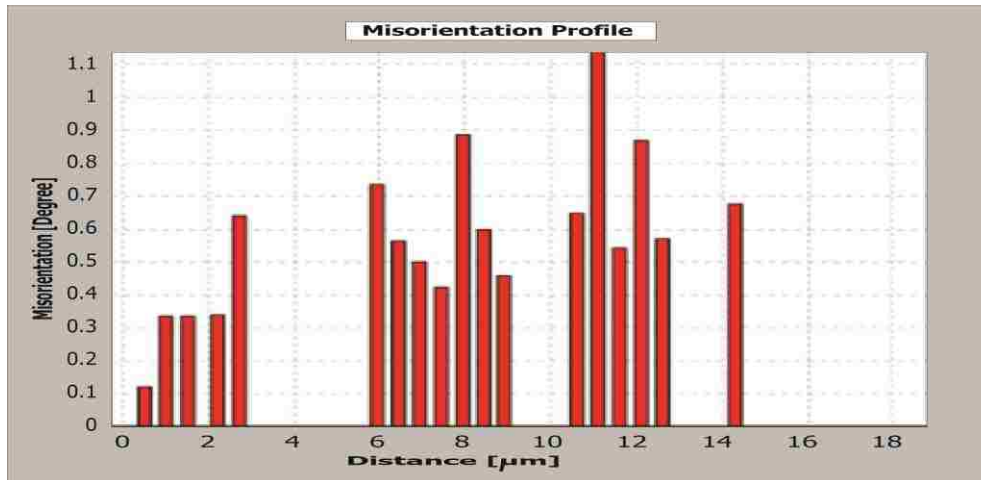
(c)



(d)



(e)



(f)

Figure 5.2 Misorientation angle measured along four different lines in the non-impacted HY100 steel, sample shows: a) EBSD shows less noise, b) EBSD shows grains, c) Line 1, d) Line 2, e) Line 3, and f) Line 4.

5.1.2.2 Misorientation Impact HY100 Steel at 6.70 km/sec Sample Location 6-B, C, E, F and G

Sample (6) location B

Figure 5.3 shows Misorientation angle measured along three different lines in impacted HY100 steelsample at 6.70 km/sec, the Misorientation angle of the crater is between 55-60 degrees, the plastic deformation is deformed and the grains dislocated the plane to another plane as a twinning deformation.

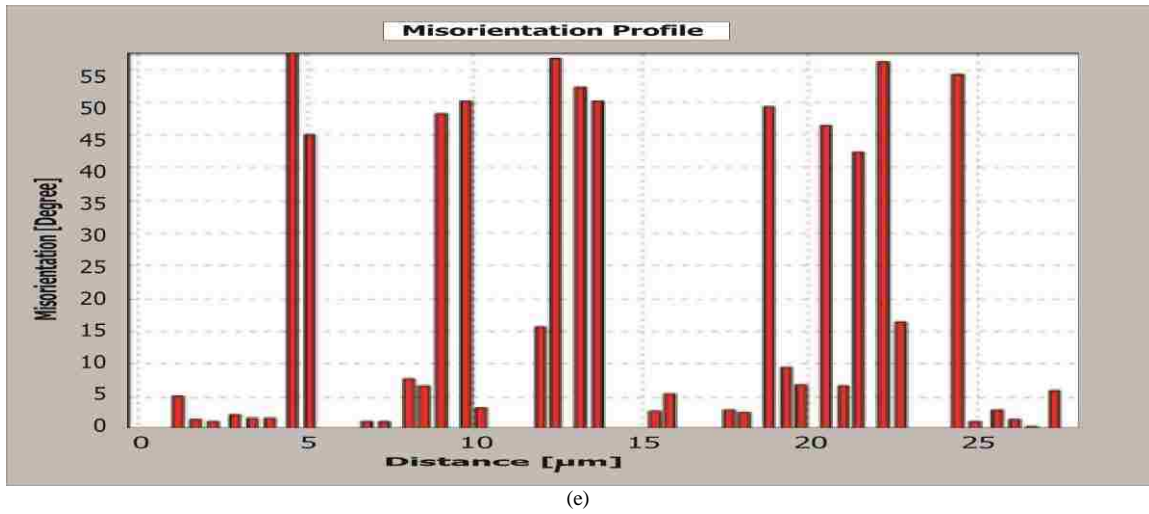
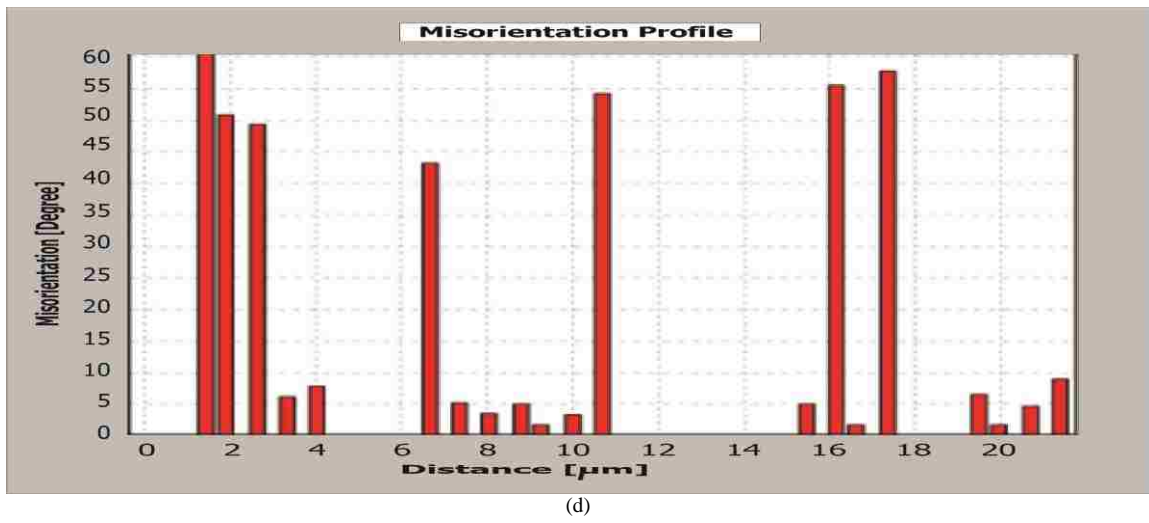
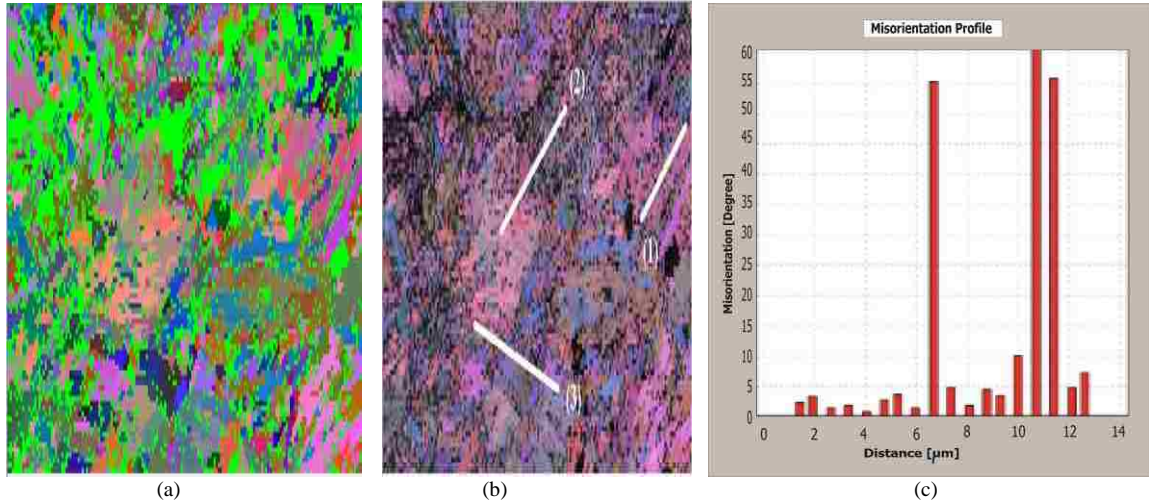


Figure 5.3 Misorientation angle measured along three different lines in impacted HY100 steel, sample location 6-Bat 6.70 km/sec shows: a) EBSD shows less noise, b) EBSD shows grains, c, d, and e, are the Lines (1, 2, and 3) respectively.

Sample (6) location C

Figure 5.4 shows Misorientation angle measured along three different lines in impacted HY100 steel sample at 6.70 km/sec in another location at the crater sample, the Misorientation angles are between (55-60) degrees, that means the plastic deformation as a twinning is so clear in this location and the HCP percentage increase.

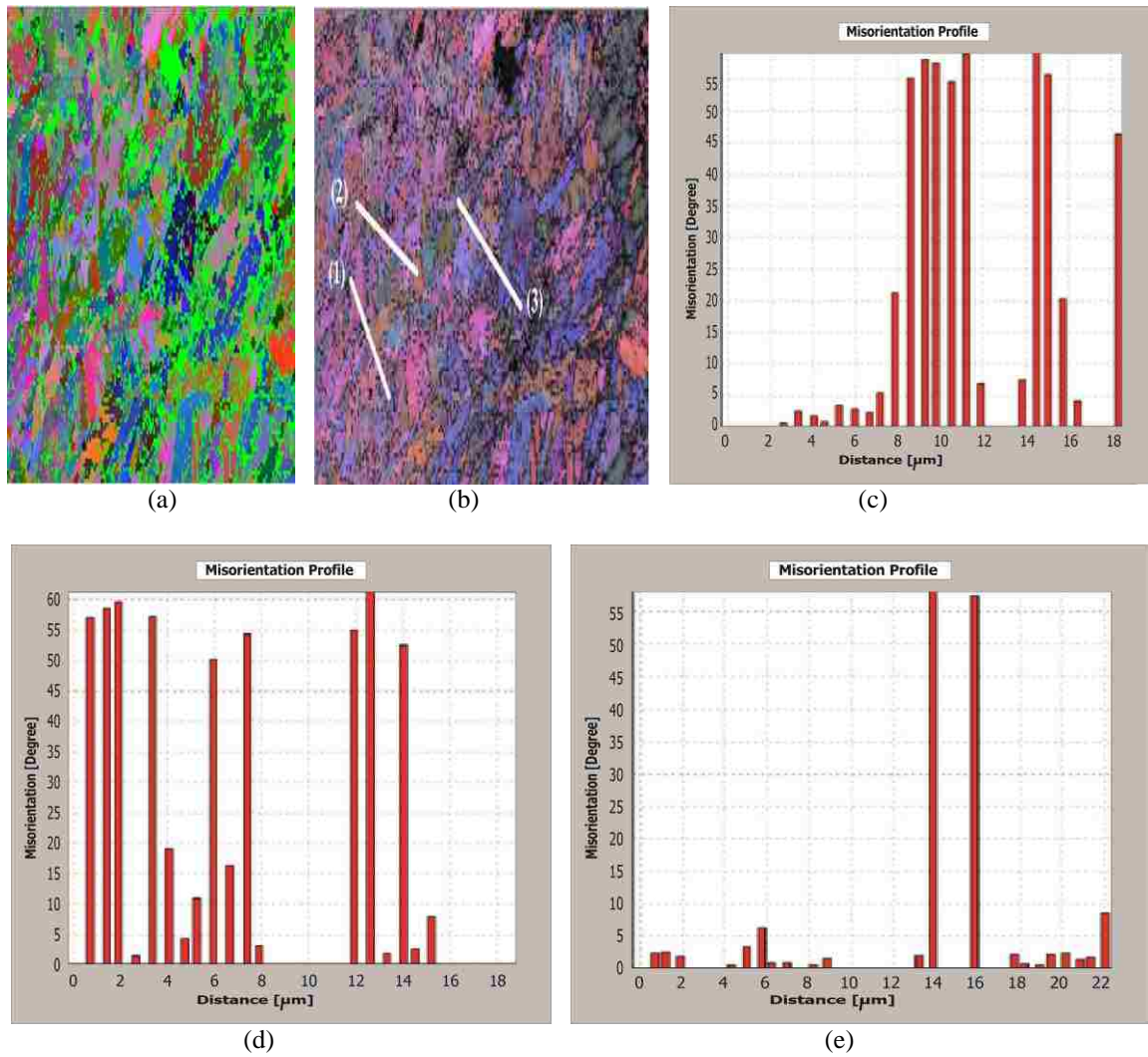


Figure 5.4 Misorientation angle measured along three different lines in impacted HY100 steel, sample location 6-C at 6.70 km/sec shows: a) EBSD shows less noise, b) EBSD shows grains, c, d, and e, are the Lines (1, 2, and 3) respectively.

Sample (6) location F

Figure 5.5 shows Misorientation angle measured along three different lines in impacted HY100 steel sample location 6-F at 6.70 km/sec in another location at the crater sample, The Misorientation angle in this location is between 55-60 degrees and the HCP phase ratio increased.

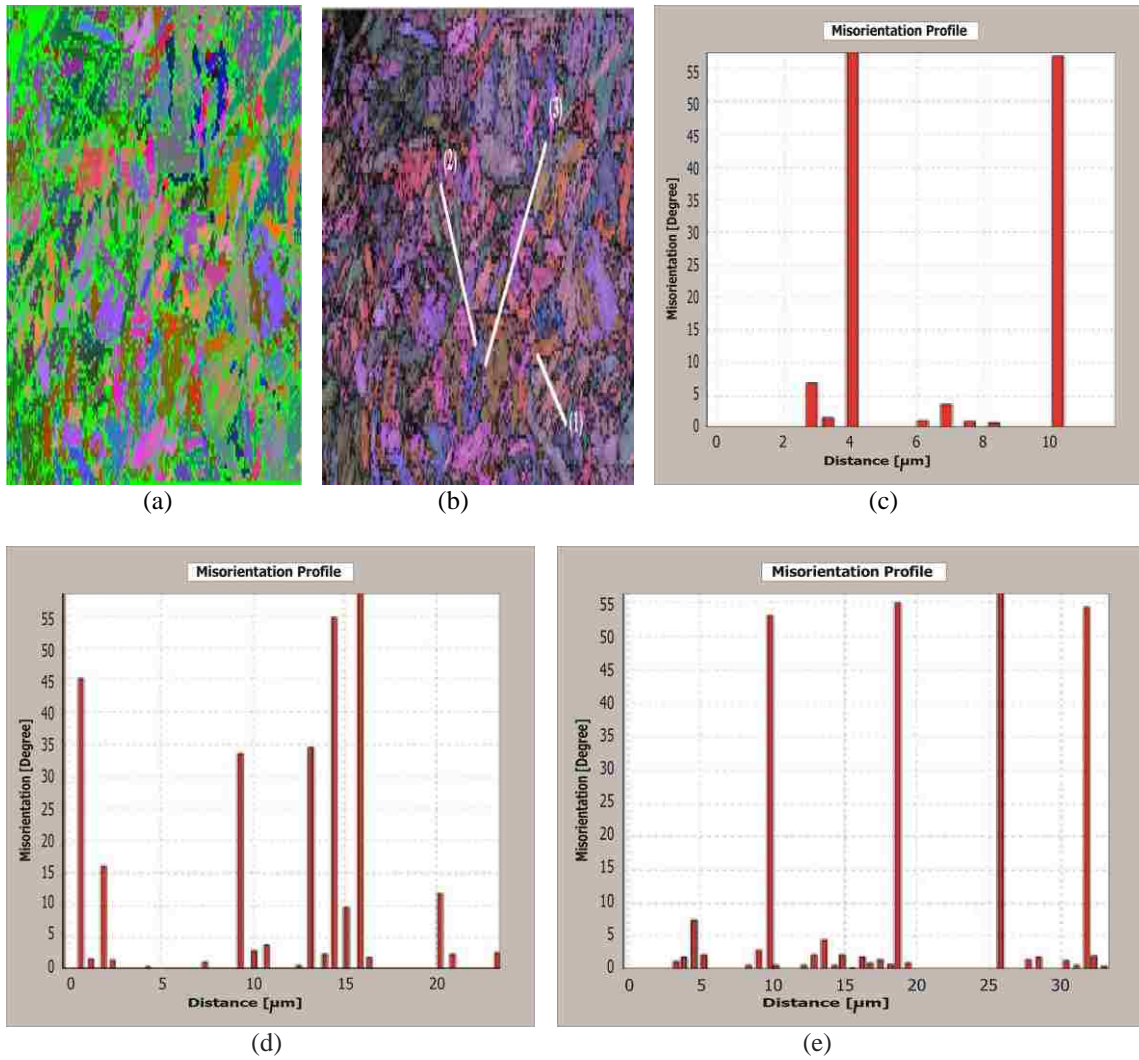


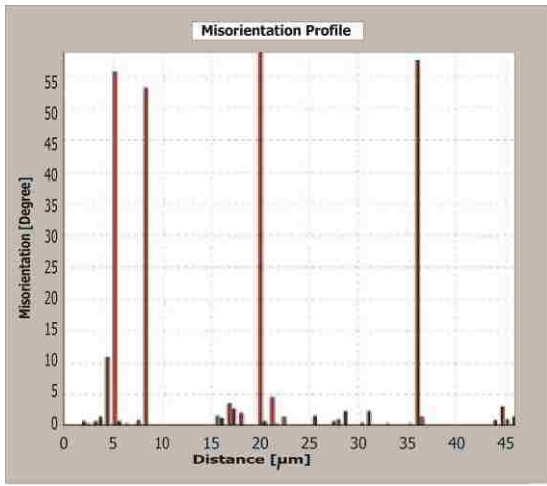
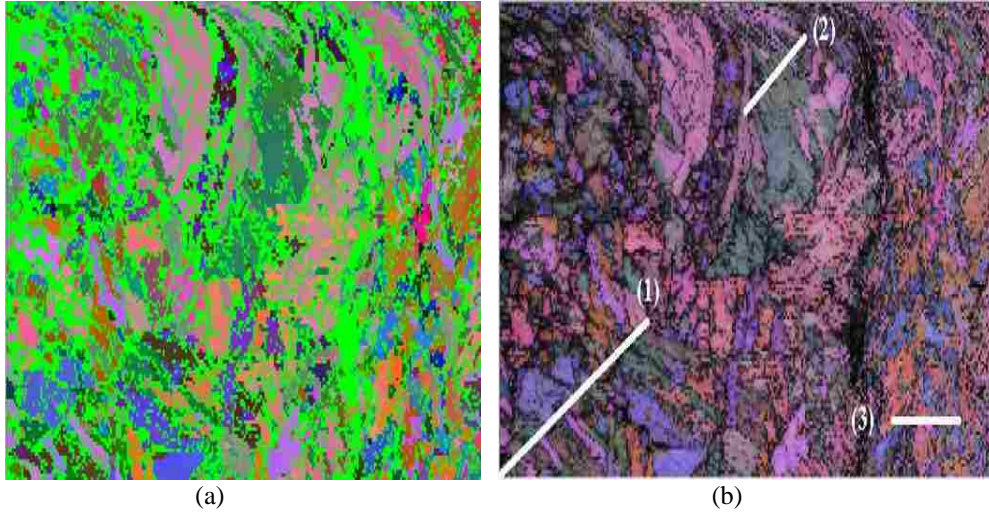
Figure 5.5 Misorientation angle measured along three different lines in impacted HY100 steel, sample location 6-F at 6.70 km/sec shows: a) EBSD shows less noise, b) EBSD shows grains, c, d, and e, are the Lines (1, 2, and 3) respectively.

Sample (6) location F

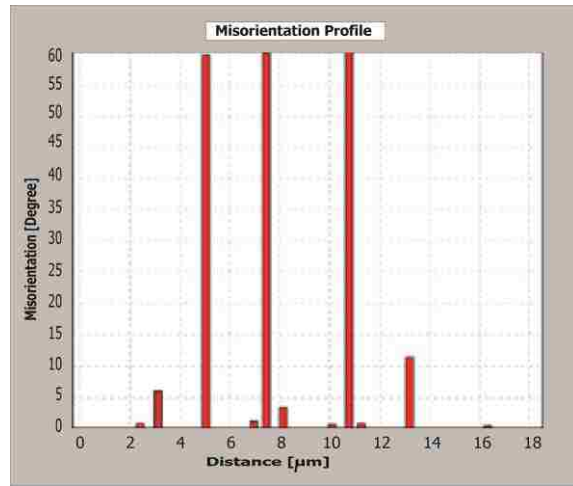
Figure 5.6 shows Misorientation angle measured along three different lines in impacted HY100 steel sample location 6-F at 6.70 km/sec. Twinning deformation appeared permanent and not naturally reversible since a long time elapsed between experiment and EPSP viewing. Conceptually, during deformation, atoms can be pushed out of place.

Sample (6) location G

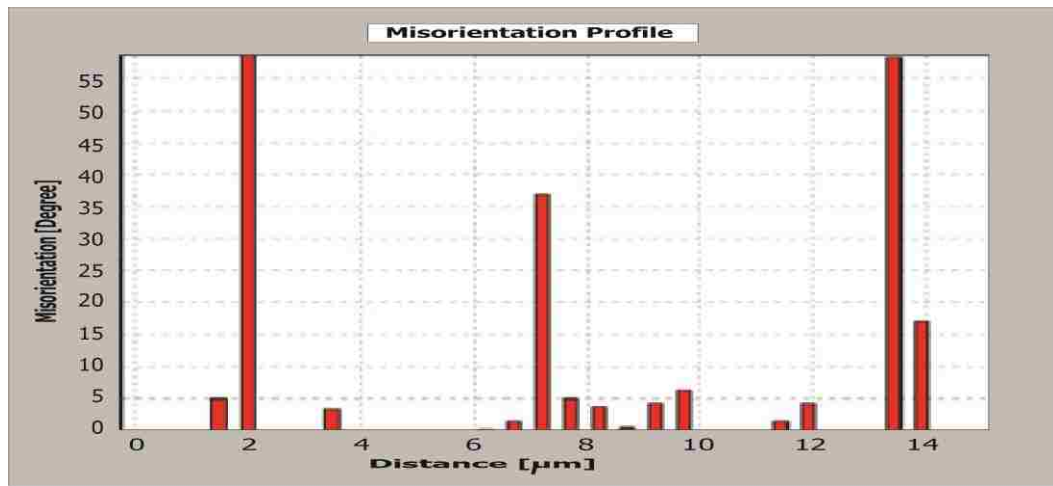
Figure 5.7 shows Misorientation angle measured along three different lines in impacted HY100 steel sample at 6.70 km/sec sample location 6-G. Misorientation angles in this location are between 55-60 degrees and the HCP phase ratio increased.



(c)

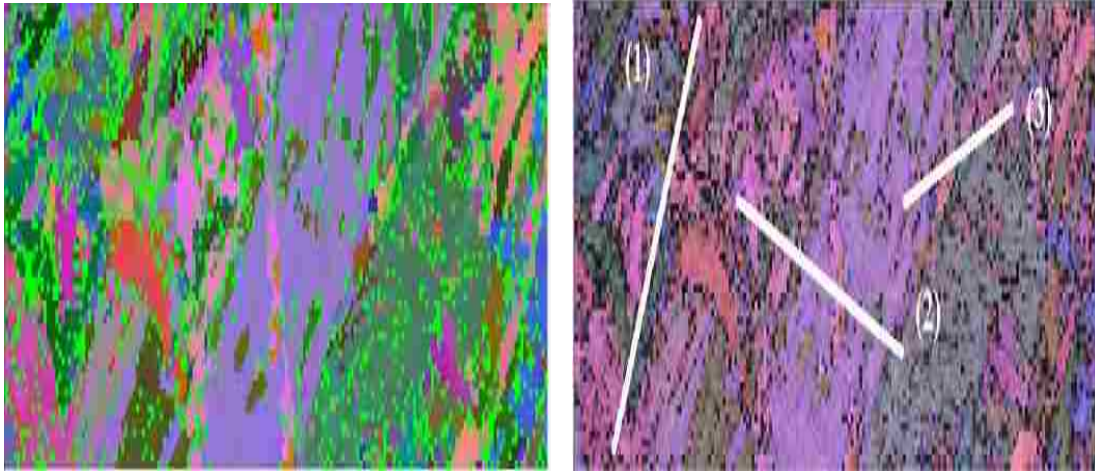


(d)



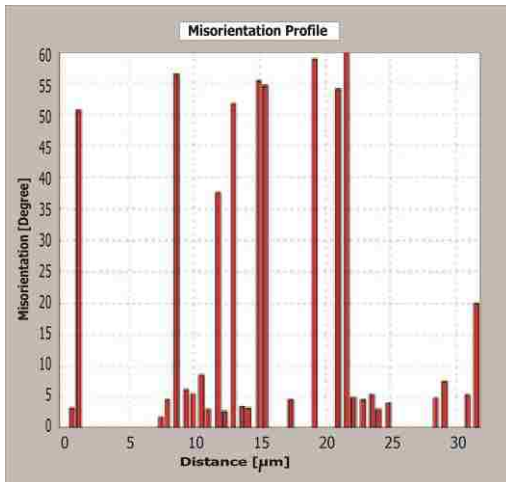
(e)

Figure 5.6 Misorientation angle measured along three different lines in the impacted HY100 steel, sample location 6-F after impact velocity of 6.70 km/sec shows: a) EBSD shows less noise, b) EBSD shows grains, c, d, and e, are the Lines (1, 2, and 3) respectively.

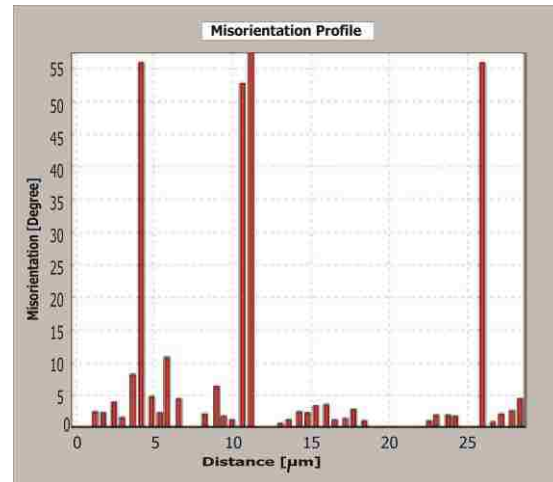


(a)

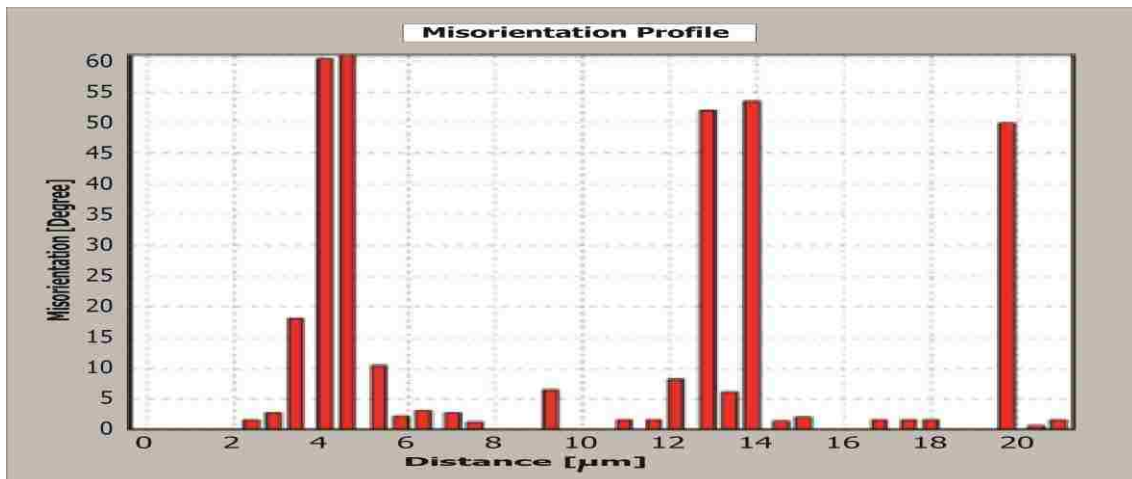
(b)



(c)



(d)



(e)

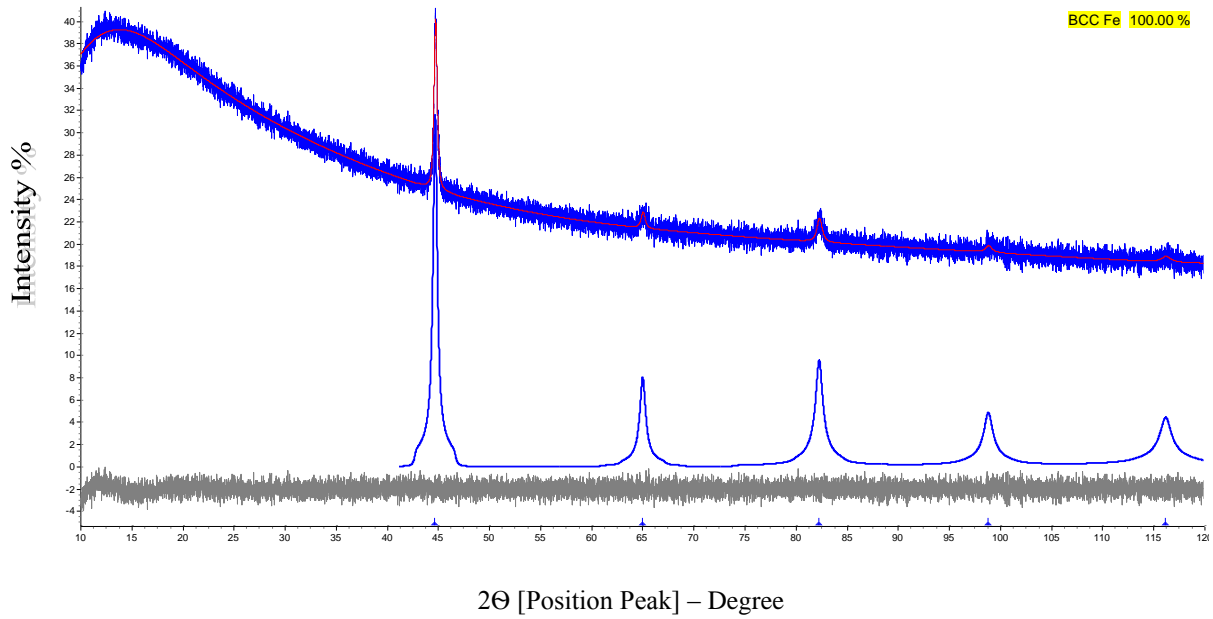
Figure 5.7 Misorientation angle measured along three different lines in the impacted HY100 steel, sample location 6-G after impact velocity of 6.70 km/sec shows: a) EBSD shows less noise, b) EBSD shows grains, c, d, and e, are the Lines (1, 2, and 3) respectively.

All notes of the results of HY100 steel this show that in kind of alloy the phase is changed during the impact of high pressure and temperature. The results also note that the crystal and grains are shaped to from a new twinning deformation and leave the plane exhibition because of the shock and the HCP ratio is increased. The angle of Misorientation is greater than 45 degrees and this means the grains of the crystal changed the direction and shape of the impact of the shock.

5.1.3 XRD Lattice Parameter Measurements

The HY100 steel is the only sample that shows no change from non-impact to impact. Only the BCC phase is seen. It is important to note that it is possible that there are other phases in the steels that are not visible in the XRD data. Indeed, electron backscatter diffraction (EBS d) data indicate the presence of a hexagonal close-packed (HCP) phase on the impacted steels, as well as the FCC phase on the HY100. A likely reason for this discrepancy is outlined above – the “invisible” phases are not sufficiently abundant to be detected by powder XRD.

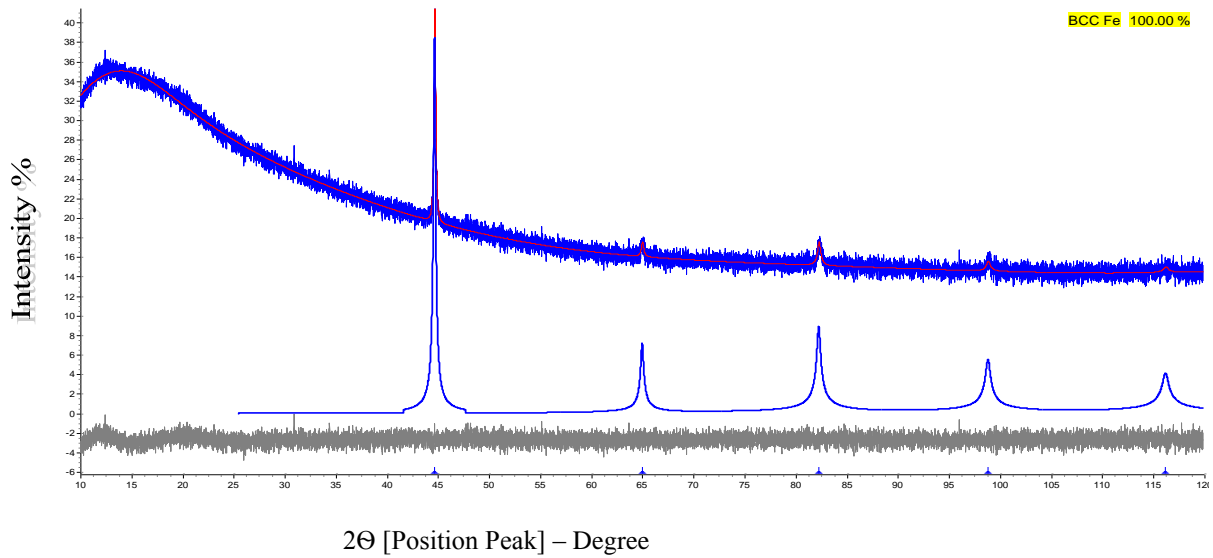
5.1.3.1 Non-Impact HY100 Steel



(a) BCC

Figure 5.8 Non-impact HY100 steel Phase 1: "BCC Fe" 100.000 %

5.3.1.2 Impact HY100 at 6.70 km/sec



b) FCC fit

Figure 5.9 Impact HY100 steel at 6.70 km/sec Phase 1: "BCC Fe" 100.000 %

Table 5.2 HY100-Lattice parameters and quantity for detectable phases

	BCC		FCC	
	Lattice Parameter.	Weight %	Lattice Parameter.	Weight %
Non-impact	2.870×10^{-10} m	100 %	0 %	0 %
Impact	2.870×10^{-10} m	100 %	0 %	0 %

BCC	Cell Mass (g)	Cell Volume (Å ³)	Crystal Density g/cm ³	Crystal Size (nm)
Non-impact HY100	111.693	23.630	7.8489	67.2(73)
Impact HY100	111.693	23.6421	7.8450	7000(57000)

5.2 Impact Velocity of 6.70 km/s in HY100 Steel

5.2.1 Cross-section Location 1-A (75 mm from impact center)

Figure 5.10 shows the EBSD microscopy data for sample location 1-A in the HY100 steel target after an impact velocity of 6.70 km/sec. The figure shows the polished sample, grain, 400X magnification and the original length of the map, the phase distribution and the Crystal Orientation. And Table 5.3 shows the impact phase ratios of HY100 at 6.70 km/sec sample location 1-A.

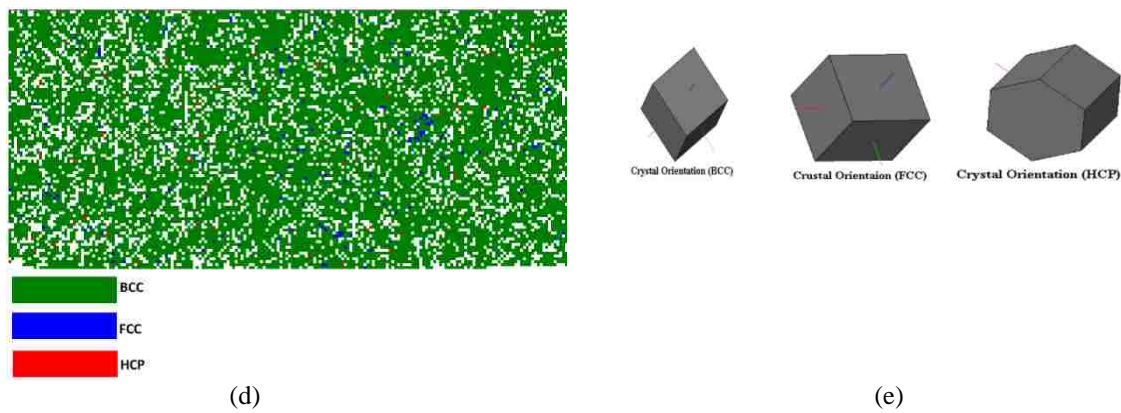
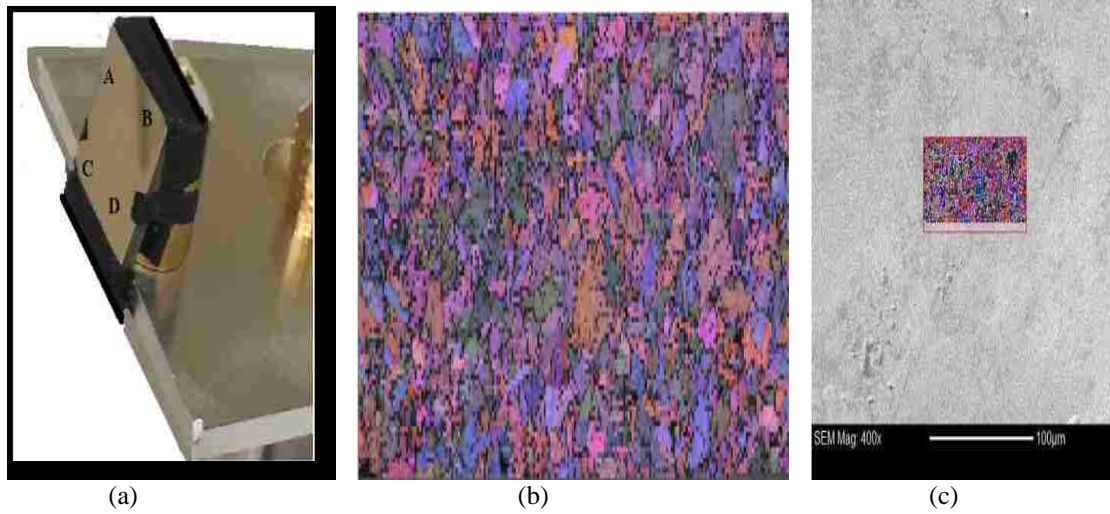


Figure 5.10 EBSD data from HY100 steel, sample location 1-A, after impact velocity of 6.70 km/sec showing: a) polished sample, b) grain, c) 400X magnification and the original length of the map, d) phase map, and e) shows the Crystal Orientation.

5.2.2 Cross-section Location 2-A (35 mm from impact center)

Figure 5.11 shows the polished sample, grain, 400X magnification and the original length of the map, the phase distribution. Table 5.4 shows the ratios percentages of each phase in this location.

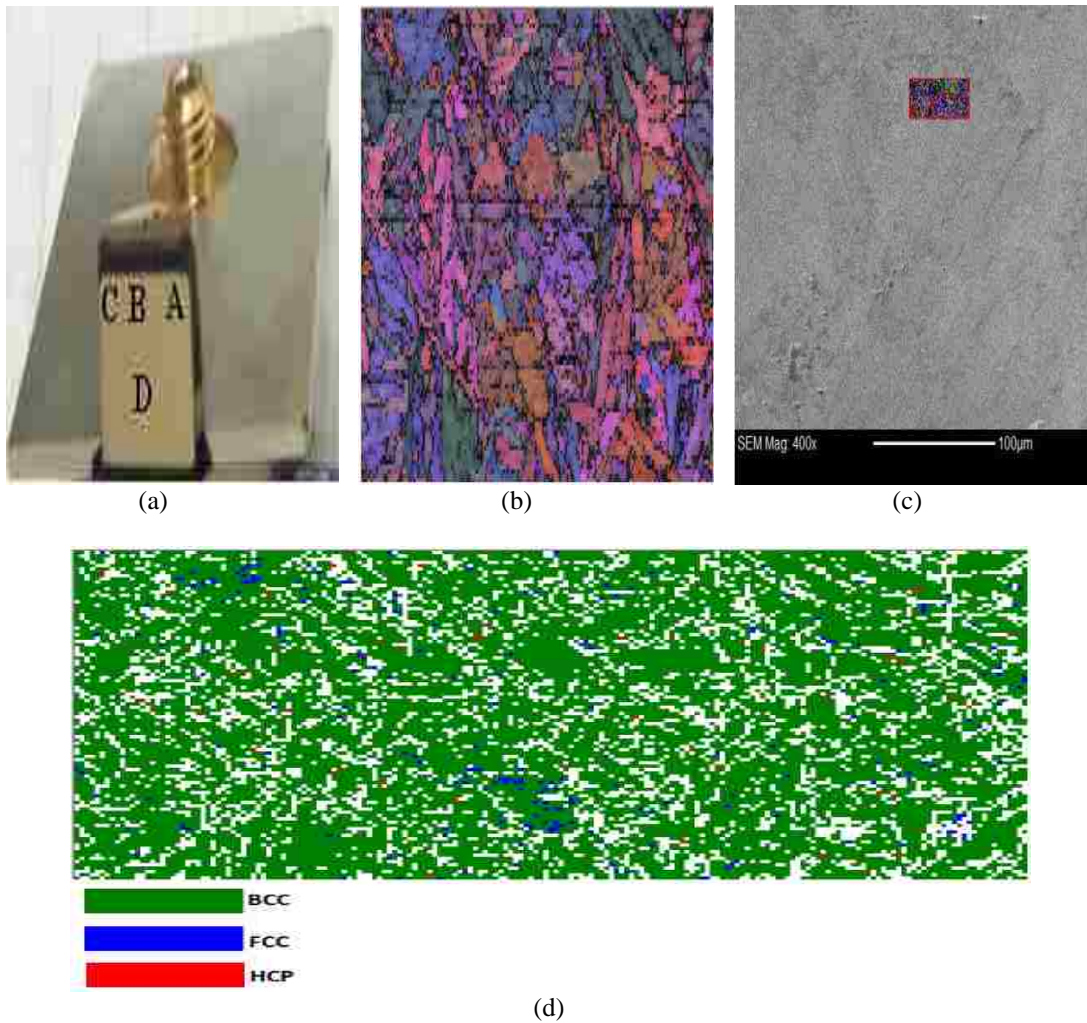


Figure 5.11 EBSD data from HY100 steel, sample location 2-A, after impact velocity of 6.70 km/sec showing: a) polished sample, b) grain, c) 400X magnification and the original length of the map, d) phase map.

5.2.3 Cross-section Location 3-D (7.5 mm from impact center)

Figure 5.12 shows the polished sample, grain, 400X magnification and the original length of the map, the phase distribution. Table 5.5 shows the ratios of all unite cell structure in this location.

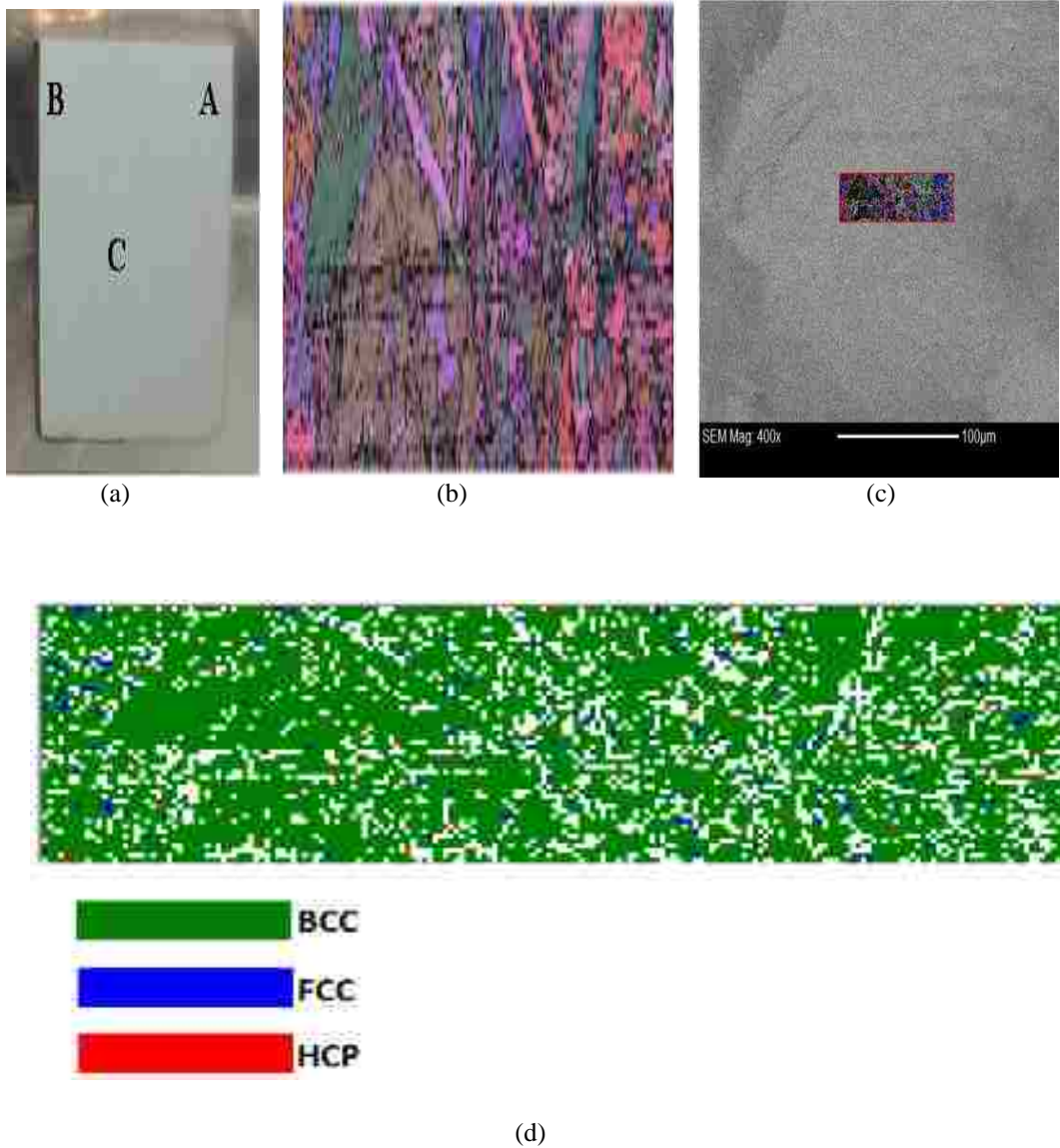


Figure 5.12 EBSD data from HY100 steel, sample location 3-D, after impact velocity of 6.70 km/sec showing: a) polished sample, b) grain, c) 400X magnification and the original length of the map, d) phase map.

5.2.4 Cross-section Location 4-C (20 mm from impact center)

Figure 5.13 shows the polished sample, grain, 400X magnification and the original length of the map, the phase distribution. This Figure shows the location that was so close to the crater, therefore the percentage of HCP is increased to 1.12 % and it explains all EBSD information, such as the sample, grains, magnification and phase photos.

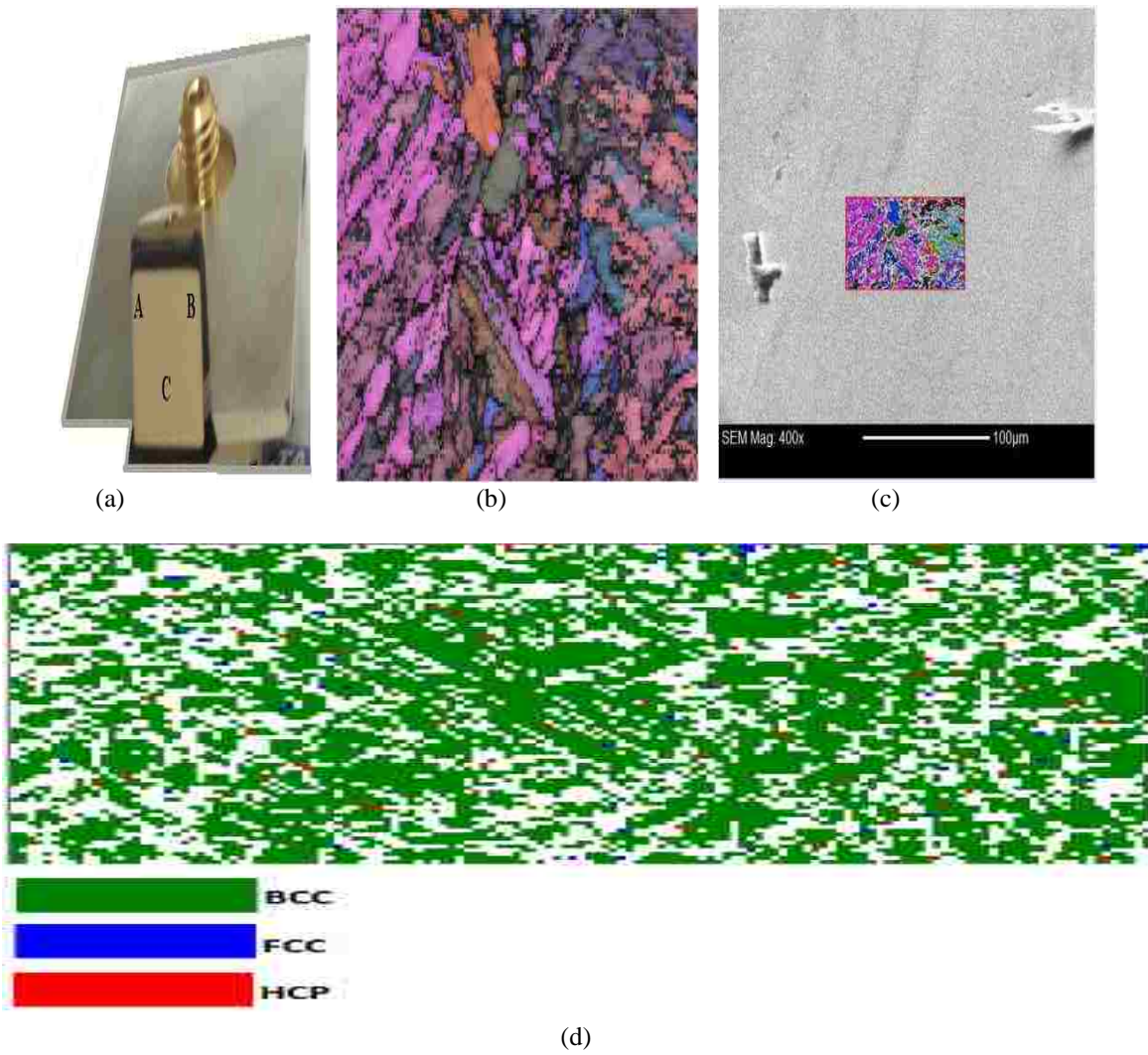


Figure 5.13 EBSD data from HY100 steel, sample location 4-C, after impact velocity of 6.70 km/sec showing: a) polished sample, b) grain, c) 400X magnification and the original length of the map, d) phase map.

5.2.5 Cross-section Location 5-B (10 mm from impact center)

Figure 5.14 shows the polished sample, grain, 400X magnification and the original length of the map, the phase distribution. Table 5.7 shows the ratios percentages of each phase in this location.

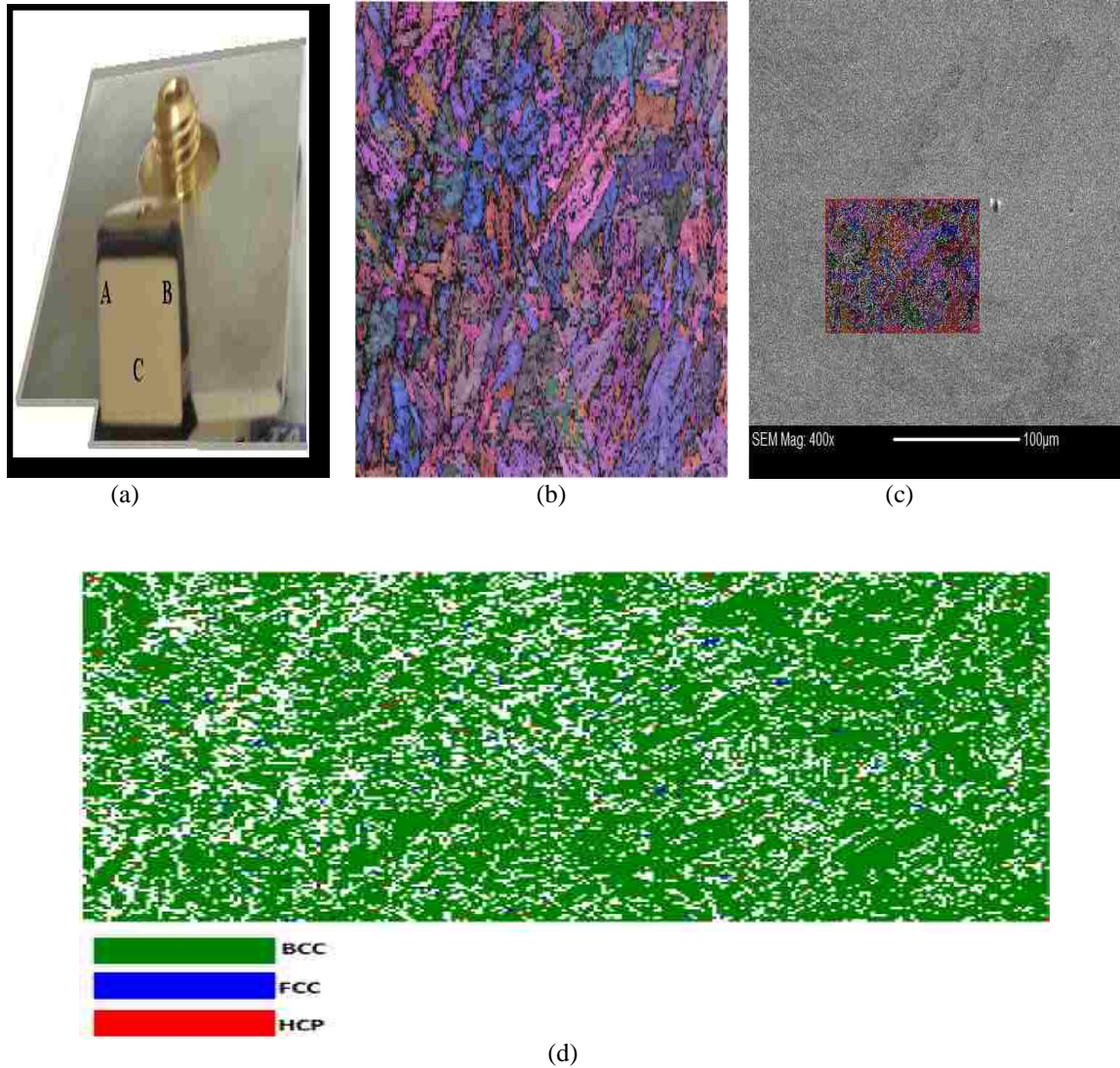


Figure 5.14 EBSD data from HY100 steel, sample location 5-B, after impact velocity of 6.70 km/sec showing: a) polished sample, b) grain, c) 400X magnification and the original length of the map, d) phase map.

Table 5.3 Impact phase ratio of HY100 steel at 6.70 km/sec sample location 1-A

Crystal Unit Cell Structures	Impact HY100 Steel Phase at 6.70 km/sec
BCC	99.55 %
FCC	1.141 %
HCP	0.31 %

Table 5.4 Impact phase ratio of HY100 steel at 6.70 km/sec sample location 2-A

Crystal Unit Cell Structures	Impact HY100 Steel Phase at 6.70 km/sec
BCC	98.03 %
FCC	1.598 %
HCP	0.373 %

Table 5.5 Impact phase ratio of HY100 steel at 6.70 km/sec sample location 3-B

Crystal Unit Cell Structures	Impact HY100 Steel Phase at 6.70 km/sec
BCC	97.742 %
FCC	1.866 %
HCP	0.40 %

Table 5.6 Impact phase ratio of HY100 steel at 6.70 km/sec sample location 4-C

Crystal Unit Cell Structures	Impact HY100 Steel Phase at 6.70 km/sec
BCC	98.18 %
FCC	0.71 %
HCP	1.12 %

Table 5.7 Impact phase ratio of HY100 steel at 6.70 km/sec sample location 5-B

crystal unit cell structures	Impact HY100 Steel Phase at 6.70 km/sec
BCC	97.65 %
FCC	1.004 %
HCP	1.342 %

5.2.6 Cross-section Location 6-A (0 mm from impact center)

In the surrounding area of the crater, the grain starts to become small at the impact under the high temperature and the pressure. Because the error rate in this region is high, calculations were taken using the average of these areas and choosing the best area to view images of EBSD microscopy as shown in Figure 5.15 shows the polished sample, grain, 400X magnification and the original length of the map, the phase distribution and table 5.8 shows the ratios of all unit cell structure in this location.

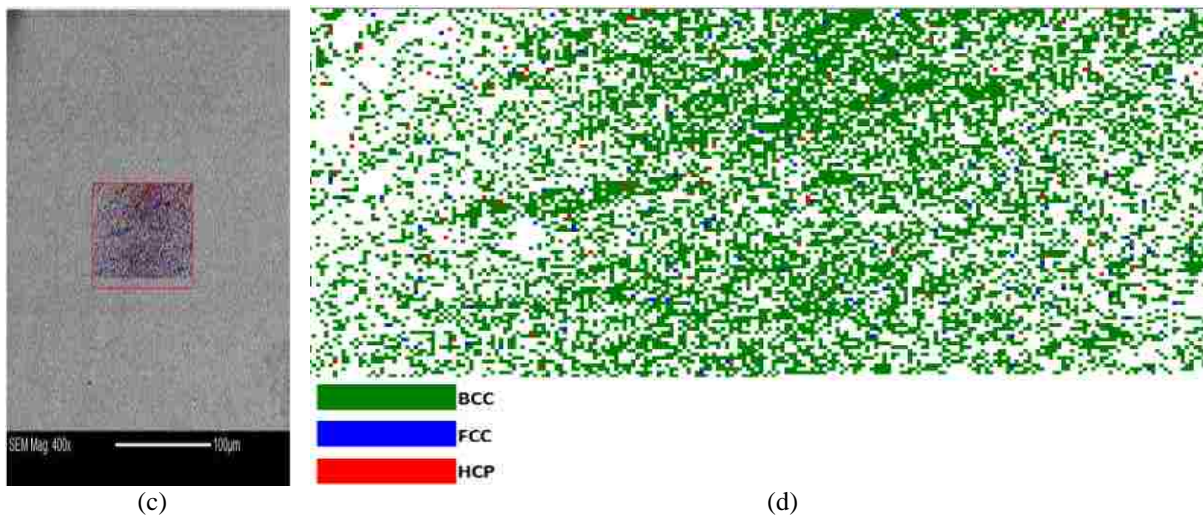
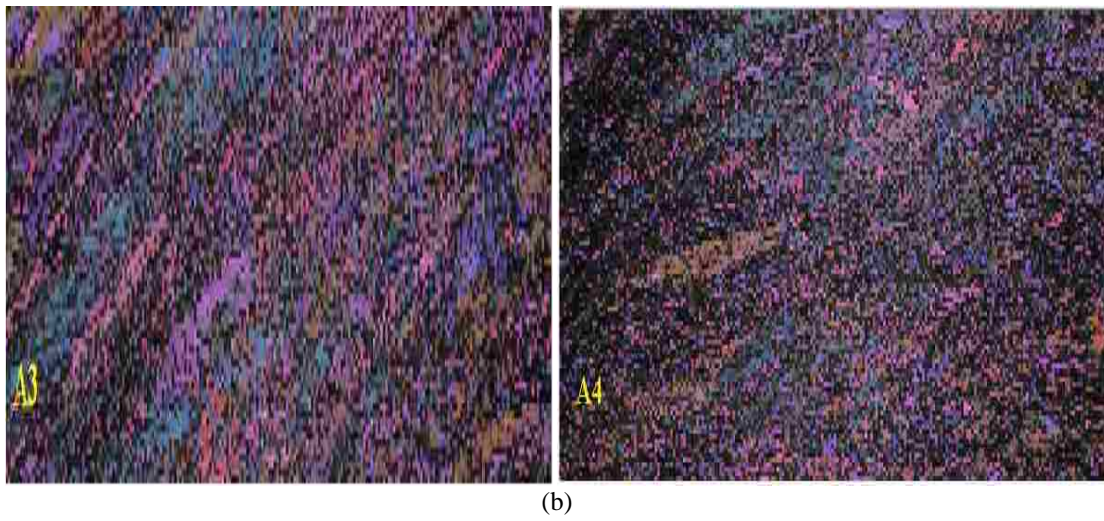
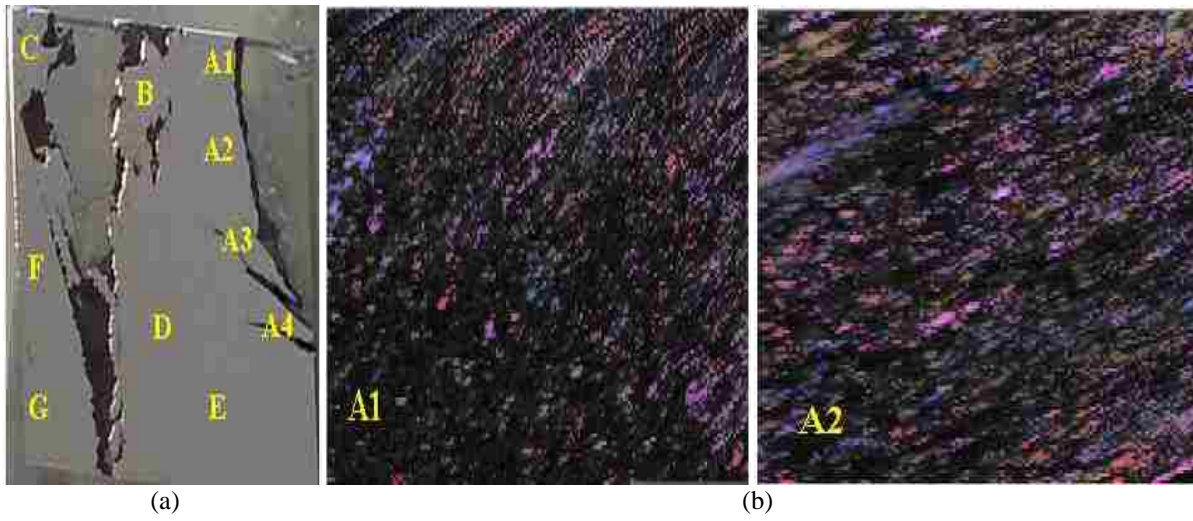


Figure 5.15 EBSD data from HY100 steel, sample location 6-A, after impact velocity of 6.70 km/sec showing: a) polished sample, b) grain, c) 400X magnification and the original length of the map, d) phase map.

5.2.7 Cross-section Location 6-B (0 mm from impact center)

Figure 5.16 shows the grain, 400X magnification and the original length of the map, the phase distribution and table 5.9 shows the ratios of all unite cell structure in this location. This site is about 2 mm diameter of the arc of the projectile shock and seems to shift into shape plastically clear and twinning is growing and the obvious HCP percentage is 1.432 % the cross section sample 6-B was etched with (HNO₃ 96 % and Ethanol 4 %) for 15 seconds.

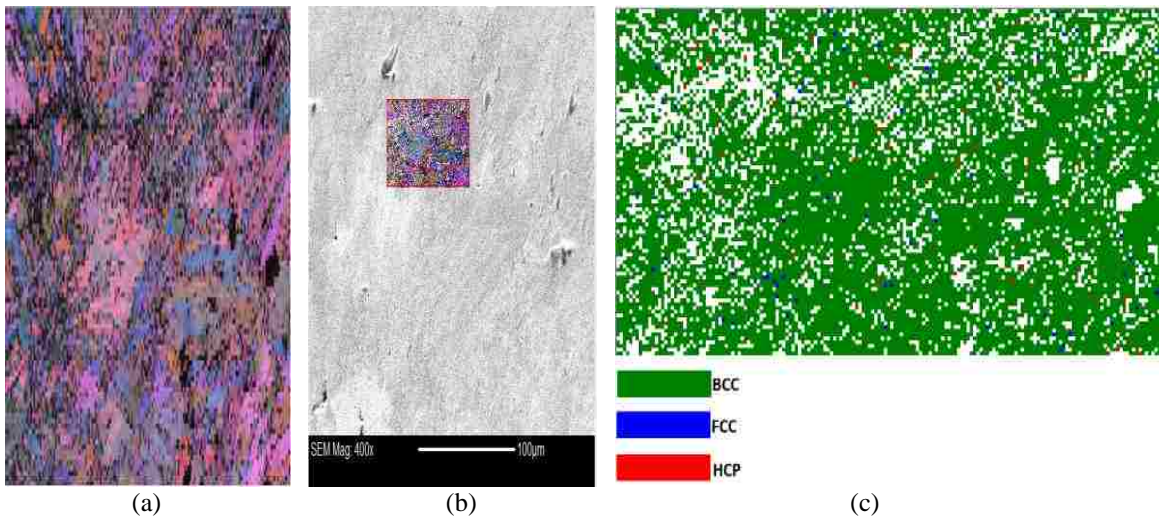


Figure 5.16 EBSD data from HY100 steel, sample location 6-B, after impact velocity of 6.70 km/sec showing: a) grain, b) 400X magnification and the original length of the map, and c) phase map.

5.2.8 Cross-section Location 6-C (0 mm from impact center)

Figure 5.17 shows the grain, 400X magnification and the original length of the map, the phase distribution and table. Table 5.10 shows the ratio of each phase.

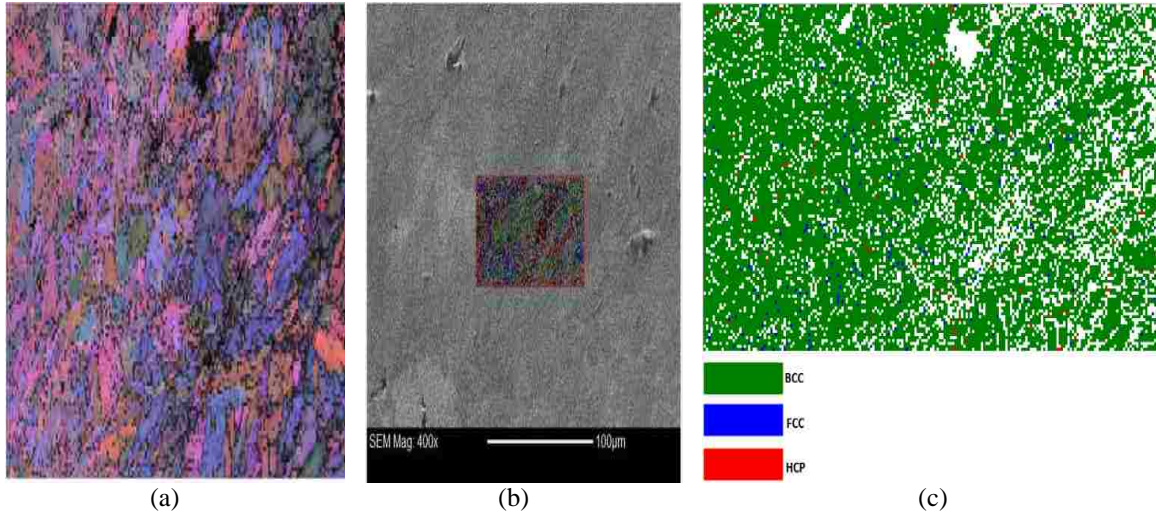


Figure 5.17 EBSD data from HY100 steel, sample location 6-C, after impact velocity of 6.70 km/sec showing: a) grain, b) 400X magnification and the original length of the map, and c) phase map.

5.2.9 Cross-section Location 6-D (0 mm from impact center)

Figure 5.18 shows the grain, 400X magnification and the original length of the map, the phase distribution.. With this location the twinning deformation increases and the HCP percentage phase increases too.

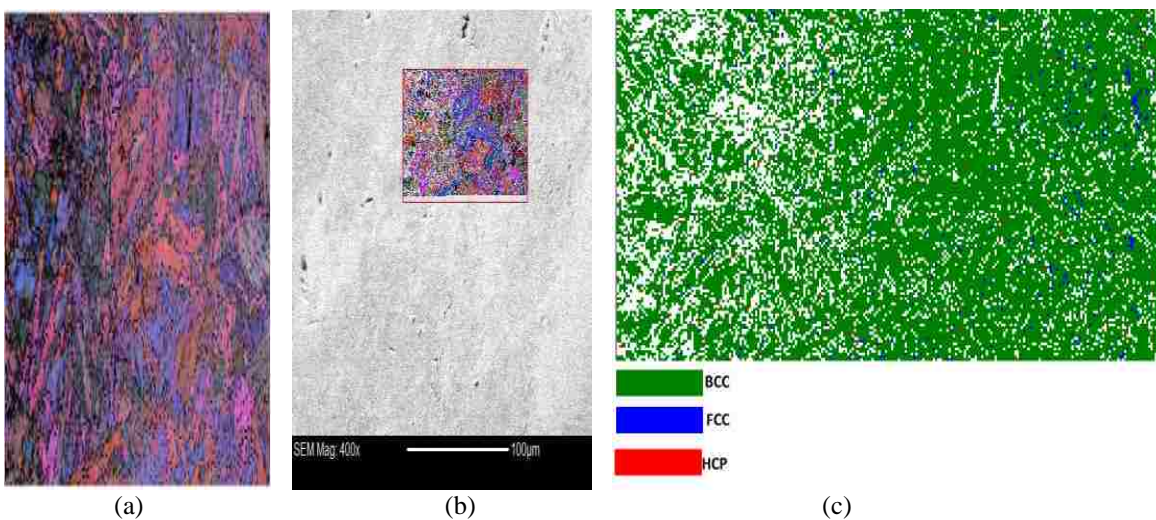


Figure 5.18 EBSD data from HY100 steel, sample location 6-D, after impact velocity of 6.70 km/sec showing: a) grain, b) 400X magnification and the original length of the map, c) phase map.

5.2.10 Cross-section Location 6-E (0 mm from impact center)

Figure 5.19 shows the grain, 400X magnification and the original length of the map, the phase distribution..Table 5.12 shows the ratio of each phase.

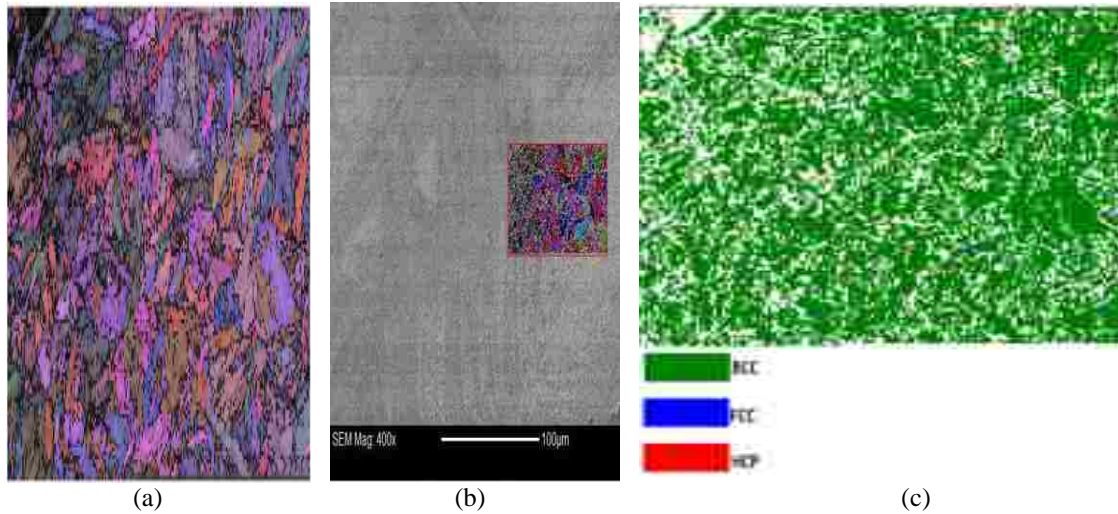


Figure 5.19 EBSD data from HY100 steel, sample location 6-E, after impact velocity of 6.70 km/sec showing: a) grain, b) 400X magnification and the original length of the map, and c) phase map.

5.2.11 Cross-section Location 6-F (0 mm from impact center)

Figure 5.20 shows the grain, 400X magnification and the original length of the map, the phase distribution, Table 5.13 observes the ratio of each phasepercentage.

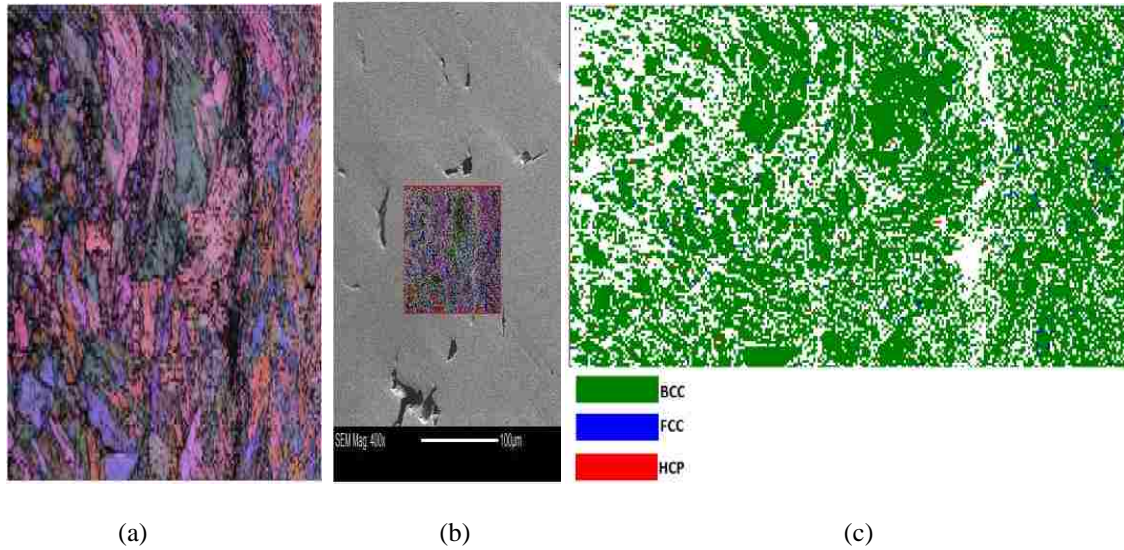


Figure 5.20 EBSD data from HY100 steel, sample location 6-F, after impact velocity of 6.70 km/sec showing: a) grain, b) 400X magnification and the original length of the map, and c) phase map.

5.2.12 Cross-section Location 6-G (0 mm from impact center)

Through the results, images and tables found that HY 100 steel change after impact, and changed the crystal phase. This steel changed from BCC to FCC and HCP. The last phase proves that the phase crystal had changed and plastic deformation and twinning started forming on the plane of the grains. The grains left the plane near the arc of the crater and changed the phase started of the crystal from body-centered cubic (BCC) hexagonal close packed (HCP), or face centered cubic (FCC). Even after the shock the crystalline system remained organized. Among other things that were not observable through the microscope to read include the immediate area of the arc crater, making the results in those areas unreliable. Sample 6 locations G was chosen as a result because the error percentage was low compared with other locations, making it a dependable result. Figure 5.21 shows the grain, 400X magnification and the original length of the map, the phase distribution.

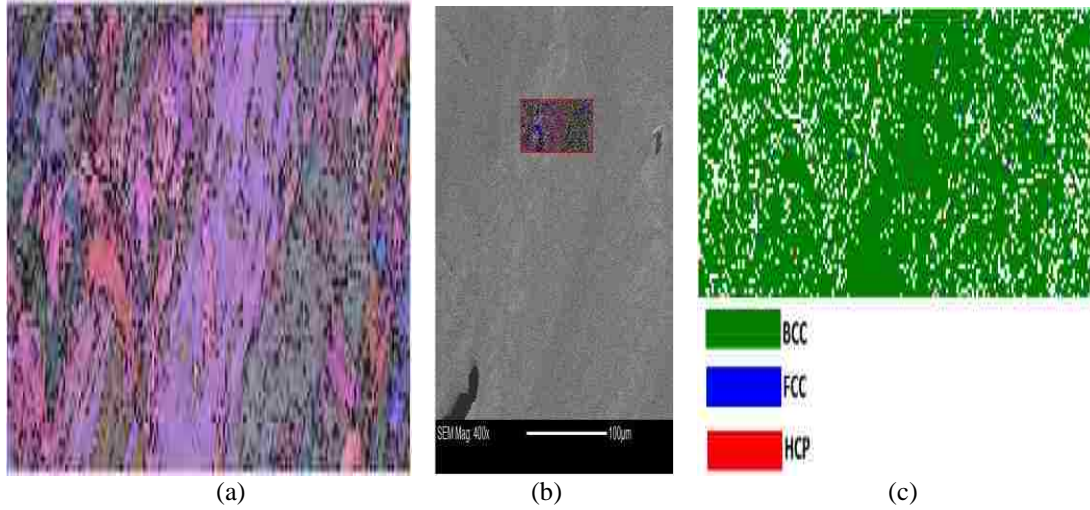


Figure 5.21 EBSD data from HY100 steel, sample location 6-G after impact velocity of 6.70 km/sec showing: a) grain, b) 400X magnification and the original length of the map, and c) phase map.

Table 5.8 Impact phase ratio of HY100 steel at 6.70 km/sec sample location 6-A

Crystal Unit Cell Structures	Impact HY100 Steel Phase at 6.70 km/sec
BCC	97.336 %
FCC	1.658 %
HCP	1.1587 %

Table 5.9 Impact phase ratio of HY100 steel at 6.70 km/sec sample location 6-B

Crystal Unit Cell Structures	Impact HY100 Steel Phase at 6.70 km/sec
BCC	97.61 %
FCC	0.56 %
HCP	1.432 %

Table 5.10 Impact phase ratio of HY100 steel at 6.70 km/sec sample location 6-C

Crystal Unit Cell Structures	Impact HY100 Steel Phase at 6.70 km/sec
BCC	96.455 %
FCC	1.0633 %
HCP	2.50 %

Table 5.11 Impact phase ratio of HY100 steel at 6.70 km/sec sample location 6-D

crystal unit cell structures	Impact HY100 Steel Phase at 6.70 km/sec
BCC	97.21 %
FCC	1.536 %
HCP	1.255 %

Table 5.12 Impact phase ratio of HY100 steel at 6.70 km/sec sample location 6-E

crystal unit cell structures	Impact HY100 Steel Phase at 6.70 km/sec
BCC	97.98 %
FCC	0.59 %
HCP	1.433 %

Table 5.13 Impact phase ratio of HY100 steel at 6.70 km/sec sample location 6-F

Crystal Unit Cell Structures	Impact HY100 Steel Phase at 6.70 km/sec
BCC	97.88 %
FCC	0.754 %
HCP	1.356 %

Table 5.14 Impact phase ratio of HY100 steel at 6.70 km/sec sample location 6-G

Crystal Unit Cell Structures	Impact HY100 Steel Phase at 6.70 km/sec
BCC	97.32 %
FCC	0.391 %
HCP	2.29 %

5.3 Experimental Grain Size Measurements

5.3.1 Non-impact HY100 Steel

In this type of iron alloy it was hard to measure the grain boundary under the shock because the grain size seemed compressed. The result of this measurement was not accurate compared to XRD diffraction. Grain size near impact is compacted near impact site. One such observation was the presence of “twinning”, which was present closer to the impact area, and gradually dissipated further from the impact zone. When the twinning percentage increased the grain size decreased, that is why it is so difficult to measure the grain’s boundaries at this area.

At $r = 22.0\mu\text{m}$ $n = 75$

$$\text{Grain size} = \frac{2\pi r}{n-1}$$

$$G.S = \frac{2 * 3.14 * 22.0\mu\text{m}}{75 - 1}$$

$$G.S = 1.8670\mu\text{m}$$

$$G.S \text{ average} = 1.870\mu\text{m}$$

5.3.2 Impact HY100 Steel at 6.70 km/sec

At $r = 32.50\mu\text{m}$ $n = 120$

$$\text{Grain size} = \frac{2\pi r}{n-1}$$

$$G.S = \frac{2 * 3.14 * 32.50\mu\text{m}}{120 - 1}$$

$$G.S = 1.715\mu\text{m}$$

$$G.S \text{ average} = 1.720\mu\text{m}$$

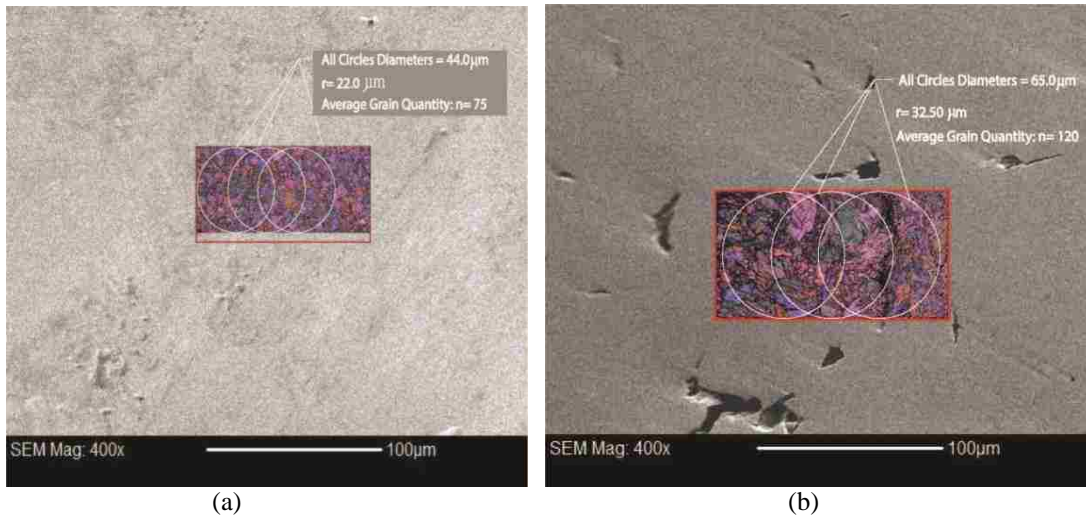


Figure 5.22 Experimental Grain Size Measurements of a) Non-impactHY100steel, b) impact at 6.70 km/sec

Sample location C.

CHAPTER 6

DISCUSSION OF RESULTS

This experimental work evaluates the effect of applied high pressure impact to three kinds of steel to determine microstructural changes. This chapter discusses the results acquired in chapters 3, 4, and 5. We show here the objectives that were met of microstructural phase changes due to the pre-determined set of impacts. Also it gives an overview for the related work that can be done in light of the acquired results. Test results as listed in chapter 3 have been acquired and quantified through the use of EBSD and XRD. Results are discussed qualitatively and quantitatively.

The EBSD microscopy test is used to provide a qualitative signature of the existence or dominance of one phase, new phase formation or changes as a result of impact; in addition to the quantitative ratios between phases in the pre and post impact condition of the target materials. The XRD is used to find additional evidence of phase differentiation such as lattice constant which cannot be identified from EBSD alone. The collected two sets of data gave enough evidence on the specific phase signature. The underlying concluding discussion addresses the fingerprints of phase change difference due to impact loading. Our primary focus shall be on the three A36 steel plate specimens impacted by three predetermined impact speeds.

Our confidence in the EBSD and XRD data relied on the certainty according to the error estimation of quantified data and viewed figures described in chapter 3. Numerous points of viewed locations have been examined. Only those points that had a confidence level of 90 percent or higher were considered. Results for other points are documented in the Appendices.

Unit cell misorientation and dislocation angles found in the neighborhoods of crater sections in many locations will be shown in the following sections. Values detected in the range of 55-60 degrees show the existence of the twinning we know from previous documentation that a misorientation angle greater than 45 degrees means that there is a change in a crystals position and orientation under impact of this high

pressure and temperature; a clear indication of the new formation of HCP phase from BCC phase. Figures in chapters 3, 4, and 5 demonstrate these facts regarding misorientation.

6.1 A36 Steel

EBSD test results have shown a dominance of BCC crystalline phase unit cell, while merely a trace of FCC existed, and no noticeable HCP have been detected. Among the three projectile speeds, the lowest projectile test speed that has been conducted is 3.54 km/sec. That speed of impact is translated into a 60 GPa at first contact with the steel plate specimen, which is damped to 14.2 GPa in a period of 3 milliseconds, which are both within the transformation impact as intended. These pressures were estimated from a finite element analysis simulation. Therefore, intuitively, the higher projectile speeds that have been chosen for testing are also within the transformation impact as well. Observations and comments about the results will address the relationship of impacted versus non impacted specimens as stage one of our discussion.

6.1.1 First Steel Test Speed for A36 Steel: 3.54 km/sec

At 3.54 km/sec all figures show six different location points for EBSD views of the designated locations. Notice the obvious twinning traces points located near the crater center. Also, some little twinning appears on sections 3, 4, and 5 and almost null cross sections 1 and 2. As seen in Figure 6.1, the percentages of crystals modes post-impact speed of 3.54 km/sec as shown from Table 3.3 to 3.13 in chapter 3. The HCP percentage varied from 0.063 % to 1.05 %. The proportion of the crystalline phase HCP and FCC values have also changed, in the same sample, depending on the crater location and direction. For example, in the crater cross section, the FCC and HCP phases are different ratios in location C than in location D.

The ratio of HCP at the cross-sections (1 through 5), in order are: [0.063 %, 0.072 %, 0.079 %, 0.081 %, and 0.091 %]. At the section sample 6, points C, D, and E, the percentage of HCP is around 0.146 %

with a 3.73 % error, 1.0402 %, and 0.2155 % with a 2.73 % error. It is obvious that the crater section has little significant change of HCP value.



Figure 6.1 Section of A36 steel at 5.80 km/sec speed

6.1.2 Second Test Speed for A36 Steel: 4.51 km/s

Results of higher impact for A36 steel test at 4.51 km/sec speed show a little twinning pattern started at cross section number 4. However, the region with most twinning is around the shock crater center. Tabulated results for each section at 4.51 km/sec impact speed indicate that there are mixed phase relationship with BCC ratio being the dominant phase. However, HCP started to appear near impact and existed in further away selected test locations points, with insignificant proportion of FCC existing. Yet, an insignificant pre-impact HCP ratio became obvious after impact, but only at the impact site and in its near neighborhood. At 4.51 km/sec, which results in the second highest compression tests of A36 steel with a dynamic pressure at the projectile first contact of 75 GPa reduced to 14.9 GPa after 2.5 milliseconds during impact with the plate surface. The resulted EBSD inspection showed HCP percentage ratio at the cross sections 1 to 5 are consecutively 0.075, 0.078, 0.117, 0.1190, and 0.220 percent, with an accuracy more than 90 percent. The percentage of HCP at cross section 6, locations A, B, and C, in order is 0.44 %, with a 3.91 % error, 1.17 % with a high error, and 1.1536 % with an error higher than 10 %.

6.1.3 Third Test Speed for A36 Steel: 5.81 km/sec

At speed of 5.81 km/sec, significant errors have been observed near the edges and neighborhood of the projectile hole in the plate. Post-Impact EBSD imaging shows grain sizes were significantly decreased closer to the impact area, near the crater and arc of projectile. That indicates that at these points, EBSD

cannot scan accurately with reliable images or estimated values of phase changes. Typically, the cross section 1 through 5 results show not so much considerable phase changes, yet, a little higher than the two previous speeds. HCP percentage values estimated by the EBSD at cross sections 1, 2, 3, 4, and 5 were 0.442 %, 0.452 %, 0.523 %, 0.556 %, and 0.88 % respectively in the same order, with less than 10 % errors. However, as shown in Figure 3.27 (B), location A, the largest error of 15.2 %, therefore we could not consider it for comparison. However, at cross crater sections, points B, C, D, and G 1.2 %, 1.488 %, 1.222 %, and 2.215 % respectively have a 9.85 % error which can be considered. When section 6 sample was etched with HNO₃ 96 % and Ethanol 4 % solution for 15 seconds, the viewing error of scanned locations near the crater arc of the shock had improved. This is possibly because of the minute size of particles attached to the section as a result of the grinding in this area. The densest twinning region is around the shock center. Results of cross section sample 6 viewing of locations B, C, D, and G quantitatively indicate the ratios of the phase mix relationship, in addition an estimation of BCC. That estimated measure proves the dominance, or the BCC phase pre-impact, which remains so post-impact at all cross section slides. Clearly, inspection of sections 7500 microns or more, away from the edge of impact, HCP existed with less than a significant ratio. However, HCP started to appear near impact, as close as 2000 microns or less with considerable proportion coming closer to the edge of impact, at section 6, at impact section.

Also, FCC existed with insignificant pre-impact and became significant after impact at the neighborhood near impact; however, with a lower percentage and became insignificant again away from the edge and crater. As a result of the noticeable phase changes in the nearby sites of the crater, it appears that plastic deformation has occurred. Twinning resulted from cooperative displacement of atoms as well as a change in direction. Twinning produces a permanent shape change (plastic deformation) as a result of grains translation. The near impact planes moves to another plane as a referred to original system phase of HCP, which results in a new angle change (misorientation), up to 55-60 degrees. This high change of angle is an indication of the phase change into HCP. All Figures in chapters 3, 4, and 5 shows a clear

misorientation, which seems to be self-evident in the nearby sites of shock site. When the misorientation becomes greater than 45 degrees, the plastic deformation begins.

6.2 304L Steel with Impact Velocity of 6.58 km/sec

EBSD results of 304L steel plate shows two phases, BCC and FCC co-exist in its microstructure, both in significant amounts, yet with a trace of HCP with the non-impact ratios of 33.109 %, 66.718 % and 0.1724 %. This result shows that the main phase contents of this kind of steel are BCC and FCC.

Post-impact examination of the 304L steel cross sections samples 1 to 6 shows the percentage values of HCP were, in sequence, 0.0188 %, 0.1225 %, 0.221 %, 0.281 %, 1.6445 and 1.699 %, with an estimation error of less than 10 % as shown in Tble 6.7. One test location point was selected about 2000 microns away from the edge of impact. Analyzing the EBSD test results showed that this type of steel 304L does not change its crystalline phase during impact shock under a high temperature and pressure. This type of alloy already has a significant amount of FCC phase combined with the original BCC that exists in the pre-impact test. FCC is a transitional phase pre-formed to the hexagonal HCP phase. This explains the high percentage of FCC throughout all test point locations for the 304L steel, as well as the phase alteration did not exceed the plastic limits or twinning deformation. Grains in this alloy are obviously more stable at the crystalline level. This kind of iron alloys shows resistance to phase changes behavior under high pressure shocks even close to the crater and impact holes as Figures show in chapters 3, 4, and 5.

Figures in chapter 4 of cross sections post-impact test sample show the percentage values of HCP at sections 1, 2, 3, 4, and 5, are in order: 0.0188 %, 0.1223 %, 0.221 %, 0.281 %, and 1.644 % respectively. However, at cross section number 6, at impact site, selected point C, at 1000 micron from the edge of the hole shows an insignificant value of HCP 0.092 % and 9.17 % accuracy. The location test of point A results have been ignored, which shows low confidence error of more than 20 % and HCP percentage of 1.699 %, which is less reliable than point C.

6.3 HY 100 Steel with Impact Velocity of 6.70 km/s

The pre-impact EBSD shows a reliable test results value of 0.002 % FCC and 99.98 % BCC, with null-HCP content in HY100 steel.

The post-Impact HY100 steel test results show the percentage of HCP ratios for the cross signal section sample 1 to 5 to be, in order, 0.31 %, 0.373 %, 0.40 %, 1.12 % and 1.50 %. As for the cross section sample 6, at the impact section, the percentage of HCP is around 2.29 percent at point G, taken as a reliable comparing point located at 2000 micron near the crater and projectile hole edge, its error is acceptable at 9.15 percent. Estimation certainty at this point is over 90 percent. Other points located at the same cross section 6 are A, B, and C a gage value of HCP of: 1.432 %, 2.50 %, and 2.29 %, with reasonable confidence as shown in Table 6.8. The crystal phase change from BCC to FCC and HCP, in this kind of steel is in contrast to the 304L. The EBSD results for 304L steel post-impact test proves that the microstructure phase has changed and plastic, twinning and plastic deformation start forming on the plane of the grains near the arc of the projectile and the crater section from body-centered cubic BCC into hexagonal close packed HCP, and face centered cubic, FCC. Also, Figures and tables in chapter 5 show the misorientation angles of more than 45 degrees; this means the crystal grains have changed the direction and shape due to the shock impact.

Among other things, EBSD reading results of the immediate area of the arc crater are very dull and dark and reflect a very high error, making the results in those areas inaccurate and not reliable.

6.4 General Discussion and Overview

Acquired EBSD data shows that there are general agreements with high certainty that at points 10 mm, or more, away from the projectile edges, i.e. cross sections 1, 2, 3, 4 and 5, there is no considerable amount of HCP change. Researchers have found that high purity ferrous alloys exposed to post impact have a tendency for increase of mechanical properties upon transition impact of 13.0 GPa. On the other hand, there is a gradient in shock hardening that is increasing as a function of propagation distance of the

impacted specimen. The comparisons in the five stages tabulated show the experimental and are results documented in chapters 3, 4 and 5.

Five stages of data comparisons are presented in the next sections. Stage one compares the non-impacted phase constructs for all the alloys combined. Stage two compare the propagation impact effect that can be modeled mathematically among the progressive same sample section according to the distance from the crater. Stage three addresses the effect of the power of impact on the same relative distant cross section location. Stage four, gives an overall discussion about the steel alloy, same plate sample steel plate. Stage five discusses one speed impact effect on all the three steel alloys under consideration: A36, 304L and HY100 consecutively. The discussed results shall be a convenient basis for future work. It proves valuable for directing the demand and imagination for the kinds of mechanical and other properties that are necessary, relevant, and must be accounted for.

6.4.1 Five-Stage Tabulated Comparisons: Stage One

We start with the three A36 steel plate specimens impacted by three predetermined impact speeds. The lists of Tables in the following sections are clearly valuable data for comparisons and sources of future research and information. Non-Impact Table 6.1 shows A36 steel crystalline phase ratios before impact. Clearly the BCC ratio is predominant, without a trace of HCP; however, the FCC merely exists with a minimal trace. During the heat treatment caused by the conventional cutting methods, a transformation of a small quantity of FCC took place in some insignificant trace, in addition to some intrinsic contamination in the committal alloy itself. However, the A36 cold steel alloy without impurities is expected to be of a pure 100 % BCC phase alone.

Table 6.1 non-impact phase ratio A36 steel

Crystal Unit Cell Structures	Non-Impact A36 Steel Phase
BCC	99.98 %
FCC	0.002 %
HCP	0 %

6.4.2 EBSD Results for All Sections and Speeds for A36 Steel

In a previous section, tabulated results in Tables 6.2, show the microstructure phase ratios at the reference location. The ratios, at the crater center, of BCC, FCC and HCP of A36 steel 90.30 %, 9.5583 %, and 0.1460 %. But at cross section number 4, the ratios are: 97.076 %, 2.9514 %, 0.081 %. Clearly, that point that near crater shows a higher HCP than the furthest from the crater, and the same thing for the same number 5, in Table 6.3 Points that seemed to change the most are those in the crater area. Many points were taken but the points selected in the table limited location points out the many that are scanned by EBSD are selected for the study. That is depending on the level of confidence. EBSD mapping have shown grain size in the vicinity of the crater, especially on the arc shock limits.

In Table 6.2 cross section sample 3 which is located 7.5 mm away from the impact section one can observe the higher percentage of FCC is significantly increased and an obvious significant reduction of BCC. This significant change can be interpreted as a corresponding transformation of phases between the BCC 96.35 % and FCC 3.629 %. Additionally a new phase started to appear which is the HCP 0.079 %. But the highest change of the BCC was obvious at the impact area exactly that is sample 6, location C. At that section BCC was 90.30 %, FCC 9.56 % and HCP 0.15 %.

The Table 6.3 list results for A36 steel alloy test under 4.51 km/s impacts. At this speed, a crater has started to appear. The pattern observed at Table 6.2 modified not as expected for BCC to decrease further at the same point of the impact section and can be explained by the existence of a crater. The produced crater has absorbed some of the transformation energy due to the resulted strains. Even that has propagated, not only at this portion, but rather at all sections. However, the HCP did consistently increase proportionally with the increase of speed and the twinning percentage increase too.

Table 6.2: The ratio of all phases depending on crater location A36 steel at 3.54 km/sec

Section Sample Numbers	Crystal Unit Cell Structures	Phase Content (%)
Sample 1	BCC	98.074
	FCC	1.8366
	HCP	0.063
Sample 2	BCC	98.382
	FCC	1.546
	HCP	0.072
Sample 3	BCC	96.35
	FCC	3.629
	HCP	0.079
Sample 4	BCC	97.076
	FCC	2.9514
	HCP	0.081
Sample 5	BCC	98.1262
	FCC	1.9212
	HCP	0.091
Sample 6 Location C	BCC	90.30
	FCC	9.5583
	HCP	0.1460
Non-Impact A36 Steel	BCC	99.98
	FCC	0.002
	HCP	0

Table 6.3 The ratio of all phases depending on crater location A36 steel at 4.51 km/sec

Section Sample Numbers	Crystal Unit Cell Structures	Phase Content (%)
Sample 1	BCC	98.3105
	FCC	1.6865
	HCP	0.075
Sample 2	BCC	98.507
	FCC	1.485
	HCP	0.078
Sample 3	BCC	96.82
	FCC	3.246
	HCP	0.082
Sample 4	BCC	96.096
	FCC	3.953
	HCP	0.1190
Sample 5	BCC	91.65
	FCC	8.31
	HCP	0.220
Sample 6 Location A	BCC	96.68
	FCC	2.87
	HCP	0.44
Non-Impact A36 Steel	BCC	99.98
	FCC	0.002
	HCP	0

Table 6.4 The ratio of all phases depending on crater location A36 steel at 5.81 km/sec

Section Sample Numbers	Crystal Unit Cell Structures	Phase Content (%)
Sample 1	BCC	98.876
	FCC	10.079
	HCP	0.442
Sample 2	BCC	99.4806
	FCC	0.928
	HCP	0.452
Sample 3	BCC	91.1078
	FCC	9.3748
	HCP	0.523
Sample 4	BCC	98.4246
	FCC	1.6866
	HCP	0.556
Sample 5	BCC	99.03
	FCC	0.88
	HCP	0.88
Sample 6 Location G	BCC	96.180
	FCC	0.6157
	HCP	3.204
Non-Impact A36 Steel	BCC	99.98
	FCC	0.002
	HCP	0

6.4.3 Stage 3: Effect of Impact Speed Demonstrated for A36 Steel

The phase content from EBSD images at crater location A and B in the A36 target impacted at 3.54 km/sec is shown in Figure 6.2. At this speed, the percentage of error is small and the percentage of reliability significantly higher. Tble 6.5 shows the error of each crater location (A, B) of A36 steel at 3.54 km/sec.

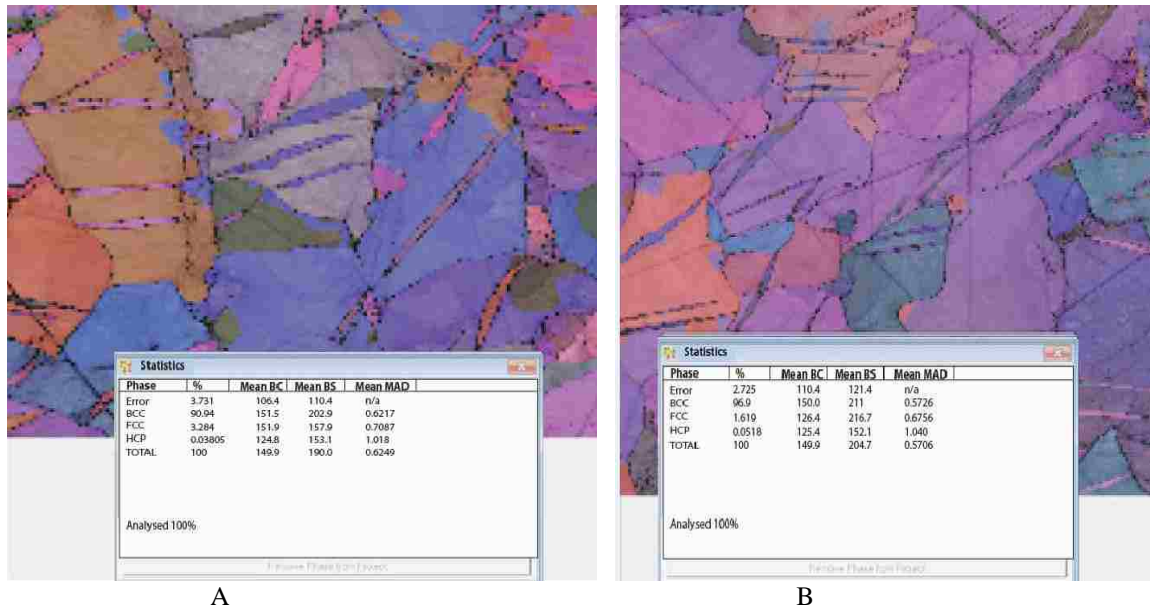


Figure 6.2 The error of each crater location (A, B) of A36 steel at 3.54 km/sec

Table 6.5 The error of each crater location (A, B) of A36 steel at 3.54 km/sec

Sample location 6-A, and B of A36 steel at 3.54 km/sec	Error
6-A	3.711 %
6-B	2.75 %

And because of the speed, a few that did not find many small granules around the arc crater compared to other speeds. In the crater area the HCP phase and plastic deformation twinning was observed around this area the misorientation angle 55-60 degrees.

Table 6.6 Effect of Impact Velocity Change

Section Samples Numbers	Crystal Unit Cell Structures	Impact A36 Steel Phase at 3.54 km/sec %
Sample 6 Location C	BCC	90.30
	FCC	9.5583
	HCP	0.1460
Section Samples Numbers	Crystal Unit Cell Structures	Impact A36 Steel Phase at 4.51 Km/sec %
Sample 6 Location A	BCC	96.68
	FCC	2.87
	HCP	0.44
Section Samples Numbers	Crystal Unit Cell Structures	Impact A36 Steel Phase at 5.81 km/sec %
Sample 6 Location Point G	BCC	96.180
	FCC	0.6157
	HCP	3.204

At A36 steel notes have been observed from the Tables 6.1, 6.2, 6.3 and 6.4.

- Near crater, the HCP is higher percentile than in far region. Grain size near impact is compacted near impact site as shown in Table 6.6.
- Twinning existed in the neighbor of the crater.
- Non-Impacted zone does not have any HCP or significant amount of FCC.
- Increasing impact momentum increased the HCP percentage.
- The low percentage of HCP is possibly because of the noise level of the system, but additional statistical analysis is needed to determine this for sure in Furthermore, and it is of interest to determine whether increasing the velocity of the projectile, thereby increasing the pressure, will increase the amount of non-BCC phases.
- Observing different orientations also provide further insight on the decreasing grain size Post-Impact BCC, FCC, and HCP Varies with test points.
- Grain size near impact is compacted near impact site. For example the presence of “twinning”

- Twinning was present closer to the impact area, and gradually dissipated away further from the impact zone.
- More twinning was present in the higher speed impact samples than the lower speed impact samples.
- The twinning was most significant during the testing of the samples from the 5.80 km/sec speed impact.
- Whenever the HCP ratio is high and the FCC ratio is Low and vice versa, and this was evident in the samples away from the crater since the FCC phase this is a transitional phase it shows that the new deformation start with HCP.

6.4.4 Stage 4: Comparison of All Three Steel Alloys

Tables 6.7, and 6.8 lists the EBSD scanning results for the other set of tested alloys, 304L and HY100 steels. Notice that the 304L steel alloy shows minimal effects due to even higher impact than the A36 steel was exposed, to as have been seen in the phase transformation from BCC. The 304L steel has already contained a significant amount of both FCC and HCP, in other words it did not get affected too much of neither the significant and sudden rise neither in dynamic pressure of impact nor the sudden rise of heat treatment. That would explain the heat resistance of this kind of steel alloy.

As for the HY100 steel, it went through a significant phase change within the same order of magnitude of impact as the 304L steel has been exposed to. The same pattern of expressed in the A36 steel alloy have been observed at the HY100 steel test.

Table 6.7 The ratio of all phases depends on crater location 304L steel at 6.58 km/sec

Section Sample Numbers	Crystal Unit Cell Structures	Phase Content (%)
Sample 1	BCC	16.340
	FCC	83.64
	HCP	0.0188
Sample 2	BCC	44.045
	FCC	55.84
	HCP	0.1223
Sample 3	BCC	12.54
	FCC	87.599
	HCP	0.221
Sample 4	BCC	46.2524
	FCC	53.9614
	HCP	0.281
Sample 5	BCC	27.308
	FCC	71.047
	HCP	1.644
Sample 6 Location A	BCC	32.7754
	FCC	68.67
	HCP	1.699
Non-Impact 304LSteel	BCC	33.1092
	FCC	66.718
	HCP	0.1724

Table 6.8 The ratio of all phases depending on crater location HY100 steel at 6.70 km/sec

Section Sample Numbers	Crystal Unit Cell Structures	Phase Content (%)
Sample 1	BCC	99.55
	FCC	1.141
	HCP	0.31
Sample 2	BCC	98.03
	FCC	1.598
	HCP	0.373
Sample 3	BCC	97.742
	FCC	1.866
	HCP	0.40
Sample 4	BCC	98.18
	FCC	0.71
	HCP	1.12
Sample 5	BCC	97.70
	FCC	0.804
	HCP	1.50
Sample 6 Location A	BCC	97.32
	FCC	0.391
	HCP	2.29
Non-Impact HY100 Steel	BCC	99.78
	FCC	0.22
	HCP	0

6.4.5 Stage 5: Overall Comparison of the Three Alloys

Pre-impact BCC, FCC and HCP ratios for 304L steel is 16.340 %, 83.64 % and 0.0188 % to 32.7754 %, 68.67 % and 1.699 %. This type of steel did not experience any change in the crystalline phase as it seemed clear Table 6.7. Depending on the location of the sample section, BCC, FCC and HCP of HY100 99.55 %, 1.141 % and 0.31 % to 97.32 %, 0.391 % and 2.29 %, as shown in Table 6.8 this type of iron ore is similar to large extent A36 steel in terms of the change in the crystalline phase and the existence of the twin.

When compared to the crater area in A36 steel, according to the three speeds, the error rate in all the sites that have been selected for the sample number 6 of A36 steel in different speed as shown in Table 6.9. At 3.54 km/sec at location A, the error was 3.73 % and the proportion of reliability 96.27 %. At the same sample location B, the error was 2.726 % and the proportion of reliability 97.274 %. Comparison of the types of Steels (A36, 304L, and HY100) choice a high speed of all (5.81 km/sec, 6.58 km/sec and 6.70 km/sec) is shown in Table 6.9 at Impact cross section site.

Table 6.9 Comparison of phase content in different steels when impacted at similar velocities

Section Samples Numbers	Crystal Unit Cell Structures	Impact HY 100 Steel Phase at 6.70 km/sec
Sample 6 Location A	BCC	97.32 %
	FCC	0.391 %
	HCP	2.29 %
Section Samples Numbers	Crystal Unit Cell Structures	Impact 304L Steel Phase at 6.58 km/sec %
Sample 6 Location A	BCC	32.7754 %
	FCC	68.67 %
	HCP	1.699 %
Section Samples Numbers	Crystal Unit Cell Structures	Impact A36 Steel Phase at 5.81 km/sec
Sample 6 Location Point G	BCC	96.180 %
	FCC	0.6157 %
	HCP	3.204 %

Table 6.10 Non-impact phase ratio A36, 304L, and HY100 steel

Crystal Unit Cell Structures	Non-Impact A36 Steel Phase %
BCC	99.98
FCC	0.002
HCP	0
Crystal Unit Cell Structures	Non-Impact 304L Steel Phase %
BCC	33.1092
FCC	66.718
HCP	0.1724
Crystal Unit Cell Structures	Non-Impact HY100 Steel Phase %
BCC	99.78
FCC	0.22
HCP	0

The test sites A or B and C are for A36 Steel at 5.81 km/sec. It has been found that the HCP ratio varies between 0.556 % 0.88 % and 2.215 % respectively as shown in Table 6.4. The test sites A or B and C on 304L Steel at 6.58 km/sec.

It has been found that the HCP ratio varies between 0.281 % 1.644 % and 1.699 % respectively. The test sites A or B and C on HY100 Steel at 6.70 km/sec, it has been found that the HCP ratio varies between 1.12 %, 1.50 %, and 2.29 % respectively.

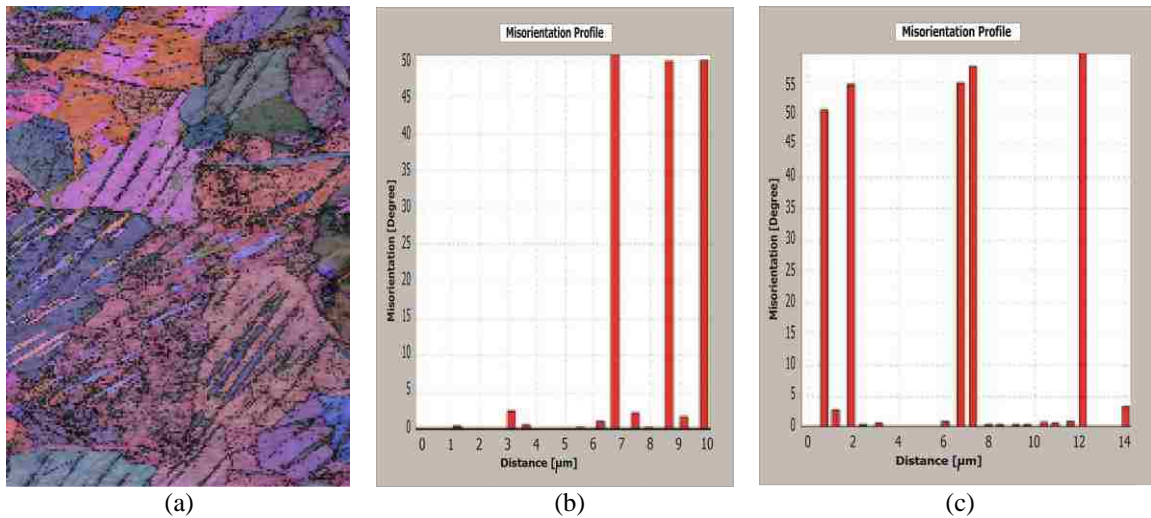


Figure 6.3 Impact A36 steel 5.80 km/sec sample (6) Misorientation angle (0-60°)

At 5.81 km/sec at location G the error is 9.85 % and the proportion of reliability 90.15 % In this speed we observe a higher error rate than the previous two-speeds caused due to the presence of grains around the crater area which are so little the EBSD cannot scan as a micro photo and may be mechanical polishing is not enough and we need to Ion-polishing.

The 304L kind of steel did not change between impact and Non-Impact because the original phase of 304L steel has already two phases BCC , FCC and some percentage of HCP as shown in Table 6.10 the percentage ratios are 33.1092 % , 66.718 % and 0.1724 % respectively. After impact the percentage ratios are 32.7754 % , 68.6 7 % and 1.699 % respectively as shown in Table 6.7.

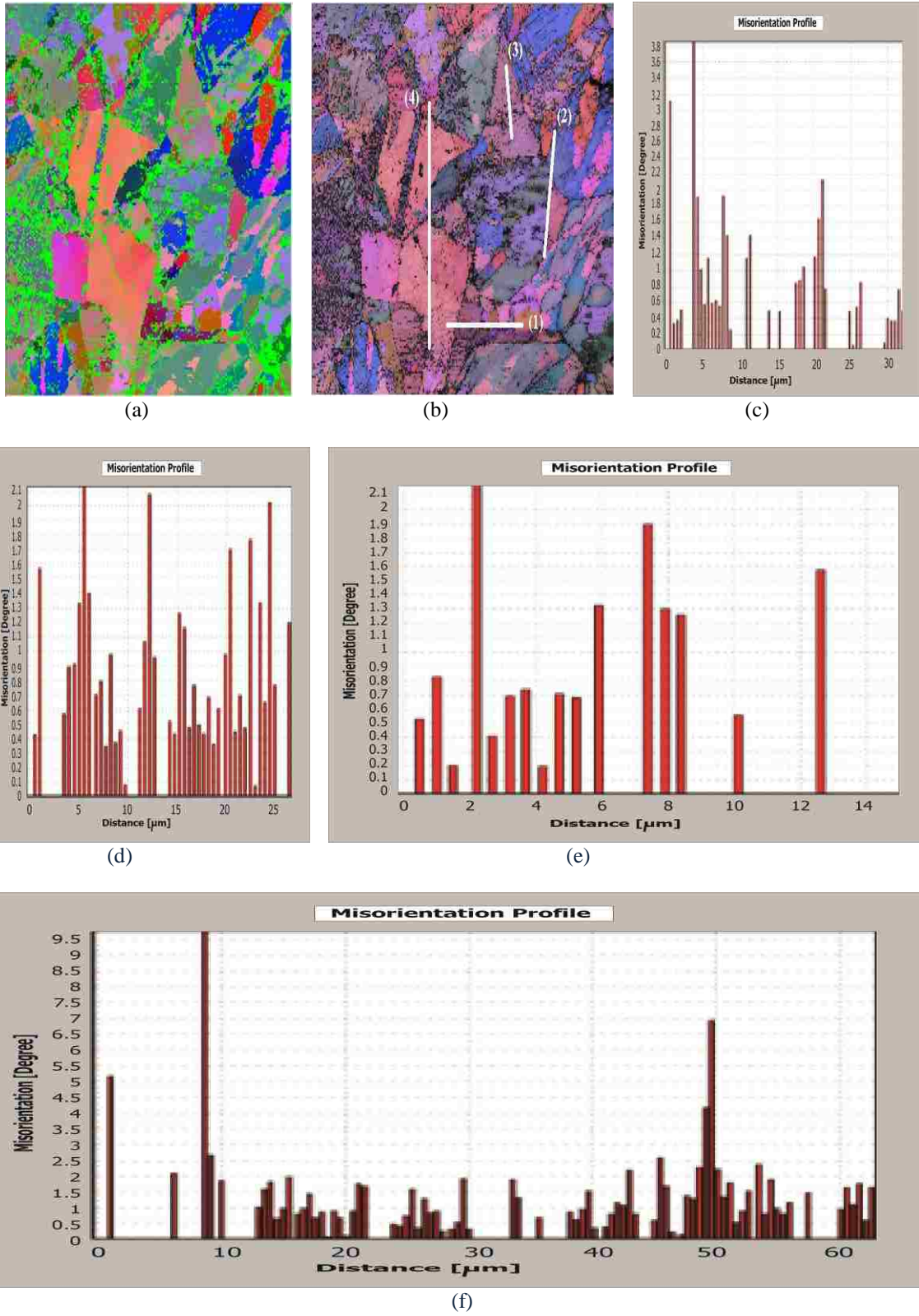


Figure 6.4 Misorientation angle measured along four different lines in the Impacted 304L 6.58 km/sec, sample location 6-A, shows: a) EBSD shows less noise, b) EBSD shows grains; c) Line 1, d) Line 2, e) Line 3, and f) Line 4

HY100 steel at 6.70 km/sec

The HY100 steel test result shown in table 6.8 HY100 steel has the original phase BCC and the percentage is 99.78 % and FCC 0.22 % after impact the phase change and the HCP phase increase and BCC decrease and some percentage of FCC transmission phase 97.32 %, 0.391 % and 2.29 %. At 6.70 km/sec at location A the error was 3.91 % and the proportion of reliability 96.09 %. This point location was the areas around the crater carrying hexagonal crystalline phase and the ratio of the misorientation angle of (50 - 60) degrees.

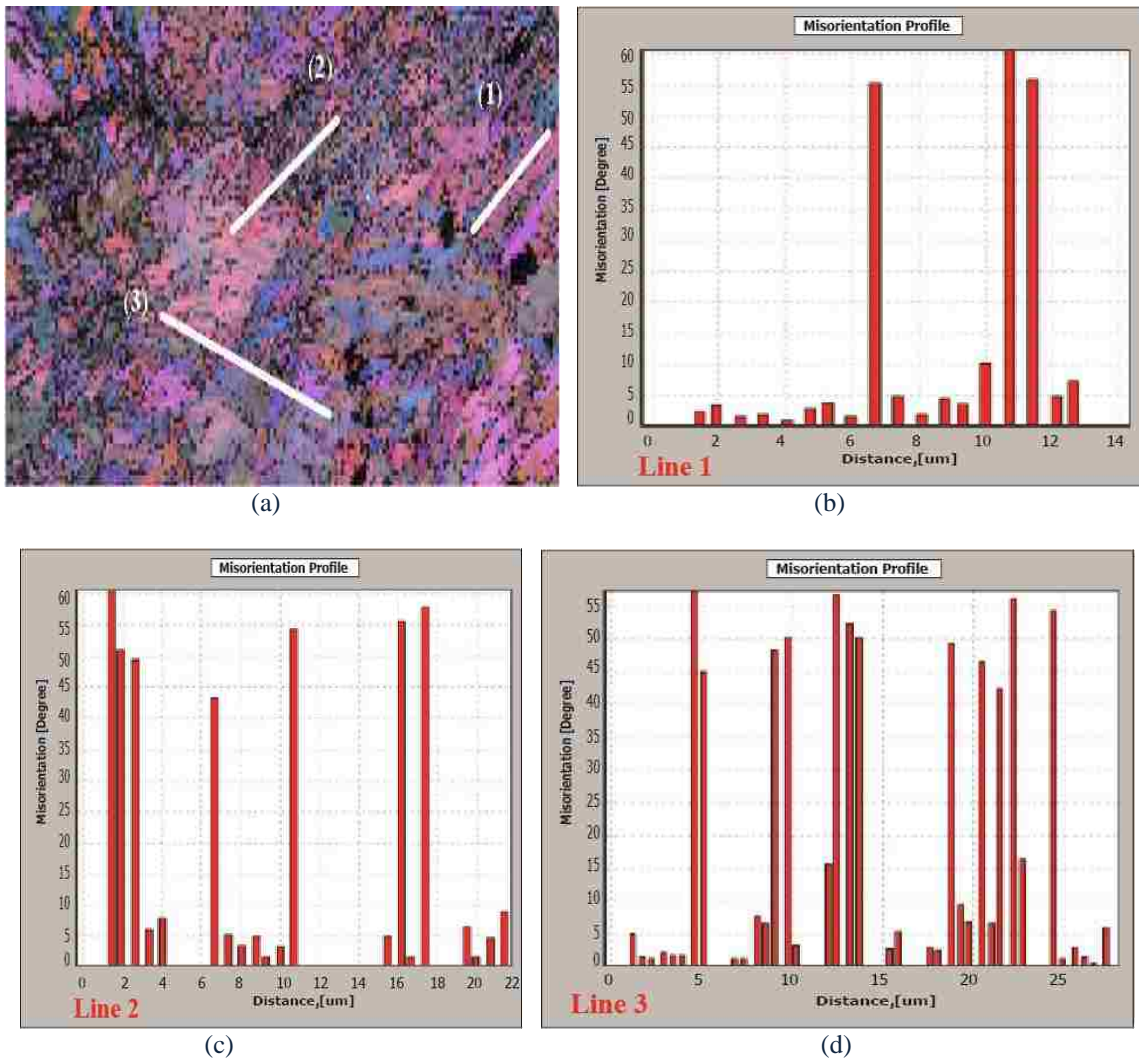


Figure 6.5 Misorientation angle measured along three different lines in the Impacted HY100 steel at 6.70 km/sec, sample location 6-A, shows: a) EBSD shows grains; b) Line 1, c) Line 2, and d) Line 3.

Tables 6.4, and 6.9 indicates that the phase change in A36 steel and HY100 are similar to large extent. The grain shape scanning seems viable and clear in the electron microscope images EBSD. Sample (6) of A36 and HY100 steels was etched with (HNO₃ 96 % and Ethanol 4 %) at 15 second because the microscopy photos are not clear before etching.

At table 6.4 near crater, the HCP is higher percentile than in far region. Grain size near impact is compacted near impact site. Twinning existed in the neighbor of the crater. Non-Impacted zone does not have any HCP or significant amount of FCC. Increasing impact momentum increased the HCP percentage. The low percentage of HCP is possibly because of the noise level of the system, but additional statistical analysis is needed to determine this for sure in Furthermore, and it is of interest to determine whether increasing the velocity of the projectile, thereby increasing the pressure, will increase the amount of non-BCC phases. Different orientations also provide further insight on the decreasing grain size Post-Impact BCC, FCC, and HCP Varies with test points. Grain size near impact is compacted near impact site. One such observation was the presence of twinning was present closer to the impact area, and gradually dissipated away further from the impact zone. More twinning was present in the higher speed impact samples than the lower speed impact samples. The twinning was most significant during the testing of the samples from the 5.80 km/sec speed impact Whenever the HCP ratio is high and the FCC ratio is Low and vice versa, and this was evident in the samples away from the crater since the FCC phase this is a transitional phase it shows that the new deformation start with HCP.

Several point location were scanned to build the discussion on more valid confidence level. Ion-Polishing shall be needed in order to increase the scanning visibility of the EBSD. Aiming to increase confidence and reduce the error of estimation. Here the clearest point was chosen in terms of minimum error to the EBSD. The comparison will be at by high velocities for each of the (A36, 304L and YH100) steel at the (5.80, 6.58 and 6.70) km/sec by arrangement as shown in Table 6.9.

Sample 1: centered 75mm away from impact crater, thickness is 2 mm (Rare)

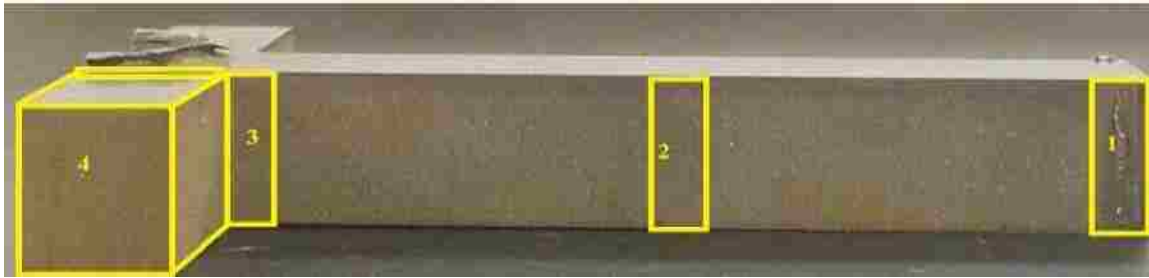
At A36 steel at 5.80 km/sec sample 1 has percentage of BCC, FCC and HCP (89.876, 10.079 % and 0.442 %) and sample 5 has (99.03 %,0.88 % and 0.88 %) by arrangement the plastic deformation and the twinning is only shown on sample 5 and sample 1, some little Twinning appears on sample 5, and almost null on sample 1. Most tense twinning region is around the shock center as shown in Table 6.4.

Quantitatively, Tables 6.2, 6.3, and 6.4 indicates the ratios of the mix relationship phase and shows estimation of BCC, being the dominant phase pre-impact, remains so after impact at all slides. However, HCP started to appear near impact and existed in the far locations but with insignificant proportion. FCC existed with insignificant pre-impact and became significant after impact at the impact and the neighborhood near impact, however with lower percentage and became insignificance again away for impact.

For 304L steel at 6.58 km/sec impact, sample 1 has a percentage ratio of unit cells of BCC, FCC and HCP phases (16.340 %, 83.64 % and 0.0188 %) and sample 5 has (27.308 %, 71.047 % and 1.644 %) by arrangement as shown in Table 6.7. This type of steel did not experience any change in the crystalline phase after shock, that is because the original crystalline phases contain BCC and FCC mix.

Sample (1): centered 75mm away from impact crater, thickness is 12.77 mm (Rare)

Sample (5): centered 10 mm and thickness is 12.77 mm (Near-Neighbor)



(a)



(b)

Figure 6.6 Impact A36 Steel location of sample 1 and 5. a) Side View shows sections 1-4. b) Cross section 4 and 5.

The cross-section location 1 from the A36 steel target with an impact speed of 5.80 km/sec has a percentage of unit cell phase of BCC, FCC and HCP (89.876 %, 10.079 % and 0.442 %) and sample 5 has (99.03 %, 0.88 % and 0.88 %) by arrangement the plastic deformation and the twinning is only shown on sample 5 and sample 1, some little twinning appears on sample 5, and almost null on sample 1. The percentages of crystals modes are for impact speed of 5.80 km/sec the figures of EBSD are a qualitative Figure which shows the trend of twinning change. Most tense twinning region is around the shock center. Quantitatively, Table 6.2, 6.3, and 6.4 indicates the ratios of the phase mix relationship and shows estimation of BCC, being the dominant phase pre-impact, remains so after impact at all slides. However, HCP started to appear near impact and existed in the far locations but with insignificant proportion. FCC existed with insignificant pre-impact and became significant after impact at the impact and the neighborhood near impact, however with lower percentage and became insignificant again away for impact.

At 304L steel at 6.58 km/sec sample 1 have a percentage rate of phase of BCC, FCC and HCP (16.340 %, 83.64 % and 0.0188 %) and sample 5 has (27.308 %, 71.047 % and 1.644 %) by arrangement. This type of steel did not experience any change in the crystalline phase after shock, because the original crystalline structure already contained BCC and FCC.

The HY100 steel at 6.58 km/sec, sample 1 has a percentage rate of BCC, FCC and HCP (99.55 %, 1.141 % and 0.31 %) and sample 5 has (97.70 %, 97.70 % and 1.50 %) in order. This type of steel behaved under impact as A36 steel extent where it was noted that the sample number 1. did not have the same high HCP ratio. There is a high proportion of phase transition from FCC to HCP, as seen in sample 5. The change is clear and appeared to have a plastic deformation and clear and the proportion of the change in the phase seemed clearly high compared to cross section sample 1.

Points of Interested of Low Error and High Confidence

Points that are useful because they carry small percentages of error and high confidence to compare between the three types of steel, near 1000 microns of the arc of projectile edge are shown in the table 6.11.

Table 6.11 Less error high reliability at 1000 micron far from the arc of projectile

Kind of steel	Speed km/sec	Error %	HCP %
A36	5.81 km/sec	9.65	3.204
304L	6.58 km/sec	9.17	1.699
HY100	6.70 km/sec	9.15	2.29

Table 6.9 shows that A36 steel and HY100 is similar in a large extent in the crystalline change of HCP change, even in the margin of error. 304L experienced no phase change before or after impact or in grain size.

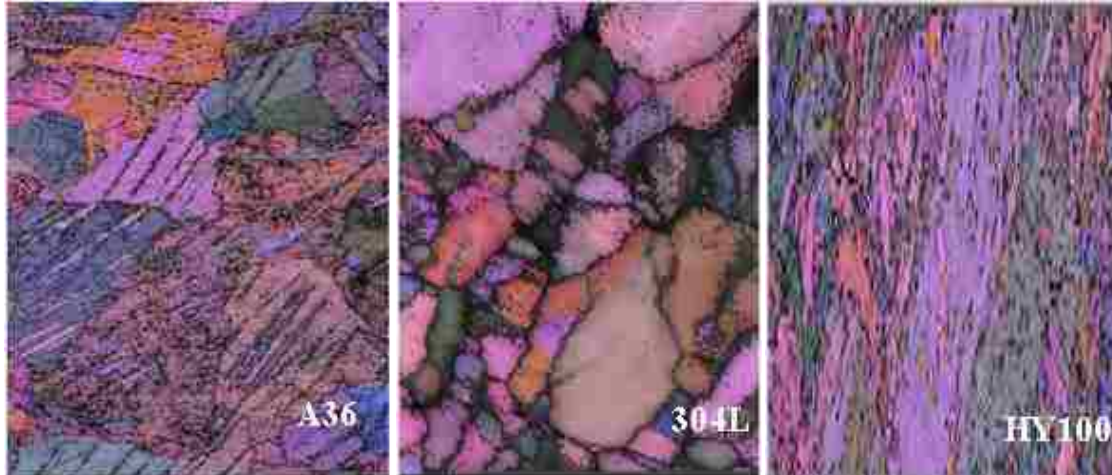


Figure 6.7 A36, 304L and HY100 EBSD Photos Less Error High Reliability at 1000 Micron far from the Arc of Projectile.

6.4.6 XRD Diffraction

Diffraction occurs when light is scattered by a periodic array with long-range order, producing constructive interference at specific angles. The electrons in an atom coherently scatter light. We can regard each atom as a coherent point scattered. The strength with which an atom scatters light is proportional to the number of electrons around the atom. The atoms in a crystal are arranged in a periodic array and thus can diffract light. The wavelength of x-rays is similar to the distance between atoms. The crystal system describes the shape of the unit cell, while the lattice parameters describe the size of the unit cell, the unit cell, and repeats in all dimensions to fill space and produce the macroscopic grains or crystals of the material.

The position and intensity of peaks in a diffraction pattern are determined by the crystal structure. The scattering of X-rays from atoms produces a diffraction pattern, which contains information about the atomic arrangement within the crystal. The diffraction pattern for every phase is as unique as one's fingerprint. Phases with the same chemical composition can have drastically different diffraction patterns, and use the position and relative intensity of a series of peaks to match experimental data to the reference patterns in the database. The electrons in an atom coherently scatter light. We can regard each atom as a scattered coherent point. The strength with which an atom scatters light is proportional to the number of

electrons around the atom. The atoms in a crystal are arranged in a periodic array and thus can diffract light. The wavelength of x-rays is similar to the distance between atoms.

The XRD can be used to measure patterns of solid surfaces, such as metals. However, the S/N ratio will be much lower than that of a crystalline powder. Several reasons for this include fewer reflective atomic planes in the solid, which reduces the signal, S . Contrasted to that in a powder, statistically all possible reflections (hkl planes) are readily abundant. Another reason the S/N will be lower is that a metal will often fluoresce, which increases the background, N . Nevertheless, measuring an XRD pattern on a metal can be helpful to confirm phases present in the metal, provided the phase has a weight percent of about 1 % or greater. The body-centered cubic BCC phase of iron, α -Fe, is found in all samples. The strongest peak of the BCC phase, the reflection from the (111) plane, has a peak value of about 1200 counts on a background of about 150 counts. This gives an S/N value of about 32. On the 304L steel, the face-centered cubic phase of Iron, γ -Fe, is the predominant phase (as is expected for an austenitic steel), but the BCC phase is also present. The Bruker D8 X-ray Diffractometer (XRD) is used to examine the designated steel alloy samples.

The XRD scanning machine is optimized for powder samples. Under ideal circumstances, one could expect a signal-to-noise ratio on the order of 200. Such circumstances would include having a very crystalline powder sample, such as a NIST standard, with a particle size on the order of 10 micron. On a recently measured pattern of a NIST silicon standard, the Si (111) peak had a peak value of about 50,000 counts, and it had a background of about 500 counts. This peak would therefore have an S/N ratio of about 220. For a “typical” sample, an S/N ratio on the order of 100 would be considered good data.

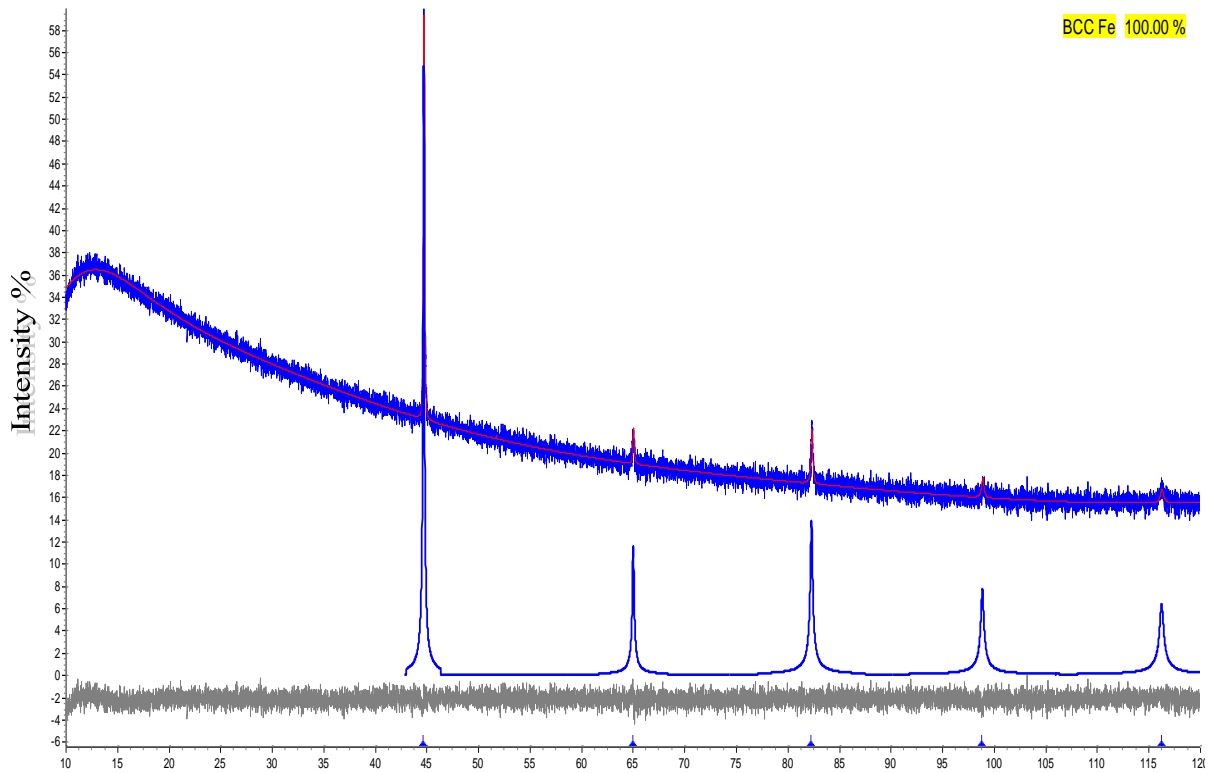
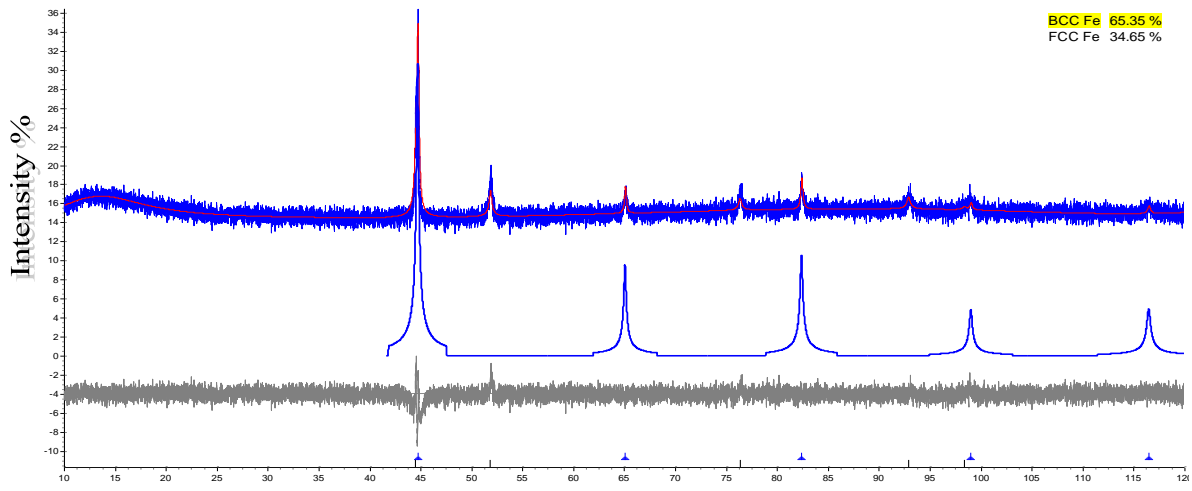


Figure 6.8 Non-impact A36 steel (phase 1 "BCC Fe" 100.000 %)

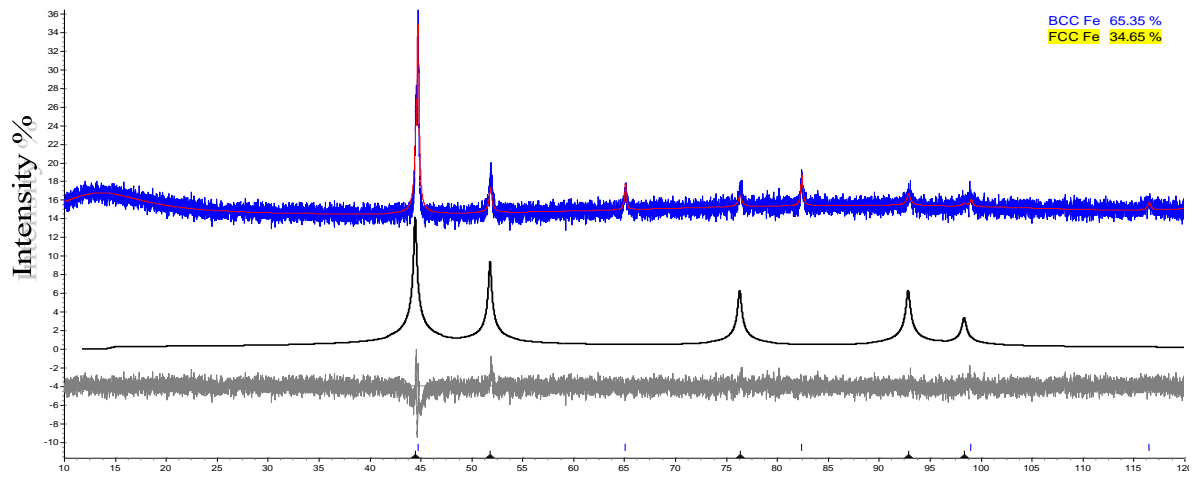
(a) BCC fit

Impact A36 Steel at 5.80 km/sec

On the non-impact A36 steel, only the BCC phase appears, as one would expect. On the impact sample, however, the FCC phase appears. Table 6.12 shows A36 steel lattice parameters and quantity for detectable phases before and after Impact speed at 5.80 km/sec.



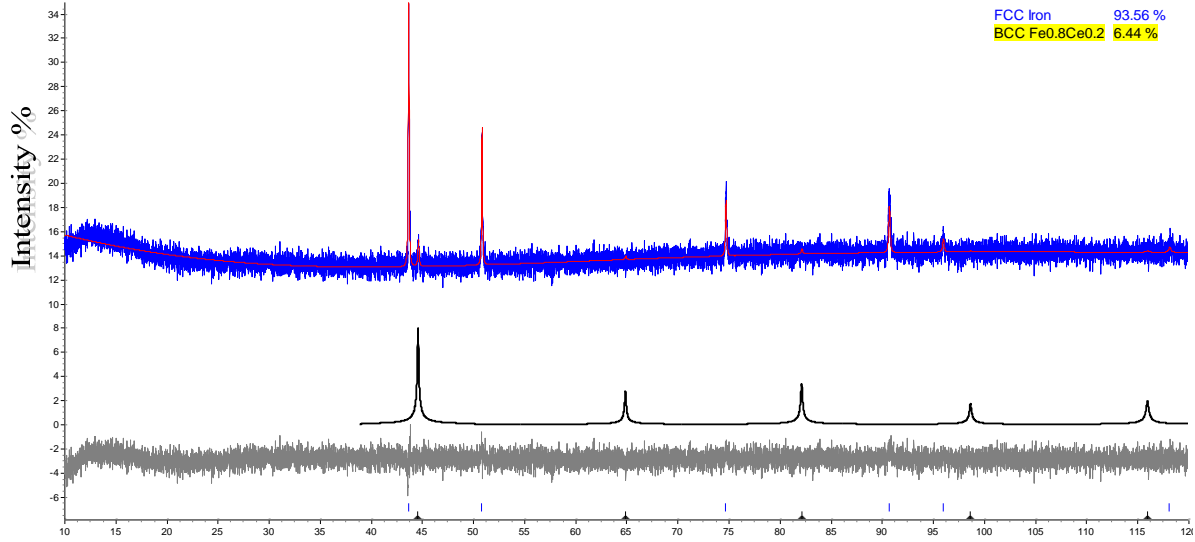
(a) BCC fit



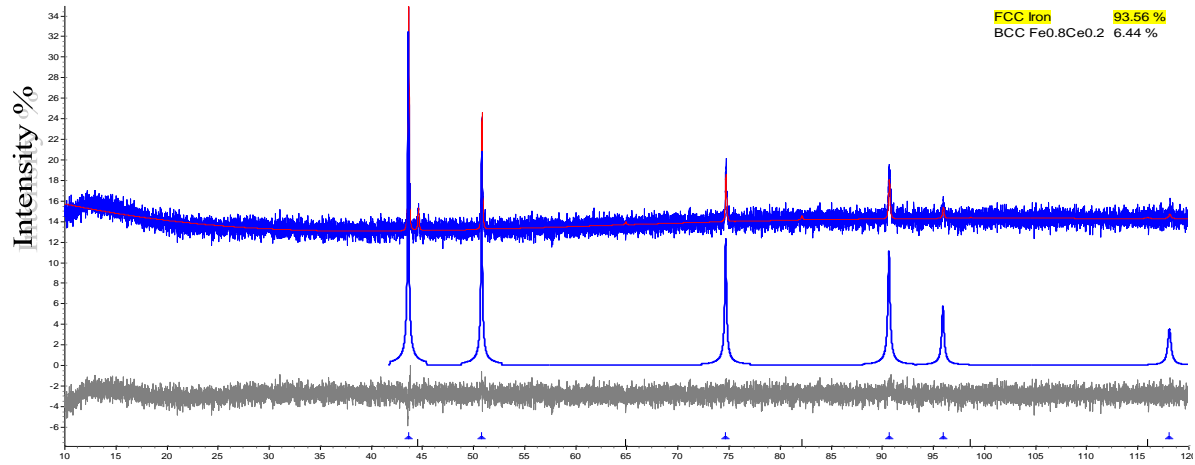
(b) FCC fit

Figure 6.9 A36 Steel impact at 5.80 km/sec Phase1:"BCC Fe" 65.35 % and Phase 2:"FCC"34.65 %.
a) BCC fit and b) FCC fit.

Non-Impact 304L Steel



(a) BCC fit



(b) FCC fit

Figure 6.10 Non-impact 304L Steel Phase 1: FCC Iron 93.56 % Phase 2: BCC Fe 0.8 Cr 0.2 6.44 a BCC fit, b FCC fit.

Impact 304L at 6.50 km/sec

In the case of 304L, the predominant FCC phase of the non-impact sample is reduced and the BCC phase is increased on the impact sample. Table 6.13 shows 304L steel lattice parameters and quantity for detectable phases before and after Impact speed at 6.58 km/sec.

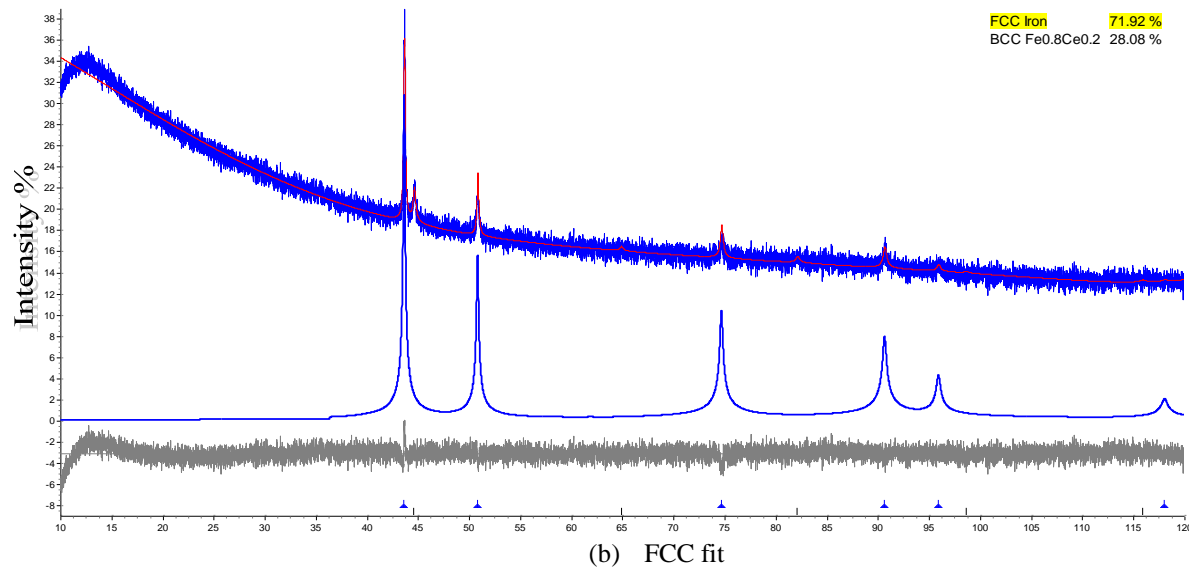
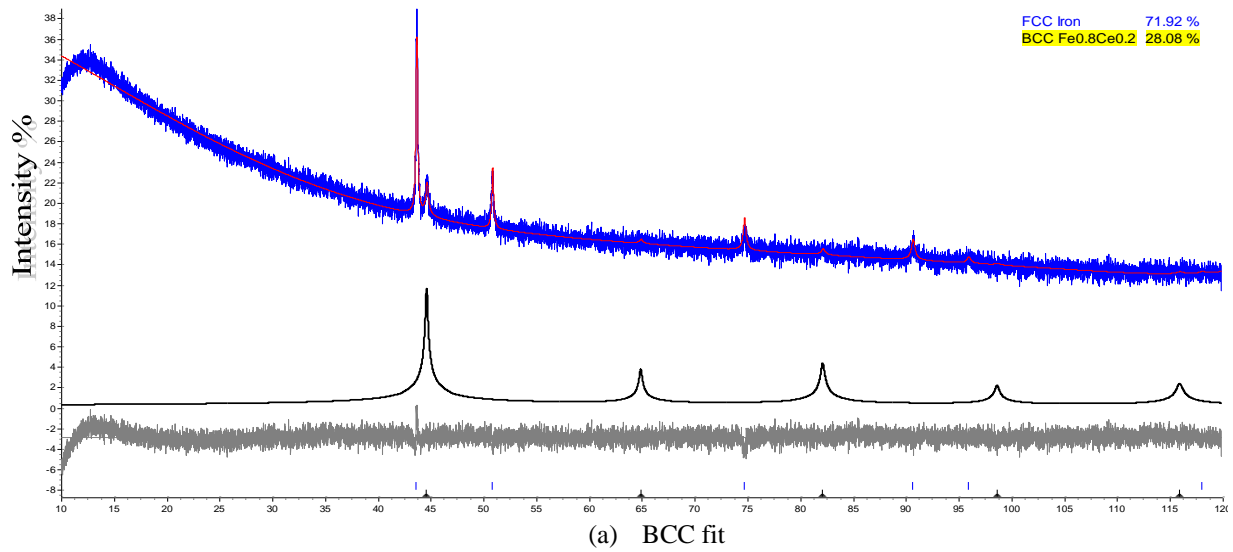
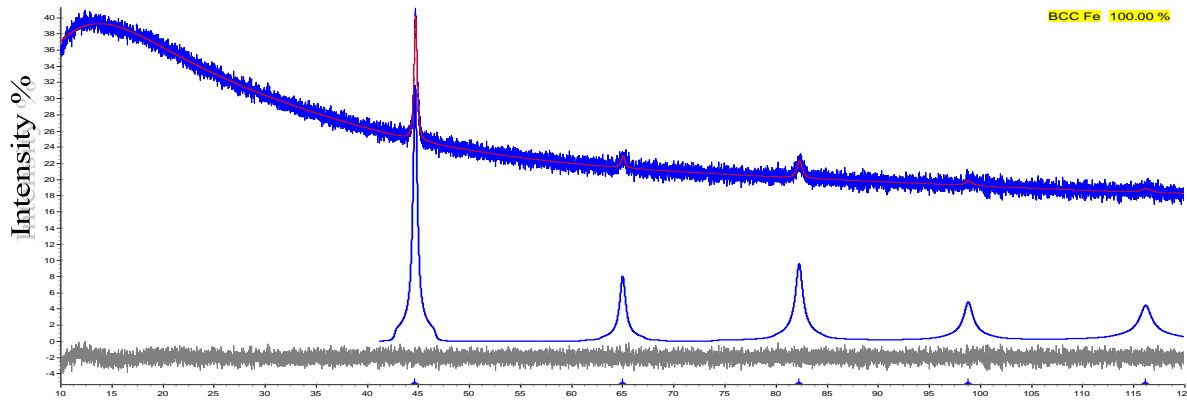


Figure 6.11 Impact 304L steel at 6.58 km/sec Phase 1: "FCC Iron" 72 % Phase 2: "BCC Fe 0.8 Ce 0.2" 28 %

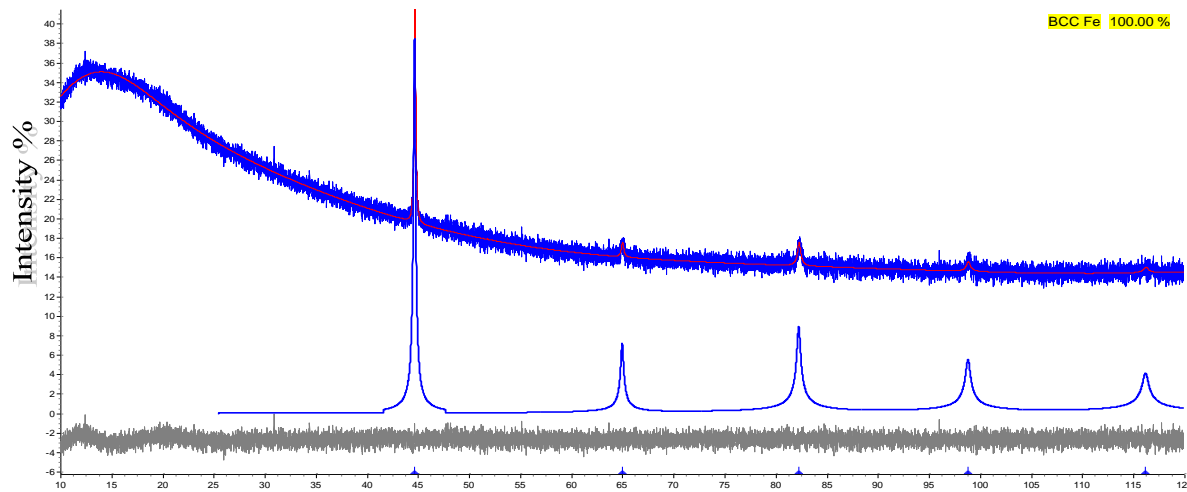
Non-Impact HY100 Steel



(a) BCC fit

Figure 6.12 Non-impact HY100 Steel Phase 1: "BCC Fe" 100.000 %

Impact HY100 at 6.70 km/sec



(b) FCC fit

Figure 6.13 Impact HY100 Steel at 6.70 km/sec Phase 1: "BCC Fe" 100.000 %

The HY100 steel is the only sample that shows no change from non-impact to impact. Only the BCC phase is seen. It is important to note that it is possible that there are other phases in the steels that are not visible in the XRD data Table 6.14 shows HY100 steel lattice parameters and quantity for detectable

phases before and after Impact speed at 6.58 km/sec. Indeed, electron backscatter diffraction (EBSD) data indicates the presence of a hexagonal close-packed (HCP) phase on the impacted steels, as well as the FCC phase on the HY100. A likely reason for this discrepancy is outlined above the “invisible” phases are not sufficiently abundant to be detected by powder XRD.

Table 6.12 A36 – Lattice parameters and quantity for detectable phases

	BCC		FCC	
	Lattice Parameter.	Weight %	Lattice Parameter.	Weight %
Non-impact	2.869×10^{-10} m	100 %	0 %	0 %
Impact	2.875×10^{-10} m	65 %	3.526×10^{-10} m	35 %

BCC	Cell Mass (g)	Cell Volume (Å ³)	Crystal Density g/cm ³	Crystallite Size (nm)	FCC	Cell Mass (g)	Cell Vol (Å ³)	Crystal Size (nm)
Non-impact A36	111.7	23.606	7.857	10000 (44000)	Non-impact A36	0	0	0
Impact A36	110.2	23.74	7.704	10000 (160000)	Impact A36	223.39	46.44	66 (25)

Table 6.13 304L – Lattice parameters and quantity for detectable phases

	BCC		FCC	
	Lattice Parameter.	Weight %	Lattice Parameter.	Weight %
Non-impact	2.873×10^{-10} m	6 %	3.593×10^{-10} m	94 %
Impact	2.874×10^{-10} m	28 %	3.594×10^{-10} m	72 %

BCC	Cell Mass (g)	Cell Volume (Å ³)	Crystal Density g/cm ³	Crystal Size (nm)	FCC	Cell Mass (g)	Cell Vol (Å ³)	Crystal Size (nm)
Non-impact 304L	110.153	23.7162	7.7126	100(19)	Non-impact 304L	234.761	46.3714	8.4067
Impact 304L	110.153	23.744	7.7036	66(25)	Impact 304L	223.387	46.435	7.9884

Table 6.14 HY100 – Lattice parameters and quantity for detectable phases

	BCC		FCC	
	Lattice Parameter.	Weight %	Lattice Parameter.	Weight %
Non-impact	2.870×10^{-10} m	100 %	0 %	0 %
Impact	2.870×10^{-10} m	100 %	0 %	0 %

BCC	Cell Mass (g)	Cell Volume (Å ³)	Crystal Density g/cm ³	Crystal Size (nm)
Non-impact HY100	111.693	23.630	7.8489	67.2(73)
Impact HY100	111.693	23.6421	7.8450	7000(57000)

CHAPTER 7

CONCLUSIONS AND RECOMMENDATIONS FOR FUTURE WORK

7.1 The Summary of Conclusions

7.1.1 Comparison, Comments, and Conclusion

Near the impact crater zone, the grain size was compressed the most, being exposed directly to the highest speed. Obviously that has resulted in crystalline displacement and new grains size, which did produce, plastic deformation twinning. The grain formed to plastic deformation twinning and dislocation into different planes creates new shapes. Ultimately it produces a deformation.

- Conceptually, during deformation atoms can be pushed out of place. When this happens, a symmetrical arrangement takes place. This produces a symmetrical deformation twins.
- From the above figures and diagram it is obvious that:
 - A non-Impacted zone does not have any HCP or significant amount of FCC.
 - Increasing impact momentum increased the HCP Percentage.
 - Near the crater, the HCP is a higher percentile than in far regions.
- Twinning deformation appeared permanent and not naturally reversible since a long time elapsed between experiment and EBSD viewing. Conceptually, during deformation atoms can be pushed out of place. When this happens a symmetrical arrangement takes place. This produces a symmetrical deformation twins.
- Descent from differentiated HCP, we find that the sample close to the crater is a higher proportions where plastic deformation of a higher rate exists, and the presence of twinning is largest and whenever we moved away from the crater side this opportunity, is also noted that surrounded arc crater the EBSD microscope cannot scan this area because the grains become small sizes in this area and cause the large number of error which had not been adopted in the results.

- When increasing the speed of the shock increased, the proportion of the crystalline phase change was increased, both in faraway areas of the crater and as well as the crater, but with different proportions. The proportion of the twinning deformation in the vicinity of the crater have been found, as expected, larger than that for a smaller speed. That explains the emergence of plastic deformation and twinning phenomenon near the crater, as expected. That has been demonstrated by the realization of large angles of misorientation which became apparent on the XRD chart, larger than 45 degrees between 55-60°. The nearby areas have a greater chance of changing the regional characteristics into the plastic deformation (twinning). As the results which shown in Table 7.1 and 7.2 A36 steel has the original phase BCC and the percentage is 99.98 % and FCC 0.002 %. After impact the phase changed and the HCP phase increased and BCC decreased and some a transmission phase percentage of FCC 96.6808 %, 1.1043 % and 2.215 %.
- A future work might significantly focus on both mechanical response and hardening as a function of propagation distance to verify that fact applied on all underlying test subjects steel alloys, A36, 304L, and HY100. Attention must be paid to the trends and the forms of change of physical properties due to impacts.

Table 7.1 Non-impact phase ratio A36 steel

Crystal Unit Cell Structures	Non-Impact A36 Steel Phase %
BCC	99.98
FCC	0.002
HCP	0

Table 7.2 Impact A36 steel phase at 5.80 km/sec

Crystal Unit Cell Structures	Impact A36 Steel Phase at 5.80 km/sec %
BCC	96.6808
FCC	1.1043
HCP	2.215

HCP ratio is at the section samples 1 to 5 is 0.063 %, 0.072 %, 0.079 % and 0.081% respectively. At the section sample 6 or impact area, the percentage of HCP is around 0.091 %, 0.1460 %, 0.2155 % and 1.0402 %.

Monitoring the relationship between the increases in HCP, we have found that the sample closest to the crater obtained a higher proportion of HCP, which explained the plastic higher deformation rate and the presence of a larger amount of twinning at these sections close to the crater. The further away from the crater the twinning was found less significant. Surrounding the arc and crater the EBSD microscope was not able to produce a reliable effective scanning with high confidence or acceptable predicted error. This reaction is in part, attributed to the smaller grain sizes at these areas.

HCP in a single sample was found to vary by its location relative to the crater. For example, section sample 4, HCP was found to vary from the site (location A and D), the same thing for section sample 5, the obvious trend was the high rates of HCP near the crater. Calculating and plotting the misorientation and dislocation angles, found that in the crater and nearby areas the misorientation values are 55-60 degrees. This indicates the existence of the twinning, (Misorientation angles are greater than 45°). The crystals change their positions and orientation under the impact of this high pressure and temperature. HCP had changed from BCC as has been shown. The Misorientation angles schematic representation is shown in chapter 3, 4, and 5.

High-rate compression tests were conducted from 75 to 14.9 GPa after 2.5 milliseconds at 4.51 km/sec. At A36 steel, the percentage of HCP ratio is at the sections samples 1 to 5, 0.075 %, 0.078 %, 0.117 %, 0.1190 % and 0.220 %. At the section sample 6, or impact areas the percentage of HCP is around 0.44 %, 1.17 % and 1.1536 %.

When increasing the shock speed the proportion of the crystalline phase, as well as the proportion of the deformation twinning, at the crater and in the vicinity of the crater were increased. The angles of misorientation were found to be between 55-60° and the nearby areas have a greater chance of changing the form plastic deformation and twinning.

Pressures of 95 GPa have decayed to a 14.9 GPa at 5.80 km/sec after 2 milliseconds. Tabulated results showed that A36 steel HCP phase percentage were 0.442 %, 0.452 %, 0.523 %, 0.556 % and 0.88 % at the sections samples 1 to 5.

At sample 6 impact area, the percentages of HCP were around 1.20 %, 1.488 %, 1.222 %, 2.215 % and 3.204 % at location G and the error 9.85 % Sample 6 was etched with HNO₃- 96 % and Ethanol 4 % for 15 second.

The densest twinning regions have been around the shock center. Quantitatively, all tables of sample 6 starting from location B have ratios of the phase mix and show an estimation of BCC, to be the dominant phase pre-impact. It remained so after impact for all slides. However, HCP started to appear near impact and existed in the far locations in insignificant proportions. FCC existed with an insignificant pre-impact and became significant. At the impact and the neighborhood near impact, however, with a lower percentage and became insignificant again away from the impact.

The results of 304L steel shows has three phases: BCC, FCC and some little percentage of HCP 33.109 %, 66.718 % and 0.1724 % respectively. The real phase of this kind of steel is BCC and FCC. In this kind of steel, the choice is only one high speed impact 6.58 km/sec and after that, it was found that the high speed of A36 steel have had the biggest share of the appearance of change-phase HCP and twinning deformation. The 304L steel the percentage of HCP ratio is at the sections samples 1 to 6, 0.0188 %, 0.1225 %, 0.221 %, 0.281 %, 1.6445 % and 1.699 %.

Of all the results stated above in the tables and images as shown in chapter 4 of this type of iron alloy it was found that this type of steel 304L does not change its crystalline phase during impact shock under a high temperatures and pressure. This is because this type of alloy has the original phase before impact BCC and FCC since FCC is the transitional first phase to reach the hexagonal HCP phase. This is the reason the percentage of FCC is high throughout all locations and samples of 304L. The grained stability on the crystalline level did not exceed the plastic limits or twinning deformation crystalline. This shows that this kind of Iron alloy shocked unimpaired under high pressure and temperature has been the crater area test and near crack figures as shown in chapter 4.

The HY100 steel scanning shows HCP percentage at the sections samples 1 to 5, to be 0.31 %, 0.373 %, 0.40 %, 1.12 % and 1.342 % with a high accuracy estimate. At the section sample 6 impact areas, the percentage of HCP was around 1.432 %, 2.50 %, and 2.29 %. Figures and Tables show that HY100 steel has changed the crystal phase from BCC to FCC and HCP, and that plastic deformation and twinning start forming. The change occurred is partial from body-centered cubic BCC into hexagonal close packed HCP, or face centered cubic, FCC. In addition misorientation had occurred greater than 45 degrees and this means the grain size of the crystal changed the direction due to the shock impact.

The crystalline system remained out of the original initial order, however, it has remained orderly, in a new, but still organized nature.

Quantitatively, among other things, the immediate areas of the arc crater were not certain and do not have any reliable accuracy. And additionally, mapping on EBSD scanning quality was very poor and non-visible, making the results in those areas possibly and unreliable. An Ion-polishing technique for better quality is suggested for future research work at the very near point of both crater and ark of the impact hole.

7.2 Future Work

This chapter has examined and discussed the experimental results of examined impacted specimens of three kinds of steel alloys in terms of fingerprints changed in microstructure of impacted areas with different impact momentum and location of tested points relative to the generated craters. The twinning phenomenon has been also, addressed. Results were acquired mostly by EBSD and XRD. Quantified parameters obtained from both devices are used in the underlying discussions. Additionally, comparisons between the three kinds of steels under consideration have been covered. Finally, Recommendation for future work of significant value is presented.

APPENDIX A

Table A1 A36 steel mechanical properties

Condition	Tensile Strength (PSI)	Yield Strength (PSI)	Reduction of Area	Elongation in 2"	Brinell Hardness
ASTM A36	58,000-80,000	36,000	60	30	149

C	Si	Mn	S	P	Cr	Mo	V	Cu
max 0.4	max 0.5	max 1.6	max 0.04	max 0.04	max 0.5	max 0.4	max 0.1	max 0.3

Carbon, Max %	0.026
Manganese, Max %	0
Phosphorus, Max %	0.04
Sulphur, Max %	0.05
Silicon, Max %	0.4
Copper, Max %	0.20

Typical Mechanical Properties

Tensile Strength ksi	58-80
Yield 2 % Offset ksi	36

Plates and Bars: D, E

Elongation in 8 in (min)	20 %
Elongation in 2 in (min)	23 %

Shapes:

Elongation in 8in (min)	20 %
Elongation in 2in (min)	21 %

APPLICATIONS

ASTM A36 is used for general purpose structural, machinery parts, frames, fixtures, automotive and agricultural implements and equipment, brackets, stakes, ornamental works, forgings, base plates, gears, cams, sprockets, jigs, rings, templates, fixtures, bearing plates, tanks, bins, various parts obtained by flame cutting, and miscellaneous non-critical applications that involve mild cold bending, mild hot forming, punching, machining, and welding.

A36 steel is a standard steel alloy that is a common structural steel in the United States. The A36 standard was established by the standards organization ASTM International. Steels, A36 has a density of $7,800 \text{ kg/m}^3$ (0.28 lb/cu in). Young's modulus for A36 steel is 200 GPa (29,000,000 psi). A36 steel has a Poisson's ratio of 0.32, and a shear modulus of 75 GPa (10,900,000 psi).

A36 Steel Crystal Structure

Metal	Crystal Structure	Atomic Radius (nm)
Iron (Alpha)	BCC	0.1241

APPENDIX B

TEST PROTOCOL

Test Sample Description

15.4 x 15.4 cm A36 steel plates of 1.27 cm A36 steel thickness are impacted. Test preparation includes:

- Cut sections from target plate
- Mechanical polishing
- Electro-polishing
- Chemical etching
- Ion beam milling / Ion etching
- Coating
- Sample storage

The impacting gun is a 2-stage light gas gun uses a powder breech to fire a plastic piston into a pump tube filled with helium or hydrogen. The light gas is compressed as the piston moves through the pump tube. A petal valve separates the light gas from the launch tube, which is under vacuum. The petal valve ruptures from the compressed gas causing the projectile to rapidly accelerate down the launch tube and into the containment tank where it will impact the target. These experiments are designed so that the projectile causes severe damage to the target but does not penetrate all the way through. A successful experiment will leave the target plate with a large crater in the front and a smooth bump in the back.

- The impacting momentum range is at velocities between 3 km/sec and 6 km/sec.

The damage zone develops in the target within 5 microseconds. Some steel materials go through a reversible phase change when subject to elevated temperature and high quasi-static pressure. It is unknown whether A-36 steel experiences this phase change during high velocity impact.

The reviewed metals were classified into one of eight different material categories:

Mild- Mild carbon steel with less than 0.29 % carbon by weight

Medium- Medium carbon steel with carbon weight percent between 0.30 % and 0.59 %

High Strength- Low alloy steel with yield strength between 250 MPa and 600 MPa

Dual Phase- High strength steel that has a ferrite and martensitic microstructure

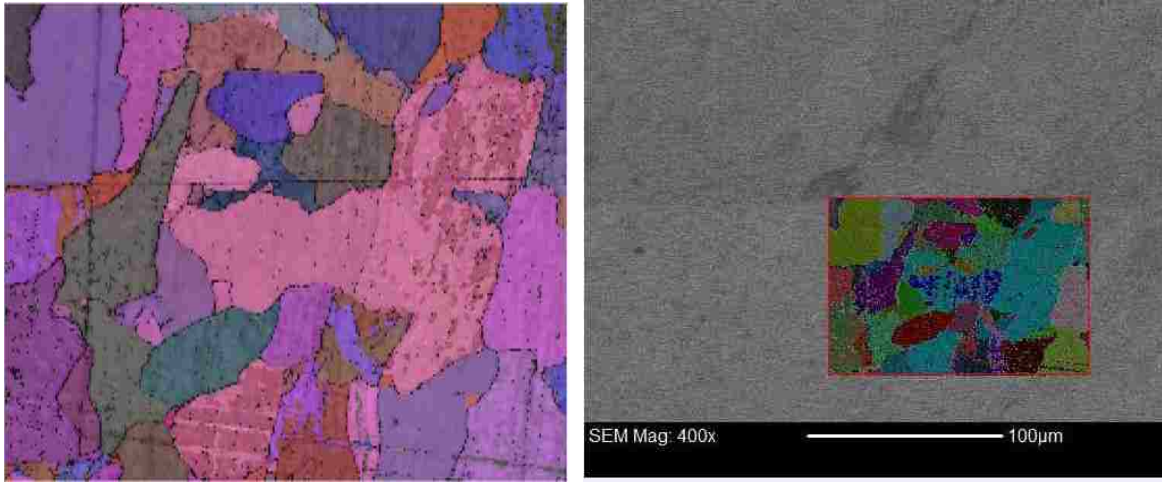
TRIP- High strength that has a ferrite, bainite, and retained austenite microstructure

Stainless- Steel alloy with minimum of 11 % chromium content by mass

Aluminum Alloy- Metallic alloy in which aluminum is the predominant metal

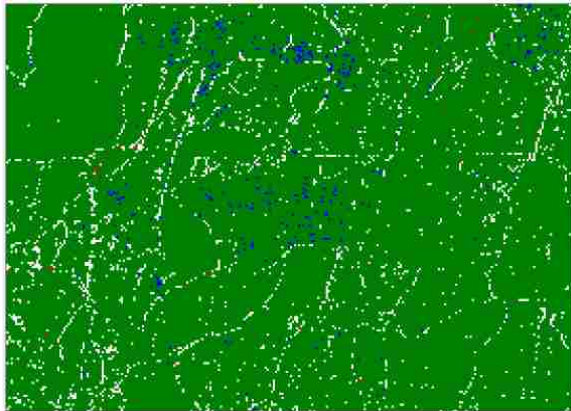
Magnesium Alloy- Metallic alloy in which magnesium in the predominant metal

APPENDIX C



(a)

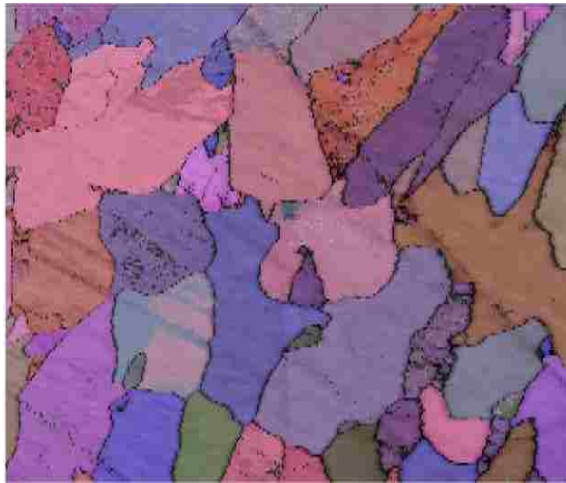
(b)



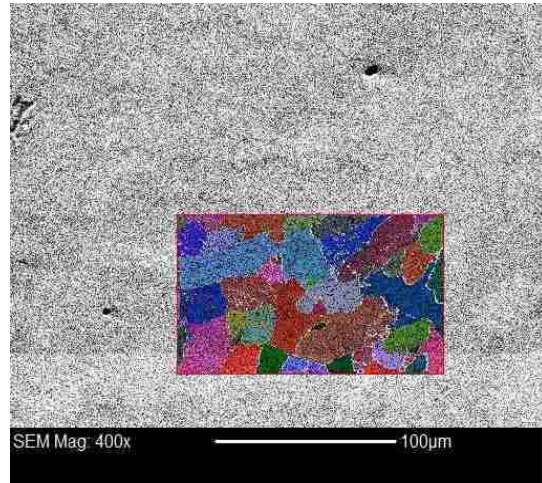
(c)

Table C1 Impact phase ratio of A36 steel at 3.54 km/sec sample location 1-D.	
crystal unit cell structures	Impact A36 Steel Phase at 3.54 km/sec
BCC	99.047 %
FCC	0.873 %
HCP	0.080 %

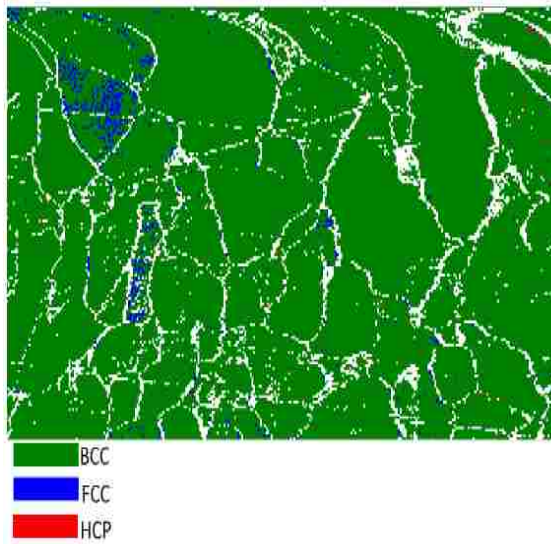
Figure C1: EBSD data from A36 steel, sample location 1-D, after impact velocity of 3.54 km/sec showing: a) grain, b) 400X magnification and the original length of the map, and c) phase map.



(a)



(b)



(c)

Table C2 Impact phase ratio of A36 Steel at 3.54 km/sec sample location 2-D	
Crystal Unit Cell Structures	Impact A36 Steel Phase at 3.54 km/sec
BCC	98.542 %
FCC	1.41075 %
HCP	0.050 %

Figure C2 : EBSD data from A36 steel, sample location 2-D, after impact velocity of 3.54 km/sec showing: a) grain, b) 400X magnification and the original length of the map, and c) phase map.

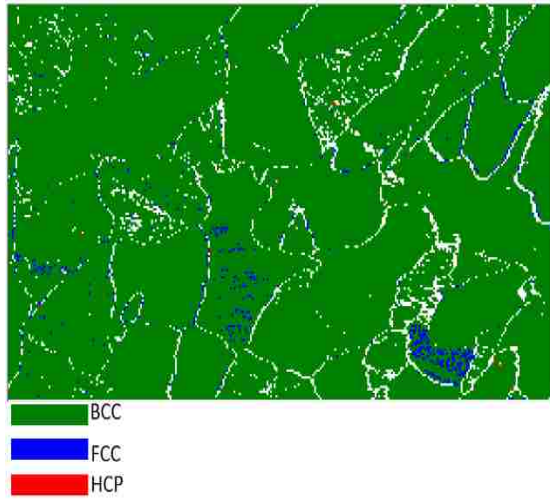
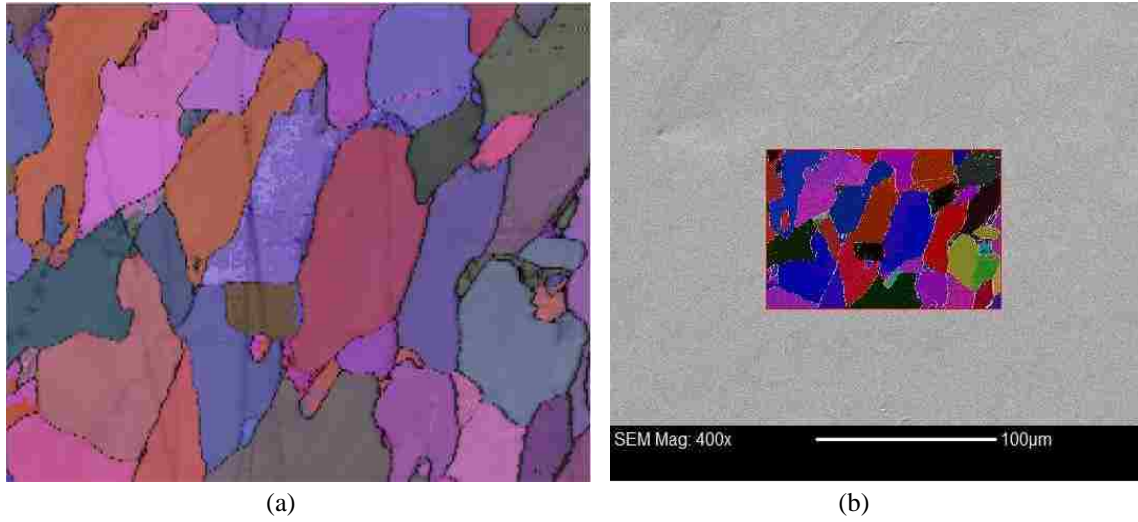
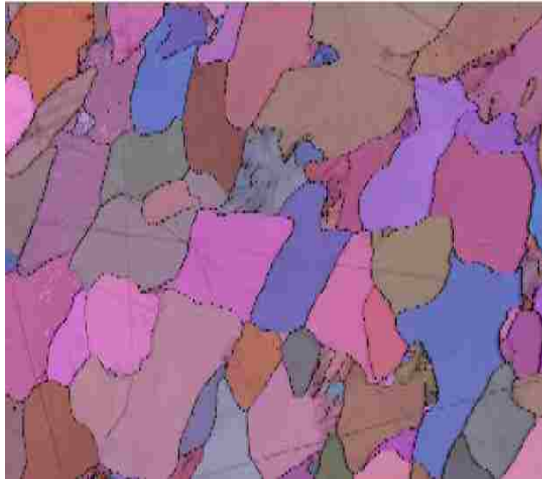


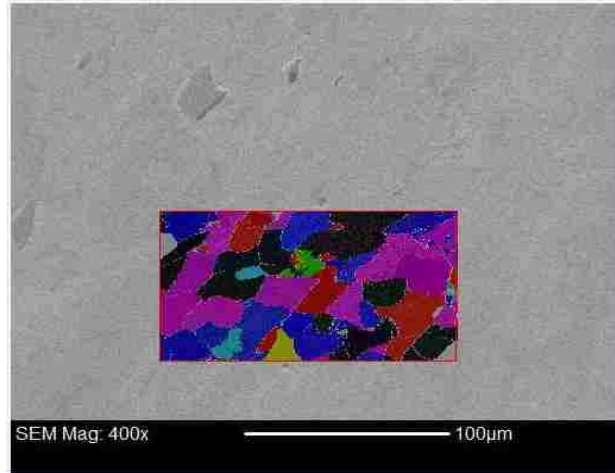
Table C3 Impact phase ratio of A36 Steel at 3.54 km/sec sample location 3-D	
Crystal Unit Cell Structures	Impact A36 Steel Phase at 3.54 km/sec
BCC	96.71 %
FCC	3.264 %
HCP	0.030 %

(c)

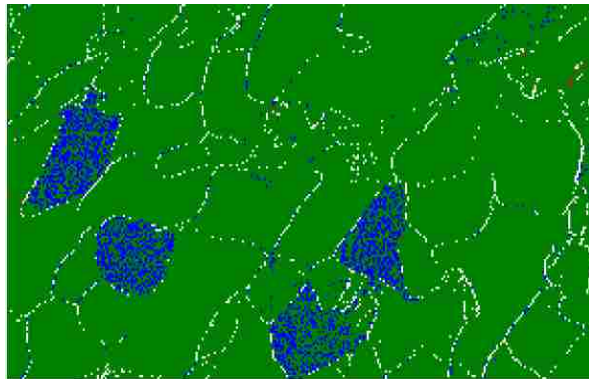
Figure C3: EBSD data from A36 steel, sample location 3-D, after impact velocity of 3.54 km/sec showing: a) grain, b) 400X magnification and the original length of the map, and c) phase map.



(a)



(b)

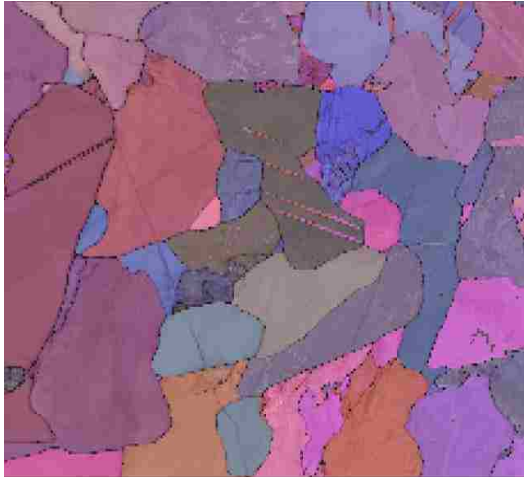


■ BCC
■ FCC
■ HCP

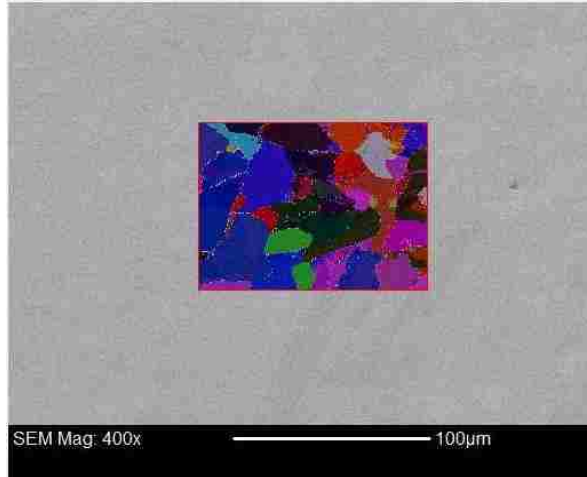
(c)

Table C4 Impact phase ratio of A36 Steel at 3.54 km/sec sample location 4-C	
Crystal Unit Cell Structures	Impact A36 Steel Phase at 3.54 km/sec
BCC	94.974 %
FCC	4.99 %
HCP	0.035 %

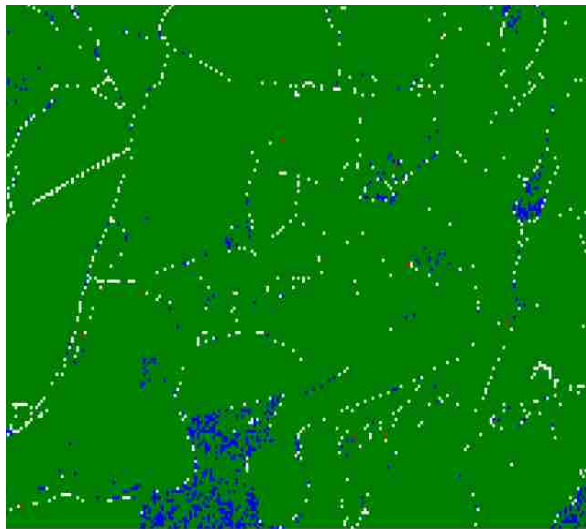
Figure C4: EBSD data from A36 steel, sample location 4-C, after impact velocity of 3.54 km/sec showing: a) grain, b) 400X magnification and the original length of the map, and c) phase map.



(a)



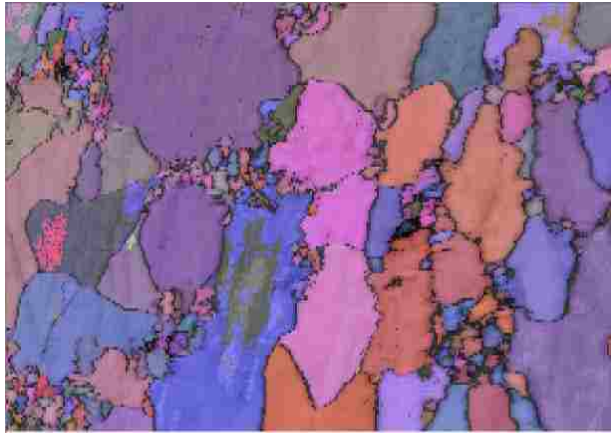
(b)



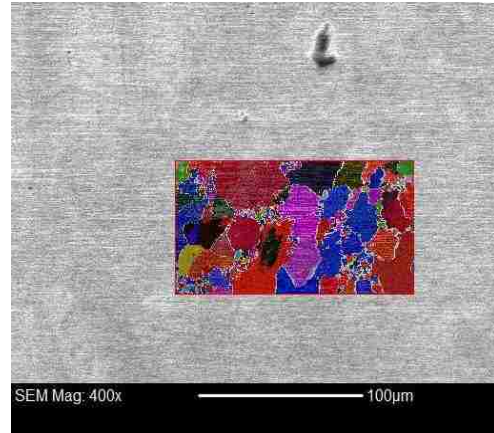
(c)

Table C5 Impact phase ratio of A36 steel at 3.54 km/sec sample location 5-B	
Crystal Unit Cell Structures	Impact A36 Steel Phase at 3.54 km/sec
BCC	98.1262 %
FCC	1.852 %
HCP	0.022 %

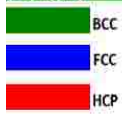
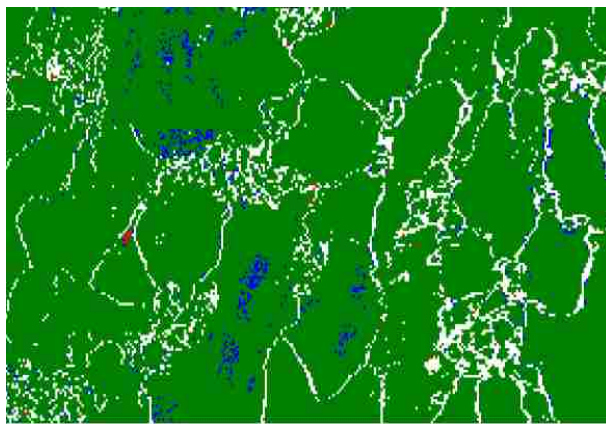
Figure C5: EBSD data from A36 steel, sample location 5-B, after impact velocity of 3.54 km/sec showing: a) grain, b) 400X magnification and the original length of the map, and c) phase map.



(a)



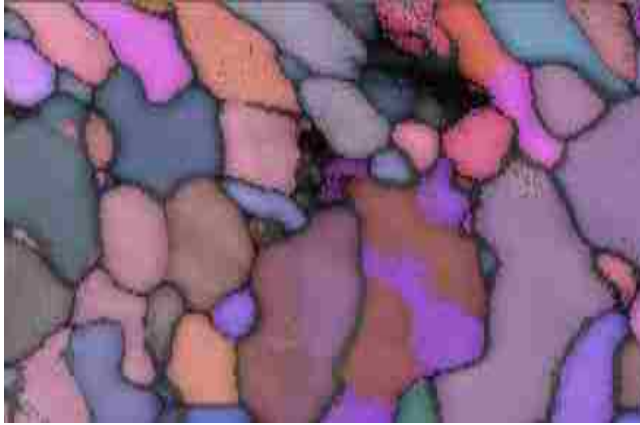
(b)



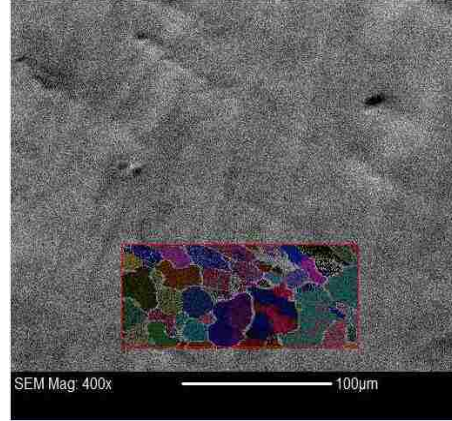
(c)

Table C6 Impact phase ratio of A36 steel at 4.51km/sec sample location 1-C	
Crystal Unit Cell Structures	Impact A36 Steel Phase at 4.51km/sec
BCC	98.82 %
FCC	1.69 %
HCP	0.1054 %

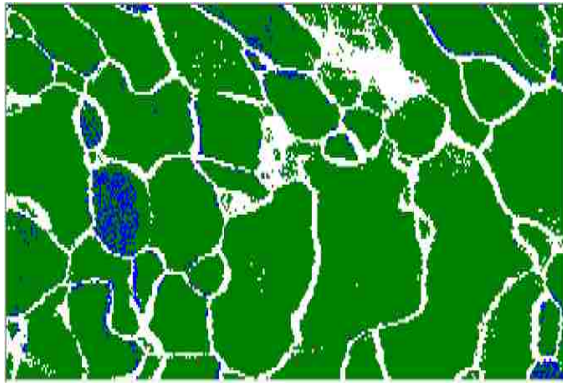
Figure C6: EBSD data from A36 steel, sample location 1-C, after impact velocity of 4.51 km/sec showing: a) grain, b) 400X magnification and the original length of the map, and c) phase map.



(a)



(b)

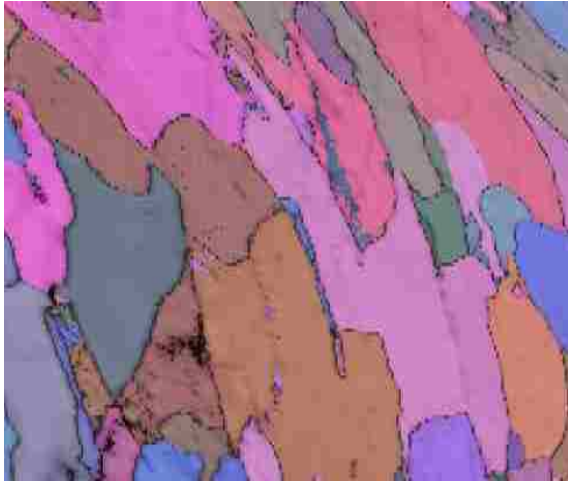


■ BCC
■ FCC
■ HCP

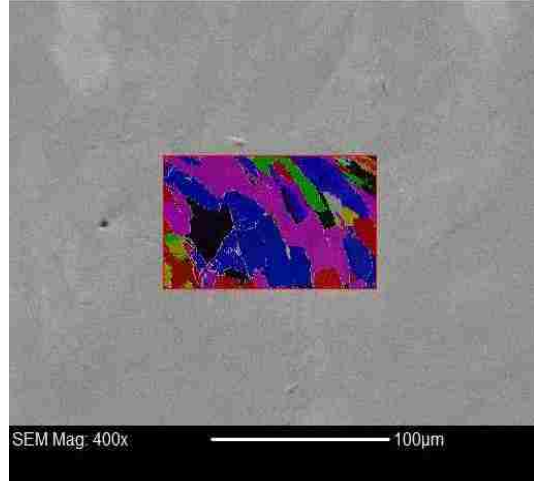
(c)

Table C7 Impact phase ratio of A36 Steel at 4.51 km/sec sample location 2-B	
Crystal Unit Cell Structures	Impact A36 Steel Phase at 4.51 km/sec
BCC	97.2071 %
FCC	2.757 %
HCP	0.036 %

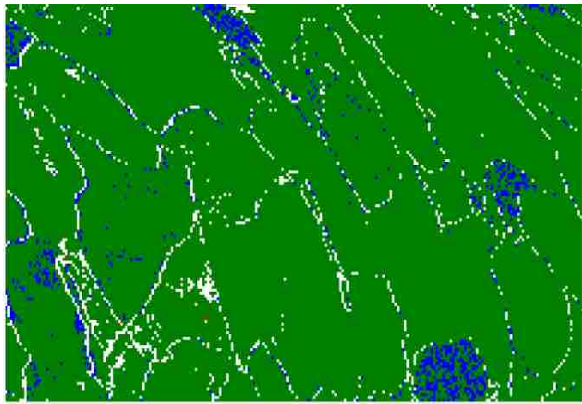
Figure C7: EBSD data from A36 steel, sample location 2-B after impact velocity of 4.51 km/sec showing: a) grain, b) 400X magnification and the original length of the map, and c) phase map.



(a)



(b)

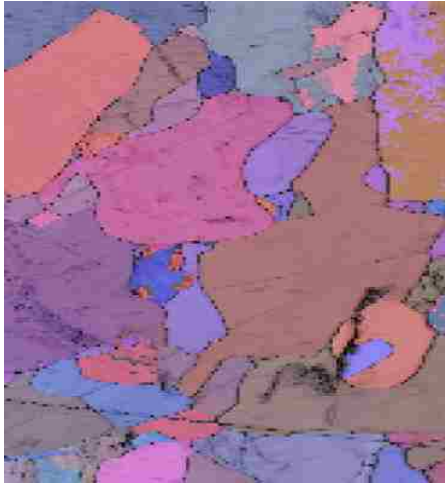


■ BCC
■ FCC
■ HCP

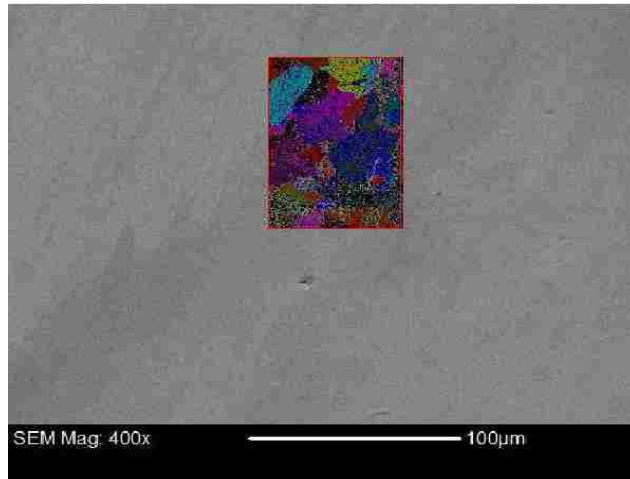
(c)

Table C8 Impact phase ratio of A36 Steel at 4.51 km/sec sample location 3-A	
Crystal Unit Cell Structures	Impact A36 Steel Phase at 4.51 km/sec
BCC	96.82 %
FCC	3.172 %
HCP	0.012 %

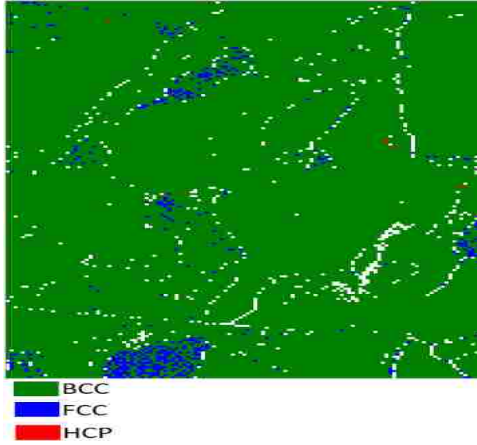
Figure C8: EBSD data from A36 steel, sample location 3-A after impact velocity of 4.51 km/sec showing: a) grain, b) 400X magnification and the original length of the map, and c) phase map.



(a)



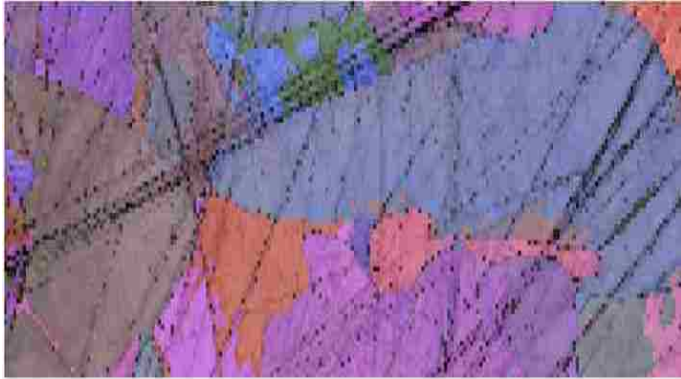
(b)



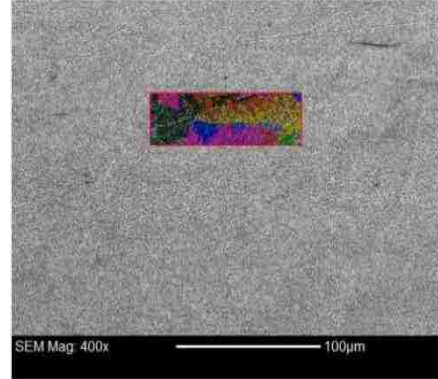
(c)

Table C9 Impact phase ratio of A36 Steel at 4.51 km/sec sample location 4-B	
Crystal Unit Cell Structures	Impact A36 Steel Phase at 4.51 km/sec
BCC	97.82 %
FCC	2.147 %
HCP	0.035 %

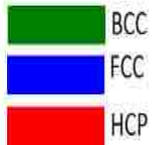
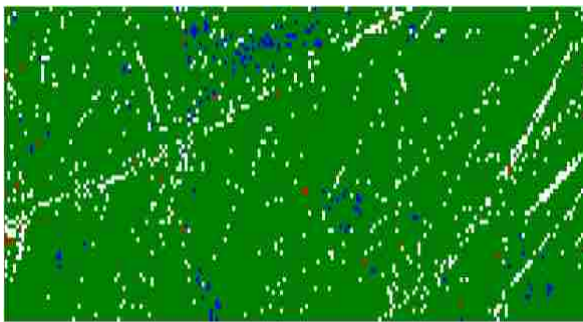
Figure C9: EBSD data from A36 steel, sample location 4-B after impact velocity of 4.51 km/sec showing: a) grain, b) 400X magnification and the original length of the map, and c) phase map.



(a)



(b)

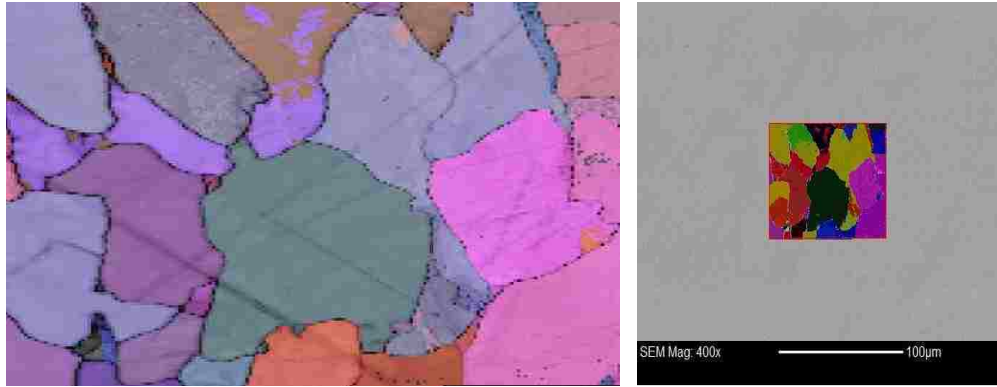


(c)

Table C10 Impact phase ratio of A36 Steel a 4.51 km/sec sample location 5-C

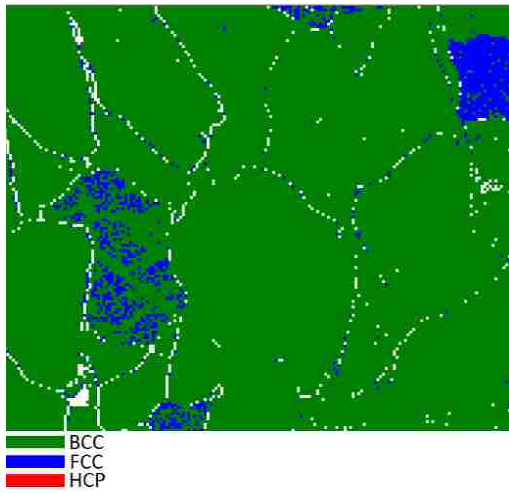
Crystal Unit Cell Structures	Impact A36 Steel Phase at 4.51 km/sec
BCC	98.81 %
FCC	1.087 %
HCP	0.110 %

Figure C10: EBSD data from A36 steel, sample location 5-C after impact velocity of 4.51 km/sec showing: a) grain, b) 400X magnification and the original length of the map, and c) phase map.



(a)

(b)



(c)

Table C11 Impact phase ratio of A36 Steel at 5.80 km/sec sample location 1-D	
Crystal Unit Cell Structures	Impact A36 Steel Phase at 5.80 km/sec
BCC	94.968 %
FCC	5.028 %
HCP	0.003550 %

Figure C11: EBSD data from A36 steel, sample location 1-D after impact velocity of 5.80 km/sec showing: a) grain, b) 400X magnification and the original length of the map, and c) phase map.

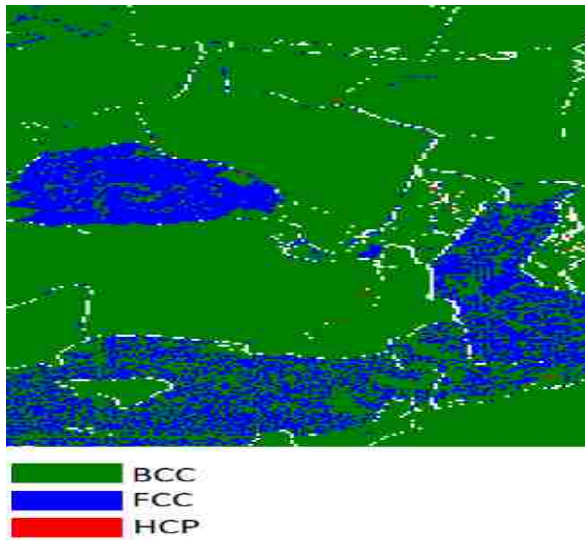
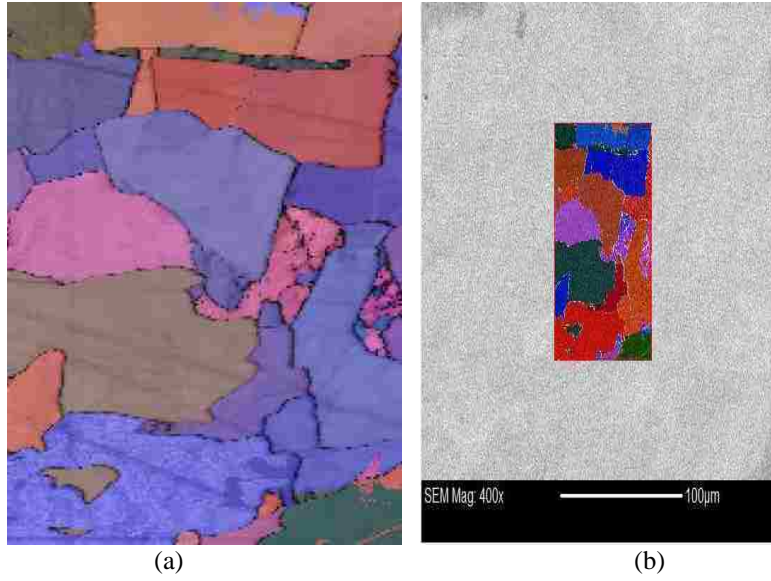


Table C12 Impact phase ratio of A36 Steel at 5.80 km/sec sample location 2-D	
Crystal Unit Cell Structures	Impact A36 Steel Phase at 5.80 km/sec
BCC	83.794 %
FCC	16.139 %
HCP	0.0671 %

Figure C12: EBSD data from A36 steel, sample location 2-D after impact velocity of 5.80 km/sec showing: a) grain, b) 400X magnification and the original length of the map, and c) phase map.

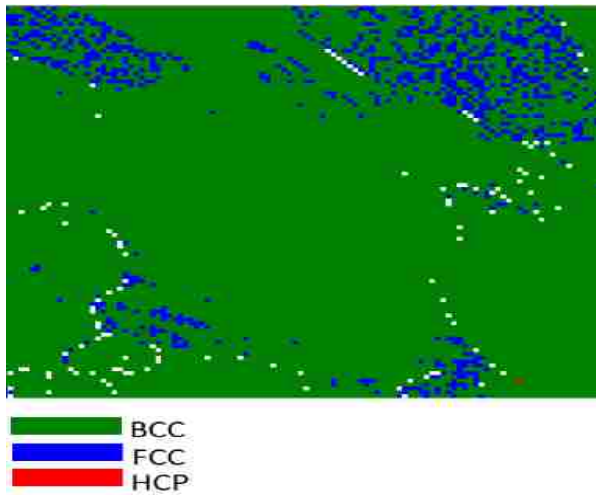
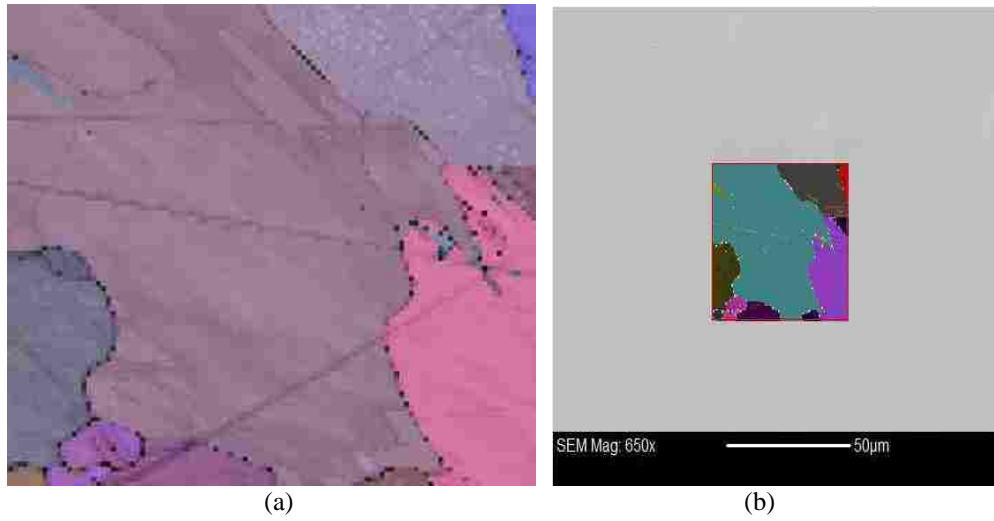
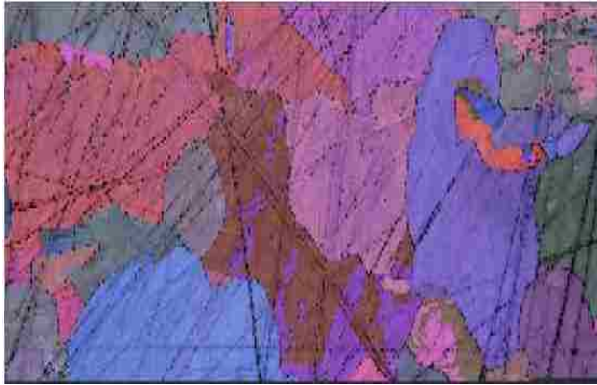
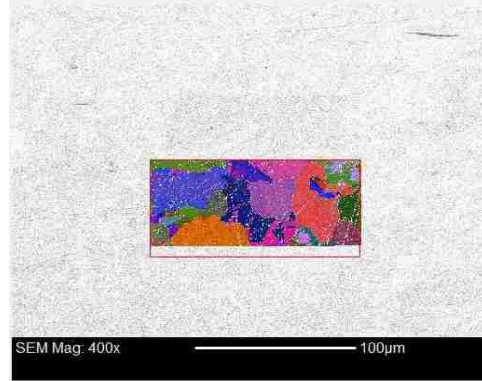


Table C13 Impact phase ratio of A36 Steel at 5.80 km/sec sample location 3-A	
Crystal Unit Cell Structures	Impact A36 Steel Phase at 5.80 km/sec
BCC	92.676 %
FCC	7.3145 %
HCP	0.00892 %

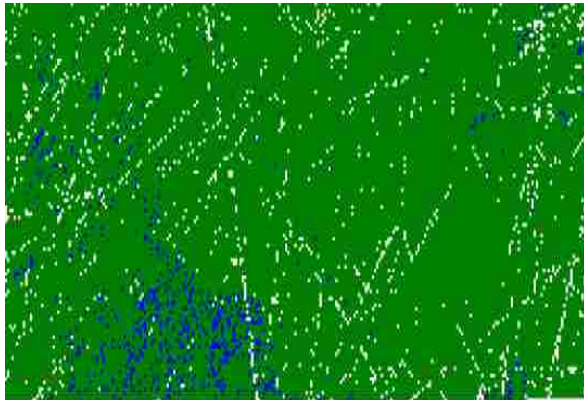
Figure C13: EBSD data from A36 steel, sample location 3-A after impact velocity of 5.80 km/sec showing: a) grain, b) 400X magnification and the original length of the map, and c) phase map.



(a)



(b)



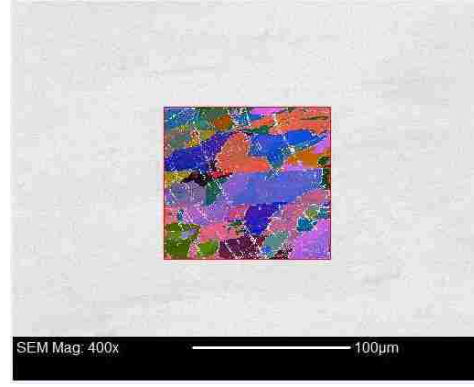
(c)

Table C14 Impact phase ratio of A36 Steel at 5.80 km/sec sample location 4-A	
Crystal Unit Cell Structures	Impact A36 Steel Phase at 5.80 km/sec
BCC	97.520 %
FCC	2.543 %
HCP	0.054 %

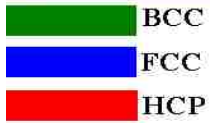
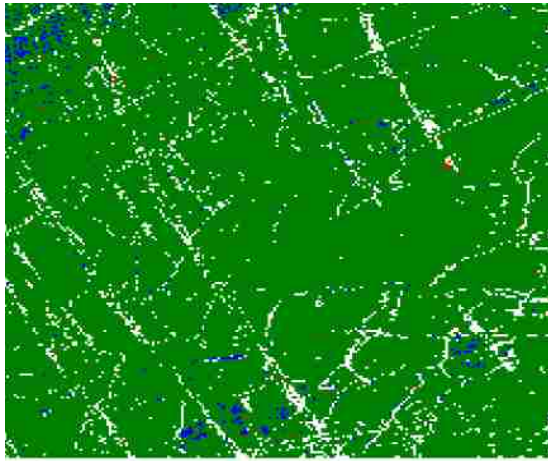
Figure C14: EBSD data from A36 steel, sample location 4-A after impact velocity of 5.80 km/sec showing: a) grain, b) 400X magnification and the original length of the map, and c) phase map.



(a)



(b)



(c)

Table C15 Impact phase ratio of A36 Steel at 5.80 km/sec sample location 5-A	
Crystal Unit Cell Structures	Impact A36 Steel Phase at 5.80 km/sec
BCC	98.66 %
FCC	1.242 %
HCP	0.09 %

Figure C15 : EBSD data from A36 steel, sample location 5-A after impact velocity of 5.80 km/sec showing:
a) grain, b) 400X magnification and the original length of the map, and c) phase map.

APPENDIX D

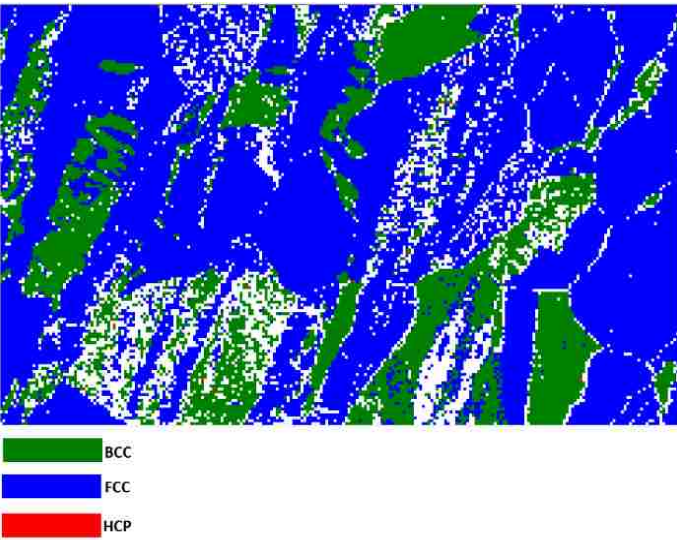
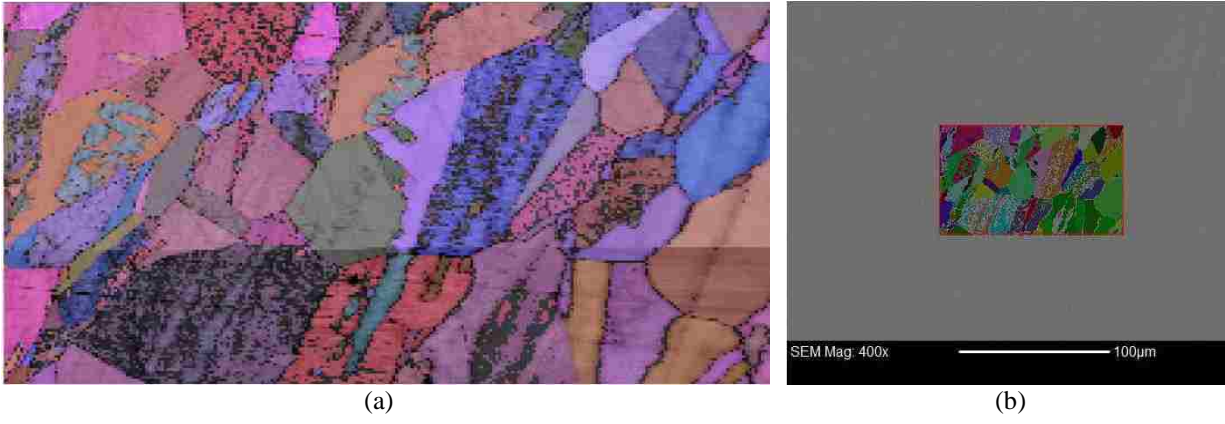
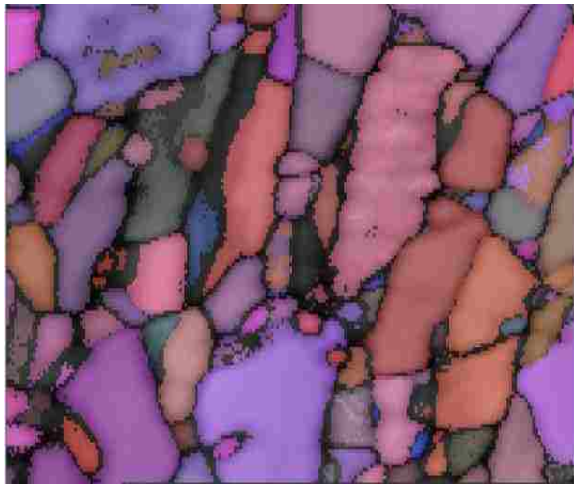


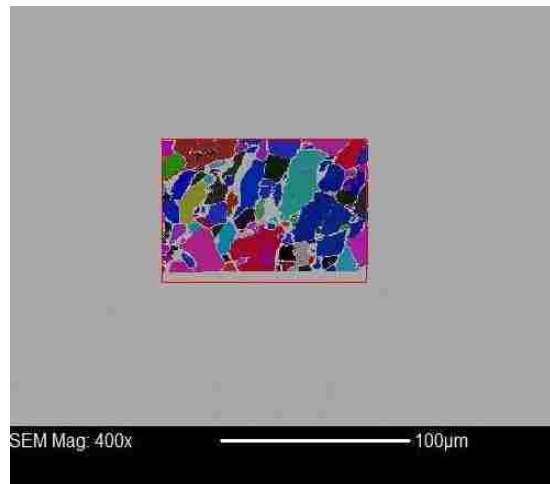
Table D1 Impact phase ratio of 304L Steel at 6.58 km/sec sample location 1-C	
Crystal Unit Cell Structures	Impact A36 Steel Phase at 5.80 km/sec
BCC	24.92 %
FCC	75.038 %
HCP	0.043 %

(c)

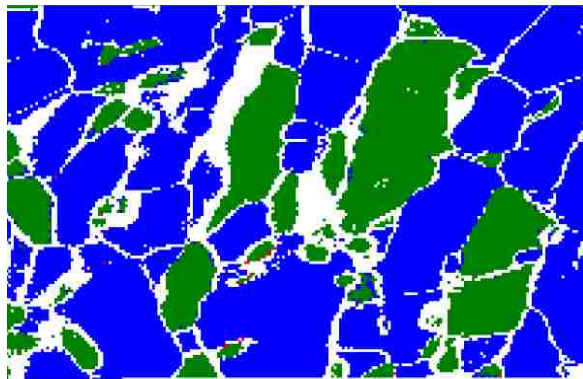
Figure D1: EBSD data from 304L steel, sample location 1-C after impact velocity of 6.58 km/sec showing: a) grain, b) 400X magnification and the original length of the map, and c) phase map.



(a)



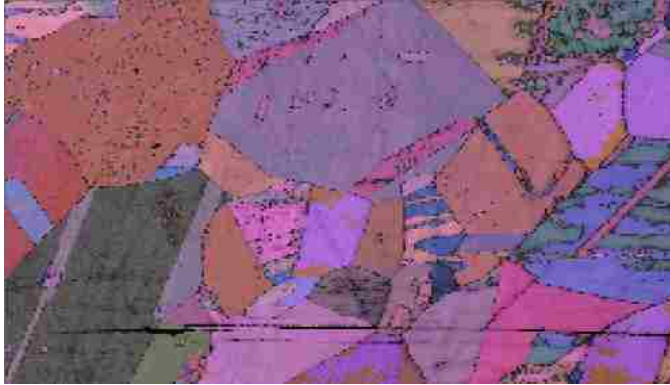
(b)



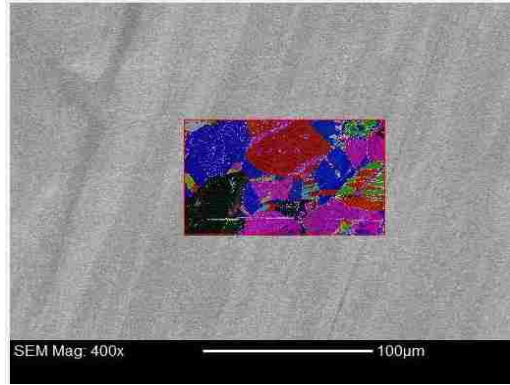
(c)

Table D2 Impact phase ratio of 304L Steel at 6.58 km/sec sample location 2-E	
Crystal Unit Cell Structures	Impact A36 Steel Phase at 5.80 km/sec
BCC	28.0872 %
FCC	71.822 %
HCP	0.09078 %

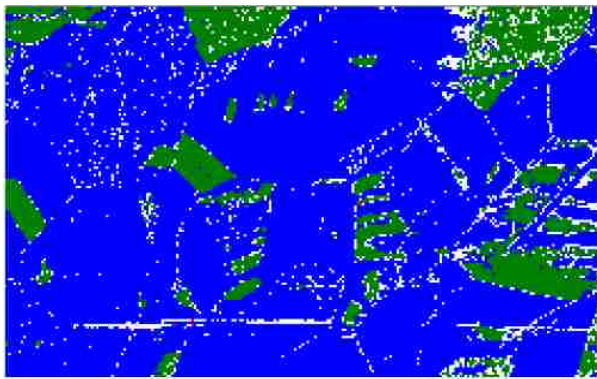
Figure D2: EBSD data from 304L steel, sample location 2-E after impact velocity of 6.58 km/sec showing: a) grain, b) 400X magnification and the original length of the map, and c) phase map.



(a)



(b)

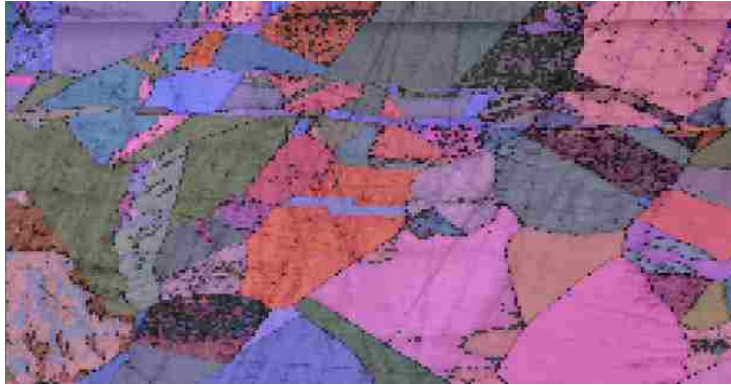


■ BCC
■ FCC
■ HCP

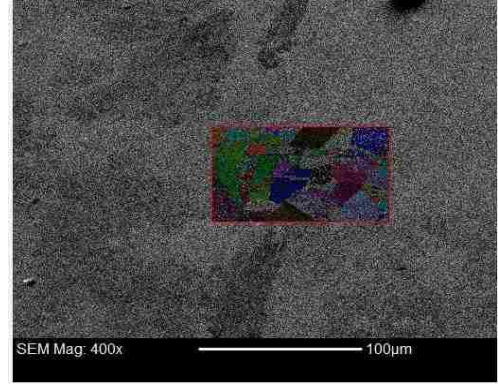
(c)

Table D3 Impact phase ratio of 304L Steel at 6.58 km/sec sample location 3-F	
Crystal Unit Cell Structures	Impact A36 Steel Phase at 5.80 km/sec
BCC	28.0872 %
FCC	71.822 %
HCP	0.09078 %

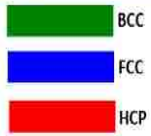
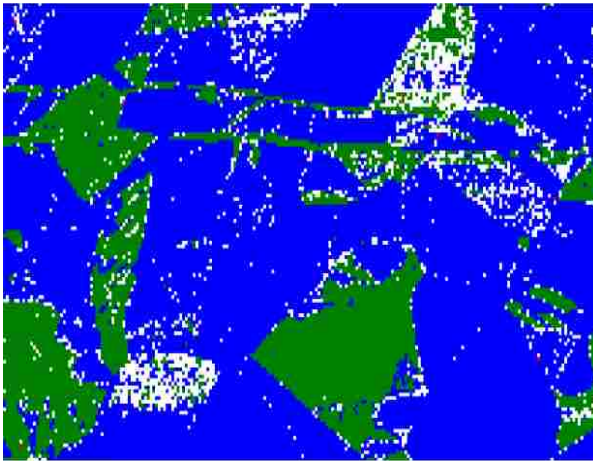
Figure D3: EBSD data from 304L steel, sample location 3-F after impact velocity of 6.58 km/sec showing: a) grain, b) 400X magnification and the original length of the map, and c) phase map.



(a)



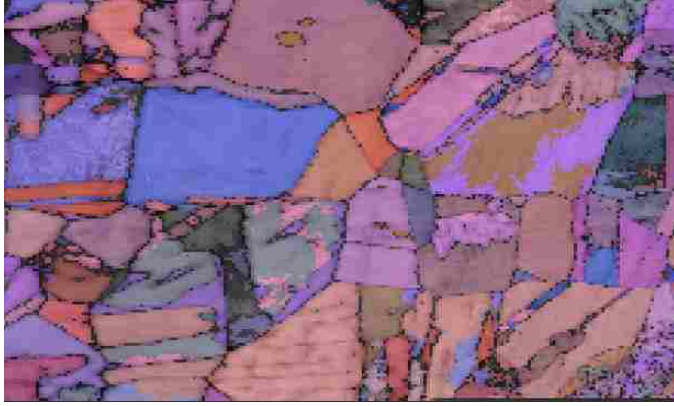
(b)



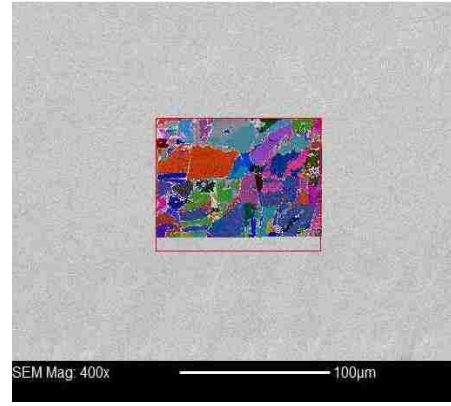
(c)

Table D4 Impact phase ratio of 304L Steel at 6.58 km/sec sample location 4-A	
Crystal Unit Cell Structures	Impact A36 Steel Phase at 5.80 km/sec
BCC	23.75 %
FCC	76.216 %
HCP	0.0313 %

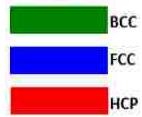
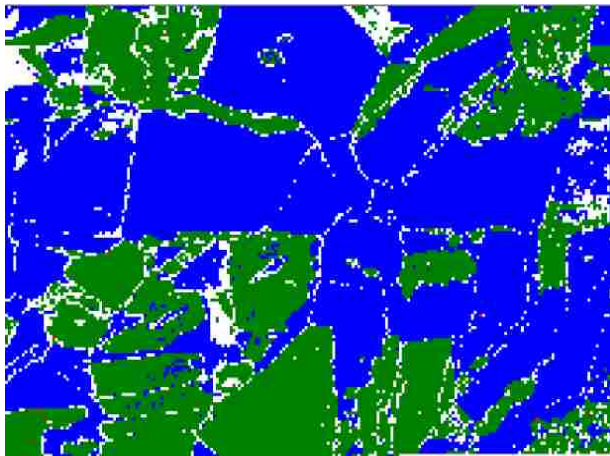
Figure D4: EBSD data from 304L steel, sample location 4-A after impact velocity of 6.58 km/sec showing: a) grain, b) 400X magnification and the original length of the map, and c) phase map.



(a)



(b)



(c)

Table D5 Impact phase ratio of 304L Steel at 6.58 km/sec sample location 5-A	
Crystal Unit Cell Structures	Impact 304L Steel Phase at 6.58 km/sec
BCC	73.388 %
FCC	62.5681 %
HCP	0.044 %

Figure D5: EBSD data from 304L steel, sample location 5-A after impact velocity of 6.58 km/sec showing: a) grain, b) 400X magnification and the original length of the map, and c) phase map.

APPENDIX E

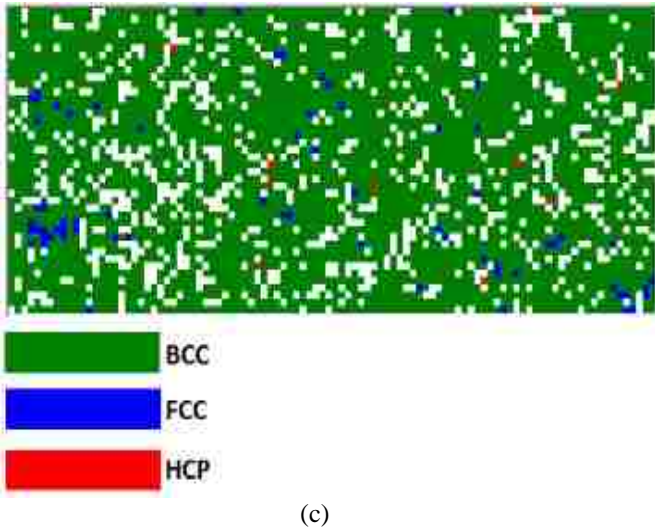
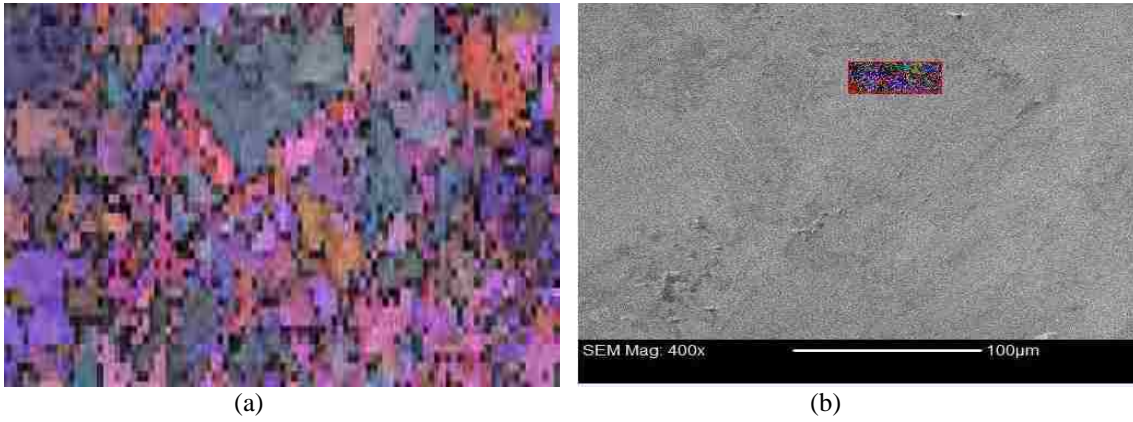
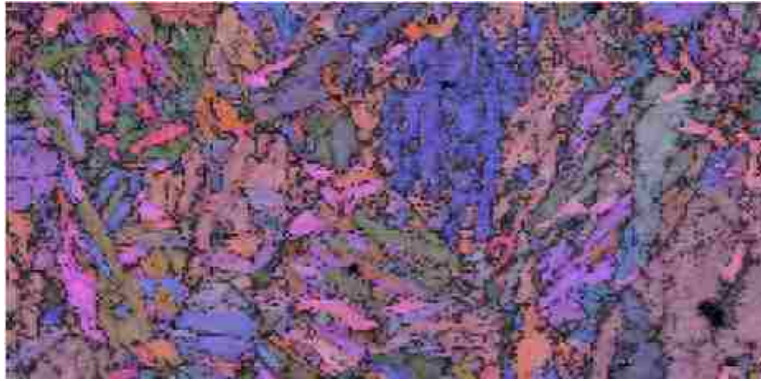
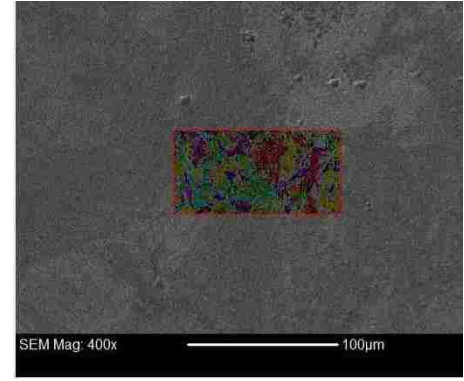


Table E1 Impact phase ratio of HY 100 Steel at 6.70 km/sec sample location 1-D	
Crystal Unit Cell Structures	Impact HY100 Steel Phase at 6.70 km/sec
BCC	97.70 %
FCC	2.01 %
HCP	0.295 %

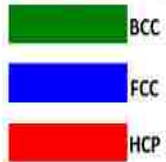
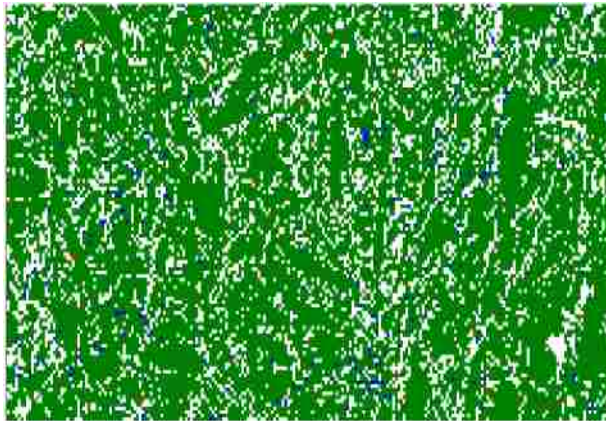
Figure E1: EBSD data from HY100 steel, sample location 1-D after impact velocity of 6.70 km/sec showing: a) grain, b) 400X magnification and the original length of the map, and c) phase map.



(a)



(b)



(c)

Table E2 Impact phase ratio of HY 100 Steel at 6.70 km/sec sample location 2-D	
Crystal Unit Cell Structures	Impact HY100 Steel Phase at 6.70 km/sec
BCC	98.39 %
FCC	1.3577 %
HCP	0.257 %

Figure E2: EBSD data from HY100 steel, sample location 2-D after impact velocity of 6.70 km/sec showing: a) grain, b) 400X magnification and the original length of the map, and c) phase map.

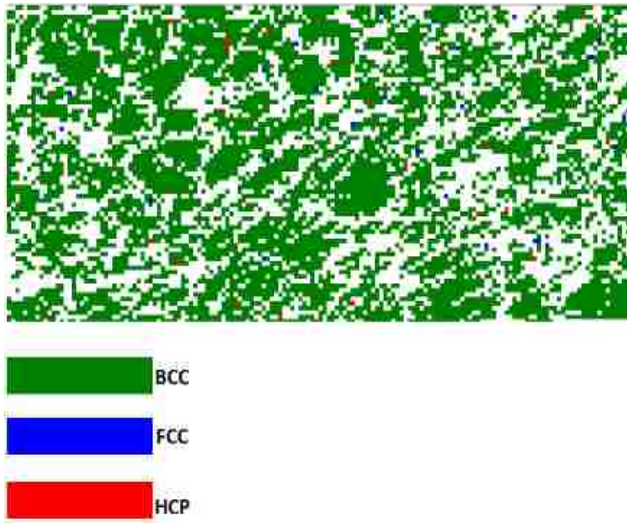
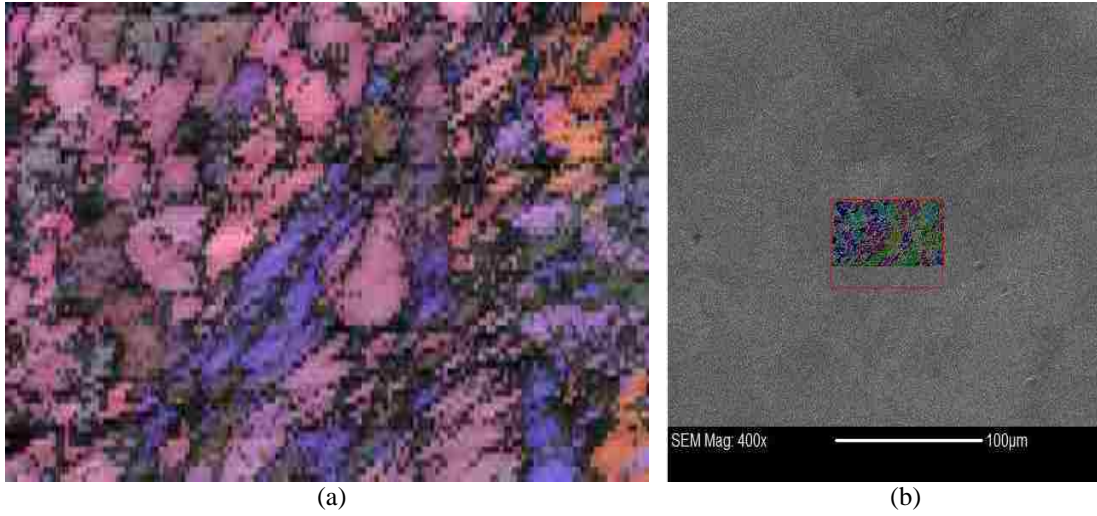
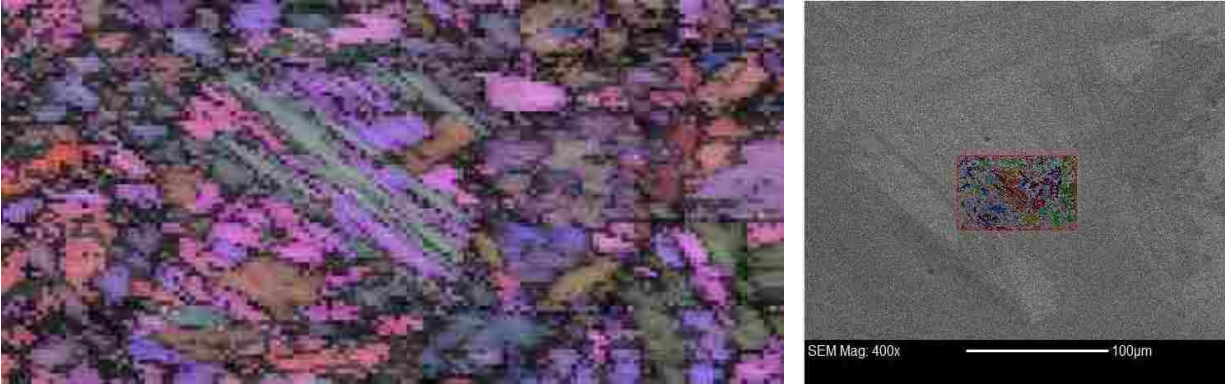


Table E3 Impact phase ratio of HY 100 Steel at 6.70 km/sec sample location 3-C	
Crystal Unit Cell Structures	Impact HY100 Steel Phase at 6.70 km/sec
BCC	99.20 %
FCC	0.41 %
HCP	0.391 %

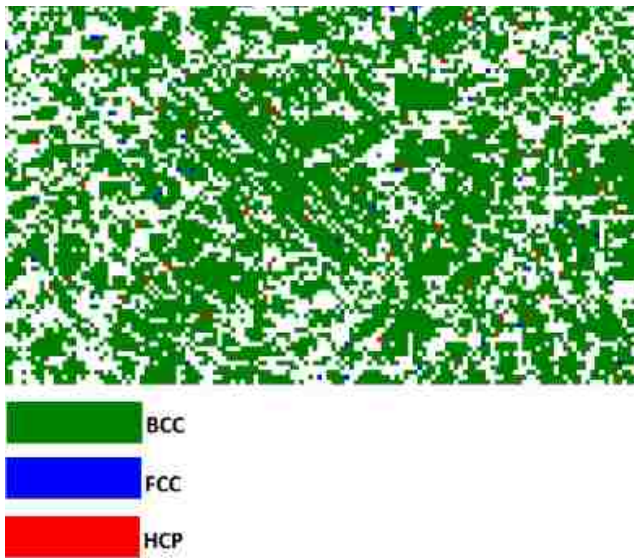
(c)

Figure E3: EBSD data from HY100 steel, sample location 3-C after impact velocity of 6.70 km/sec showing: a) grain, b) 400X magnification and the original length of the map, and c) phase map.



(a)

(b)



(c)

Table E4 Impact phase ratio of HY 100 Steel at 6.70 km/sec sample location 4-C

Crystal Unit Cell Structures	Impact HY100 Steel Phase at 6.70 km/sec
BCC	98.48 %
FCC	0.703 %
HCP	0.820 %

Figure E4: EBSD data from HY100 steel, sample location 4-C after impact velocity of 6.70 km/sec showing: a) grain, b) 400X magnification and the original length of the map, and c) phase map.

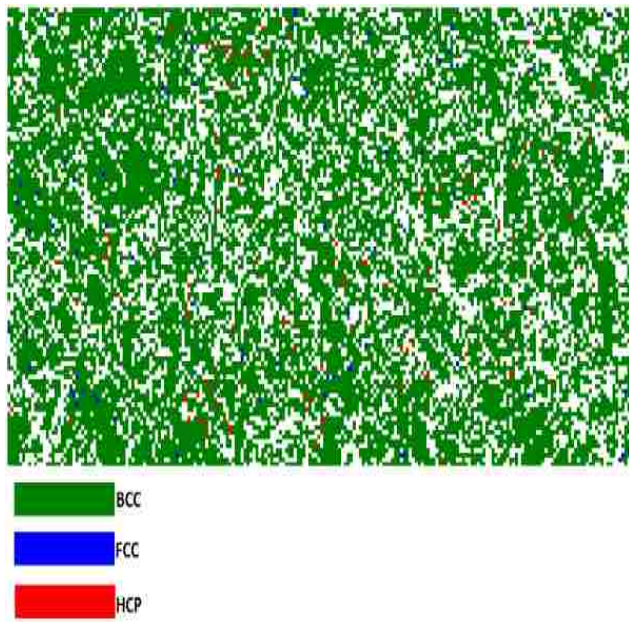
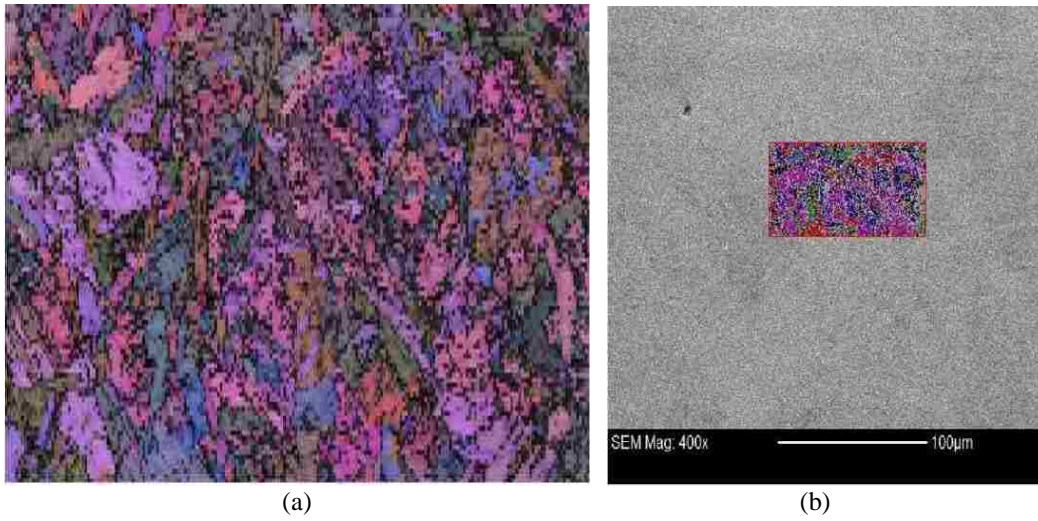


Table E5 Impact phase ratio of HY 100 Steel at 6.70 km/sec sample location 5-A	
Crystal Unit Cell Structures	Impact HY100 Steel Phase at 6.70 km/sec
BCC	98.61 %
FCC	0.467 %
HCP	0.93 %

(c)

Figure E5: EBSD data from HY100 steel, sample location 5-A after impact velocity of 6.70 km/sec showing: a) grain, b) 400X magnification and the original length of the map, and c) phase map.

REFERENCES

1. S. J. Wang, et al., “Microstructural fingerprints of phase transitions in shock-loaded iron”, *Scientific Reports*, 2013; 3:1086. Published online 2013 January 18. doi: 10.1038/srep01086. Website: <http://www.ncbi.nlm.nih.gov/pmc/articles/PMC3548189/>.
2. O.H. Ibrahim, “Comparison of Impact Properties for Carbon and Low Alloy Steels”, *J. Mater. Sci. Technol.*, 2011, 27(10), 931-936.
3. H. Yang, et al., “EBSD study on deformation twinning in AZ31 magnesium alloy during quasi-in-situ compression”, *Advanced Engineering Materials*, 2008, v10, n10, pp. 955 - 960.
4. S. K. Haxena and L. S. Dubrovnik, “Iron phases at high pressures and temperatures phase transition and melting”. *Am. Mineral.* 85, 372–375 (2000).
5. W. D. Crozier and W. Hume, 1957, “High Velocity Light Gas Gun”, *J. Appl. Phys.*, 28, pp. 892-894.
6. W. P. Schonberg and D. Cooper, 1994, "Repeatability and Uncertainty Analysis of NASA/MSFC Light Gas Gun Test Data", *AIAA Journal*, 32(5), pp. 1058-1065.
7. A. C. Mitchell and W. J. Nellis, 1981, “Diagnostic System of the Lawrence Livermore National Laboratory Two-stage Light-gas Gun”, *Review of Scientific Instruments*, 52(3), pp. 347-359.
8. M. Pena, S. Becker, A. Garza, M. Hanache, R. Hixson, R. Jennings, M. Matthes, B. O’Toole, , S. Roy, M. Trabia, “Many Point Optical Velocimetry for Gas Gun Applications”, abstract submitted for the 19th Biennial Conference on Shock Compression of Condensed Matter (SCCM-2015), American Physical Society, Tampa, FL, June 14-19, 2015.
9. M. Pena, R. Hixson, S. Becker, E. Daykin, M. Walling, B. O’Toole, M. Trabia, S. Roy, R. Jennings, M. Matthes, “Use of Multiplexed Photonic Doppler Velocimetry (MPDV) System to Study Plastic Deformation of Metallic Steel Plates in High Velocity Impact”, accepted, proceedings of 2015 SEM Conference & Expo, Costa Mesa CA, June 8-11, 2015.
10. B. O’Toole, M. Trabia, R. Hixson, S. Roy, M. Pena, S. Becker, E. Daykin, E. Machorro, R. Jennings, M. Matthes, “Modeling Plastic Deformation of Steel Plates in Hypervelocity Impact

- Experiments”, to appear in proceedings of 13th Hypervelocity Impact Symposium, Boulder CO, April 27 – May 1, 2015.
11. A. Luttman, M. Howard, E. Machorro, R. Kelly, N. Snipe, K. Crawford, B.T. Meehan, R. Hixson, M. Pena, B. O’Toole, “Analysis Methods for Benchmarking Laser Velocimetry with High-Speed Video in Impact Experiments”, to appear in proceedings of 13th Hypervelocity Impact Symposium, Boulder CO, April 27 – May 1, 2015.
 12. R. Hixson, B. O’Toole, M. Trabia, S. Roy, M. Pena, S. Becker, E. Daykin, E. Machorro, R. Jennings, M. Matthes, “Computational model verification using multiplexed photonic Doppler velocimetry for high velocity projectile impact on steel target”, Abstract & Poster, 7th Multiscale Materials Modeling International Conference, Berkeley, CA, Oct 6-10, 2014.
 13. B. O’Toole, M. Trabia, R. Jennings, S. Roy, M. Matthes, M. Pena, E. Daykin, R. Hixson, S. Becker, C. Perez, E. Machorro, “Multiplexed Photonic Doppler Velocimetry (MPDV) Application in Plastic Deformation Experiments under Hypervelocity Condition”, Abstract, Photonic Doppler Velocimetry Workshop, Las Vegas, NV, June 24-26, 2014.
 14. M. Slewa, B. O’Toole, M. Trabia, “Effect of High Velocity Impact on Grain Structure of A36 Steel”, Abstract, Photonic Doppler Velocimetry Workshop, Las Vegas, NV, June 24-26, 2014.
 15. M. Trabia, B. O’Toole, S. Roy, D. Somasundaram, R. Jennings, M. Matthes, R. Hixson, S. Becker, E. Daykin, M. Pena, E. Machorro, “An Approach for Measuring and Modeling of Plastic Deformation of Metallic Plates During High Velocity Impact”, Extended Abstract, NAFEMS Americas Conference, Colorado Springs CO, May 28-30, 2014.
 16. S. Roy, M. Trabia, B. O’Toole, J. Thota, R. Jennings, D. Somasundaram, S. Becker, E. Daykin, E. Machorro, T. Meehan, R. Hixson, M. Pena, C. Perez, N. Snipe, K. Crawford, S. Gardner, “Plastic Deformation of Steel Plates under High Impact Loading”, Abstract, 84th Shock & Vibration Symposium, Atlanta GA, Nov 3-7, 2013.
 17. B. O’Toole, M. Trabia, R. Jennings, S. Roy, D. Somasundaram, J. Thota, S. Becker, E. Daykin, E. Machorro, T. Meehan, R. Hixson, M. Pena, C. Perez, N. Snipe, A. Luttman, K. Crawford, S.

- Gardner, "Computational Simulation and Experimental Study of Plastic Deformation in A36 Steel during High Velocity Impact", Abstract, ASME Verification & Validation Symposium 2013-13014, May 22-24, 2013, Las Vegas NV.
18. Johnson, G. R., Cook, W. H., 1983. A Constitutive Model and Data for Metals Subjected to Large Strains, High Strain Rates and High Temperatures, 7th International Symposium on Ballistics, The Hague, Netherlands, p. 541.
 19. R. Hixson, personal conversations. Dr. Hixson ran the shock physics gas gun laboratory at Los Alamos National Laboratory, NM for many years.
 20. W.-S. Lee and C.-F. Lin, "Impact Properties and Microstructure Evolution of 304L Stainless Steel", Materials Science and Engineering A 308 (2001), pp 124-135.
 21. Primary Metallic Crystalline Structures (BCC, FCC, HCP)", NDT Resource center, accessed April 4, 2015. Website: https://www.ndeed.org/EducationResources/CommunityCollege/Materials/Structure/metallic_structures.htm
 22. "ASTM A36 Steel Plate", O'Neal The Metals Company, accessed April 4, 2015. Website: <http://www.onealsteel.com/carbon-steel-plate-a36.html>.
 23. "ASTM A36 Mild/Low Carbon Steel", AZO Materials, last update: May 23, 2014, accessed April 4, 2015. Website: <http://www.azom.com/article.aspx?ArticleID=6117#>.
 24. "HY 100 Alloy Steel – UNS K32045", AZO Materials, April 4, 2015. Website: <http://www.doitpoms.ac.uk/tlplib/superelasticity/twinning.php>
<http://www.azom.com/article.aspx?ArticleID=6734>
 25. Flax R. W., Keith R. E., and Randall M. D., 1971, "Welding the HY Steels", American Society for Testing and Materials, ASTM Special Technical Publication 494, ISBN 0-8031-0073-6. Website: http://www.astm.org/DIGITAL_LIBRARY/STP/SOURCE_PAGES/STP494_foreword.pdf
 26. "304/304L Stainless Steel", Brown McFarlane, accessed April 4, 2015. Website: <http://www.brownmac.com/products/stainless-steel-plate/Stainless-Steel-304-and-304l.aspx>.

27. “Stainless Steels – Stainless 304 Properties, Fabrication and Applications, Supplier Data by Aalco, accessed April 4, 2015. Website.
http://www.azom.com/article.aspx?ArticleID=2867#_304L_Stainless_Steel.
28. “304L Stainless Steel”, Penn Stainless Products, Inc., accessed April 4, 2015. Website.
<http://www.pennstainless.com/stainless-grades/300-series-stainless-steel/304l-stainless-steel-2/>.
29. “Deformation Twinning”, University of Cambridge, accessed April 4, 2015. Website.
<http://www.doitpoms.ac.uk/tlplib/superelasticity/twinning.php>
30. Ibrahim, O.H, “Comparison of Impact Properties for Carbon and Low Alloy Steels” Elsevier J. Mater. Sci. Technol., 2011, 27(10), 931-936.
31. U. F, Kocks, C.N. Tomé, and H.-R. Wenk (1998). “Texture and Anisotropy: Preferred Orientations in Polycrystals and their Effect on Materials Properties”, Cambridge University Press.
32. A. Sutton and R. Balluffi, “Interfaces in Crystalline Materials”, Oxford, 1996.
33. U.F. Kocks, C.N. Tomé, and H.-R. Wenk (1998). “Texture and Anisotropy: Preferred Orientations in Polycrystals and their Effect on Materials Properties”, Cambridge University Press
34. A. Sutton and R. Balluffi, “Interfaces in Crystalline Materials”, Oxford, 1996
35. Misorientation diagram “accessed April 7, 2015. Website.
<http://www.ebsd.com/popup/misorientation.htm>
36. V. Randle, and O. Engler, O. (2000).” Texture Analysis: Macrotecture, Microtexture and Orientation Mapping. Amsterdam, Holland, Gordon and Breach”. Materials Science Forum Vols. 467-470 (2004) pp. 573-578 online at <http://www.scientific.net>© 2004 Trans Tech Publications, Switzerland.
37. L.M. Dougherty, et al “Rare twin linked to high-pressure phase transition in iron”, January, 2009, Elsevier Ltd., Acta Materialia Inc.
38. Y. Huajie, et al.” EBSD Study on Deformation Twinning in AZ31MagnesiumAlloy during Quasi-in-Situ Compression” Advanced Engineering Materials 2008, 10, No. 10.

39. S.K. Haxena, and L.S. Dubrovnik, "Iron phases at high pressures and temperatures Phase transition and melting". *Am. Mineral.* 85, 372–375 (2000).
40. A. Halfpenny¹, et al "Using electron backscatter diffraction (EBSD) to measure misorientation between 'parent' and 'daughter' grains, Implications for recrystallization and nucleation." *Materials Science Forum Vols. 467-470 (2004) pp. 573-578.*
41. A.D. Rollett, P.N. Kalu, "Advanced Characterization & Microstructural Analysis" 2007
42. O.N. Senkov¹, et al, "Microstructure of Aluminum-Iron Alloys Subjected to Severe Plastic Deformation" Pergamon PII S1359-6462(98)00073-6 September 8, 1997.
43. W.D. Crozier, and W. Hume, ,1957, "High velocity light gas gun", *J. Appl. Phys.*, 28, 892-894.
44. T. T. De Bues, 2003," An h-adaptive finite element compressible flow solver applied to light-gas gun design". PhD thesis. University of Nevada, Las Vegas
45. A.C. Mitchell, W.J. Nellis, 1981, "Diagnostic system of the Lawrence Livermore National Laboratory two-stage light-gas gun". *Review of Scientific Instruments.* Volume 52, Issue 3, Pages 347-359.
46. W.J. Nellis, A.C. Mitchell, F.H. Ree, M. Ross, N.C. Holmes, R.J. Trainor, and D.J. Erskine, 1991," Equation of state of shock-compressed liquids carbon dioxide and air", *Journal of Chemical Physics*, vol. 95, no. 7, pp. 5268-5272.
47. M. von Ardenne, (1938). "Das Elektronen-Rastermikroskop. Theoretische Grundlagen". *Zeitschrift für Physik (in German)* 109 (9–10): 553–572. Bibcode:1938ZPhy..109..553V. doi:10.1007/BF01341584.
48. VA. Zworykin, J. Hillier, RL. Snyder, (1942) "A scanning electron microscope". *ASTM Bull* 117, 15–23.
49. D. McMullan, (1953). "An improved scanning electron microscope for opaque specimens". doi:10.1049/pi-2.1953.0095.
50. CW. Oatley, WC. Nixon, RFW. Pease (1965) "Scanning electron microscopy". *Advanced Electronics Electron Phys* 21, 181–247.

51. KCA .Smith, CW. Oatley, (1955). "The scanning electron microscope and its fields of application".
British Journal of Applied Physics 6 (11): 391.
52. OC. Wells, (1957) "The construction of a scanning electron microscope and its application to the
study of fibres" PhD Dissertation, Cambridge University
53. "Scanning Electron Microscope" Purdue University accessed April 7, 2015. Website:
<https://www.purdue.edu/ehps/rem/rs/sem.htm>
54. E. Jumate, and D.L. Manea, (2011), "X-Ray diffraction study of hydration processes in the Portland
cement", Journal of Applied Engineering Sciences, Vol. 1(14), Issue 1, pp.79-86.
55. C. Gheorghie, (1990)," Control structure fine a metalelor cu radial ii X "Control the fine structure of
metals with radiation X", Ed.Tehnic Bucure ti.
56. E. Jumate, , D.L. Manea, "X-Ray Diffraction Study of Hydration Processes in the Portland
Cement", JAES_1(14)_1_2011
57. "Powder X-ray Diffraction" UCDavis accessed April 7, 2015. Website.
[http://chemwiki.ucdavis.edu/Analytical_Chemistry/Instrumental_Analysis/Diffraction/Powder_X-
ray_Diffraction](http://chemwiki.ucdavis.edu/Analytical_Chemistry/Instrumental_Analysis/Diffraction/Powder_X-ray_Diffraction)
58. B.D. Cullity, "Elements of X-ray diffraction Addison–Wesley", 1978 ISBN 0-201-01174-3 Chapter
14
59. B.E. Warren, (1969/1990) "X-ray diffraction ", Addison–Wesley, Reading MA/Dover, Mineola
NY ISBN 0-486-66317-5.
60. S.E. Dann," Reactions and Characterization of Solids", R oyal Society of Chemistry, USA (2002).
61. D.A Skoog, Holler, F.J.; Crouch, S.R. "Principles of Instrumental Analysis". Sixth Edition,
Thomson Brooks/Cole, USA (2007)
62. "Introduction to Orientation Imaging Microscopy" EDAX accessed April 7, 2015. Website.
<http://web.stanford.edu/group/snl/SEM/OIMIntro.htm>
63. U.F. Kocks, C.N. Tomé, and H.-R. Wenk (1998). "Texture and Anisotropy: Preferred Orientations
in Polycrystals and their Effect on Materials Properties", Cambridge University Press.

64. A. Sutton and R. Balluffi, "Interfaces in Crystalline Materials", Oxford, 1996
65. "Misorientation diagram" accessed April 7, 2015. Website.
<http://www.ebsd.com/popup/misorientation.htm>
66. V. Randle, and O. Engler, (2000). "Texture Analysis: Macrotecture, Microtexture and Orientation Mapping. Amsterdam, Holland, Gordon and Breach". Materials Science Forum Vols. 467-470 (2004) pp. 573-578 online at <http://www.scientific.net> © 2004 Trans Tech Publications, Switzerland.

CURRICULUM VITAE

Graduate College
University of Nevada, Las Vegas

Muna Slewa

Degrees:

Bachelor of Science Mechanical Engineering University of Technology, Baghdad – Iraq	2000
Master of Science in Material Engineering University of Technology- Iraq	2002
Doctorate of Philosophy in Material Engineering University of Technology, Baghdad – Iraq	2005

Honors and Awards:

- Instructor,
 - University of Technology, Baghdad Aug. 1997- Aug. 2007
 - Measurement Lab
 - Computer Lab
 - Heat Transfer
 - Undergraduate Math course
 - Metallurgy of Materials
 - Machine Workshop
 - AL Sham University, Damascus, Syria Aug 2007 - Aug. 2008
 - Taught Numerical Analysis
- Graduate Assistant, Aug. 2011 - Dec. 2013
 - University of Nevada, Las Vegas, NV
 - Taught Lab 421 Automatic Control
 - Taught Lab 302 Materials Mechanics
 - Research study on the Fischer Space Pen
- Graduate Assistant, Aug. 2013 – Dec. 2015
University of Nevada, Las Vegas, NV
 - Taught Lab 302 Materials Mechanics
 - Research study at Fischer Space Pen
 - Research study at Gas Gun Lab
 - Extensive practical experience using SEM (Scanning Election Microscope) XRD Microscope, EBSD. Electron Back Scattered Diffraction
 - Work as a Graduate Research with PDV workshop June 2014

- Work as a Graduate Research in Los Alamos/ National laboratory Dec. 2014
- Member of The National Society of Leadership and Success

Publications:

- M.Slewa, A.Yousif, University of Technology, Baghdad Treatment of Iraq “Bauxite and its Application in Melting Crucibles “ 2005
- M. Slewa, B. O’Toole, M. Trabia, “Effect of High Velocity Impact on Grain Structure of A36 Steel”, Abstract, Photonic Doppler Velocimetry Workshop, Las Vegas, NV, June 24-26, 2014.
- B. O’Toole, M. Trabia, M. Slewa, et al. “Plastic Deformation of Steel Plates under High Impact Loading” Department of Energy and supported Workshop, Las Vegas, NV, Mar, 28 2014.
- M.Slewa, Department of Mechanical Engineering “Investigation of Phase Change in A36 Steel as a Result of High Velocity Impact Loading” Workshop, Las Vegas, NV, May 2014

Dissertation Title: Crystalline Phase Change in Steel Alloys due to High Speed Impact

Dissertation Examination Committee:

Chairperson, Dr. Brendan O’Toole, Ph.D.

Committee Member, Dr. Mohamed Trabia, Ph.D.

Committee Member, Dr. Samaan Ladkany, Ph.D.

Committee Member, Dr. Zhiyong Wang, Ph.D.

Graduate College Representative, Dr. Moses Karakouzian, Ph.D.